Role of CO^2 in the transfer of economic metals by geological fluids

Maria Kokh

To cite this version:

Maria Kokh. Role of CO^2 in the transfer of economic metals by geological fluids. Soil study. Université Paul Sabatier - Toulouse III, 2016. English. NNT : 2016TOU30006 . tel-01371895

HAL Id: tel-01371895
https://theses.hal.science/tel-01371895

Submitted on 26 Sep 2016

THÈSE

En vue de l'obtention du

DOCTORAT DE L'UNIVERSITÉ DE TOULOUSE

Délivré par :

Université Toulouse 3 Paul Sabatier (UT3 Paul Sabatier)

Présentée et soutenue par :
Maria KOKH
le vendredi 22 janvier 2016

Titre :

Rôle du CO2 dans les transferts des métaux d'intérêt économique par les fluides géologiques

---

École doctorale et discipline ou spécialité :
ED SDU2E : Sciences de la Terre et des Planètes Solides

Unité de recherche :
Géosciences Environnement Toulouse (GET)

Directeur/trice(s) de Thèse :

Gleb Pokrovski (directeur de thèse),
Damien Guillaume (co-directeur de thèse), Stéfano Salvi (co-directeur de thèse)

Jury :
Isabelle Daniel, Professeur U. Claude Bernard Lyon 1, Laboratoire de Géologie de Lyon (Rapporteur)
Michel Cathelineau, Directeur de Recherche CNRS, GeoRessources (Rapporteur)
Isabelle Martinez, Maître de Conférences, Université Paris Diderot, IPGP (Examinateur)
Andri Stefánsson, Associated Professeur, U. of Iceland (Examinateur)
François Martin, Professeur, U. Paul Sabatier Toulouse III, GET (Président du jury)
Gleb Pokrovski, Directeur de Recherche CNRS, GET (Directeur de thèse)
Stéfano Salvi, Chargé de Recherche CNRS, GET (Co-directeur de thèse)

THÈSE

En vue de l'obtention du

DOCTORAT DE L'UNIVERSITÉ DE TOULOUSE

Délivré par *l'Université Toulouse III – Paul Sabatier*
Discipline ou spécialité : *Géochimie*

Présentée et soutenue par *Kokh Maria*
Le 22 janvier 2016

Titre :
Rôle du CO_2 dans les transferts des métaux d'intérêt économique par les fluides géologiques

JURY

Isabelle Daniel, Professeur U. Claude Bernard Lyon 1, Laboratoire de Géologie de Lyon (Rapporteur)
Michel Cathelineau, Directeur de Recherche CNRS, GeoRessources (Rapporteur)
Isabelle Martinez, Maître de Conférences, Université Paris Diderot, IPGP (Examinateur)
Andri Stefánsson, Associated Professeur, U. of Iceland (Examinateur)
François Martin, Professeur, U. Paul Sabatier Toulouse III, GET (Président du jury)
Gleb Pokrovski, Directeur de Recherche CNRS, GET (Directeur de thèse)
Stéfano Salvi, Chargé de Recherche CNRS, GET (Co-directeur de thèse)

Ecole doctorale : *Sciences de l'Univers, de l'Environnement et de L'Espace (SDU2E)*
Unité de recherche : *Géosciences Environnement Toulouse (GET)*
Directeur(s) de Thèse : *Gleb Pokrovski (directeur de thèse),*
Damien Guillaume (co-directeur de thèse), Stéfano Salvi (co-directeur de thèse)

REMERCIEMENTS

Ce travail de thèse a été réalisé au sein du laboratoire Géosciences Environnement Toulouse (UMR 5563, Université de Toulouse, UPS, CNRS, IRD). Cette thèse a bénéficié d'une allocation de recherche du Ministère de l'Éducation Nationale de l'Enseignement Supérieur et de la Recherche (bourse MENSR accordé par le président de l'UPS), et d'un financement de l'Université Paul Sabatier dans le cadre de l'AO du conseil scientifique de l'UPS (projet CO2MET) et d'un financement de l'ANR (projet SOUMET ANR-2011-Blanc SIMI 5-6 009).

Je tiens tout d'abord à remercier mon directeur de thèse, Gleb Pokrovski, pour m'avoir fait confiance malgré les connaissances plutôt légères que j'avais en septembre 2012 sur la métallogénie, puis pour m'avoir guidée, encouragée, conseillée, fait voyager pendant presque quatre ans tout en me laissant une grande liberté. J'ai pu grâce à lui me perfectionner dans des disciplines qui n'étaient pas, initialement, mes disciplines de prédilection, en particulier la thermodynamique et la chimie analytique. Je remercie également mes co-directeurs de thèse, Damien Guillaume et Stefano Salvi, qui ont toujours su donner de leur temp pour discuter avec moi la méthodologie de la géochimie expérimentale et la géologie des gisements métallifères.

Je remercie également Nikolay Akinfiev qui a trouvé le temps pour m'apprendre à utiliser correctement son logiciel pendant ma visite en Russie que j'ai pu effectuer durant ma thèse grâce à une bourse ATUPS (août-septembre 2014).

Merci aussi à tous les techniciens et ingénieurs qui ont toujours été prêts à me donner leur assistance professionnelle. En particulier, merci à Pascal Gisquet, Alain Castillo, Stéphanie Mounic, Philippe Besson, Carole Causserand, Aurélie Lanzanova, Frédéric Candaudap, Jérôme Chmeleff, Manuel Henry, Jonathan Prunier, Thierry Aigouy, Michel Thibaut, Sophie Gouy et Philippe de Parseval.

Merci à Jacques Schott, Pascale Bénézeth, Alexandre Zotov et Dmitriy Grichuk pour des discussions scientifiques productives.

Un grand merci aux doctorants du laboratoire pour leur sympathie. Je remercie tout particulièrement mes collègues de bureau Léandre Ponthus, Sylvain Block, Damien Roques et Santiago Yepes qui ont su détendre l'atmosphère lors des moments difficiles.

Je remercie mes parents qui m'ont motivée et soutenue tout au long de mes études supérieures.

Table des matières

Introduction générale

Le carbone est un élément omniprésent dans toutes les enveloppes terrestres, depuis le noyau jusqu'à l'atmosphère. Par conséquant, il est largement impliqué dans la quasi totalité des processus géologiques et biologiques. Une recherche d'article sur Web of Science en mettant «CO_2» dans le titre retourne 115 973 entrées (au 25 Octobre 2015). La très grande majorité de ces études a été consacrée au cycle géologique/biologique *externe* du carbone, et au rôle du gaz carbonique dans la vie, le climat, la sédimentation et l'altération à la surface de la Terre. Par contre, un aspect important du CO_2, encore très mal connu à présent, concerne son impact dans les profondeurs de notre planète. À l'intérieur de la Terre, il n'y pas que des roches, il y a aussi des fluides essentiellement aqueux mais très souvent enrichis en CO_2 et qui sont les acteurs principaux dans les processus géologiques opérant dans la lithosphère terrestre aux hautes températures et pressions. Ces fluides altèrent et dissolvent les roches, affectent la cristallisation des magmas et l'activité volcanique, ils forment des dépôts métallifères d'intérêt économique. *Le but ultime de ce travail de thèse est de mieux comprendre le rôle du CO_2 dans ces processus de transfert des métaux par les fluides géologiques menant à la formation des ressources minérales sur Terre.*

La formation d'un gisement hydrothermal métallifère implique une source de fluide, une source de métaux (comme une roche ou un magma, ces deux sources pouvant être réunies dans un même endroit), une source de chaleur et un milieu perméable (porosité de roches ou présence de fractures et failles). Un mouvement de fluide enrichi en métaux, sels et volatils est alors possible jusqu'à la précipitation des minerais qui est déclenchée par un changement subit des conditions du milieu (e.g., refroidissement, ébullition, mélange de fluides, interaction avec des roches de compositions contrastées). Tous les gisements hydrothermaux des métaux d'intérêt économique comme, par exemple, l'or, le platine, le cuivre, le zinc, le molybdène, l'étain et bien d'autres, se sont formés via la mobilisation, le transport et la précipitation des éléments à partir d'une phase fluide. Pour expliquer ces processus complexes, il est nécessaire de *connaître la solubilité des minéraux et l'état chimique des éléments dissous, ainsi que leur spéciation en phase fluide.* Aujourd'hui grâce à de nombreux travaux expérimentaux, analytiques et de modélisation, nous connaissons relativement bien l'effet des constituants majeurs des fluides terrestres que sont l'eau, les sels et le soufre sur la spéciation chimique, la solubilité et le transport des métaux. Paradoxalement, le CO_2 qui est le deuxième volatil par abondance (après l'eau) dans les fluides associés à tous les grands types de gisements de différentes origines (magmatique, métamorphique ou skarn) a reçu très peu d'attention dans la plupart des modèles géochimiques et métallogéniques.

Cette 'négligeance' est due au fait que le CO_2 a toujours été considéré comme une substance chimiquement neutre, c'est à dire, très peu réactive en phase fluide vis-à-vis des éléments dissous et des minéraux, contrairement aux autres constituants majeurs des fluides comme le soufre, les acides et les sels qui complexent les métaux et réagissent fortement avec les roches. Le CO_2 est connu comme un acide très faible qui se dissocie dans l'eau en produisant les ions bicarbonates et carbonates suivant les réactions :

$$CO_2 + H_2O = HCO_3^- + H^+ \quad (1.1)$$

$$HCO_3^- = CO_3^{2-} + H^+ \quad (1.2)$$

Cependant, les constantes d'équilibre de ces réactions en solution aqueuse aux conditions ambiantes sont de l'ordre de 10^{-6} et 10^{-10}, respectivement, impliquant qu'elles ne sont importantes qu'aux pH neutres et basiques. Les valeurs de ces constantes d'équilibre diminuent avec l'augmentation de la température et la diminution de la densité de l'eau, ce qui implique que les ions carbonatés sont encore moins abondants dans la plupart des fluides et vapeurs hydrothermaux d'origine magmatique ou métamorphique, caractérisés généralement par des pH acides. En effet, si des complexes (bi)carbonatés sont connus pour certains métaux en solution aqueuse à basse température, il n'existe pas de données explicites pour aucun des métaux (notamment ceux d'intérêt économique) en conditions hydrothermales (T > 200°C) dans la plupart des fluides et vapeurs où la molécule neutre CO_2 est supposée être prédominante.

Dans de telles conditions, la présence du CO_2 (comme celle de tout autre gaz) dans le fluide a pour effet d'élargir le champs d'immiscibilité, en terme de température, pression et salinité, dans le système eau-sel en permettant la coexistence d'une phase liquide riche en eau et sel et d'une phase vapeur riche en CO_2 et, éventuellement, d'autres composés volatils moins abondants (e.g., H_2, H_2S, SO_2). Il en résulte une démixtion à plus haute température et pression et plus faible salinité comparée à celle dans un système eau-sel sans CO_2. Cependant, si ces relations de phase eau-gaz-sel sont connues depuis longtemps, aucune donnée directe n'existe sur le comportement, la spéciation et le partage des métaux dans ces systèmes biphasés omniprésents lors de l'évolution des fluides dans la croûte terrestre.

Enfin, un effet du CO_2, toujours en tant que composé chimiquement neutre et apolaire, qui est beaucoup moins connu, est d'abaisser la constante diélectrique (la permittivité) et l'activité de l'eau dans le solvant H_2O-CO_2 supercritique. Il en résulte une diminution de la solubilité de la plupart des composés ioniques et des minéraux dont la dissolution est contrôlée par les phénomènes d'hydratation. Les rares données expérimentales sur les minéraux majeurs (e.g., quartz) et les modèles thermodynamiques disponibles attestent de ce comportement. Cependant, cette connaissance contraste avec le phénomène de solvatation sélective par le CO_2 supercritique de certains composés organiques et complexes soufrés et phosphorés de métaux (un phénomène utilisé dans l'industrie agroalimentaire, pharmaceutique et cosmétique pour la synthèse et la purification chimique de divers composés organiques, par exemple, e.g. la décaféination du café).

Ces deux effets contrastés du CO_2 n'ont jamais été investigués pour les métaux d'intérêt économique dans les fluides naturels riches en CO_2. Par conséquant, l'effet du CO_2 sur le comportement des métaux dans les fluides d'origine magmatique et métamorphique ou dans les fluides des réservoirs de stockage géologique du CO_2, ainsi que les nombreuses observations d'associations des gisements d'or, de cuivre et de fer avec des fluides riches en CO_2, demeurent dans la plupart des cas inexpliqués.

Cette thèse a pour but de tenter de combler cette lacune dans notre connaissance des fluides géologiques en mettant en œuvre une approche combinée expérimentale, analytique et de modélisation.

Les objectifs concrets de ce travail sont les suivants :

1) systématiser notre connaissance sur l'abondance, le comportement géochimique et le rôle du CO_2 (et d'autres formes chimiques de carbone) dans les transferts des métaux et la formation des dépôts économiques par les fluides géologiques ;

2) obtenir de premières données directes et quantitatives sur la solubilité de divers métaux d'intérêt économique (métaux de base comme Fe, Zn, Cu ; métaux critiques comme Sn, Mo, et métaux précieux comme Au et Pt) dans les fluides supercritiques riches en CO_2 aux conditions contrôlées du laboratoire choisies proches de celles des gisements hydrothermaux de ces métaux ;

3) étudier l'effet de démixtion du fluide sur la distribution et la spéciation des métaux entre la phase liquide riche en sel et la phase vapeur riche en CO_2 aux conditions typiques de ces phénomènes en milieu hydrothermal ;

4) développer, en se basant sur ces nouvelles données expérimentales, un modèle physico-chimique capable de prédire les capacités des fluides à transporter et déposer les métaux en présence du CO_2 aux conditions de la formation des gisements; ce modèle pourrait aussi être applicable aux conditions industrielles d'utilisation du CO_2 supercritique comme solvant et dans les sites de stockage géologique du CO_2 ;

5) évaluer les conditions géologiques favorables pour le transfert ou la précipitation des métaux en présence du CO_2 et confronter nos résultats avec des cas géologiques concrets.

Le présent manuscrit est constitué de cinq chapitres.

Le chapitre 1 présente l'état de l'art sur la géochimie du carbone, ses grands cycles externes et internes et ses flux globaux entre les grandes enveloppes terrestres. Ce chapitre passe également en revue les teneurs, la distribution et la spéciation chimique du carbone dans les fluides géologiques opérant dans la lithosphère. Cette révision critique de données de la littérature nous permet d'identifier les lacunes dans notre connaissance du comportement du carbone et, en particulier, de sa forme la plus abondante, le CO_2, et de son rôle dans les transferts des métaux et la formation de leurs ressources minérales sur Terre.

Le chapitre 2 fournit la description détaillée des méthodes expérimentales, analytiques et de modélisation mises en œuvre dans ce travail pour tenter de combler ces lacunes. Bien que certaines de ces approches aient été développées dans des études précédentes, la plupart des méthodes utilisées ont été améliorées et adaptées au besoin de notre étude sur les fluides complexes, riches en CO_2, sous des hautes températures et pressions. En particulier, un grand effort a été fait dans cette thèse pour mettre en œuvre des méthodes expérimentales sur des fluides supercritiques et des techniques analytiques afin de quantifier l'ensemble des métaux et volatils dans de tels fluides. Enfin, nous présenterons les principes de calcul d'équilibre chimique, les modèles décrivant les propriétés thermodynamiques des espèces aqueuses et les bases de données que nous avons utilisées pour interpréter les résultats de nos mesures.

Le chapitre 3, présenté sous la forme d'un article complet soumis à Geochim. Cosmochim. Acta en octobre 2015, décrit les mesures de solubilité pour un grand nombre de métaux d'intérêt économique (Fe, Cu, Zn, Si, Mo, Sn, Au, Pt) dans des fluides CO_2-H_2O-sel-soufre dans les gammes de températures 350-450°C et de pression 500-1000 bar. Sur la base de ces données systématiques sur les métaux dans les fluides riches en CO_2 qui n'ont pas d'équivalent dans la litérature, nous avons développé un modèle thermodynamique basé sur la constante diélectrique du solvant H_2O-CO_2 et qui permet la prédiction de la spéciation des métaux et de la solubilité de leurs minéraux dans une large gamme de température, pression, teneurs en CO_2 et composition du fluide. Ces résultats permettent d'interpréter le fractionnement et le transport des métaux par les fluides riches en CO_2 lors de la formation de divers types de gisements hydrothermaux.

Le chapitre 4, présenté sous forme d'article qui sera prochainement soumis à Geochim. Cosmochim. Acta, décrit les résultats des mesures des coefficients de partage pour le même ensemble des métaux entre la phase liquide et la phase vapeur en fonction du CO_2 dans les systèmes eau-sel(-soufre) à 350°C et 150-300 bar qui simulent les conditions typiques d'ébullition des fluides hydrothermaux. Ces données permettent d'évaluer, pour la première fois, l'effect du CO_2 et du soufre sur le fractionnement des métaux dans les systèmes hydrothermaux lors de la séparation de phases.

Enfin, le chapitre 5 présente les grandes conclusions de ce travail et discute les perspectives et les directions nouvelles ouvertes par nos études, en particulier une meilleure compréhension de la spéciation du carbone lui-même dans les fluides de haute température et pression et du rôle des formes de valence intermédiaire (e.g., CO, ligands organiques) dans la mobilisation et le transport des métaux.

En outre, le manuscrit contient des annexes décrivant certains développements techniques de réacteurs hydrothermaux et de protocoles analytiques effectuées dans ce travail. Ces détails pourraient servir de notice technique pour des études futures qui utiliseront les mêmes équipements expérimentaux ou analytiques. Deux articles publiés dont je suis co-auteur sont également joints à cette annexe. Bien que ces études ne fassent pas directement partie de mon sujet de thèse sur le CO_2, j'ai pu y apporter ma modeste contribution.

Chapitre 1. État de l’art

État de l'art (résumé en français du chapitre 1)

Le carbone est le 4^{ème} élément le plus abondant dans le Système Solaire (dominé en masse par le soleil) après H, He et O (Anders and Ebihara, 1982). Cette grande abondance du carbone dans le Système Solaire contraste avec ceux qui est connu sur Terre où la plupart des estimations de la concentration moyenne du carbone avoisinent seulement 0.1 wt%[1] (McDonough, 2003; Marty, 2012; Dasgupta, 2013), le carbone étant supposé être largement perdu pendant l'accrétion et le dégazage de la Terre (Abe, 1997; Genda and Abe, 2003). Parmi les enveloppes terrestres accessibles à l'observation directe (i.e., en excluant le manteau et le noyau), la lithosphère est le réservoir du carbone le plus grand par rapport aux autres réservoirs comme l'océan, l'atmosphère et la biosphère.

Si le cycle géochimique externe et les flux du carbone dans le système croûte-océan-atmosphère sont relativement bien compris grâce à de nombreux travaux, les flux et le bilan du carbone entre le manteau et les enveloppes externes sont beaucoup moins contraints et les incertitudes sur les flux ou les amplitudes de variation entre différentes estimations sont comparables aux valeurs elles-mêmes. Ceci concerne notamment le comportement du carbone lors de la subduction et lors de la fusion partielle des roches et la naissance des magmas d'arc. La composition des fluides profonds, la spéciation chimique du carbone ainsi que la solubilité et la stabilité des minéraux comme les carbonates et le graphite à haute température et haute pression sont parmi les grands inconnus.

Les inclusions fluides piégées dans les minéraux lors de leurs croissance ou déformations postérieures sont les seuls témoins directs de la composition des fluides géologiques d'origine magmatique, métamorphiques ou météorique qui opèrent dans la lithosphère. Bien que ces témoins des fluides profonds restent très rares, ils nous révèlent clairement que les gisements des métaux sont souvent associés à des fluides riches en CO_2. Par exemple, dans les gisements de Cu et Au de type porphyre, les teneurs en CO_2 atteignent 10-20 wt%, alors que dans les gisements d'or orogénique et de skarns elles peuvent souvent dépasser 50 wt% (e.g., Rusk et al., 2008, 2011; Phillips and Evans, 2004). Les autres formes de carbone comme CO, CH_4, C_nH_m, COS et les acides carboxyliques simples ont aussi été détectées dans les inclusions, mais le CO_2 est le composé qui apparait le plus souvent et de manière la plus abondante dans les fluides géologiques. En plus, les analyses de concentrations élevées de différents métaux (e.g., Cu, Au, Pd, As, Sb) dans les fluides riches en CO_2 et les associations courantes des minerais d'or, de cuivre et de fer avec des minéraux carbonatés ou des inclusions fluides riches en CO_2 sont autant d'évidences de la participation de

---

[1] Dans ce manuscrit nous avons adopté l'unité « wt% » (weight percent) pour exprimer les concentrations en pds%. De même, le séparateur décimal est un point selon le format anglais.

cette molécule réputée inerte dans les processus de formation des gisements. Malgré les progrès considérables réalisés dans le domaine de la géochimie expérimentale et de la modélisation thermodynamique des processus hydrothermaux-magmatiques, l'effet du CO_2 sur les transferts des métaux demeure quasiment inconnu. Dans des conditions hydrothermales caractérisées par des systèmes eau-sel-soufre-CO_2, le CO_2 peut affecter le comportement des métaux de façons différentes qui sont brièvement résumées ci-dessous.

Premièrement, la présence du CO_2 affecte les relations d'équilibre vapeur-liquide par rapport à un système sans CO_2. Une quantité modérée de CO_2 peut élargir le domaine d'immiscibilité vapeur-liquide. Par exemple, la présence de 10 wt% CO_2 dans un liquide monophasique contenant 10 wt% NaCl à 400°C va augmenter la pression de démixtion de phase de 270 (sans CO_2) à 450-500 bar (Bakker et al, 2009). Deuxièmement, le CO_2 peut influencer le pH du liquide et donc la solubilité des métaux, car c'est un acide faible. L'ébullition ou la séparation de phases conduit à l'augmentation du pH de la phase liquide à cause du départ du CO_2 et d'autres constituants volatils acides (HCl, H_2S, SO_2) dans la phase vapeur. Troisièmement, les ions bicarbonate (HCO_3^-) et carbonate (CO_3^{2-}), peuvent potentiellement agir comme ligands directs pour les éléments «hard» telles que les terres rares, Sn, Zr, U, Nb, et probablement le Fe (e.g., Pearson, 1963; Seward and Barnes, 1997; Wood and Samson, 1998). Au contraire, les métaux «soft», comme Ag, Pt et Au, ne devraient pas être affectés par la complexation avec les ions carbonates en raison de leur faible affinité chimique pour ces ligands «hard». Cependant, aucune preuve expérimentale directe n'existe à ce jour pour les complexes carbonatés des métaux aux températures élevées (>200-300°C) pour les fluides dont l'acidité est souvent contrôlée par les équilibres avec des roches alkali-aluminosilicatés ou par la présence des acides comme HCl ou H_2SO_4. De plus, la concentration des ions carbonatés eux-mêmes est infiniment petite aux pH acide-neutre (pH < ~5) des fluides typiques des systèmes magmatiques-hydrothermaux. Enfin, l'abaissement de la constante diélectrique du solvant et de l'activité de l'eau en présence du CO_2 peut conduire à des changements de solubilité opposés selon le métal et son minéral. Par exemple, si la solubilité du quartz (SiO_2), de la portlandite ($Ca(OH)_2$), de la chrorargirite (AgCl) et de la halite (NaCl) décroit lorsque la teneur en CO_2 (ou autre volatil inerte comme l'argon) en phase fluide supercritique augmente (Walther and Orville, 1983; Newton and Manning, 2000, 2009; Akinfiev and Zotov, 1999; Fein and Walter, 1989; Zakirov et al., 2007), celle de la magnétite (Fe_3O_4) croît avec l'ajout du CO_2 (Tagirov and Korzhinsky, 2001). Ces tendances contrastées sont dues à des différences de nature des espèces majeures des métaux en phase fluide, qui sont difficiles à prédire à présent dans le cadre d'un modèle unique dans des systèmes multi-élémentaires pertinents des contextes naturels.

Paradoxalement, rien n'est connu en ce qui concerne l'effet du CO_2 sur la solubilité des métaux d'intérêt économiques comme Cu, Zn, Au, Pt ou Mo, qui sont souvent associés dans la nature à des fluides riches en CO_2. L'acquisition de telles données nouvelles dans des systèmes multi-élémentaires représente un des objectifs de cette thèse. Cette approche est un grand pas en avant par rapport à celle des systèmes simples monométalliques étudiés jusqu'à présent. Il convient de noter que le CO_2 a un effet sur les constantes d'équilibre de *toutes les réactions* impliquées dans la mobilisation et le transport et le dépôt des métaux. L'analyse de ces réactions exige des modèles thermodynamiques des fluides CO_2-H_2O-sel-soufre qui tiennent compte de la spéciation des métaux et des changements des propriétés du solvant. La mise en application d'un tel modèle est un autre grand chalenge de ce travail.

1. State of the art

Before going into the heart of the thesis's subject, which is the role of CO_2 in metal transport by geological fluids, we will overview the global geochemistry of carbon, its distribution and speciation in the different terrestrial envelopes and materials and its geochemical fluxes. We hope that this analysis of the literature will help us to better place our specific results (Chapters 3 and 4) into a more global geochemical picture, and to better identify potential new directions for future research.

1.1. Abundance of carbon on Earth

Carbon is one of the most abundant elements in the Solar system (the 4th element after hydrogen, helium, and oxygen; Anders and Ebihara, 1982). The building blocks of the Earth, which are traditionally thought to be carbonaceous chondrites, contain several weight percent of carbon (2.7-4.4 wt% C; Anders and Grevesse, 1989; Lodders, 2003; Lodders, 2010). However, most of the estimates of the average Earth carbon concentration (called Clarke, 1889) fall below 0.1 wt% (McDonough, 2003; Marty, 2012; Dasgupta, 2013), because carbon is thought to be largely lost during the Earth's accretion (Abe, 1997; Genda and Abe, 2003). According to Goldschmidt's geochemical classification (Goldschmidt, 1926, 1937) based on the distribution of elements in meteorites, rocks and some synthetic materials (e.g., alloys), carbon is considered to be a siderophile element (i.e., iron-loving). Solubility of carbon in molten iron is 4.3 wt% at 1420 K under atmospheric pressure and further increases with the temperature and pressure rise (Wood, 1993). Consequently, carbon is expected to sink into the core in the course of the planetary differentiation. Thus, Earth's differentiation accompanied by the mantle convection has resulted in carbon distribution in the major terrestrial envelopes shown in Fig. 1.1. In terms of the global budget, the mantle carbon pool is one order of magnitude greater than the crustal one and the core carbon pool is one to two orders of magnitude greater than the mantle one (Table 1.1).

Carbon's atmophile and biophile properties were expressed during the planetary evolution due to its capacity to form C-O, C-H and C-C covalent bonds. Despite carbon tendency to enrich the ocean, atmosphere and biosphere, the Earth's lithosphere remains the largest exosphere reservoir of carbon (Table 1.2), and carbonates dominate among other carbon-bearing substances (graphite, organic matter, CO_2, and hydrocarbons). Carbon exchange between terrestrial reservoirs involves geological fluids, which control carbon fluxes and the geochemical cycle, as will be discussed below.

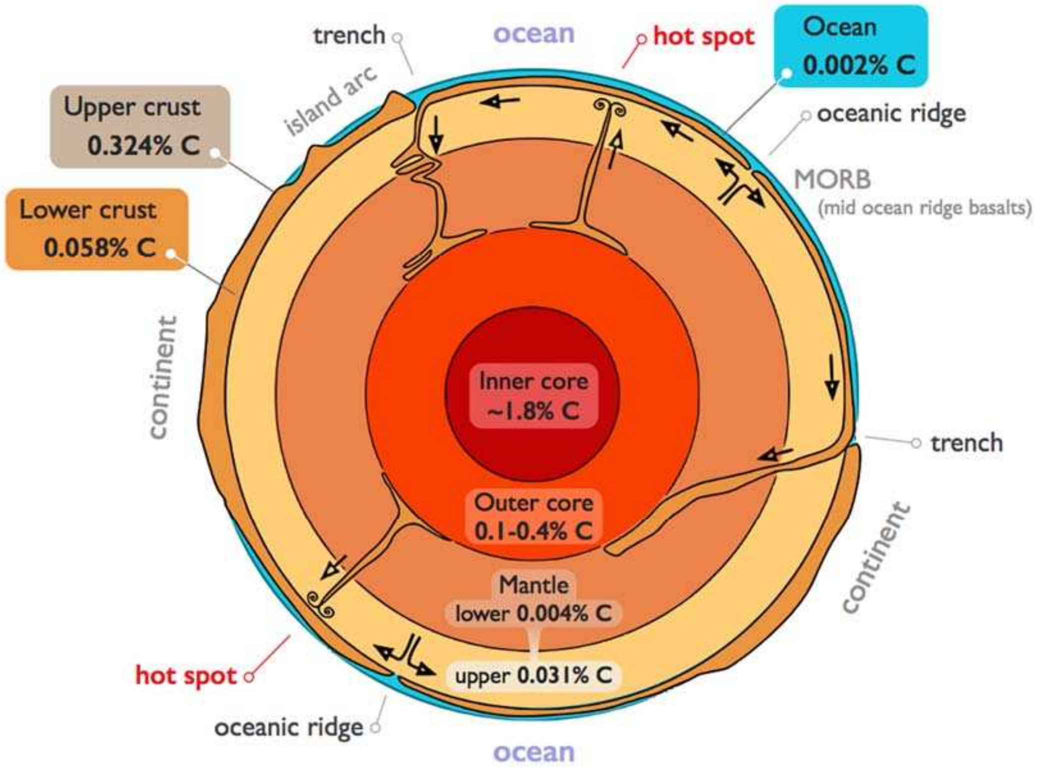

Fig. 1.1. Estimations of carbon concentration (in weight % C) in the Earth's major reservoirs. Clarkes for upper and lower continental crust are given according to Wedepohl (1995). Carbon contents in upper and lower mantle come from masses of carbon in each pool (Javoy et al., 1982) and masses of the mantle shells (Table 1). Carbon contents in outer and inner core were calculated from masses of core shells and estimations of Dasgupta and Hirschmann (2010) and Mookherjee et al. (2011) respectively. The average carbon concentration in seawater is taken from the review of Millero, 2003. Earth's structure scheme modified from http://atropos.as.arizona.edu/aiz/teaching/nats102/.

Table 1.1. Carbon amounts and concentrations in the Earth's major inner reservoirs (masses of envelopes taken from Taylor and McLennan, 2010; Davies, 1999; and McDonough, 2003).

Reservoirs (total mass, Gt × 10^{10})	Mass of carbon, Gt × 10^{8}	wt% C	Reference
Crust (2.1)	≤0.8	0.38	Javoy et al., 1982
Mantle (400)	5	0.01	Javoy et al., 1982
	0.8–2.2	0.002-0.005	Sleep and Zahnle, 2001
	0.3–2.4	0.001-0.006	Cotlice et al., 2004
	0.8–12.5	0.002-0.03	Dasgupta and Hirschmann, 2010
Upper mantle (130)	4	0.03	Javoy et al., 1982
Lower mantle (270)	1	0.004	Javoy et al., 1982
Core (190)	230	1.2	Yi et al., 2000
	780	2–4	Hillgren et al., 2000
	38	0.2	McDonough, 2003; Wood and Halliday, 2010
	19–133	0.1–0.7	Zhang and Yin, 2012
	19–77	0.1–0.4	Dasgupta et al., 2013a
	110	0.6	Wood et al., 2013
Outer core (180)	20–80	0.1–0.4	Dasgupta and Hirschmann, 2010
Inner core (10)	17	1.8	Mookherjee et al., 2011

Table 1.2. Carbon amount in the Earth's exosphere reservoirs (Falkowski et al., 2000[a]; Javoy et al., 1982[b]; Kempe, 1979[c])

Pools	Quantity, Gt C	Reference
Crust	≤80 000 000	b
Continental sediments	35 640 000	c
Carbonates	*25 640 000*	c
Non-carbonates	*10 000 000*	c
Oceanic sediments	20 160 000	c
Carbonates	*14 160 000*	c
Non-carbonates	*6 000 000*	c
Continental granitic crust	9 050 000	c
Carbonates	*7 910 000*	c
Non-carbonates	*1 140 000*	c
Basaltic oceanic crust	660 000	c
Carbonates	*340 000*	c
Non-carbonates	*320 000*	c
Carbonates (total)	48 050 000	c
Metamorphic	*~10 000 000*	b
Non-carbonates (total)	17 460 000	c
Kerogens	*15 000 000*	a
Fossil fuels (total)	4 130	a
Coal	*3 510*	a
Oil	*230*	a
Gas	*140*	a
Other (peat)	*250*	a
Oceans	38 400	a
Terrestrial biosphere	2 000	a
Living biomass	600 – 1 000	a
Dead biomass	1 200	a
Aquatic biosphere	1 – 2	a
Atmosphere (CO_2, CO, CH_4)	720	a

1.2. Carbon cycle

Carbon is exchanged in the earth system at all-time scales. Processes that last from hundreds to millions of years were contingently assigned to long-term carbon cycle, whereas short-term cycle involves processes that last from seconds to years (e.g. Falkowski et al., 2000 and references therein). The carbon cycle is schematically illustrated in Fig. 1.2.

Long-term carbon cycle operating on geological timescale transports carbon between reservoirs of the exosphere (crust, ocean, atmosphere and biosphere) and mantle through tectonic activity. Carbon is being released from the mantle to the exosphere by volcanic emissions, and returns back through subduction processes. This exchange is called deep carbon cycle (Dasgupta and Hirschmann, 2010). Indeed, mineral parageneses and isotope ratios in some diamonds suggest their origin from the lower mantle (e.g. Cotlice et al., 2004). Deep sources of carbon are also witnessed by carbonatite and kimberlite magmas (e.g. Deines and Gold, 1973; Kaminsky et al., 2009; Tappe et al., 2013). The long-term carbon cycle also implies metamorphism and diagenesis, weathering of silicates, carbonate storage in deep ocean, organic matter burial, and weathering of organic sediments.

Short-term carbon cycle bears directly on its fluctuations over human time scales. This cycle includes the atmosphere-ocean CO_2 exchange and terrestrial photosynthesis and respiration. Additional intensive flux of carbon appeared in nature due to combustion of fossil fuels by humans. Natural carbon fluxes are further perturbed by human activities such as agricultural soil usage (acceleration of respiration), mining (silicate weathering acceleration), forest combustion and plantation. A brief quantitative analysis of the long- and short-term carbon cycles is given below.

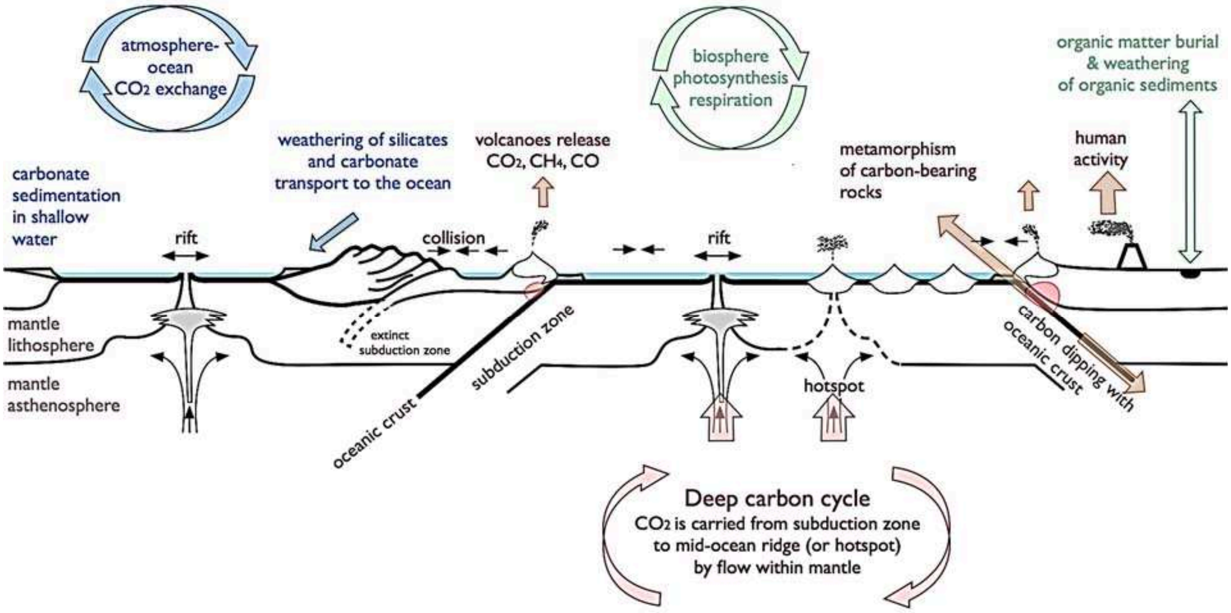

Fig. 1.2. Scheme of global carbon cycles in the context of plate tectonics (modified from http://csmres.jmu.edu/geollab/vageol/vahist/plates.html). Short-term carbon cycle is shown on this picture by two blue and green circles: 'atmosphere-ocean CO_2 exchange' and 'biosphere photosynthesis-respiration'. Other fluxes belong to the long-term carbon cycle.

1.2.1. Long-term carbon cycle

Estimations of long-term carbon fluxes rates involve different types of data and approaches such as: data on isotope fractionation during photosynthesis and on the rapid recycling of carbon in younger rocks (Berner, 2003); spatial distribution measurements; empirical correlation equations showing dependence of basalts consumption rates of CO_2 on rock weathering (runoff) and temperature; a global geologic map (Gaillardet et al., 1999); calculations of the contribution of main lithologies, rain and atmosphere to river dissolved loads using compiled data on the 60 Earth's largest rivers (Dessert et al., 2003); direct sampling and chemical analyses of volcanic gases and rocks; SO_2 emission estimates and remote sensing of eruption plumes, ice core acidity, ash leachates, satellite-based remote measurements (Williams et al., 1992); measurements of the oceanic ^{3}He flux and $CO_2/^3He$ ratios of hydrothermal vent fluids, with $CO_2/^3He$ values of MORB glasses as proxies (Gerlach, 1991); measurements of $CO_2/^3He$ ratios in magmatic volatiles, ^{3}He content estimates in the magmatic sources, and magma emplacement rates in various tectonic settings (Marty and Tolstikhin, 1997); petrologic and geochemical estimations of the Eocene plutonic-metamorphic belt flux in New England (Kerrick and Caldeira, 1998); proportion between metamorphic and sedimentary rocks (Garrels and Mackenzie, 1972), and sedimentation rates (Kempe, 1979).

Figure 1.3 summarizes the results of these works in terms of the long-term carbon cycle. It consists of sediment-related sub-cycles, which are involved or not in the mantle carbon cycle. The two sediment-related sub-cycles can be represented by the generalized reactions (Berner, 2003):

$$CO_2 + CaSiO_3 \leftrightarrow CaCO_3 + SiO_2 \quad (1.3)$$

$$CO_2 + H_2O \leftrightarrow CH_2O + O_2 \quad (1.4)$$

Equation (1.3) represents the uptake of atmospheric CO_2 during the weathering on land of calcium and magnesium silicates, with the dissolved weathering products (Ca^{2+}, Mg^{2+}, HCO_3^-) delivered to the ocean and precipitated as calcium and magnesium carbonates in sediments. Going from right to left, equation (1.3) represents thermal decomposition of carbonates during metamorphism with carbon dioxide release. Hydrothermal fluids formed by metamorphism of carbonates are enriched in CO_2 and migrate upward in the crust. They can repeatedly interact with calcium and magnesium silicate host rocks and re-precipitate carbonates without exchange with ocean or atmosphere. Equation (1.4) represents net global photosynthesis (i.e., photosynthesis minus respiration) as manifested by the burial of organic matter (CH_2O) in sediments. The buried organic matter is eventually transformed, mostly to kerogen, but some part of it becomes oil, gas and coal at some specific temperature and pressure conditions. Equation (1.4), going from right to left, represents the oxidative weathering of organic matter exposed to erosion on the continents (Berner, 2003).

Metamorphic and diagenetic fluxes of carbon are poorly understood. A significant amount of CO_2 is released into the atmosphere through regional metamorphism of carbon-rich sedimentary sequences, but retrograde metamorphism may be a sink for CO_2 (Hazen, Schiffries, 2013). Kempe (1979) calculated average rate of metamorphic flux as $0.8\text{-}1.6\times10^{-2}$ Gt C yr^{-1} using estimations of ratio of the total masses of metamorphic vs sedimentary rocks (1:16) and net uplift rates of sediments entering in the zone of subduction ($1.2\text{-}2.6\times10^{-1}$ Gt C yr^{-1}). Kerrick and Caldeira (1998) calculated that New England metamorphic belt (area 2×10^6 km^2) produced an integrated CO_2 flux of $\sim3.6\times10^{-2}$ Gt C yr^{-1} during the Cordilleran orogen. If a significant fraction of that CO_2

entered the atmosphere, this degassing flux would alone account for the Eocene greenhouse global warming.

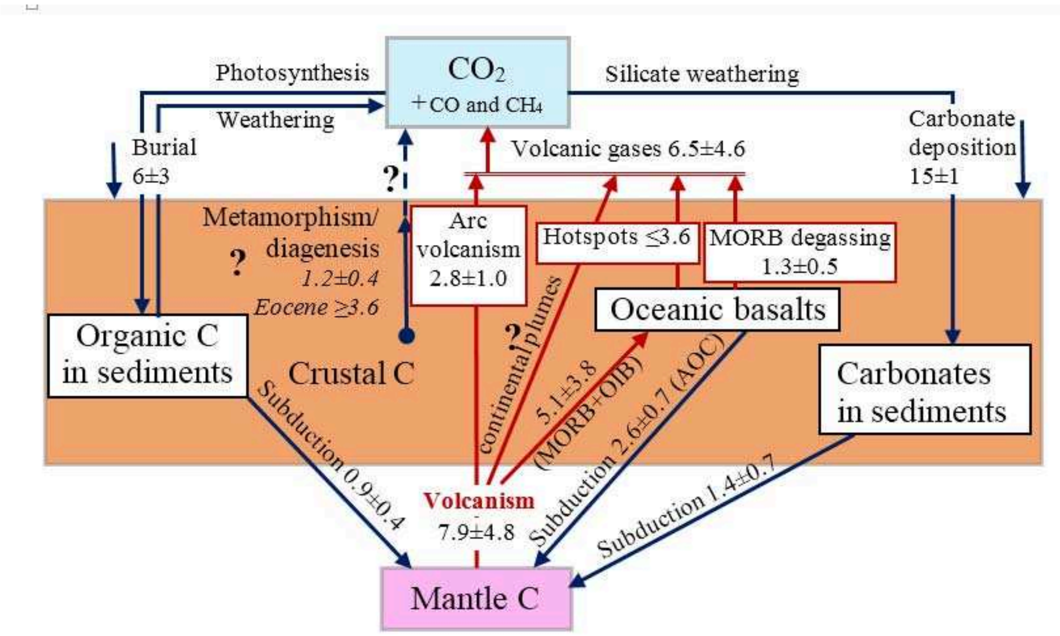

Fig. 1.3. Long-term carbon fluxes between active reservoirs (atmosphere, biosphere and hydrosphere – in blue colour), crust (orange) and mantle (rose). This cycle includes two subcycles: one involving organic matter (left side of the figure), and one involving carbonates (right side of the figure), both involved in the mantle carbon cycle (bottom side of the figure). Weathering of carbonates via dissolution in the deep ocean and deposition of carbonates essentially balance one another and are not presented here. Carbon fluxes are given in $10^{-2}\cdot$Gt C yr^{-1}. References for estimations of carbon fluxes: burial (Berner, 2003), silicate weathering (Gaillardet et al., 1999; Dessert et al., 2003), subduction of sediments and AOC (altered oceanic crust) (Evans, 2012), volcanic total output from mantle, MORB (mid-ocean ridge basalts), OIB (ocean island basalts) and arc output contributions (Dasgupta and Hirschmann, 2010), total volcanic degassing (Williams et al., 1992), MORB degassing (Gerlach, 1991), hotspots degassing (Marty and Tolstikhin, 1997), methamorphism and diagenesis (Kempe, 1979; Kerrick and Caldeira, 1998). Carbon volcanic flux from continental hotspots (plumes) involving both magmatic rocks (e.g. carbonatites and kimberlites) and volcanic degassing is poorly known.

Mantle carbon cycle consists of carbon input into subduction zones and global volcanic output. One part of the subducted carbon returns to the exosphere via regional metamorphism and arc volcanism, another part returns to the exosphere with rift and hotspot magmatism. In long-term carbon cycle models (e.g. Dasgupta and Hirschmann, 2010) oceanic basalts are classified as mid-ocean ridge basalts (MORB), ocean island basalts (OIB, oceanic hotspots) and altered oceanic crust (AOC, basalts modified by oceanic water during hydrothermal and weathering processes). Input of carbon into subduction zone consists of three contributions that have nearly the same rates (see Fig. 1.3): carbonates, organic matter and altered oceanic crust. Global carbon output from mantle to exosphere also consists of three contributions: oceanic basalt volcanism (both MORB and OIB), arc volcanism and continental hotspot volcanism. Arc volcanic rocks contain negligible quantities of carbon compared to values of carbon released with volcanic gases (Evans, 2012).

Quantities of carbon released through hotspots (both continental and oceanic) to the exosphere are poorly known. Quantities of carbon released in the form of basalts and in the form of gases have the same orders of magnitude (Fig. 1.3). Table 1.3 summarizes various studies on mantle carbon fluxes. The resulting flux into the mantle is not well-known (Houghton, 2014 for a recent review): different budgets yield different signs because of large error bars, so that further systematic studies are needed to better constrain this issue.

Table 1.3. The global mantle carbon budget (10^{-2}·Gt C yr^{-1}). Total flux for each set shows either a net exhalation from (–) or a deposition to (+) the mantle.

Fluxes out of the mantle			Subduction into mantle	Total flux	Reference
MORB[a]	Hotspots	Arc			
1.8	0.04	3.4	3.7	−1.5	Sano and Williams, 1996
2.6	*≤3.6*	~3.0			Marty, Tolstikhin, 1997
(2.4±1.1)		(2.0±1.7)	4.2		Coltice et al., 2004
(3.6±2.4)	(1.5±1.4)[b]	(2.8±1.0)	(8.7±2.7)	≥–4.4 ≤+8.1	Dasgupta and Hirschmann, 2010
(13±11)		1.9	4.6		Shilobreeva et al., 2011
		(3.0±0.9)[c]	(5.5±4.8)[d]		Evans, 2012

a – mid-ocean ridge basalts; b – data only for oceanic island basalts (oceanic hotspots); c – estimation of arc out flux include igneous rocks (negligible values), volcanic gases and non-volcanic fluid release with dominant mad volcanoes' CH_4 contribution; d – total carbon input implies not only crustal carbon, but also serpentinised mantle lithosphere contribution producing the essential uncertainty in total error bar's estimation.

1.2.2. Short-term carbon cycle

Short-term carbon cycle involves fluxes between the atmosphere, biosphere and hydrosphere, and may be divided into terrestrial and oceanic carbon sub-cycles. The carbon uptake from the atmosphere in the terrestrial ecosystem is regulated by photosynthesis, and carbon release into the atmosphere is regulated by respiration of living organisms (both autotrophic and heterotrophic) and microbial decomposition of dead organic matter (Fig. 1.4). The total carbon uptake by plants through photosynthesis is about 120 Gt yr^{-1}, but after excluding both autotrophic (60 Gt C yr^{-1}) and heterotrophic respiration (60 Gt C yr^{-1}), as well as natural disturbances (such as fires and drought), net biome production is known to be near the zero in 1980s (0.2±0.7 Gt C yr^{-1}) and positive in 2000s (2.2±0.5 Gt C yr^{-1}). In a summary report of IPCC (Intergovernmental Panel on Climate Change, 2000) net biome production was estimated at 0.7±1.0 Gt C yr^{-1}. Part of the net biome production is released from the biosphere into the lithosphere (burial). This process was estimated to be at the rate of 0.06±0.03 Gt C yr^{-1} (Berner, 2003). Thus, the current carbon burial process is three orders of magnitude slower than the short-term carbon exchange between terrestrial biosphere and atmosphere, and two orders of magnitude slower than the storage of carbon in net biome production. Additionally, the burial rate is one order of magnitude smaller than reasonable error bars of the land-atmosphere flux rate estimation (±0.5-0.7 Gt C yr^{-1}) (Table 1.4).

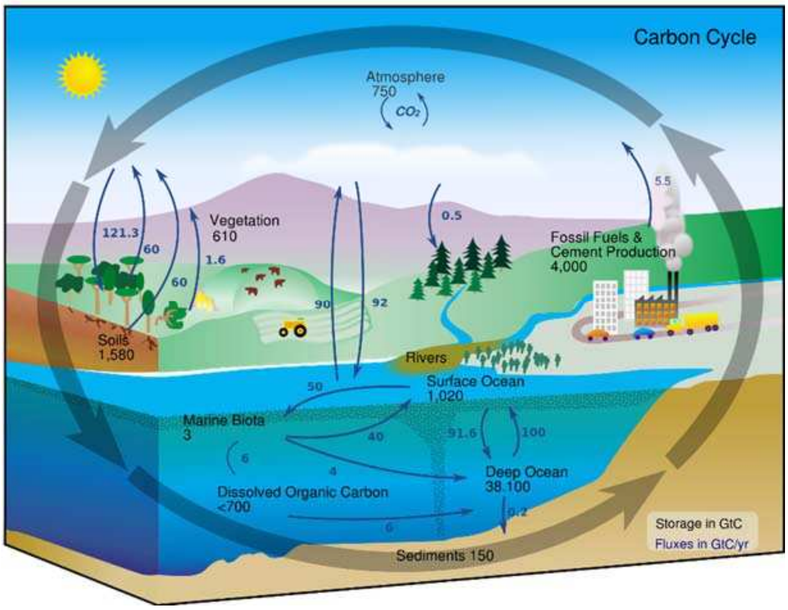

Fig. 1.4. Contemporary short-term carbon cycle, NASA, 2001.

In seawater, carbon is present in various forms, namely dissolved inorganic carbon (DIC: HCO_3^- and CO_3^{2-}), dissolved organic carbon (DOC), and particulate organic carbon (POC), with an approximate ratio DIC:DOC:POC of 2000:38:1 (Denman et al., 2007). Heinze et al. (1991) identified three key ocean carbon pumps that define possible ways for the atmospheric CO_2 to exchange with the oceanic pool: solubility pump, organic carbon pump, and $CaCO_3$ 'counter pump'. Alkaline surface seawater (pH between 7.5 and 8.4) absorbs vast amounts of atmospheric CO_2 due to its buffering capacity to neutralize the acidity of CO_2 (reactions 1.1, 1.2).

Table 1.4. Global carbon budget (Gt C yr^{-1}) in the context of short-term fluxes of carbon cycle (error bars were estimated in this work from Prentice et al., 2001, Achard et al., 2002, DeFries et al., 2002, Houghton, 2003, Le Quéré et al., 2003, Sabine et al., 2004, Denman et al., 2007).

Pools	1980s	1990s	2000-2005
Emissions (fossil fuel, cement)	5.4±0.1	6.3±0.1	7.2 ± 0.3
Atmosphere increase	3.3±0.1	3.2±0.1	4.1± 0.1
Net ocean-atmosphere flux	-1.9±0.7	-1.7±0.6	-0.9 ± 0.6
Residual terrestrial sink[a]	-4.0 to +0.3	-5.0 to -0.9	N/A
Net land-atmosphere flux	-0.2±0.7	-1.4±0.7	-2.2 ± 0.5
Land-use change (e.g. fires)	1.7 (0.3 to 2.8)	1.6 (0.5 to 3.0)	N/A

a – the difference between the net land-to-atmosphere flux (net biome production) and the land use change flux; N/A – not available.

Bicarbonate-rich oceanic water is generally found at high latitudes during the cold season because of higher solubility of carbonates in cold water. Cold CO_2-rich water sinks from surface layer to the deep ocean via the Meridional Overturning Circulation. This process is referred to as ‘solubility pump’. Oceanic buffering capacities are not infinite and depend on the addition of Ca^{2+} and Mg^{2+} ions from weathering of silicate rocks (equation 1.3). Atmospheric CO_2 can also be taken up for photosynthesis by the phytoplankton, which afterwards either sinks as dead organic matter or transforms into DOC. Some fraction of DOC is respired by bacteria and is consequently recycled in the surface ocean as DIC. The remaining small-particle fraction reaches the deep ocean; some of the particles are then re-suspended, and some are buried in the sea floor (known as ‘organic carbon pump’). Lots of oceanic organisms form their shells, consuming calcium and carbonate ions. This process is called ‘$CaCO_3$ counter pump’.

The exchange of carbon between the atmosphere and oceans amounts to ~90 Gt C yr^{-1} in each direction, annually ocean stores about ≤2.0 Gt C yr^{-1} (Table 4). For comparison, the flux of carbonate sediments stored in the deep ocean is ~0.2 Gt C yr^{-1} (long-term carbon cycle).

At the beginning of the 21th century, humans have liberated 7.2±0.3 Gt C yr^{-1} to the atmosphere due to combustion of fossil fuels. Natural short-term carbon cycle regulating processes are not sufficient to establish equilibrium between CO_2 input to the atmosphere enhanced by humans and natural CO_2 output. As a result, a constant increase of carbon content in the atmosphere is observed (Table 1.4). Rates of long-term carbon storage mechanisms are one-two orders of magnitude slower than short-term ones. That is why injection of carbon dioxide in basalts (see equation 1.3 of long-term carbon cycle) seems not to be a good way of CO_2 storage compared to other ones like enhanced oil recovery, plantation, or storage in deep aquifers.

1.3. Sources of carbon in geological fluids

The primary sources of carbon in geological fluids are melts, carbonate rocks, and organic matter. Carbonate-rock carbon pool is 4.5 times bigger than the kerogen one (Table 1.2). Oceanic and meteoric waters may also contribute to crustal fluids, but their carbon concentrations are modest (e.g. 0.002% C in seawater, Fig. 1.1). The essential processes leading to an effective carbon release into geological fluids are magmatic activity and metamorphism (both regional metamorphism and more locally skarns, i.e., interaction of silicate magmas with carbonate rocks). Subduction zones and orogenic belts are the most favorable geological settings for carbon volatile enrichment of crustal fluids. Hydrothermal processes in oceanic crust (alteration of oceanic basalts) also involve carbon from seawater during circulation of fluids in convective cells that operate in seafloor due to a magmatic source of heat. At the same time, all these geological environments with substantial tectonic activity are favorable for ore deposit formation. Therefore, a systematic study of the interactions of carbon volatiles with metals in relevant natural conditions is essential for the progress of economic geology.

1.4. Solubility and speciation of carbon in silicate and carbonate melts

Silicate melts are the main agent for transporting carbon from Earth's interior to the surface. Carbon is dissolved in silicate melts as molecular CO_2 or in the form of carbonate groups (CO_3^{2-}), depending on temperature, pressure, and melt composition (Ni and Keppler, 2013 and references therein). Under strongly reducing conditions CH_4 and CO may prevail in C-O-H fluids (Manning et al., 2013). Solubility of CO_2 in silicate melts systematically increases with increasing pressure. However, in contrast to other volatiles like water, chloride, and sulfur, CO_2 has low solubility in silicate melts and there is no mineral phases capable of retaining it in magmatic rocks. These properties are responsible for early degassing of CO_2 from magmas (Lowenstern, 2001). Early degassing of CO_2 during magma ascent appears to explain why CO_2 is a dominant compound of fluid inclusions in xenoliths of mantle olivine (e.g. Stango, 2011 and references therein). The effect of temperature on CO_2 solubility is complex and depends on the type of melt. Furthermore, the direction of temperature effect may be reversed upon pressure change. The solubility of CO_2 increases from 1000 ppm to 2000 ppm in a series of basalts with increase of their alkalinity and weakly decreases with an increase of SiO_2 content in the calcalkaline magmatic series excluding basalt: from andesite melt (~1600 ppm) to dacite melt (~1300 ppm) and to rhyolite melt (~1000 ppm), with basalt melt having the same CO_2 solubility as rhyolite in the same alkaline series (Ni and Keppler, 2013 for a recent review).

Infrared and Raman spectroscopic studies of silicate glasses (e.g., Brey 1976; Fine and Stolper 1985, 1986; Stolper et al. 1987) showed that all CO_2 is dissolved as carbonate in basaltic glasses, whereas rhyolite, albite and other silica-rich glasses contain molecular CO_2 coexisting with minor amounts of carbonate. In andesite and phonolite glasses, molecular CO_2 and carbonate coexist (e.g., Brooker et al. 2001). Depolymerization of the melt, expressed by the increase of quantity of non-bridging oxygen atoms per tetrahedron, favors the formation of carbonate in the glasses at the expense of molecular CO_2 according to the reaction:

$$CO_{2\ \mathrm{molecular}} + O^{2-}_{\mathrm{react}} = CO_3^{2-} \qquad (1.5),$$

where "O^{2-}_{react}" is a non-bridging oxygen atom (e.g., Eggler and Rosenhauer, 1978). However, the degree of polymerization is certainly not the only parameter that controls the carbonate/CO_2 ratio in glasses. For example, replacing of sodium cations by calcium in melt composition appears to strongly enhance carbonate at the expense of CO_2. Increasing temperature shifts the equilibrium of reaction (1.5) towards molecular CO_2 and the enthalpy of the reaction (which determines the reaction sign versus temperature) increases with the depolymerization of the melt (Morizet et al., 2001, Nowak et al., 2003).

Carbonatite melts are a relatively rare phenomenon compared to silicate melts. Oldoinyo Lengai in Tanzania is the only active volcano on Earth directly producing alkali-carbonatite lavas (Krafft and Keller, 1989). However, carbonatites, defined as magmatic rocks with >50 wt% of carbonate minerals, are widely spread in the word. There are now 527 recognized carbonatite occurrences, ranging in age from Archean to present (Jones et al., 2013 for a recent review). Carbonatites are located within both continental and oceanic lithosphere, mostly in intraplate settings, in large igneous provinces. This distribution precludes a direct link of carbonatites with mantle plumes and favors a fundamental link to the same underling mantle source of carbon, which is manifested in kimberlites (Woolley and Bailey, 2012).

Carbonatite melts are ionic liquids consisting of carbonate CO_3^{2-} anions and metal cations that interact principally due to coulombic attraction and are thus very different from silicate melts, which have structures characterized by a polymerized O-Si-O-Si network (Mysen, 1983). As a result, carbonatite melts have low viscosity and the highest known melt capacities for dissolving water and halogens; they show very high solubilities of many elements that are usually rare in silicate magmas (REE, Nb, U, Ta, Cu, P, F, Ba, PGE, Ag, Au; Richardson and Birkett, 1996; Ni and Keppler, 2013). The transformation of carbon from the CO_3^{2-} triangular to the CO_4^{4-} tetrahedral group is predicted at lower mantle pressure by quantum-chemical modeling (Boulard et al., 2011).

Another form of carbonate material is that found in kimberlites. Kimberlitic melts, notorious for their capacity of transporting diamonds to the surface great depth, differ in many of their geochemical and mineralogical properties from carbonatites. Kimberlites are devoid of alkalis, and lack the typical association with sodic-potassic igneous rocks (Le Bas, 1981). Kimberlites and carbonatites also differ in their styles of eruption: explosive – for kimberlite pipes, and effusive or extrusive – for carbonatites. Kimberlite magmas are believed to carry high concentrations of volatiles, primarily CO_2 and H_2O, which help to explain their explosive eruption, high ascent rates, and the carrot-like shape of kimberlite bodies (Mitchell, 1986). For example, initial content of CO_2 in magma before eruption of the Udachnaya-East kimberlite pipe was estimated to be 23 mol % (20 wt%) and during the eruption the kimberlite magma lost almost half of the CO_2 budget (Shatskiy et al., 2014). For comparison, kimberlites and MORB samples have very different CO_2 contents: generally ~0.1-0.2 wt% CO_2 for MORBs and up to 15 wt% or more for kimberlites (Guillot et al., 2013).

1.5. Speciation of carbon in hydrothermal fluids

Within the wide range of geologically relevant redox conditions, carbon may exhibit the whole variety of chemically allowed valence states (+4, +2, 0, -4). Information on the valence and speciation of carbon in hydrothermal fluids is provided by analyses of fluid inclusions in minerals, sampling of active hydrothermal systems, experimental solubility measurements and spectroscopic experiments done in-situ. Thermodynamic modelling put our empirical knowledge in order. In addition, the slow kinetics of some carbon reactions may also be important to consider for interpreting the compositions of natural fluids.

Analyses of fluid inclusions using in-situ Raman spectroscopy, crush-leach technique coupled with gas chromatography and microthermometric observations reveal that minerals can trap a plethora of different carbon species under a broad range of geological settings: e.g., solid CO_2 in diamonds under ≥5 GPa pressure trapped at 220 to 270 km depth (Schrauder and Navon, 1993), liquid CO_2 in olivine-bearing nodules and phenocrysts from basalts (Roedder, 1965), bicarbonate (HCO_3^-) and carbonate (CO_3^{2-}) in granite pegmatites (Thomas et al., 2011), CO_2–COS in ruby from marble-hosted deposits (Giuliani et al., 2003), CO_2-CO in andesine-amphibole veins from mantle peridotite xenoliths (Bergman and Dudessy, 1984), CH_4 in olivine from ophiolite complexes (Sachana et al., 2007), CH_4 and higher hydrocarbons (C_2H_4, C_3H_6) in peralkaline igneous rocks (Salvi and Williams-Jones, 1992; Potter et al., 2013), and even ethanol (C_2H_5OH) in diamonds from Africa, Brazil and Russia (e.g. Melton and Giardini, 1974; Tomilenko et al., 1995). This diversity of carbon species occurring in fluid inclusions in minerals is illustrated in Fig. 1.5. However, the information from fluid inclusions is mostly qualitative and very scarce, as compared to the large amount and diversity of natural fluids, due to limitations of analytical techniques (e.g., molecular species have generally much stronger Raman signals than ionic ones), rarity of fluid inclusions, and artifacts of their preservation (e.g. Roedder, 1965, 1971). In the great majority of fluid inclusions, CO_2 (gas) is the most frequently detected and likely the most abundant C-bearing component.

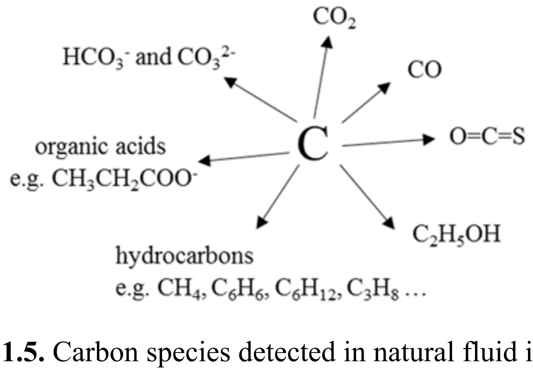

Fig. 1.5. Carbon species detected in natural fluid inclusions.

Thermodynamic modelling, in conjunction with experimental studies at controlled laboratory conditions, can help providing additional quantitative information on the abundance of carbonic species in hydrothermal fluids. Under high temperatures, pressures and typical pH and redox conditions of the Earth's crust and upper mantle, thermodynamic calculations suggest that carbon dioxide is by far the major carbon form (Pawley et al. 1992; Holloway and Blank 1994; Manning et al. 2013), which is consistent with the observations mentioned above. The distribution of C-species is illustrated in Fig. 1.6, where I calculated the domains of predominance of carbon species in the C-H-O system at 450˚C and 700 bar as a function of pH and oxygen fugacity in the fluid. The boundaries between fields of CO_2, HCO_3^-, CO_3^{2-} and CH_4 correspond to equal concentrations of the corresponding major species. As a result, minor species like C_2H_6, CO(aq), $Ca(HCO_3)^+$, $CaCO_3^0$, $HCOO^-$, CH_3COO^- cannot be shown on this type of diagram. Minor species concentrations are reported for several points shown in the Figure: e.g. in equilibrium with graphite (reduced conditions) species such as C_2H_6 and CO do not exceed 0.02 mol% of total carbon. However, carbon speciation different from that shown in Fig. 1.6 may occur in particular geological environments. For example, species such as $NaHCO_3^0$ and $NaCO_3^-$ may dominate in fluids in contact with carbonatite rocks.

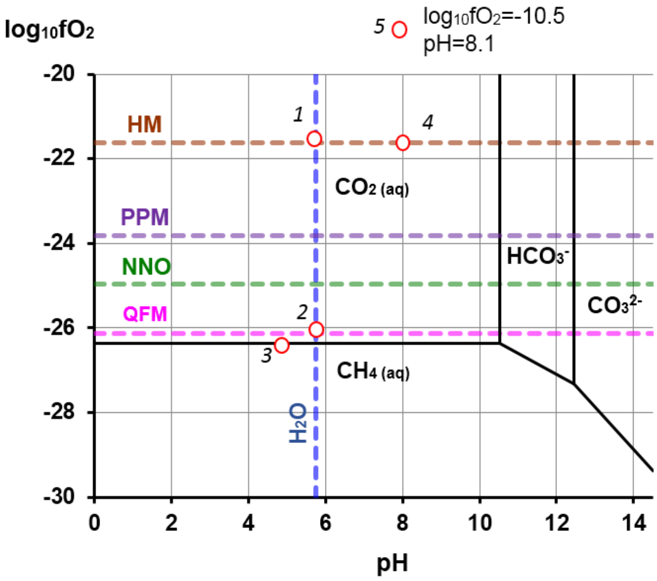

Fig. 1.6. pH-fO_2 diagram of carbon speciation in the system C-O-H at 450˚C and 700 bar. Mineral buffers of oxygen fugacity (fO_2): HM – hematite-magnetite, PPM – pyrite-pyrrhotite-magnetite, NNO – Ni-NiO, QFM – quartz-fayalite-magnetite (shown by dashed horizontal lines). The value of pH of the neutrality of pure water (pH~5.8) is shown by dashed vertical line. Carbon species concentrations (mol/kg water) calculated at thermodynamic equilibrium with the minerals HM (point 1), QFM (point 2), graphite (point 3), HM + calcite (point 4), calcite (point 5):

1 – CO_2 $1.0{\cdot}10^{-1}$, HCO_3^- $1.2{\cdot}10^{-6}$, CO $1.9{\cdot}10^{-8}$, $HCOO^-$ $9.5{\cdot}10^{-10}$, CH_4 $3.1{\cdot}10^{-11}$;

2 – CO_2 $7.4{\cdot}10^{-2}$, CH_4 $2.6{\cdot}10^{-2}$, CO $2.6{\cdot}10^{-6}$, HCO_3^- $8.6{\cdot}10^{-7}$, $HCOO^-$ $1.2{\cdot}10^{-7}$;

3 – CH_4 $6.1{\cdot}10^{0}$, CO_2 $6.1{\cdot}10^{0}$, C_2H_6 $1.2{\cdot}10^{-3}$, CO $2.5{\cdot}10^{-4}$, CH_3COO^- $1.4{\cdot}10^{-8}$;

4, 5 – CO_2 $4.7{\cdot}10^{-4}$; HCO_3^- $2.1{\cdot}10^{-6}$; $Ca(HCO_3)^+$ $4.9{\cdot}10^{-7}$; $CaCO_3^0$ $1.3{\cdot}10^{-7}$.

At very high pressures (e.g. 5 GPa, 600ºC) this speciation may change. Sverjensky et al. (2014) predicted, using the modified HKF model, a dramatic increase in the thermodynamic stability and abundance of aqueous organic species at the expense of CO_2 and CH_4, such as the propionate ion ($CH_3CH_2COO^-$) (Fig. 1.7). However their estimations need in-situ spectroscopic verification because the thermodynamic properties of organic species at high temperatures and pressures are poorly known and are based exclusively on extrapolations from low T-P conditions.

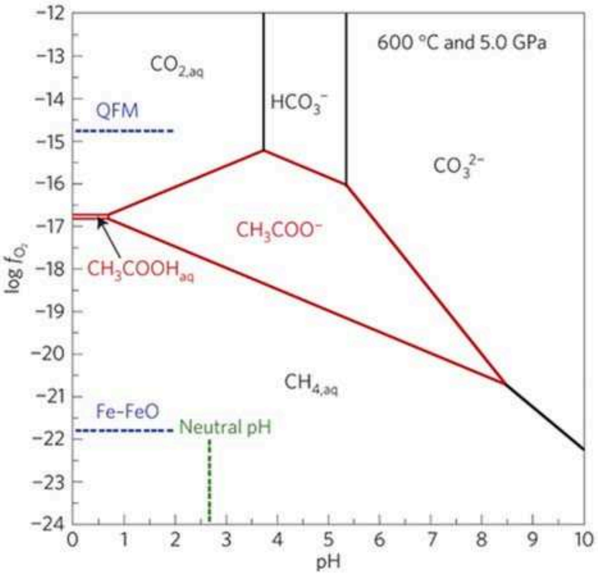

Fig. 1.7. pH-fO_2 diagram of carbon speciation in the system C-O-H at 600 °C and 5.0 GPa, according to the modified HKF model predictions. It can be seen that equilibrium stability fields appear for aqueous organic species such as acetic acid and acetate below oxygen fugacity of the QFM mineral buffer (Sverjensky et al., 2014).

Recent experimental studies at subduction zone conditions (Facq et al., 2014) suggest that the relative abundance of carbonate species may also change at high pressure. Facq et al. (2014) performed an in-situ Raman spectroscopic study of calcium carbonate dissolution in a diamond anvil cell at 300-400˚C and pressures extending up to 70 kbar (7 GPa). Their experimental results show an increasing dissociation of carbonic acid with increasing pressure: HCO_3^- predominates over CO_3^{2-} at pressures below ~40 kbar, whereas CO_3^{2-} becomes dominant at higher pressures. In addition, this change favors the formation of ion pairs such as $CaHCO_3^+$ and $CaCO_3{}^0{}_{aq}$. No in-situ studies are available, however, in the CO_2-CH_4 coexistence domain (Fig. 1.6 and 1.7), which is the only direct way to reveal carbon species with intermediate oxidation states (like those in Fig. 1.7).

It should be noted, however, that reactions between carbon species of different redox states like CO_2 and CH_4 are very slow (Ohmoto and Goldhaber, 1997), as illustrated in Fig. 1.8. Therefore, attainment of thermodynamic equilibrium requires very long durations, of the order of 10 000s years, at moderate temperatures (<300˚C). This issue should be taken into account while interpreting carbon speciation in geothermal fluids (Giggenbach, 1982) and during laboratory experiments. In contrast to redox reactions, protonation and ion pairing reactions such as those between carbonate species (e.g. CO_2 and HCO_3^-) are very fast processes reaching equilibrium within seconds to minutes (Martell and Hancock, 1996; Roughton, 1941).

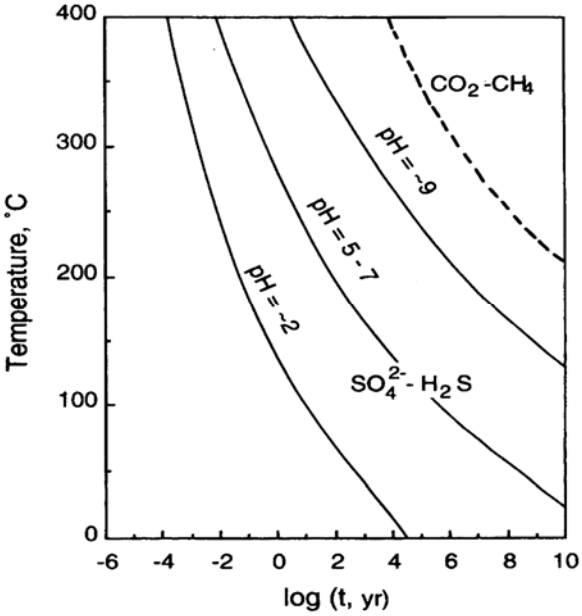

Fig. 1.8. Time (in years) necessary to reach 90% of equilibrium for the 'sulfate – sulfide' (solid lines) and 'carbon dioxide – methane' (dashed line) pairs in aqueous solution with ΣS and ΣC = 0.01m/kg, as a function of temperature and pH (Ohmoto and Goldhaber, 1997).

1.6. Typical concentrations of carbon dioxide in fluid inclusions from ore deposits

The above overview shows that carbon dioxide is a major component of most crustal fluids, including those responsible for ore deposit formation at redox conditions of the Earth's crust, which is generally at or above QFM. However, the quantification of CO_2 contents in fluid inclusions is not routine, and requires detailed microthermometric measurements (e.g., Rusk et al., 2008a), and/or in-situ spectroscopic methods such as Fourier Transform Infrared or Raman spectroscopy, and apropriate calibration procedures (e.g., Wopenka and Pasteris, 1986; Dubessy et al., 1989; Burke et al., 2001; Frezzotti et al., 2012). Another difficulty in identifying the impact of CO_2 on the formation of ore deposits is the ambiguity in deposit classification. The Wilson cycle (aggregation/dispersal of continental crust, Fig. 1.2) leads to overprinting of processes and complicates reconstruction of ore deposits formation and fluid origin. Below we overview CO_2 contents in different types of ore deposits as they were classified in the original literature. Typical CO_2 concentrations for various ore deposits are summarized in Table 1.5.

Table 1.5. Typical CO_2 concentrations and salinities for various ore deposits by type

Deposits by type	**Metals**	**CO_2, mol%**	**Salinity, wt% NaCl eq.**	**Reference**
Mafic pegmatite-related copper e.g. North Roby zone, Lac des Iles Complex, Ontario	Cu-Ni-Fe	**>50**	0.1-1	Hanley and Gladney, 2011
Magmatic rare earth elements (REE) deposits		***from 0 to 50 as function of origin***		
iron-oxide Cu-Au association: Olympic Dam, Australia	Cu-U-Au-Ag-REE	0.3-0.6 to 1.2	7-24 up to 42	Oresces and Einaudi, 1992
carbonatite association: Bayan Obo, Inner Mongolia, China	REE–Nb	8-54	1-10	Smith et al., 2015
granite pegmatite: Borborema province, Brazil	REE	5 and 14-23	up to 8	Beurlen et al., 2000
Strange Lake Pluton, Canada	Zr Nb Y REE	3.8 and 48	12-27	Salvi and Williams-Jones, 2006
Orogenic Gold Deposits	Au	***mostly high, even up to "pure" CO_2***	0– 10 up to 40	
Mother Lode, California		10	3	Phillips and Evans, 2004
Witwatersrand, South Africa		-	12	Robb and Meyer, 1991
Warrawoona Syncline, Pilbara Craton, Western Australia		20-65 9-87	up to 7	Thébaud et al., 2006
Brusson, Val d'Ayas, Alps		4.6-6.4 and 65-75	up to 6	Diamond, 1990
El-Sid orogenic gold deposit, Eastern Egypt		65-75	5	Loizenbauer and Neumayr, 1996
Carlin-Type Au Deposits	Au	***low but ubiquitous***	0 – 7 up to 15	
Carlin deposit, Nevada		CO_2 up to 10 CH_4 <0.4	mostly ≤6	Kuehn and Rose, 1995; Phillips and Evans, 2004; Cline et al., 2005; Muntean et al., 2011
Fu Ning, Yunnan Province, China		~ 0.1	early fluid 0.8–7 late fluid 12–13	Cromie and Zaw, 2003
Skarn Deposits	Au, Cu, Fe, Sn, W, Zn, Pb, REE	***variable as a function of fluid source***	0 up to >60	
Mary Kathleen, Queensland, Australia	REE	5-12	32-73, mostly 40-60	Cartwright. and Oliver, 1994; Kwak and Abeysinghe, 1987
Caicayén Hill, Neuquén, Argentina	Cu, Fe	<10	2 – 45 up to 67	Franchini et al., 2000
Dúbrava, Western Carpathians	Au-W-Sb(As)	2.9 to 58.6	10	Chovan, 1994
Jurassic Nambija gold skarn deposits, Ecuador	Au	1.6 to 55	0.2-23 31-66	Vallance et al., 2009
Intrusion-related Deposits		***from 0 to 50***		

Wattle Gully, Castlemaine, Victoria	Au	20	-	Phillips and Evans, 2004
Cordilleran polymetallic vein from Morococha, central Peru	Cu, Fe (Pb, Zn, Ag)	up to 5±4	2.0±0.1 up to 5.5±0.6	Catchpole et al., 2011
Ryan Lode, Alaska, U.S.A.	Au As Bi Sb	12	0-8	McCoy et al., 1997
Dongping Gold Telluride Deposit, Heibei Province, North China	Au Te Pb Zn Cu	28-54	1.5-10	Zhang et al., 1995 Mao et al., 2003
Porphyry Cu, Mo and Sn–W deposits	Cu, Au, Mo, and Sn, W	***low to moderate***	~ 0 up to >60	
Butte, Montana	Cu, Mo	0; 3-9; 10-20	30-48; 1-8; 0-3	Rusk et al., 2008a
Trout Lake, British Columbia	Mo	8-20	6-16	Linnen and Williams-Jones, 1990
Climax, Colorado	Mo, REE	0.06-0.12 up to 4.9	35-46 and 3.3	Roedder, 1971
Huanuni, Bolivia	Sn, W, Mo	barely detectable	up to 22	Müller et al., 2001
Mississippi Valley-Type Deposits (MVT)	Pb, Zn, Ag	***low***		
e.g. Polaris, Canada		0.3-0.7	25-31	Savard et al., 2000
Volcanogenic Massive Sulfide Deposits (VMS)	Cu, Pb, Zn, Ag, Au	***variable***	mostly < 5 up to 10	
Mt. Morgan, Australia		~0.1 or below the detection limit	0.5-3.0 up to 15	Ulrich et al., 2002 Ioannou and Spooner, 2007
Neves Corvo VHMS deposit, Portugal	Cu-Sn	CO_2 5-9, CH_4 0.05-0.17	up to 4.8	Moura, 2008
Ducktown, Tennessee	Cu, Fe (Ag-Au)	CO_2 10 CH_4 5	3	Hall et al., 1991
Epithermal Gold and Silver Deposits	Ag, Au	***low***		
e.g. Banská Hodruša, Slovakia		e.g. 0.4–0.9	0-17 up to >40	Koděra et al., 2005

Fluids from mafic pegmatite-related copper and magmatic PGE deposits, orogenic gold deposits, skarn and intrusion-related deposits may be enriched with carbon dioxide up to >50 mol% (see Table 5 and references therein). The concentration of CO_2 in skarn fluids strongly depends on their source: it is low in the case of magmatic fluid origin by silicate magma degassing, but can reach more than 50 mol% if the fluid was produced by interactions with carbonate rocks. In porphyry deposits (e.g. Climax, Butte, Henderson, Bingham, El Salvador), CO_2 can occur at average concentrations of 5–10 mol%, locally attaining 20 mol% (Rusk et al., 2008b, 2011). Fluids operated in Carlin-type deposits have less than 5 to 10 mol% CO_2. Volcanogenic massive sulfide deposits (VMS) formed by hydrothermal activity in oceanic ridges typically have less than 1 mol% CO_2 but may exceptionally contain up to 10 mol% CO_2 in fluid inclusions. Carbon dioxide is detected in fluids from epithermal Au and Ag deposits at levels of a few wt%. Mississippi Valley-type fluids do not contain significant amounts of CO_2 (<1 mol%).

1.7. Metal concentrations in CO_2-rich natural fluids

The common findings of CO_2-rich fluids in different metal deposits overviewed above suggest that there might be a link between the presence of CO_2 and the transport and deposition of metals. It is unclear, however, whether the metal-CO_2 association implies carbon dioxide as the transporting agent for the metals or its presence merely signifies some indirect role played by CO_2 in the development of the ore. Direct data on metal concentrations in CO_2-rich fluid inclusions are needed to answer this question. However such data are extremely rare owing to analytical difficulties, the absence of calibration standards for analyses of such inclusions by LA-ICPMS, and the multiphase nature of the inclusions (Hanley and Gladney, 2011). A few rare examples are given below, and these show that CO_2-rich fluids may indeed be highly enriched in metals.

Hanley and Gladney (2011) found 10 to 100 ppm of B, Cu, Te, As, Ni, Bi and 0.1 to 10 ppm of Pd and Sb in CO_2-rich fluid inclusions from sulfide-bearing mafic pegmatites in the North Roby Zone, Lac des Iles Complex, Ontario. Garofalo et al. (2014) detected up to 5 ppm of Au and 100s ppm of Cu in CO_2 dominated low-salinity fluid inclusions from the Sigma deposits (Val d'Or, Canada). Rauchenstein-Martinek (2014) detected from 0.003 to 0.03 ppm of Au in high temperature (>400˚C) aqueous carbonic fluids inclusions from the Alpine orogenic belt. Lai and Chi (2007) reported 0.1-3.4 wt% of Cu in CO_2-rich fluid inclusions from the Fenghuangshan Cu-Fe-Au orogenic deposit in China. These still very rare natural examples show that the CO_2-rich fluids may selectively transport metals in amounts comparable with those in water-dominated fluids.

Thus, despite the ubiquity of CO_2 in the Earth's crust and considerable progress of economic geology in understanding ore deposition, the effect of CO_2 on metal transport and precipitation continues to be one of the major enigmas in ore deposit research. It is thus obvious that the presence of CO_2 and metals in fluid inclusions from different types of deposits must be more attentively studied, and the role of CO_2 on mineralization more carefully evaluated. However, the physical, chemical and geological factors that determine this role are virtually unknown. Below, we overview the state of our meagre knowledge of how CO_2 may affect metal behavior in hydrothermal fluids.

1.8. Role of carbon dioxide on metal transport by geological fluids

Under hydrothermal conditions of the Earth's crust, characterized by water-salt-sulfur fluid systems, CO_2 may affect metal behavior directly and indirectly in different ways. First, the presence of CO_2 expands the field of vapor-liquid immiscibility, which causes both changes in metal solubility in the liquid phase (mostly due to pH change), and redistribution of metals between vapor and liquid. Second, some metals may form complexes with carbon-bearing ligands (CO_3^{2-},

HCO_3^-, and CO). Third, CO_2 decreases both water activity and dielectric permittivity of the solvent, which in turn affects ion pairing, and in general leads to increasing stability of weakly charged or neutral dissolved species at the expense of more charged ones. Fourth, at very high concentrations (>50-70 wt%), CO_2 may also specifically solvate some organic complexes, thus enhancing metal solubility, a property that is used for industrialy purification of organic compounds using CO_2 at supercritical conditions (> 33°C). An in-depth discussion of the listed effects is presented below.

1.8.1. Vapor-liquid equilibria

In aqueous fluids at low pressures and temperatures, molecular carbon gas species, such as CO_2 and CH_4, saturate at low concentration to form a separate phase. With the increase of P and T, these molecular species become completely miscible with H_2O, raising the concentration of deep crustal and mantle aqueous fluids in carbon to high levels (Manning et al., 2013), which is released from the fluid to form a separate phase upon fluid ascend or cooling. Thus, the presence of CO_2 strongly affects vapor-liquid equilibrium relationships and phase immiscibility, which has been known from the pioneering studies on the PVTX properties of CO_2-H_2O solutions by Takenouchi and Kennedy (1964). Subsequent experimental studies and physical-chemical models of the PVTX properties of the H_2O-CO_2-salt systems represent a robust background for predictions of unmixing processes in typical geological conditions. In general, it can be expected that the similarity in CH_4-H_2O and CO_2-H_2O mixing properties should lead to very similar phase equilibrium behavior in the presence of methane or carbon dioxide (e.g. Manning et al., 2013). At present, physical-chemical models are available for predicting the densities of the vapor and liquid phases in these systems (e.g., Bowers and Helgeson, 1983; Duan, 1995; Bakker, 2009). However, in the presence of salts (NaCl, KCl, $FeCl_2$), the T-P conditions of phase separation and the exact phase compositions are not sufficiently known to allow accurate modeling of the evolution of CO_2-NaCl-H_2O system, in contrast to the volatile-free NaCl-H_2O system (e.g., Driesner and Heinrich, 2007) and salt-free CO_2-H_2O system. Addition of sulfur to these systems further complicates the quantitative modeling of the unmixing processes. Despite these limitations, available data indicate that even moderate quantities of CO_2 (a few wt%) may significantly extend the vapor-liquid immiscibility domain and increase the pressure of phase separation (e.g., Fig. 1.9).

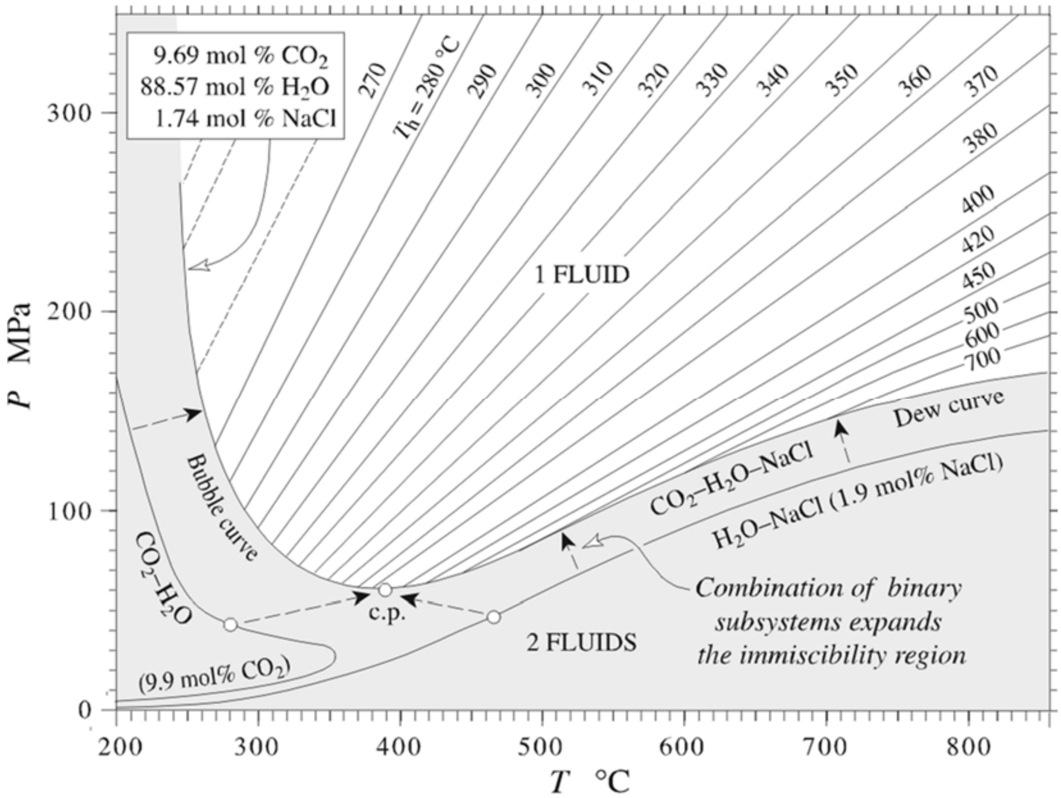

Fig. 1.9. P–T projection of phase relations in an H_2O–rich isopleth (a line in a phase diagram indicating the same mole fraction) of the CO_2–H_2O–NaCl system (according to Diamond, 2003).

A numerical example of the effect of CO_2 on vapor-liquid equilibria at typical hydrothermal conditions is given below. The presence of 10 wt% CO_2 in a single-phase fluid containing 10 wt% NaCl at 400°C will raise the pressure of phase unmixing (i.e., the pressure below which an aqueous vapor and a saline liquid coexist) from 270 bar (as estimated for CO_2-free, 10 wt% NaCl-H_2O system) to ~450-500 bar (Bakker et al., 2009). This difference corresponds to >2 km depth under hydrostatic pressure or to ~1 km depth in a lithostatic regime. As a result, in the evolution path of the cooling and ascending magmatic fluid, the presence of CO_2 will allow earlier (i.e., at greater depth) separation of the vapor phase and corresponding metal fractionation. However, knowledge of partitioning coefficients for volatiles (H_2S, HCl) and different metals between vapor and liquid are required to quantify this important phenomenon. As present, such data are very scarce, and we are aware of only one published experimental work that attempted to measure vapor-liquid partitioning of base metals (Fe, Cu and Zn) between aqueous solutions and CO_2-rich vapor below 100°C for conditions relevant to CO_2 geological storage (Rempel et al., 2011). However, due to extremely low metal concentrations in the vapor phase and the resulting analytical uncertainties, no robust conclusions could be reached in that paper as to CO_2 effect on vapor-liquid distribution for these metals. Another recent work (Tattitch et al., 2015) attempted to investigate CO_2 effect on Cu partitioning between silicate melt, brine and vapor at magmatic conditions (800°C and 1 kbar). These authors found that the presence of CO_2 is not favorable to Cu partitioning into the vapor, lowering the vapor-brine and vapor-melt partition coefficients by a factor of 5 compared to the CO_2-free system. In between these contrasting T-P regimes lies a vast domain of hydrothermal vapor-liquid systems, which are not covered by published experimental work (except a few abstracts, e.g., Rempel et al., 2014). To date, there is an obvious lack of experimental data to account for the metal redistribution between vapor and liquid through phase separation processes that are commonly active during fluid evolution from deep to shallow environments, such as from magmatic to epithermal systems.

1.8.2. Changes in the liquid phase

Another effect of phase separation is an increase in pH of the liquid phase due to preferential partitioning of acidic volatile components (CO_2, HCl, H_2S, SO_2) into the vapor. A following numerical example illustrates this phenomenon. Boiling of a 10 wt% NaCl + 5 wt% CO_2 aqueous solution accompanied by cooling from 350° to 320°C results in removal of 90% of CO_2 into the vapor phase, which decreases the acidity of the liquid by over half an order of magnitude (from pH 5.0 in the initial solution to 5.5 after the boiling). This may eventually lead to the precipitation, in the form of sulfide minerals, of some base metals transported as chloride complexes in the liquid phase such as Zn, Cu, Fe because their solubility is pH dependent (Drummond and Ohmoto, 1985).

At the low-to-moderate temperatures (<300°C) of epithermal environments, this effect may be more important, because changes in pH induced by boiling are not compensated by the buffering capacity of aliminosilicate rocks due to slowliness of the reactions, and because the partition coefficients of CO_2 and other volatiles (HCl, H_2S) are largely in favor of the vapor at these conditions. In contrast, in higher-temperature (>400°C), salt-rich fluids of porphyry environments, the pH change of the liquid phase induced by removal of CO_2 is much smaller and is likely to be compensated by rapid fluid equilibration with silicate rocks and an increase in salt content of the liquid phase, favorable for sulfide mineral solubility and metal release into solution (e.g., Kouzmanov and Pokrovski, 2012).

1.8.3. Direct complexing

Another effect of CO_2 on metals is direct complexing. Bicarbonate (HCO_3^-) and carbonate (CO_3^{2-}) ions, which are anionic counterparts of CO_2, may potentially act as *ligands* for the so-called "hard" metals such as REE, Sn, Zr, U, Nb, and probably Fe (e.g., Seward and Barnes, 1997; Samson and Wood, 1998; Pokrovski, 2010). Base (Cu, Zn, Pb) and precious (Ag, Au, Pt) metals are expected to be much less affected by carbonate complexing (if it exists at all), because of their very low chemical affinity for the hard carbonate ligand compared to chloride or sulfide (e.g., Seward and Barnes, 1997). However, even for hard metals, the available data are very scarce and stability constants of carbonate complexes at elevated temperatures are very uncertain. In addition, bicarbonate and carbonate ions are virtually negligible at elevated temperatures in slightly acidic to neutral hydrothermal fluids, making carbonate complexes (if any) very minor.

Another CO_2 derivative, carbon monoxide (CO) is known to form carbonyls with some transition metals in gas and solid state (e.g. Fe, Ni, Co, Ti, V, Cr, Mn, Rh, e.g., Cotton et al., 1999). Such complexes are used in industry, appear naturally in the active sites of a number of enzymes (such as hydrogenases), and even are detected in interstellar dust clouds (Tielens et al., 1996). It was speculated that in very reducing hydrothermal environments of the pre-biotic history, such complexes might have been formed and could have been available as catalysts for the synthesis of critical biochemical compounds such as pyruvic acid (Cody et al., 2000). However, in aqueous fluids typical of hydrothermal metal deposits, CO concentrations are generally low (ppb to ppm level, see Fig. 1.6), and thus CO might eventually complex only trace metals for which it has a strong chemical affinity (e.g., PGE). However, no direct experimental data exist on the stabilities of metal-CO complexes in hydrothermal fluids. This gap should be filled by future research.

1.8.4. Changes in solvent properties

A more general effect of CO_2 at high concentrations applicable to any dissolved compound is changes in the properties of the aqueous solvent, which affects *solvation phenomena*. The presence of high fractions of CO_2 (XCO_2>0.1-0.2) decreases both water activity (e.g., Wolfe and Bennett, 2011) and the dielectric permittivity of the solvent (e.g., Drake and Smith, 1990). These changes in turn re-inforce ion pairing, and lead to an increase in stability of weakly charged dissolved species at the expense of more charged ones. Because of the fact that most metal complexes with major ligands (OH^-, Cl^-, HS^-) are strongly hydrated (or solvated) by water molecules, lowering H_2O activity (~mole fraction) by increasing CO_2 mole fraction should decrease the complex stability and therefore metal solubility. However, there are only few studies of simple oxide and chloride solids that attest to this behavior at supercritical conditions over a wide range of T-P-XCO_2. Most of these studies were devoted to quartz solubility (Walther and Orville, 1983; Newton and Manning, 2000, 2009). For example, quartz solubility in a 20 wt% (10 mol%) CO_2–H_2O fluid at 600°C and 2 kbar (Fig. 10) is approximately two times lower than in pure water at the same pressure and temperature (Walther and Orville, 1983). A larger effect is observed for ionic compounds, for example, AgCl(s) (Fig. 1.10), whose solubility is lowered by a factor of 50 in the same CO_2-H_2O fluid compared to pure H_2O at 400°C and 0.6 kbar (Akinfiev and Zotov, 1999). Portlandite $Ca(OH)_2$ shows a similar behavior in experiments with argon instead of CO_2 (Fein and Walter, 1989).

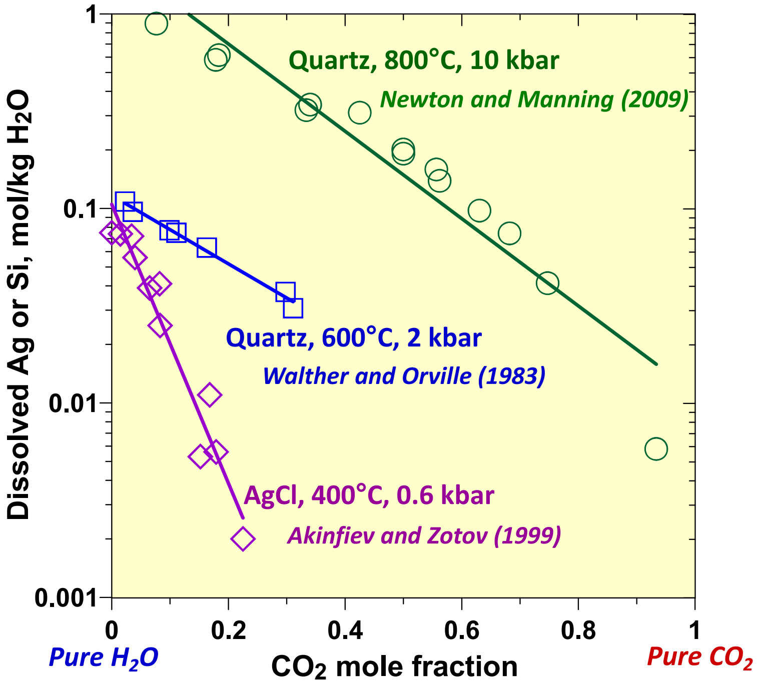

Fig. 1.10. Solubility of quartz and silver chloride in H_2O-CO_2 fluids at indicated temperatures and pressures, as a function of CO_2 mole fraction, according to rare published experimental data. Symbols stand for experimental datapoints, whereas the solid lines are drawn to guide the eye. Note a systematic decrease in solubility with increasing CO_2 content (modifyed from Kouzmanov and Pokrovski, 2012).

In contrast, an opposite effect on the solubility is observed from limited data on iron oxides solubilities in CO_2-HCl-NaCl-H_2O fluids at 500-600°C and 2 kbar (Tagirov and Korzhinsky, 2001), which are, however, difficult to interpet in the face of poor knowledge of Fe speciation at such conditions. A weak increase of NaCl(s) solubility in pure CO_2 at 350-400°C and 300-600 bar CO_2 (Fig. 11) was recently measured, which may be due to direct solvation by CO_2 (Zakirov et al., 2007); however the absolute concentrations of NaCl in such CO_2 fluid remain rediculously small, by 5 log units lower than those in an aqueous fluid at similar conditions (Driesner and Heinrich, 2007).

Specific solvation phenomena by CO_2 of certain organic ligands are also used in ingeneering systems for extracting gold and other metals into supercritical CO_2 vapor from organic-bearing aqueous solutions (e.g., Glennon et al., 1999; Erkey, 2000; Yang et al., 2010). By analogy, it was hypothesized that some neutral metal complexes with sulfide ligands might also be stabilized in CO_2-rich vapor relevant to natural hydrothermal systems (e.g., Pokrovski et al., 2008), but no experimental verification of such phenomena has been done so far.

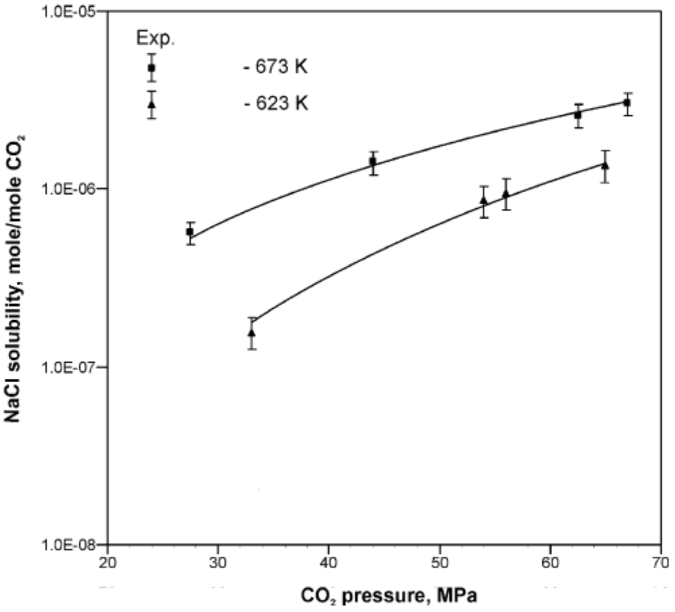

Fig. 1.11. Experimental values (symbols) and their least-squares fit (curves) of NaCl solubility in pure CO_2 as a function of CO_2 pressure (Zakirov et al., 2007).

As a conclusion, only few very simple, mono-metal systems were investigated so far. It should be noted that CO_2 affects equilibrium constants of *all reactions* involved in mobilization, transport, and deposition of ore-forming components. Thus, experimental data are needed for multicomponent systems typical of natural environments. The analysis of such data would require models for CO_2-H_2O fluids that account for changes in the solvent properties and metal speciation. The goal of this thesis is to obtain such pioneering data and to develop predictive models of CO_2 effect on metal solubility.

1.9. Goals of this thesis

The analysis of the state of the art of carbon geochemistry presented above demostrates that, despite the large place occupyed by carbon on Earth in general, and the ubiquity of its major species, CO_2, in geological fluids at depth, very little is known about the transport properies of H_2O-CO_2 fluids and their role in the formation of metal magmatic, hydrothermal and metamorphic deposits. This lack is largely due to the paucity of experimental data and robust physical-chemical models to account for metal speciation and solubility in such fluids. The first ultimate goal of this thesis is to attemp producing such pioneering data for a large set of base, pecious and trace metals and metalloids, representative of hydrothermal environments and having a large economic value (Fe, Cu, Zn, Si, Mo, Sn, Au, Pt), both in supercritical salt-sulfur-CO_2-H_2O fluids and vapor-liquid systems at conditions of the formation of ore deposits of these metals in the Earth's crust. Such experiments at carefully controlled laboratory conditions become now possible due to recent advances in high T-P experimental approaches, including specially designed hydrothremal reactors and in-situ spectroscopic methods, and large improvements in analytical technques allowing a large set of metals and volatiles to be quantified in high T-P fluids from such experiments. The second goal is to develop a simple practical thermodynamic model allowing predictions of metal solubility and speciation beyond T-P-XCO_2 parameters covered by the experiments, and to apply such a model for estimating the CO_2-rich fluid transporting capacities for metals and the effect of CO_2 on metal fractionation and precipitation.

REFERENCES

Abe Y. (1997) Thermal and chemical evolution of the terrestrial magma ocean. *Phys. Earth. Planet. Inter.* **100**, 27-39.

Achard F., Eva H.D., Stibig H.-J., Mayaux P., Gallero J., Richards T. and Malingreau J.-P. (2002) Determination of deforestation rates of the word's humid tropical forests. *Science* **297**, 999–1002.

Akinfiev N.N. and Zotov A.V. (1999). Thermodynamic description of equilibria in mixed fluids (H_2O-non-polar gas) over a wide range of temperature (25–700°C) and pressure (1–5000 bars). *Geochim. Cosmochim. Acta* **63**, 2025–2041.

Anders E. and Ebihara M. (1982) Solar-system abundances of the elements. *Geochim. Cosmochim. Acta* **46**, 2363–2380.

Anders E. and Grevesse N. (1989) Abundances of the elements: meteoritic and solar. *Geochim. Cosmochim. Acta* **53**, 197–214.

André-Mayer A.-S., Leroy J. L., Bailly L., Chauvet A., Marcoux E., Grancea L., Llosa F. and Rosas J. (2002) Boiling and vertical mineralization zoning: a case study from the Apacheta low-sulfidation epither- mal gold-silver deposit, southern Peru. *Miner. Deposita* **37**, 452–464.

Bakker R. J. (2009) Package FLUIDS. Part 3: correlations between equations of state, thermodynamics and fluid inclusions. *Geofluids* **9**, 63–74.

Bergman S.C. and Dubessy J. (1984) CO_2-CO fluid inclusions in a composite peridotite xenolith – implications for upper mantle oxygen fugacity. *Contrib. Mineral. Petr.* **85**, 1–13.

Berner R.A. (2003) The long-term carbon cycle, fossil fuels and atmospheric composition. *Nature* **426**, 323–326.

Beurlen H., Rodrigues Da Silva M. R. and De Castro C. (2000). Fluid origin and evolution during the formation of rare-element pegmatites from the Borborema province, Northeast Brazil. *Rev. Bras. Geoci.* **30**, 331–336.

Bodnar R.J., Lecumberri-Sanchez P., Moncada D. and Steele-MacInnis M. (2014) Fluid Inclusions in Hydrothermal Ore Deposits. In: Holland H.D. and Turekian K.K. (eds.) *Treatise on Geochemistry, Second Edition* (Elsevier-Pergamon, Oxford) **13**, 119–142.

Bowers T. S. and Helgeson H. C. (1983) Calculation of the thermodynamic and geochemical consequences of nonideal mixing in the system H_2O–CO_2–NaCl on phase relations in geologic systems: equation of state for H_2O–CO_2–NaCl fluids at high pressures and temperatures. *Geochim. Cosmochim. Acta* **47**, 1247–1275.

Brey G. (1976) CO_2 solubility and solubility mechanisms in silicate melts at high pressures. *Contrib. Mineral. Petrol.* **57**, 215-221.

Brooker R.A., Kohn S.C., Holloway J.R. and McMillan P.F. (2001) Structural controls on the solubility of CO_2 in silicate melts. Part II: IR characteristics of carbonate groups in silicate glasses. *Chem. Geol.* **174**, 241-254.

Boulard E., Gloter A., Corgne A., Antonangeli D., Auzende A.-L., Perrillat J.-P., Guyot F. and Fiquet G. (2011) New host for carbon in the deep Earth. *Proc. Natl. Acad. Sci. USA* **108**(13), 5184-5187.

Burke E.A.J. (2001) Raman microspectrometry of fluid inclusions. *Lithos* **55**, 139–158.

Cartwright I. and Oliver N. H. S. (1994). Fluid Flow During Contact Metamorphism at Mary Kathleen, Queensland, Australia. *J. Petrol.* **35**, 1493–1519

Catchpole H., Kouzmanov K., Fontboté L., Guillong M. and Heinrich C. A. (2011). Fluid evolution in zoned Cordilleran polymetallic veins — insights from microthermometry and LA-ICP-MS of fluid inclusions. *Chem. Geol.* **281,** 293–304.

Chovan M., Hurai V., Sachan H. K. and Kantor J. (1995) Origin of the fluids associated with granodiorite-hosted, Sb–As–Au–W mineralisation at Dubrava (Nizke Tatry Mts. Western Carpathians). *Miner. Deposita* **30**, 48–54.

Clarke F. W. (1889) The relative abundance of the chemical elements. *Philos. Soc. Washington Bull.* **11**, 135.

Cline J. S., Hofstra A. H., Muntean J. L., Tosdal R. M. and Hickey K. A. (2005). Carlin-type gold deposits in Nevada: critical geologic characteristics and viable models. *Econ. Geol.* **100**, 451–484.

Cody G. D., Boctor, N. Z., Filley T. R., Hazen R. M., Scott J. H., Sharma A., and Yoder H. S. Jr. (2000). Primordial carbonylated iron-sulfur compounds and the synthesis of pyruvate. *Science* **289**, 1337–1340.

Coltice N., Simon L. and Lécuyer C. (2004) Carbon isotope cycle and mantle structure. *Geophys. Res. Lett.* **31**, L05603.

Cotton F. A., Wilkinson G., Murillo C.A. and Bochmann M. (1999) *Adv. Inorg. Chem.* (6th Edition, Wiley, Chichester).

Cromie P. W. and Zaw K. (2003). Geological setting, nature of ore fluids and sulphur isotope geochemistry of the Fu Ning Carlin-type gold deposits, Yunnan Province, China. *Geofluids* **3**, 133–143.

Dasgupta R. and Hirschmann M.M. (2010) The deep carbon cycle and melting in Earth's interior. *Earth. Planet. Sci. Lett.* **298**, 1–13.

Dasgupta R. (2013) Ingassing, storage, and outgassing of terrestrial carbon through geologic time. *Rev. Mineral. Geochem.* **75**, 183–229.

Dasgupta R., Chi H., Shimizu N., Buono A. and Walker D. (2013a) Carbon solution and partitioning between metallic and silicate melts in a shallow magma ocean: implications for the origin and distribution of terrestrial carbon. *Geochim. Cosmochim. Acta* **102**, 191–212.

Davies G.F. (1999) Geophysically constrained mantle mass flows and the ^{40}Ar budget: a degassed lower mantle? *Earth. Planet. Sci. Lett.* **166**, 149–162.

DeFries R.S., Houghton R.A., Hansen M.C., Field C.B., Skole D. and Townshend J. (2002) Carbon emissions from tropical deforestation and regrowth based on satellite observations for the 1980s and 1990s. *P. Natl. Acad. Sci USA,* **99**, 14256–14261.

Denman K.L., Brasseur G., Chidthaisong A., Ciais P., Cox P.M., Dickinson R.E., Hauglustaine D., Heinze C., Holland E., Jacob D., Lohmann U., Ramachandran S., da Silva D.P.L., Wofsy S.C. and Zhang X. (2007). Couplings between changes in the climate system and biogeochemistry. In: *Climate Change 2007: The Physical Science Basis. Contribution of Working Group I to the Fourth Assessment Report of the Intergovernmental Panel on Climate Change* [Solomon, S., D. Qin, M. Manning, Z. Chen, M. Marquis, K.B. Averyt, M.Tignor and H.L. Miller (eds.)]. Cambridge University Press, Cambridge, United Kingdom and New York, NY, USA.

Deines P. and Gold D. P. (1973) The isotopic composition of carbonatite and kimberlite carbonates and their bearing on the isotopic composition of deep-seated carbon. *Geochim. Cosmochim. Acta* **37**, 1709–1733.

Dessert C., Dupré B., Gaillardet J., François L.M. and Allègre C.J. (2003) Basalt weathering laws and the impact of basalt weathering on the global carbon cycle. *Chem. Geol.* **202**, 257–276.

Diamond L. W. (1990) Fluid inclusion evidence for P–V–T–X evolution of hydrothermal solutions in Late-Alpine gold-quartz veins at Brusson, Val d'Ayas, northwest Italian Alps. *Am. J. Sci.* **290**, 912–958.

Diamond L.W. (2003) Introduction to gas-bearing, aqueous fluid inclusions. In: Samson I., Anderson A. and Marshall D. (eds.) *Fluid Inclusions: Analysis and Interpretation* (Mineralogical Association of Canada) **32,** 55–79.

Drake B. D. and Smith Jr. R. L. (1990), Measurement of static dielectric constants of supercritical fluid solvents and cosolvents: Carbon dioxide and argon, carbon dioxide, and methanol at 323 K and pressures to 25 MPa. *J. Supercrit. Fluid* **3**, 162–168.

Driesner T. and Heinrich C. A. (2007) The system H_2O–NaCl. Part I: correlation formulae for phase relations in temperature–pressure–composition space from 0 to 1000 8C, 0 to 5000 bar, and 0 to 1 XNaCl. *Geochim. Cosmochim. Acta* **71**, 4880–4901.

Drummond S.E. and Ohmoto H. (1985) Chemical evolution and mineral deposition in boiling hydrothermal systems. *Econ. Geol.* **80**, 126-147.

Duan Z., Moller N. and Weare J. (1995) Equation of state for NaCl–H_2O–CO_2 system – prediction of phase equilibria and volumetric properties. *Geochim. Cosmochim. Acta* **59**, 2869–2882.

Dubessy J., Poty B. and Ramboz C. (1989) Advances in C-O-H-N-S fluid geochemistry based on micro-Raman spectrometric analysis of fluid inclusions. *Eur. J. Mineral.* **1**, 517–534.

Eggler D.H. and Rosenhauer M. (1978) Carbon dioxide in silicate melts: II. Solubilities of CO_2 and H_2O in $CaMgSi_2O_6$ (diopside) liquids and vapors at pressures to 40 kbar. *Am. J. Sci.* **278**, 64–94.

Erkey C. (2000) Supercritical carbon dioxide extraction of metals from aqueous solutions: a review. *J. Supercrit. Fluid* **17**, 259–287.

Evans K.A. (2012) The redox budget of subduction zones. *Earth-Sci. Rev.* **113**, 11–32.

Facq S., Daniel I., Montagnac G., Cardon H. and Sverjensky D. A. (2014) In-situ Raman study and thermodynamic model of aqueous carbonate speciation in equilibrium with aragonite under subduction zone conditions. *Geochim. Cosmochim. Acta* **132**, 375–390.

Falkowski P., Scholes R. J., Boyle E., Canadell J., Canfield D., Elser J. , Gruber N., Hibbard K., Högberg P., Linder S., Mackenzie F. T., Moore III B., Pedersen T., Rosenthal Y. , Seitzinger S., Smetacek V. and Steffen W. (2000) The Global Carbon Cycle: A Test of Our Knowledge of Earth as a System. *Science* **290**, 291–296.

Fein J.B. and Walther J.V. (1989) Portlandite solubilities n supercritical Ar-H_2O mixtures: implications for quantifying solvent effects. *Am. J. Sci.* **289**, 975-993.

Fine G. and Stolper E. (1985) The speciation of carbon dioxide in sodium aluminosilicate glasses. *Contrib. Mineral. Petrol.* **91**, 105-121.

Fine G.J. and Stolper E.M. (1986) Dissolved carbon dioxide in basaltic glasses: Concentrations and speciation. *Earth Planet. Sci. Lett.* **76**, 263–278.

Franchini M.B., Meinert L.D. and Montenegro T.F. (2000) Skarns related to porphyry-style mineralization at Caicayen Hill, Neuquen, Argentina: Composition and evolution of hydrothermal fluids. *Econ. Geol.* **95**, 1197–1213.

Frezzotti M.L., Tecce F. and Casagli A. (2012) Raman spectroscopy for fluid inclusion analysis. *J. Geochem. Explor.* **112**, 1–20.

Gaillardet J., Dupré B., Louvat P. and Allègre C.J. (1999) Global silicate weathering and CO_2 consumption rates deduced from the chemistry of the large rivers. *Chem. Geol.* **159**, 3–30.

Garofalo P.S., Ficker M.B., Gunther D., Bersani D. and Lottici P.P. (2014) Physical-chemical properties and metal budget of Au-transporting hydrothermal fluids in orogenic deposits. *Geol. Soc. Spec. Publ. (London)* **402**, 71-102.

Garrels R. M. and Mackenzie F. T. (1972) A quantitative model for the sedimentary rock cycle. *Mar. Chem.* **1**, 27-41.

Genda H. and Abe Y. (2003) Survival of a proto-atmosphere through the stage of giant impacts: the mechanical aspects. *Icarus* **164**, 149–162.

Gerlach T.M. (1991) Present day CO_2 emissions from volcanoes. *EOS, Trans. Am. Geophys. Union* **72**, 249, 254–255.

Giggenbach W.F. (1982) Carbon-13 exchange between CO_2 and CH_4 under geothermal conditions. *Geochim. Cosmochim. Acta* **46***,* 159-165.

Guillot B., Folliet N. and Sator N. (2013) CO_2 degassing in ascending magmas: from MORBs to kimberlites. *EGU General Assembly*. Vienna, Austria. #10139 (abstr.)

Glennon J.D., Harris S.J., Walker A., McSweeney C.C. and O'Connell M. (1999) Carrying gold in supercritical CO_2. *Gold Bull.* **32**, 52–58.

Goldschmidt V.M. (1926) Geochemische verteilungsgesetze der elemente. *Skrifter Norske Videnskaps-Akad, Oslo I Mat Naturv Klasse*, 112–117.

Goldschmidt V.M. (1937) The principles of distribution of chemical elements in minerals and rocks. *The seventh Hugo Müller Lecture, delivered before the Chemical Society on March 17th*, 655–673.

Hall D. L., Bodnar R. J. and Craig J.R. (1991) Fluid inclusion constraints on the uplift history of the metamorphosed massive sulphide deposits at Ducktown, Tennessee. *J. Metamorph. Geol.* **9**, 551–565

Hanley J. J. and Gladney E. R. (2011) The presence of carbonic-dominant volatiles during the crystallization of sulfide-bearing mafic pegmatites in the North Roby zone, Lac des Iles Complex, Ontario. *Econ. Geol.* **106**, 33–54.

Hazen R.M. and Schiffries C.M. (2013) Why deep carbon? *Rev. Mineral. Geochem.* **75**, 1–6.

Heinze C., Maier-Reimer E. and Winn K. (1991) Glacial pCO_2 reduction by the World Ocean: experiments with the Hamburg carbon cycle model. *Paleoceanography* **6**, 395–430.

Hillgren V. J., Gessmann C. K. and Li J. (2000) An experimental perspective on the light element in Earth's core. In: *Origin of the Earth and Moon* (eds. R. M. Canup and K. Righter). The University of Arizona Press, Tucson, 245–263.

Hofstra A.H., Emsbo P., Christiansen W. D., Theodorakos P., Zhang X.-C., Hu R.-Z., Su W.-C. and Fu S.-H. (2005) Source of ore fluids in Carlin-type gold deposits, China: Implications for genetic models. *Mineral Deposit Research: Meeting the Global Challenge*, 533–536.

Holloway J. R. and Blank J. G. (1994) Application of experimental results to C-O-H species in natural melts. *Rev. Mineral.* **30**, 187-230.

Houghton R.A. (2003) Why are estimates of terrestrial carbon balance so different? *Global Change Biol.* **9**, 500–509.

Houghton R.A. (2014) The Contemporary Carbon Cycle, *Treatise on Geochemistry (Second Edition)* **10**, 399–435.

Ioannou S.E., Spooner E.T.C. and Barrie C.T. (2007). Fluid temperature and salinity characteristics of the Matagami volcanogenic massive sulfide district, Quebec. *Econ. Geol.* **102**, 691–715.

IPCC (Intergovernmental Panel on Climate Change) Climate Change 2001: Synthesis Report IPCC, Geneva, 2001.

Javoy M., Pineau F. and Allègre C.J. (1982) Carbon geodynamic cycle. *Nature* **300**: 171–173.

Javoy M. (1997) The major volatile elements of the Earth: Their origin, behaviour, and fate. *Geophys. Res. Lett.* **24**, 177–180.

Jones A.P., Genge M. and Carmody L. (2013) Carbonate Melts and Carbonatites. *Rev. Mineral. Geochem.* **75**, 289-322.

Kaminsky F., Wirth R., Schreiber A. and Thomas R. (2009) Nyerereite and nahcolite inclusions in diamond: evidence for lower-mantle carbonatitic magmas. *Mineralog. Mag.* **73**, 797-816

Kempe S. (1979) Carbon in the Rock Cycle. In: Bolin, B., E.T. Degens, S. Kempe and P. Ketner (eds.) *The Global Carbon Cycle* (J. Wiley & Sons, Chichester, New York, Brisbane, Toronto) **13,** 343–377.

Kerrick D.M. and Caldeira K. (1998) Metamorphic CO_2 degassing from orogenic belts. *Chem. Geol.* **145**, 213–232.

Klein E.L., Fuzikawa K. (2010) Origin of the CO_2-only fluid inclusions in the Palaeoproterozoic Carará vein-quartz gold deposit, Ipitinga Auriferous District, SE-Guiana Shield, Brazil: Implications for orogenic gold mineralisation. *Ore Geol. Rev.* **37**, 31–40.

Koděra P., Lexa J., Rankin A.H. and Fallick A.E. (2005) Epithermal gold veins in a caldera setting: Banska´ Hodrusˇa, Slovakia. *Miner. Deposita* **39**, 921–943.

Kouzmanov K. and Pokrovski G.S. (2012) Hydrothermal controls on metal distribution in Cu(-Au-Mo) porphyry systems. In: Geology and Genesis of Geology and Genesis of Major Copper Deposits and Districts of the World: A Tribute to Richard H. Sillitoe (eds. J.W. Hedenquist, M. Harris, and F. Camus). *Soc. Econ. Geol. Spec. Publ.*, **16**, 573-618.

Krafft M. and Keller J. (1989) Temperature measurements in carbonatite lava lakes and flows from Oldoinyo Lengai, Tanzania. *Science* **245**(4914), 168-170.

Kuehn C.A. and Rose A.W. (1995) Carlin gold deposits, Nevada: origin in a deep zone of mixing between normally pressured and over pressured fluids. *Econ. Geol.***90**, 17–36.

Kwak T.A.P. and Abeysinghe P.B. (1987) Rare earth and uranium minerals present as daughter crystals in fluid inclusions, Mary Kathleen U-REE skarn, Queensland, Australia. *Mineral. Mag.* **51**, 665–670.

Lai J. and Chi G. (2007) CO_2-rich fluid inclusions with chalcopyrite daughter mineral from the Fenghuangshan Cu–Fe–Au deposit, China: implications for metal transport in vapor. *Miner. Deposita* **42**, 293-299.

Le Bas M. J. (1981) Carbonatite magmas. *Mineral. Mag.* **44**, 133-140.

Le Quéré C., Aumont O., Bopp L., Bousquet P., Ciais P., Francey R., Heimann M., Keeling D., Keeling R.F., Kheshgi H., Peylin P., Piper S.C., Prentice I.C. and Rayner P.J. (2003) Two decades of ocean CO_2 sink and variability. *Tellus* **55B**, 649–656.

Linnen R.L. and Williams-Jones A.E. (1990) Evolution of aqueous-carbonic fluids during contact metamorphism, wall-rock alteration, and molybdenite deposition at Trout Lake, British Columbia. *Econ. Geol.* **85**, 1840–1856.

Lodders K. (2003) Solar system abundances and condensation temperatures of the elements. *Astrophys. J.* **591**, 1220–1247.

Lodders K. (2010) Solar system abundances of the elements. In: *Principles and Perspectives in Cosmochemistry. Lecture Notes of the Kodai School on 'Synthesis of Elements in Stars'*. (eds. A. Goswami and B.E. Reddy). Springer-Verlag, Berlin Heidelberg, 379–417.

Loizenbauer J. and Neumayr P. (1996) Structural controls on the formation of the Fawakhir gold mine, EL Sid-Eastern Desert, Egypt: tectonic and fluid inclusion evidence. *Proc. Geol. Surv. Egypt Cent. Conf.* 447–488.

Lowenstern J.B. (2001) Carbon dioxide in magmas and implications for hydrothermal systems. *Miner. Deposita* **36**, 490–502.

Manning C.E., Shock E.L. and Sverjensky D.A. (2013) The chemistry of carbon in aqueous fluids at crustal and upper-mantle conditions: experimental and theoretical constraints. *Rev. Mineral. Geochem.* **75**, 109–148.

Mao J., Li Y., Goldfarb R., He Y. and Zaw K. (2003) Fluid Inclusion and Noble Gas Studies of the Dongping Gold Deposit, Hebei Province, China: A Mantle Connection for Mineralization? *Econ. Geol.* Vol. 98, 2003, pp. 517–534.

Martell A.E. and Hancock R.D. (1996) *Metal Complexes in Aqueous Solutions*. Plenum. New York.

Marty B. and Tolstikhin I.N. (1998) CO_2 fluxes from mid-ocean ridges, arcs and plumes. *Chem. Geol.* **145**, 233–248.

Marty B. (2012) The origins and concentrations of water, carbon, nitrogen and noble gases on Earth. *Earth. Planet. Sci. Lett.* **313-314**, 56–66.

Melton C.E. and Giardini A.A. (1974) The composition and significance of gas released from natural diamonds from Africa and Brazil. *Amer. Mineral.* **59**, 775–782.

McCoy D., Newberry R. J., Layer P., DiMarchi J. J., Bakke A., Masterman S. and Minehane D.L. (1997) Plutonic-related gold deposits of Interior Alaska. in *Mineral Deposits of Alaska* (Goldfarb, R. J. and Miller, L. D., eds.), Econ. Geol. Monogr., 9, 191–241.

McDonough W.F. (2003) Compositional model for the Earth's core. In: *The Mantle and Core* (eds Carlson R.W.) *Treatise on Geochemistry, Vol. 2.* Elsevier-Pergamon, Oxford, pp. 547–568.

Millero F.J. (2003) Physicochemical Controls on Seawater. In: *The oceans and marine geochemistry* (ed. H. Elderfield) *Treatise on Geochemistry, Vol.* 6. Elsevier-Pergamon, Oxford, p. 2.

Mitchell R.H. (1986) *Kimberlites: Mineralogy, Geochemistry and Petrology.* Plenum Press, New York.

Mookherjee M., Nakajima Y., Steinle-Neumann G., Glazyrin K., Wu X., Dubrovinsky L., McCammon C. and Chumakov A. (2011) High-pressure behavior of iron carbide (Fe_7C_3) at inner core conditions. *J. Geophys. Res.* **116**(B4): B04201.

Morizet Y., Kohn S.C. and Brooker R.A. (2001) Annealing experiments on CO_2-bearing jadeite glass: an insight into the true temperature dependence of CO_2 speciation in silicate melts. *Mineral. Mag.* **65**, 701-707.

Moura A. (2008). Metallogenesis at the Neves Corvo VHMS deposit (Portugal). A contribution from the study of fluid inclusions. Departamento de Geologia and Centro de Geologia, Universidade do Porto, Rua do Campo Alegre. **687**, 4099-007.

Muller B., Frischknecht R., Seward T.M., Heinrich C.A. and Gallegos W.C. (2001) A fluid inclusion reconnaissance study of the Huanuni tin deposit (Bolivia), using LA–ICP–MS micro-analysis. *Miner. Deposita* **36**, 680–688.

Muntean J.L., Cline J.S., Simon A.C. and Longo A.A. (2011) Magmatic-hydrothermal origin of Nevada's Carlin-type gold deposits. *Nature Geosci.* **4**, 122–127.

Mysen B.O. (1983) The structure of silicate melts. *Annu. Rev. Earth. Planet. Sci.* **11**(1), 75-97.

NASA (2001) The slow carbon cycle, 21-04-2013 retrieved from http://earthobservatory.nasa.gov/Features/CarbonCycle/carbon_cycle2001.pdf.

Newton R.C. and Manning C.E. (2000) Quartz solubility in H_2O-NaCl and H_2O-CO_2 solutions at deep crust-upper mantle pressures and temperatures: 2-15 kbar and 500-900°C. *Geochim. Cosmochim. Acta* **64**, 2993-3005.

Newton R.C. and Manning C.E. (2009) Hydration state and activity of aqueous silica in H_2O-CO_2 fluids at high pressure and temperature. *Am. Mineral.* **94**, 1287-1290.

Ni H. and Keppler H. (2013) Carbon in silicate melts. *Rev. Mineral. Geochem.* **75**, 251-287.

Nowak M., Porbatzki D., Spickenbom K. and Diedrich O. (2003) Carbon dioxide speciation in silicate melts: a restart. *Earth. Planet. Sci. Lett.* **207**, 131-139.

Oreskes N. and Einaudi M.T. (1992) Origin of hydrothermal fluids at Olympic Dam: preliminary results from fluid inclusions and stable isotopes. *Econ. Geol.* **87**, 64–90.

Ohmoto H. and Goldhaber M.B. (1997) Sulfur and carbon isotopes. In: Barnes H.L. (ed) *Geochemistry of Hydrothermal Ore Deposits*, 3rd edn. Wiley, New-York, pp. 517-611.

Pawley A.R., Holloway J. R. and McMillan P.F. (1992) The effect of oxygen fugacity on the solubility of carbon-oxygen fluids in basaltic melt. *Earth. Planet. Sci. Lett.* **110,** 213-225.

Pearson R.G. (1963) Hard and soft acids and bases. *J. Am. Chem. Soc.* **85**, 3533-3539.

Phillips G. N. and Evans K. A. (2004) Role of CO_2 in the formation of gold deposits. *Nature* **429**, 860–863.

Pokrovski G. S., Borisova A. Yu. and Harrichoury J.-C. (2008) The effect of sulfur on vapor-liquid fractionation of metals in hydrothermal systems. *Earth. Planet. Sci. Lett.* **266**, 345-362.

Pokrovski G. S. (2010) Enhanced vapor-phase transport of tin in hydrothermal systems or experimental artifacts? *J. Volcanol. Geoth. Res.* **194**, 63–66.

Pokrovski G.S., Akinfiev N.N., Borisova A.Y., Zotov A.V. and Kouzmanov K. (2014) Gold speciation and transport in geological fluids: insights from experiments and physical-chemical modelling. *Geological Society, London, Special Publications* **402**, 9–70. doi:10.1144/SP402.4

Potter J., Salvi S. and Longstaffe F.J. (2013) Abiogenic hydrocarbon isotopic signatures in granitic rocks: identifying pathways of formation. *Lithos*, **182-183**, 114-124.

Prentice I. C., Farquhar G. D., Fasham M. J., Goulden R. M., Heimann L. M., Jaramillo V. J., Kheshgi H. S., Le Quéré C., Scholes R. J. and Wallace D.W.R. (2001) The carbon cycle and atmospheric carbon dioxide. *Climate Change 2001: The Scientific Basis (Contribution of Working Group I to the Third Assessment Report of the Intergovernmental Panel on Climate Change)*, edited by J. T. Houghton, Y. Ding, D. J. Griggs, M. Noguer, P. J. van der Linden, X. Dai, K. Maskell, and C.A. Johnson, Cambridge University Press, Cambridge, United Kingdom and New York, NY, USA, 183–237.

Rauchenstein-Martinek K., Wagner T., Walle M. and Heinrich C.A. (2014) Gold concentrations in metamorphic fluids: A LA-ICPMS study of fluid inclusions from the Alpine orogenic belt. *Chem. Geol.* **385**, 70–83.

Rempel K. U., Liesbcher A., Heinrich W. and Schettler G. (2011) An experimental investigation of trace element dissolution in carbon dioxide: Applications to the geological storage of CO_2. *Chem. Geol.* **289**, 224–234.

Rempel K. U., Liebscher A., Heinrich W., Dulski P. and Schettler G. (2014) CO_2 in boiling ore systems – A fundamental control on metal fractionation factors? *Goldschmidt Abstracts 2014*, 2058.

Richardson D.G. and Birkett T.C. (1996) Carbonatite-associated deposits. In: *Geology of Canadian Mineral Deposit Types.* Eckstrand OR, Sinclair WD, Thorpe RI (eds) Geological Survey of Canada, Ottawa, 541-558.

Roedder E. (1965) Liquid CO_2 inclusions in olivine-bearing nodules and phenocrysts from basalts. *Am. Mineral.* **50**, 1746–1782.

Roedder (1971) Fluid inclusion studies on the porphyry-type ore deposits at Bingham, Utah, Butte, Montana, and Climax, Colorado. *Econ. Geol.***66**, 98–120.

Robb L. J. and Meyer F. M. (1991) A contribution to recent debate concerning epigenetic versus syngenetic mineralization processes in the Witwatersrand basin. *Econ. Geol.* **86**, 396–401.

Roughton F.J.W. (1941) The kinetics and rapid thermochemistry of carbonic acid. *J. Amer. Chem. Soc.* **63**$^{(11)}$, 2930–2934.

Rusk B., Reed M. H., Dilles J. H. and Klemm L. (2004) Compositions of magmatic-hydrothermal fluids determined by LA-ICPMS of fluid inclusions from the porphyry copper-molybdenum deposit at Butte, Montana. *Chem. Geol.* **210**, 173–199.

Rusk B. G., Reed M. H. and Dilles J. H. (2008a). Fluid Inclusion Evidence for Magmatic-Hydrothermal Fluid Evolution in the Porphyry Copper-Molybdenum Deposit at Butte, Montana. *Econ. Geol.* **103**, 307–334.

Rusk B., Emsbo P., Hunt A., Hofstra, A., Landis G. and Rye R., (2008b) Fluid inclusion insights into the origins of fluids and metals in porphyry copper deposits: Pacrim Congress 2008, Gold Coast, Queensland, Extended Abstracts, 289–294.

Rusk B., Emsbo P., Hammersli J., Hofstra A., Hunt A., Landis G. and Rye R. (2011) Origin and composition of fluids that form giant porphyry Cu (Mo–Au) deposits. In: *Proc. of the 11th Biennial SGA Meeting*. Antafogasta, Chile, 414–416.

Sabine C.L., Heimann M., Artaxo P., Bakker D.C.E., Chen C.-T.A., Field C.B., Gruber N., Le Quéré C., Prinn R.G., Richey J.E., Lankao P.R., Sathaye J.A. and Valentitni R. (2004) Current Status and Past Trends of the Global Carbon Cycle. *The Global Carbon cycle: Integrating Humans, Climate, and the Natural Word*, eds. Field C.B. and Raupach M.R., SCOPE 62, Island Press, Washington DC.

Sachana H.K., Mukherjee B.K. and Bodnar R.B. (2007) Preservation of methane generated during serpentinization of upper mantle rocks: Evidence from fluid inclusions in the Nidar ophiolite, Indus Suture Zone, Ladakh (India). *Earth. Planet. Sci. Lett.* **257**, 47–59.

Salvi S. and Williams-Jones A.E. (1992) Reduced orthomagmatic C-O-H-N-NaCl fluids in the Strange Lake rare-metal granitic complex, Québec/Labrador, Canada. *Eur. J. Mineral.* **4**, 1155-1174

Salvi S. and Williams-Jones A. E. (2006) Alteration, HFSE mineralisation and hydrocarbon formation in peralkaline igneous systems: Insights from the Strange Lake Pluton, Canada. *Lithos* **91**, 19–34

Samson I.M. (1990) Fluid evolution and mineralization in a subvolcanic granite stock: The mount pleasant W–Mo–Sn deposits, New Brunswick, Canada. *Econ. Geol.***85**, 145–163.

Savard M. M., Chi G., Sami T., Williams-Jones A. E. and Leigh K. (2000). Fluid inclusion and carbon, oxygen, and strontium isotope study of the Polaris Mississippi Valley-type Zn±Pb deposit, Canadian Arctic Archipelago: implications for ore genesis. *Miner. Deposita* **35**, 495–510.

Seward T. M. and Barnes H. L. (1997) Metal transport by hydrothermal ore fluids. In: In: Barnes H.L. (ed) Geochemistry of hydrothermal ore deposits, 3rd edn. Wiley, New-York, pp. 435–486.

Shatskiy A., Litasov K., Sharygin I. and Ohtani E. (2014) Effect of CO_2 content on melting phase relations in kimberlite group I at 6.5 GPa and 1200-1600ºC. *Japan Geoscience Union Meeting*. Pacifico Yokohama, Kaganawa, Japan. #SMP06-10 (abstr.)

Shilobreeva S., Martinez I., Busigny V., Agrinier P. and Laverne C., (2011) Insights into c and H storage in the altered oceanic crust: Results from ODP/IODP hole 1256D. *Geochim. Cosmochim. Acta* **75**, 2237–2255.

Sleep N.H. and Zahnle K. (2001) Carbon dioxide cycling and implications for climate on ancient Earth. *J. Geophys. Res.* **106**: 1373–1399.

Smith M.P., Campbell L.S. and Kynicky J. (2015). A review of the genesis of the world class Bayan Obo Fe–REE–Nb deposits, Inner Mongolia, China: Multistage processes and outstanding questions. *Ore Geol. Rev.* **64**, 459–476.

Stagno V. (2011) The carbon speciation in the Earth's interior as function of pressure, temperature and oxygen fugacity. *Dissertation.* Fakultät für Biologie, Chemie und Geowissenschaften, Universität Bayreuth.

Stolper E.M., Fine G., Johnson T. and Newman S. (1987) Solubility of carbon dioxide in albitic melt. *Am. Mineral.* **72**, 1071-1085.

Sverjensky D.A., Stagno V. and Huang F. (2014) Important role for organic carbon in subduction-zone fluids in the deep carbon cycle. *Nat. Geosci.* **7**, 909–913.

Tagirov B.R. and Korzhinsky M.A. (2001) Speciation of Fe (II) in H_2O-HCl-CO_2 fluid at 500-600˚C under 2 kbar. *Geochem. Int.* **9**, 943-950. (in Russian, ISSN 0016-7525).

Tappe S., Pearson D.G., Kjarsgaard B.A., Nowell G. and Dowall D. (2013) Mantle transition zone input to kimberlite magmatism near a subduction zone: Origin of anomalous Nd–Hf isotope systematics at Lac de Gras, Canada. *Earth. Planet. Sc. Lett.*371–372, 235–251.

Takenouchi S. and Kennedy G.C., (1964) The binary system H_2O–CO_2 at high temperatures and pressures. *Am. J. Sci.* **262**, 1055–1074.

Tattitch B.C., Candela P.A., Piccoli P.M. and Bodnar R.J. (2015) Copper partitioning between felsic melt and H_2O-CO_2 bearing saline fluids. *Geochim. Cosmochim. Acta* **148**, 81-99.

Taylor S.R. and McLennan (1995) The geochemical evolution of the continental crust. *Rev. Geophys.* **33**, 241–265.

Thébaud N., Philippot P., Rey P. and Cauzid J. (2006). Composition and origin of fluids associated with lode gold deposits in a Mesoarchean greenstone belt (Warrawoona Syncline, Pilbara Craton, Western Australia) using synchrotron radiation X-ray fluorescence. *Contrib. Mineral. Petrol.* **152**, 485–503.

Thomas R., Davidson P. and Schmidt C. (2010) Extreme alkali bicarbonate- and carbonate-rich fluid inclusions in granite pegmatite from the Precambrian Rønne granite, Bornholm Island, Denmark. *Contrib. Mineral. Petrol.* **161**, 315–329.

Tielens A.G.G.M., Wooden D.H., Allamandola L.J., Bregman J. and Witteborn F.C. (1996) The infrared spectrum of galactic center and the composition of interstellar dust. *Astrophys. J.* **461**, 210-222.

Tomilenko A.A., Chepurov A.I., Pal'yanov Yu.N., Pokhilenko L.N. and Shebanin A.P. (1995) Volatile components in the upper mantle (based on data on fluid inclusion studies) *Proceedings of the Int. Kimberlite Conf. Sixth Int. Kimberlite Conf.*; *Ext. Abs.*: 628–630.

Ulrich T., Golding S.D., Kamber B.S., Zaw K. and Taube A. (2002) Different mineralization styles in a volcanic-hosted ore deposit: The fluid and isotopic signatures of the Mt Morgan Au–Cu deposit, Australia. *Ore Geol. Rev.* **22**, 61–90.

Vallance J., Fontboté L., Chiaradia M., Markowski A., Schmidt S. and Vennemann T. (2009) Magmatic-dominated fluid evolution in the Jurassic Nambija gold skarn deposits (southeastern Ecuador). *Miner. Deposita* **44**, 389–413.

Walther J. J. and Orville P. M. (1983) The extraction-quench technique for determination of the thermodynamic properties of solute complexes: application to quartz solubility in fluid mixtures. *Am. Mineral.* **68**, 731–741.

Wedepohl K. H. (1995) The composition of the continental crust. *Geochim. Cosmochim. Acta* **59**, 1217–1232.

Williams S. N., Schaefer S. J., Calvache V. M.-L. and Lopez D. (1992) Global carbon dioxide emission to the atmosphere by volcanoes. *Geochim. Cosmochim. Acta* **56**, 1765–1770.

Wolfe W.W. and Bennett P. (2011) Solubility and dissolution kinetics of gypsum as a function of CO_2 partial pressure: Implications for geological carbon sequestration. *Am. Geophys. Union*, Fall Meeting 2011, abstract #H51G-1267

Wood B. J. (1993) Carbon in the core. *Earth. Planet. Sc. Lett.* **117**, 593–607.

Wood S. A. and Samson I. M. (1998) Solubility of ore minerals and complexation of ore metals in hydrothermal solutions. *Rev. in Econ. Geol.* **10**, 33–80.

Wood B. J. and Halliday A. N. (2010) The lead isotopic age of the Earth can be explained by core formation alone. *Nature* **465**, 767-770.

Wood B. J., Li J., Shahar A. (2013) Carbon in the core: its influence on the properties of core and mantle. *Rev. Mineral. Geochem.* **75**, 231-250.

Woolley A.R. and Bailey D.K. (2012) The crucial role of lithospheric structure in the generation and release of carbonatites: geological evidence. *Mineral. Mag.* **76**, 259-270.

Wopenka B. and Pasteris J.D. (1986) Limitations to quantitative analysis of fluid inclusions in geological samples by laser Raman microprobe spectroscopy. *Appl. Spectrosc.* **40**, 144–151.

Yang Z., Yang X., Xu Z. and Yang N. (2010). Molecular simulations of structures and solvation free energies of passivated gold nanoparticles in supercritical CO_2. *J. Chem. Phys.* **133**, 094702.

Yi W., Halliday A.N., Alt J.C., Lee D.-C., Rehkämper M., Garcia M.O., Langmuir C.H. and Su Y. (2000) Cadmium, indium, tin, tellurium, and sulfur in oceanic basalts: Implications for chalcophile element fractionation in the Earth. *J. Geophys. Res.* **105**, 18927-18948.

Zakirov I.V., Stretenskaja N.G., Aranovich L.Y. and Volchenkova V.A. (2007) Solubility of NaCl in CO_2 at high pressure and temperature: first experimental measurements. *Geochim. Cosmochim. Acta* **71,** 4251-4255.

Zhang Z. and Mao J. (1995) Geology and geochemistry of the Dongping gold telluride deposit, Heibei province, North China. *Intern. Geol. Rev.* **37**, 1094–1108.

Zhang Y. and Yinb Q.-Z. (2012) Carbon and other light element contents in the Earth's core based on first-principles molecular dynamics. *Proc. Natl. Acad. Sci. USA* **109**, 19579-19583.

Chapitre 2. Matériaux et méthodes

2. Matériaux et méthodes

2.1. Réacteurs hydrothermaux utilisés

L'étude des systèmes expérimentaux complexes riches en soufre et CO_2 à haute température et pression nécessite la mise en œuvre de divers réacteurs hydrothermaux en couplage avec des techniques analytiques adaptées pour doser les différents constituants des phases fluides. Cette approche permet d'obtenir des données sur la solubilité des métaux et volatils, leurs coefficients de partage et spéciation dans une large gamme de conditions bien contrôlées.

2.1.1. Réacteur à trempe

Les réacteurs à trempe ont été utilisés pour deux types d'expériences: la synthèse hydrothermale des sulfures de platine et les mesures de la solubilité de l'or dans les solutions concentrées (≥ 0.5 ppm Au) en présence du soufre et du CO_2.

Ce type de réacteur dont le schéma est donné sur la Fig. 2.1 est fait dans un alliage de titane (VT8; Al, Fe, Zn, Si ≤ 5%) qui lui procure une résistance mécanique et chimique élevée, permettant d'opérer jusqu'à 500°C et ~ 2 kbar. Le réacteur a un volume utile de 10 à 20 cm^3. Au début de l'expérience, le réacteur est chargé par pesée avec une solution aqueuse, de la poudre de soufre, de la glace carbonique (CO_2 solide) sous la température de l'azote liquide (~ -140°C) et un morceau d'or, puis fermé et placé verticalement dans un four régulé en température. Pour les mesures de solubilité, la phase solide (Au dans notre cas) est placée dans une nacelle suspendue au couvercle du réacteur. Pendant la montée en température, la solution se dilate, remplit tout le volume et entre en contact avec la nacelle. Les gradients de température dans le four stationnaire avec une résistance chauffante ne dépassent pas 1 °C/15 cm. La température est contrôlée à l'aide de thermocouples chromel/alumel (type K, alliage Ni-Cr/Ni-Al). La pression est calculée en fonction de la densité du fluide, avec une incertitude de ~ ±50 bar. Dans le cas des mesures de solubilité, les réacteurs restent sans agitation dans le four pour toute la durée de l'expérience (~ 5-20 jours), alors que dans le cas de la synthèse des sulfures de platine, les réacteurs sont sortis du four plusieurs fois pendant l'expérience pour une agitation à la main. A la fin de l'expérience, l'autoclave est extrait du four et placé verticalement dans un bécher rempli d'eau froide pendant 10-15 min sans que le niveau de l'eau n'arrive jusqu'au couvercle pour ne pas laisser l'eau rentrer dans le filetage et fausser le poids du réacteur (voir plus bas). Lors du refroidissement, le fluide se condense dans la partie basse du réacteur et n'est plus en contact avec la phase solide suspendue en haut dans la nacelle. Après la trempe, le réacteur est pesé pour contrôler son étanchéité durant l'expérience. Les solides et solutions sont récupérés selon la procédure décrite dans le chapitre 2.2.1.

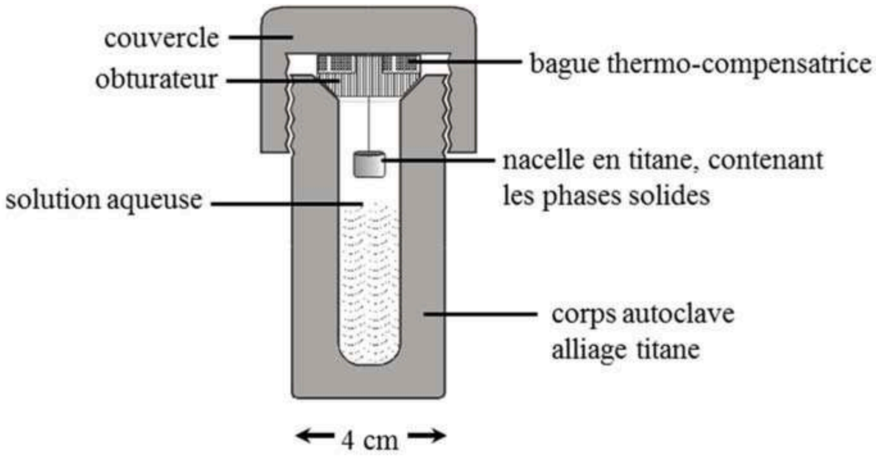

Fig. 2.1. Schéma du réacteur à trempe (T_{max} = 500°C, P_{max} = 2 kbar).

Les avantages de ce type de réacteur sont les suivants: 1) montage et démontage simples et rapides, 2) possibilité d'atteindre de hautes températures et pressions, 3) possibilité de déterminer la concentration (≥ 100 ppm) du soluté par perte de poids du solide après essai. Les inconvénients sont: 1) manque de mesure directe de la pression, 2) la récupération des solutés dans les solutions refroidies et le lavage des réacteurs (voir chapitre 2.2.1) sont délicats et donnent une mauvaise reproductibilité pour des concentrations inferieures au ppm, 3) impossibilité d'observer l'évolution du système expérimental dans le temps et de changer sa composition en cours d'expérience; plusieurs réacteurs sont donc nécessaires pour obtenir une série de données en fonction du temps ou balayer des gammes de composition du fluide.

2.1.2. Réacteur à séparation de phase

Le réacteur à séparation de phase a été adapté pour mesurer les coefficients de partage liquide-vapeur des métaux et des volatils dans deux types des systèmes expérimentaux: H_2O-CO_2-$K_2S_2O_3$-KCl-métaux ($Au_{(s)}$, sulfures de Mo, Pt, Cu et Fe, SnO_2) et H_2O-CO_2-KCl-NaCl-HCl-métaux ($Au_{(s)}$, $Pt_{(s)}$, Fe_2O_3, Fe_4O_3, Na_2MoO_4, CuCl, $ZnCl_2$, SiO_2, SnO_2). Ce réacteur, d'un volume de 380 cm^3, réalisé dans un grade de Ti(Ti2) par J.-C. Harrichoury au laboratoire de Géochimie, ont servi dans plus d'une dizaine de travaux de thèse du laboratoire depuis 1990 (Verdes, 1990; Castet, 1991; Pokrovski, 1996; Saldi, 2009; Saunier, 2011) pour des mesures de solubilité en phase liquide ou des synthèses minérales. Il permet d'opérer jusqu'à ~350°C et ~300 bar. Nous avons modifié cet autoclave afin de permettre des prélèvements contrôlés de la phase liquide et vapeur. Notre autoclave est équipé de deux systèmes de prélèvement de fluide par le haut et par le bas, constitués de tubes et vannes de prélèvement (Fig. 2.2).

L'autoclave est fixé dans un four vertical stationnaire équipé de deux résistances chauffantes régulées indépendamment à ±1°C afin de diminuer les gradients thermiques qui sont inférieurs à 10°C sur toute la longueur du réacteur (~ 30 cm). La pression est mesurée (incertitude ±5 bar) avant chaque prélèvement avec un capteur de pression fixé à la vanne vapeur. Le prélèvement du liquide ou de la vapeur s'effectue dans une ampoule rigide en titane (~2.5-3.5 cm^3) fixée à la deuxième vanne de prélèvement. Lorsqu'on ouvre les deux vannes, le fluide poussé par la pression interne, remplit l'ampoule de manière quasi instantanée. Ce dispositif, utilisé également dans d'autres types de systèmes expérimentaux (Seyfried, 1987; Pokrovski et al., 2008) assure un transfert complet des solutés et gaz en évitant toute perte du dissous par précipitation de phases insolubles (e.g., sulfures) ou par dégazage (e.g., CO_2, H_2S). Le traitement chimique du fluide ainsi prélevé est décrit dans le chapitre 2.2.2. L'injection du CO_2 s'effectue avec une pompe manuelle à cabestan attachée à la vanne d'entrée dans la phase liquide. La pression est contrôlée pendant l'injection par un capteur fixé à la vanne d'entrée dans la phase vapeur.

Les avantages de ce réacteur sont: 1) le montage assez simple et rapide, 2) possibilité de suivre l'évolution du système étudié et de modifier sa composition au cours de l'expérience, 3) possibilité d'obtenir les données directes sur les conditions physico-chimiques d'expérience (pression, concentrations et formes chimiques des ligands (S, Cl), concentration de gaz); 4) la mesure très propre des concentrations de solutés dans une très large gamme de 1s ppb (en phase vapeur) jusqu'à 1000s ppm (en phase liquide). Les désavantages sont: 1) possibilité d'explorer une gamme de température et de pression limitée, 2) gradients de température relativement importants (par rapport aux autres types de réacteurs décrits dans 2.1.1 et 2.1.3) du fait de configuration avec un four stationnaire en position verticale.

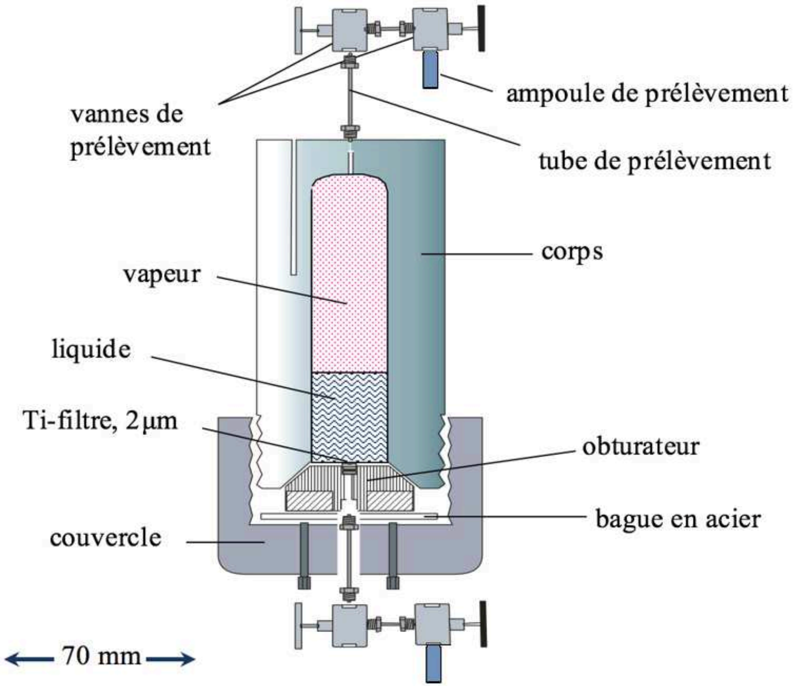

Fig. 2.2. Schéma du réacteur à séparation de phase (T_{max} = 360°C, P_{max} = 400 bar).

2.1.3. Réacteur à cellule flexible (type Coretest)

Nous avons utilisé le réacteur à cellule flexible (Coretest®) (Fig. 2.3) pour les mesures de solubilité des métaux (Au, Cu, Fe, Mo, Pt, Sn) en conditions supercritiques dans le système H_2O-CO_2-S-KCl en présence de tampons minéraux (pyrite-pyrrhotite-magnétite, quartz-muscovite-feldspath potassique, soufre). Ce réacteur est équipé d'une cellule flexible en titane ou en or (volume ~150-200 cm^3) plongée dans un grand autoclave (~1L) en acier inoxydable (marque 316 SS) rempli d'eau qui sert de fluide de pression. Une description plus détaillée du réacteur, des cellules flexibles et du mode opératoire est donnée par Seyfried et al. (1987), Gibert et al. (1998) et Tagirov et al. (2005). L'ensemble est fixé dans un four basculant chauffé par une résistance électrique dont la température est régulée à ±1°C. Une pompe permet d'injecter de l'eau dans l'autoclave externe pour augmenter la pression, alors qu'une vanne de fuite permet de libérer l'eau pour baisser la pression en cours de chauffe ou d'expérience. Ainsi la pression et la température peuvent être choisies et ajustées indépendamment. Les manipulations avec ce type de réacteur nécessitent une bonne estimation du volume de la cellule flexible (selon la masse et la densité du fluide aux conditions de l'expérience) pour que son expansion soit limitée idéalement entre 60 et 90% du volume initial, afin d'éviter un gonflement excessive (risquant de faire exploser la cellule) ou une compression trop forte (déformant la cellule de manière irrécupérable).

Les avantages de ce type de réacteur sont: 1) utilisable dans une large gamme de températures et de pressions pouvant ajustées indépendamment, 2) possibilité d'effectuer un prélèvement contrôlé de fluides riches en soufre, sel ou volatils sans perte de dissous, 3) la possibilité de modifier la composition du système expérimental en cours d'expérience en injectant une solution aqueuse (ou du CO_2 liquéfié) à l'aide d'une pompe manuelle calibrée, 4) mesures précises de solubilité des métaux dans une très large gamme de concentrations, de 1 ppb à ~1000 ppm, dans les fluides prélevés. Les inconvénients de ce réacteur sont: 1) montage et démontage fastidieux (1 journée minimum est nécessaire), 2) refroidissement lent (≥5h) après l'expérience (risque de recristallisation de certaines phases solides), 3) difficultés d'effectuer des expériences dans les systèmes liquide-vapeur (calcul du volume de la cellule imprécis, risque de contamination d'une des phases pendant le prélèvement avec un seul tube), 4) risque de fuite au niveau des nombreuses connections du système, 5) corrosion des thermocouples. Ces deux derniers aspects ont été systématiquement étudiés et améliorés au cours de ce travail (voir annexe 1).

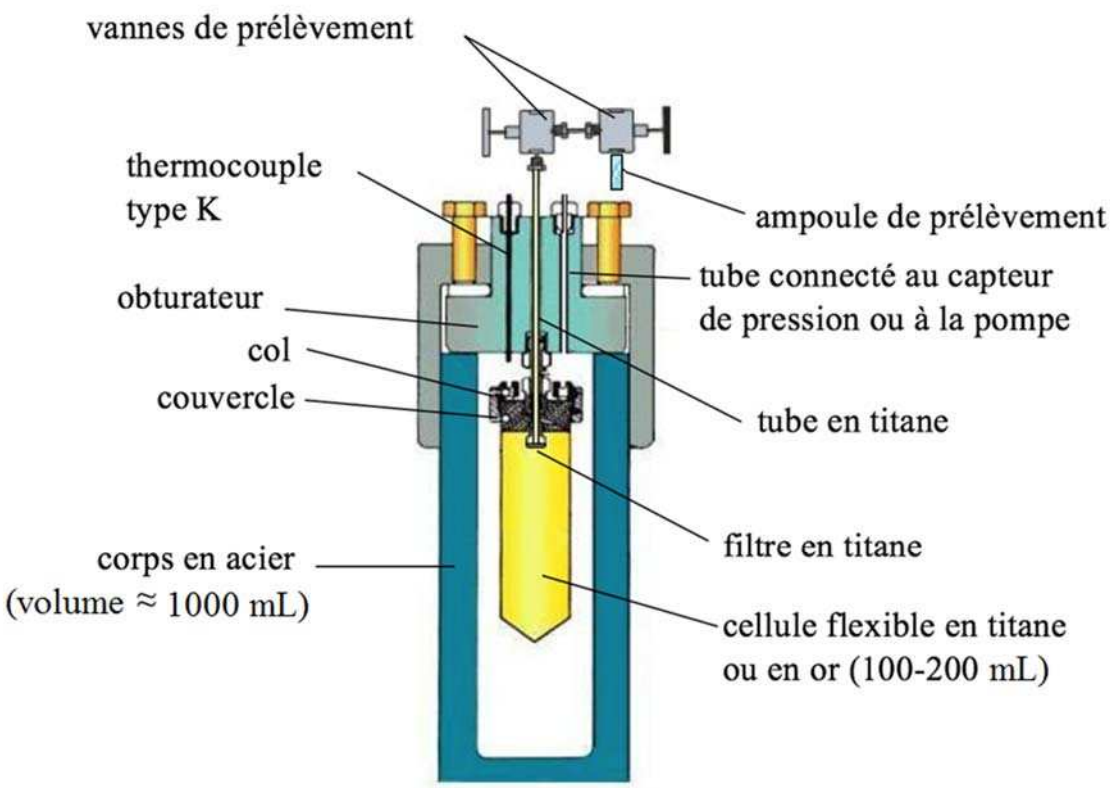

Fig. 2.3. Schéma du réacteur à cellule flexible (T_{max}=500°C, P_{max}~1.5 kbar).

2.2. Traitement des échantillons expérimentaux

2.2.1. Solutions après trempe

Les solutions récupérées après les expériences en autoclave à trempe sont transférées dans des béchers en téflon (Savilex®) pour évaporation et traitement à l'eau régale (similaire aux solutions prélevées, voir Annexe 2). Cependant, une partie de l'or, dissout à haute température durant l'expérience, peut se redéposer sur les parois du réacteur lors du refroidissement. C'est pourquoi une attention particulière a été donnée au lavage de ces réacteurs afin de récupérer la totalité de l'or dissout. Le lavage s'effectue une première fois avec quelque mL de l'eau régale à chaud et donne généralement 80-95% de Au total pour les concentrations totales dissoutes ≥35 ppm et 40-95% de Au total pour les concentrations faibles (<35 ppm). Un deuxième lavage avec de l'eau régale à chaud donne ≤20% de Au total pour les concentrations ≥35 ppm et jusqu'à 60% pour les concentrations inférieures à 35 ppm. Un troisième lavage avec la solution 0.5 wt% HCl et 1.5 wt% HNO_3 enfermé dans l'autoclave pendant une semaine donne ≤5% de Au total, ce qui confirme que l'or est récupéré quasi-complètement après les deux premiers lavages. D'après la comparaison des résultats obtenus aux mêmes conditions expérimentales mais dans des réacteurs différents, l'incertitude sure la mesure de solubilité atteint un ordre de grandeur (2 et 0.2 ppm pour les mêmes conditions expérimentales). Par conséquent, dans cette étude nous avons évité d'utiliser les données de solubilité obtenues dans les réacteurs à trempe qui sont inférieures à 2 ppm Au.

2.2.2. Solutions prélevées (autoclaves à séparation de phase et à cellule flexible)

Les méthodes de prélèvement des solutions expérimentales couplées aux techniques analytiques différentes ont été adaptées aux analyses des formes chimiques de soufre et des teneurs totales en métaux et chlorure. Le schéma de traitement des échantillons expérimentaux est présenté sur la Fig. 2.4. Toutes les dilutions depuis le prélèvement jusqu'à l'analyse ont été accomplies par pesées.

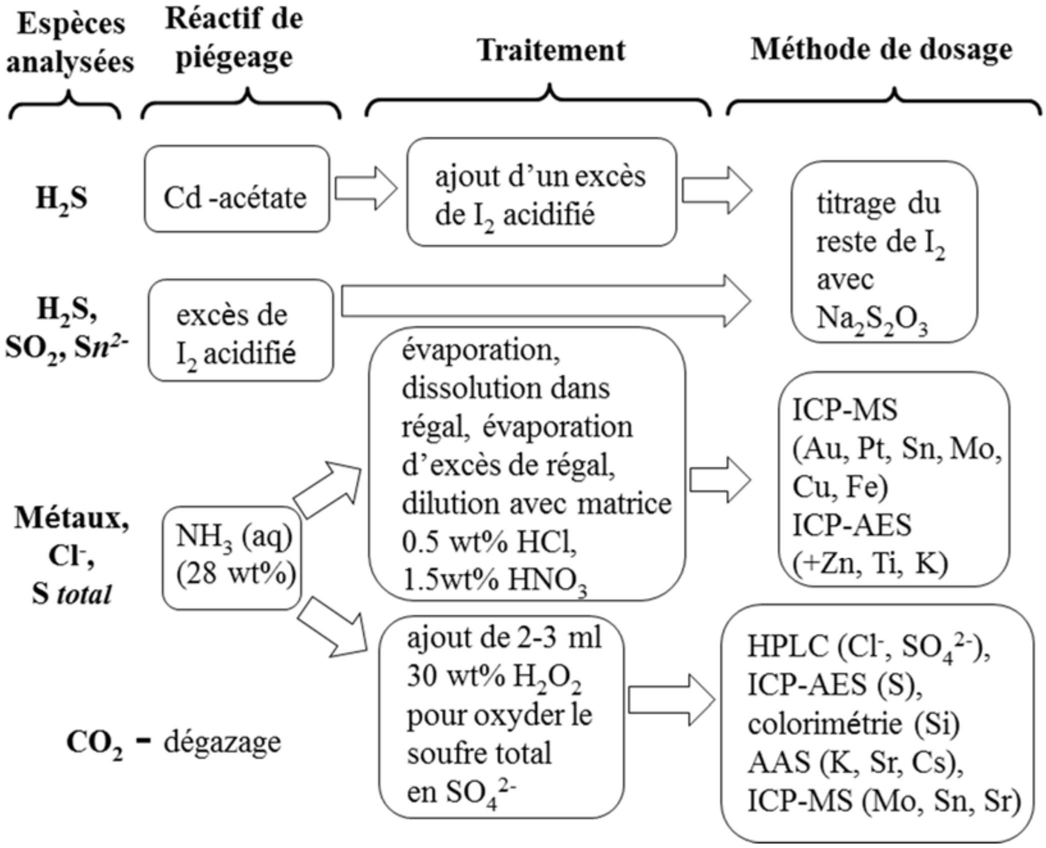

Fig. 2.4. Schéma de traitement et d'analyse des fluides expérimentaux prélevés.

Les deux premières extractions de fluide s'effectuent dans une solution d'iode dans l'ampoule de prélèvement pour piéger le soufre réduit (H_2S, S_n^{2-}, SO_2). Un troisième prélèvement se fait avec de l'ammoniac (pH~10) dans l'ampoule pour transformer H_2S en HS^-, et empêcher le dégazage de H_2S et la précipitation du soufre natif avec les métaux sur les parois de la vanne de prélèvement. Ainsi l'analyse du soufre total dans l'échantillon devient possible. L'échantillon prélevé dans l'ammoniac est divisé en deux parties: une aliquote est traitée par de l'eau régale (voir l'Annexe 2) et l'autre par du peroxyde d'hydrogène (H_2O_2). Un quatrième prélèvement s'effectue dans une solution d'acétate de cadmium pour piéger H_2S sélectivement. La quantité de

CO_2 dans les solutions prélevées est estimée par la mesure de masse de l'échantillon avant et après le dégazage.

2.3. Méthodes analytiques pour le dosage les solutions aqueuses

2.3.1. Spectrométrie d'émission atomique couplée à un plasma inductif (ICP-AES)

La spectrométrie d'émission atomique couplée à un plasma inductif (Inductively Coupled Plasma Atomic Emission Spectroscopy, ICP-AES) est une méthode d'analyse quantitative permettant de doser plusieurs éléments simultanément. La détection est basée sur le fait que la longueur d'onde des photons émis par les atomes et les ions de l'échantillon suite à leur excitation dans le plasma est caractéristique de chaque élément.

Le plasma est obtenu par la mise en place d'un champ magnétique sur le gaz d'argon qui circule à l'intérieur de la bobine d'induction. La solution à analyser injectée dans un plasma subit une vaporisation, une atomisation et une ionisation grâce à la température élevée générée par le plasma (de 6000 à 10000°C). Les électrons des couches externes des atomes excités (ionisés), lorsqu'ils retournent à leur état fondamental, émettent un photon dont l'énergie est caractéristique de l'élément. Cette énergie se trouve généralement dans la partie visible ou ultra-violette du spectre électromagnétique. Dans notre étude, nous avons utilisé un spectromètre optique Ultima 2 (Jobin Yvon ®) qui couvre le domaine spectral 160-800 nm. Les différentes longueurs d'ondes sont séparées par un réseau de diffraction et analysées par un détecteur photoélectrique. L'intensité de la ligne caractéristique (≈ nombre de photons émis) est proportionnelle à la concentration de l'élément dans l'échantillon. Cette intensité est ensuite comparée avec celles de solutions étalons dont les concentrations sont connues.

L'ICP-AES a été utilisée pour doser Cu, Fe, K, Zn, Ti, Au et S dans nos solutions expérimentales. La gamme de concentrations typiques mesurées pour ces éléments couvre l'intervalle ~0.01-10 ppm. Les concentrations de Pt, Mo et Sn dans les échantillons expérimentaux étaient généralement été trop faibles qu'il soit possible de les quantifier par ICP-AES. Les concentrations de Si étaient sous la limite de détection (≤8 ppb, voir plus bas) dans les échantillons traitées à l'eau régale, ce qui est due à la perte de $SiCl_{4(g)}$ lors de l'évaporation. Les étalons ont été préparés à partir de solutions standardisées de chaque élément (1000±5 ppm, Aldrich) dans une matrice de HCl 0.5 wt% et HNO_3 1.5 wt% préparée à partir d'acides bi-distillés.

Le signal de la matrice HCl-HNO_3 a été mesuré plusieurs fois (entre 3 et 10) afin d'estimer les limites de détection pour les métaux analysés (Tableau 2.1). *La limite de détection* (LD) est la plus petite concentration c_L de l'élément dosé pouvant être détectée avec une certitude raisonnable dans les conditions expérimentales. Celle-ci est calculée avec l'équation:

$$c_L = k \cdot \sigma / S, \qquad (2.1)$$

où σ est l'écart-type sur les n mesures du signal analytique de matrice, S est la sensibilité (la tangente d'angle de la pente de la courbe d'étalonnage, voir Fig. 2.5), k est un facteur numérique, qui reflète une probabilité considérable de trouver la valeur de c_L dans un intervalle de confiance mesuré par la *déviation standard relative* (RSD), ici k=3[2]. La déviation standard relative représente l'écart-type divisé en moyenne sur les n-mesures. *La limite de quantification* est aussi calculée à l'aide de l'équation 2.1, mais avec k=10 (IUPAC, 1976; Carré et al., 1997).

Tableau 2.1. Les limites de détection et de quantification des métaux par ICP-AES

Elément	Raie, nm	Gamme d'étalonnage, ppb	Limite de détection, ppb	Limite de quantification, ppb	Blancs de préparation[a], ppb	Gamme de concentrations typiques [b], ppb
Au	267.595	100-2000	2	6	bdl	10-10000
Au	242.795		1	5	bdl	
Cu	224.700	200-2000	2	8	bdl	10-100
Cu	324.754		2	6	3-15	
Fe	259.940	200-5000	5	16	7-26	30-4500
Zn	213.856	500-5000	2	5	9	7-450
Ti	337.280	500-5000	1	4	1-9	30-750
K	766.490	5000-50000	10	30	bdl	1000-10000
Si	251.611	1000-10000	8	25	bdl	bdl
Pt	214.423	5-50	0.5	2	bdl	bdl
Sn	189.930	5-50	2	6	bdl	bdl
Mo	284.823	0.5-5	>2.5	nm	nm	nm
S	181.978	5000-100000	100	400	nm	10000-50000

a - concentrations dans les solutions préparées par évaporation d'eau régale et diluées avec une matrice 0.5 wt% HCl + 1.5 wt% HNO_3, blancs expérimentaux; b - concentrations typiques dans les échantillons expérimentaux; nm – non mesuré; bdl - en dessous de la limite de détection.

La plupart des éléments ont été dosés avec une seule raie (la plus sensible) recommandée par le constructeur (voir tableau 2.1), tandis que pour Au et Cu nous avons utilisé deux raies pour chaque élément. Les raies de Cu sont en bon accord et donnent les mêmes valeurs de concentrations dans la limite des incertitudes (±20%). La raie 242.795 nm de Au est deux fois plus sensible que la raie 267.595 nm, la première donnant des valeurs de concentrations deux ou trois fois plus élevées que la deuxième pour des concentrations qui sont inférieures à 10 ppb. Nous avons pris la moyenne des deux valeurs de concentrations obtenues avec ces deux raies de Au. Les concentrations obtenues avec la courbe d'étalonnage ont été corrigées dans les cas suivants: a) la concentration mesurée est en dessous de l'étalon le moins concentré mais au-dessus de la limite

---

[2] Pour le facteur numérique k=3, la valeur de c_L se trouve dans un intervalle de confiance RSD≈33% avec une probabilité 90%, k=10 correspond à RSD≤5%

de détection, b) le blanc de préparation contient une quantité détectée d'élément dosé (voir Annexe 3).

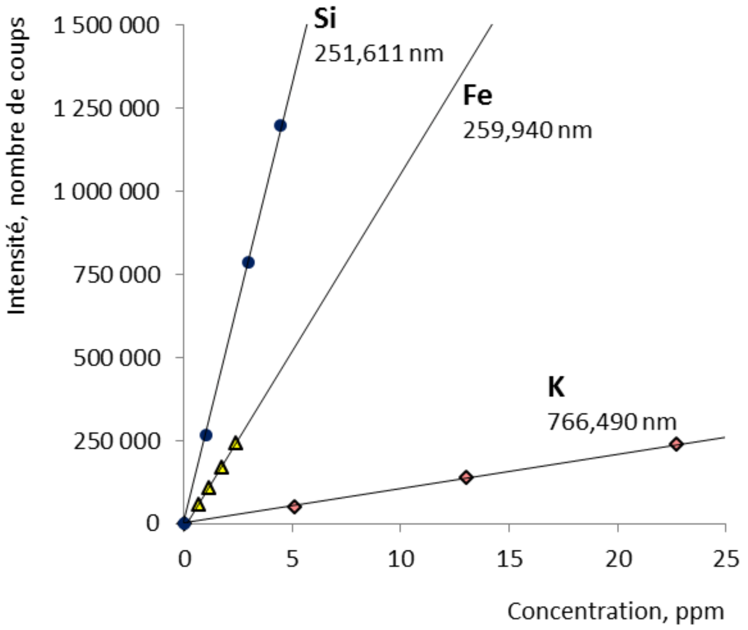

Fig. 2.5. Exemples des courbes d'étalonnage ICP-AES pour le silicium, le fer et le potassium.

Les avantages de l'ICP-AES sont: a) une analyse multi élémentaire, b) une excellente linéarité du signal dans une large gamme de concentration (e.g., Fig. 2.5), c) une faible influence de la composition de la matrice sur le signal, d) une bonne stabilité et reproductibilité du signal (RSD ≈ 2÷5%), e) des limites de détection et de quantification suffisamment basses pour permettre l'analyse de la plupart de nos métaux (à l'exceptions de Pt, Sn et Mo). Le seul inconvénient de cette méthode est qu'il faut disposer d'une grande quantité de solution nécessaire pour le dosage. Ce volume d'échantillon est fonction du nombre d'éléments à doser et du nombre de raies utilisées. A titre d'exemple, pour une mesure d'une concentration ≥ 1 ppm d'un élément avec une seule raie il faut minimum 4 mL de solution, tandis que pour un dosage d'une concentration ≤ 10 ppb, 8 mL sont nécessaires. Dans le dernier cas la quantité plus importante de la solution permet d'augmenter le temps de comptage et donc d'abaisser la limite de détection.

2.3.2. Spectrométrie atomique à la flamme (en absorption et en émission, AAFS et AEFS)

La spectrométrie atomique à la flamme (en mode d'absorption et d'émission) est une technique d'analyse mono-élémentaire d'échantillons aqueux dans une gamme de concentrations de l'ordre de 1-10 ppm. Dans cette étude nous avons utilisé le spectromètre AAnalyst 400 (Perkin Elmer®) avec une flamme air-acétylène afin de doser le potassium (en mode d'émission) et le strontium (en mode d’absorption). Le schéma de principe (Fig. 2.6) et les caractéristiques «pratiques» de la méthode sont brièvement présentés comme suit.

Grace à un nébuliseur, l’échantillon aqueux est aspiré et transformé en aérosol. La flamme générée par la combustion d’un mélange air/acétylène (~2500°C) pour les alcalins (Na, K, Rb) et les alcalinoterreux (Ca, Na, Ca) ou un mélange protoxyde d’azote/acétylène (~3100°C) pour les éléments réfractaires (comme Al, Mo, Sr), atomise les éléments contenus dans l’aérosol. Dans le cas de la spectrométrie d’émission atomique (atomic emission flame spectroscopy, AEFS) les processus physiques mis en jeu sont les mêmes que ceux décrits pour l’ICP-AES (chapitre 2.3.1), sauf que l’excitation des atomes et ions se passe dans la flamme sous une température plus basse que celle de plasma de l’ICP-AES. En mode d’absorption atomique (atomic absorption flame spectroscopy, AAFS), l’énergie fournie aux atomes provient d’une lampe «à cathode creuse» qui contient l’élément dont le spectre lumineux doit être produit. Un potentiel électrique appliqué entre l’anode et la cathode de la lampe transfère les atomes du métal de la lampe de l’état de base à un état excité; ils retournent aussitôt à leur état de base en émettant des photons caractéristiques de l’élément analysé. La lumière provenant de la lampe est divisée en faisceau de mesure et faisceau de référence par un hachoir mécanique. Quand l’échantillon passe à travers la flamme, les atomes de l’élément à doser absorbent l’énergie du faisceau. L'absorbance est le rapport entre l’énergie du faisceau de mesure et celle du faisceau de référence. L'absorbance A_λ à une longueur d'onde λ est convertie en concentration d’analyte selon la loi de Bouguer-Lambert-Beer (Beer, 1852):

$$A_\lambda = -\log(I/I_0) = \varepsilon_\lambda \cdot \ell \cdot C \qquad (2.2)$$

où I/I_0 est la transmittance de la solution ou du gaz, ε_λ est le coefficient d'extinction, ℓ est la longueur du trajet optique traversée dans la solution ou le gaz et C est la concentration volumique.

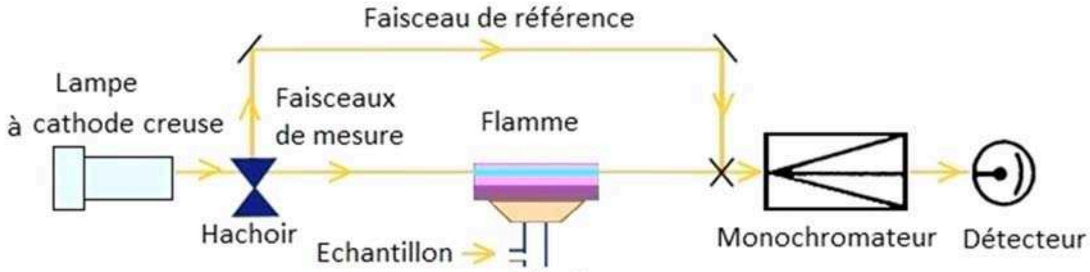

Fig. 2.6. Schéma du spectromètre d’absorption atomique à double faisceau (d’après Beaty et Kerber, 1993).

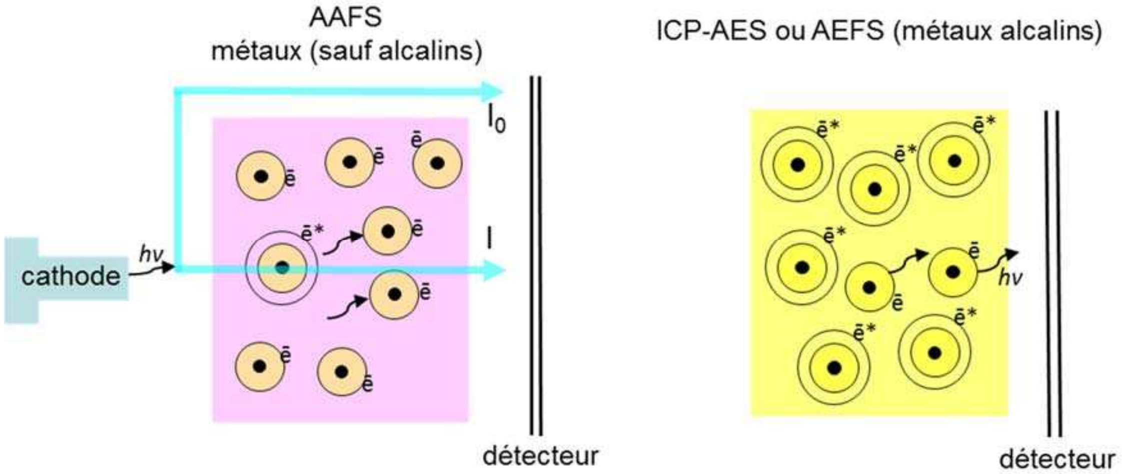

Fig. 2.7. Schéma de la distribution des atomes dans un état excité et non excité pendant l'analyse AAFS et ICP-AES ou AEFS.

La comparaison de l'ICP-AES, AEFS et AAFS est schématiquement présentée sur la Fig. 2.7. Dans le cas de l'AAFS, la plupart des atomes sont dans leur état non excité et sont prêts à absorber une énergie supplémentaire fournit par la cathode, alors que dans le cas de l'ICP-AES la haute température du plasma (≥6500°C) fait que la majorité des atomes sont excités et leur quantité est plus grande pour émettre, en se retournant à leur état fondamental, suffisamment de photons pour être détectés.

Les calculs des limites de détection et de quantification ont été établis à partir de plusieurs (de 4 à 5) analyses de la matrice 0.5 wt% à l'aide de la formule 2.1 (chapitre 2.3.1). La courbe d'étalonnage pour les analyses AEFS et AAFS n'est pas linéaire dans tout l'intervalle des standards (e.g., Fig. 2.8), c'est pourquoi pour le calcul de la sensibilité S on utilise la formule:

$$S = I_{stand\ 1}/C_{stand\ 1} \qquad (2.3),$$

ou $I_{stand\ 1}$ est l'intensité du standard le moins concentré et $C_{stand\ 1}$ est la concentration du standard le moins concentré qui correspond à l'intervalle linéaire de la courbe. Les gammes d'étalons et les limites de détection et de quantification sont reportées dans le Tableau 2.2.

Tableau 2.2. Les limites de détection et de quantification des métaux par AAFS.

Elément	Longueur d'onde, nm	Limite de détection, ppm	Limite de quantification, ppm	Gamme d'étalons, ppm
K	766.49	0.06	0.20	1.0-10
Sr	460.73	0.05	0.17	0.5-5.0
Cs	852.12	0.07	0.23	1.5-15

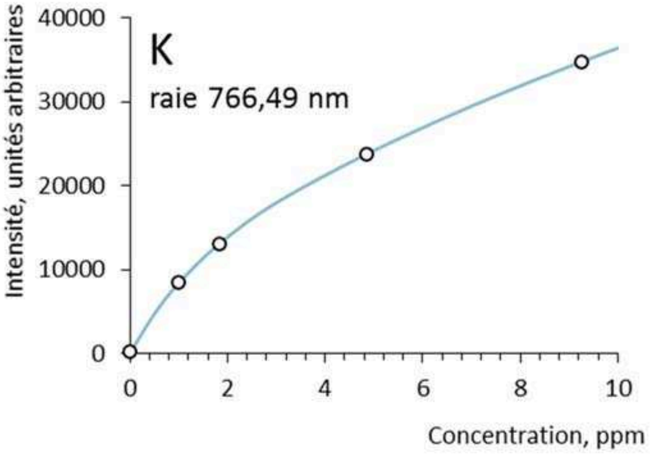

Fig. 2.8. Exemple d'une courbe d'étalonnage AEFS pour le potassium.

Les réglages pour le dosage du potassium sont: la flamme – air/acétylène, temps d'intégration – 3 fois 5 secondes, largeur de la fente du monochromateur – 2.7 mm, hauteur de la fente – 0.45 mm. Les réglages pour le dosage du strontium sont: la flamme – protoxyde d'azote/acétylène, l'intensité de la lampe – 20 mA, temps d'intégration – 3 fois 5 secondes, largeur de la fente du monochromateur – 1.8 mm, hauteur de la fente – 0.6 mm. Les réglages pour le dosage du césium: la flamme – air/acétylène, l'intensité de la lampe – 20 mA, temps d'intégration – 2 fois par 15 secondes, largeur de la fente du monochromateur – 2.7 mm, hauteur de la fente – 1.8 mm.

Les avantages de cette technique sont: a) faible coût, b) facilité de réglage, c) bonne stabilité et reproductibilité du signal (RSD ±2-5%). Les inconvénients sont: a) analyse mono élémentaire, b) linéarité de la courbe d'étalonnage limitée en concentration (e.g., Fig. 2.8), c) la quantité minimale de la solution pour un dosage est de 4 mL, d) forte influence de la composition de la matrice sur le signal analytique.

2.3.3. La spectrométrie de masse couplée à un plasma inductif (ICP-MS)

La spectrométrie de masse est une technique analytique permettant de séparer les ions en fonction de leur rapport masse/charge en phase gazeuse. La spectrométrie de masse couplée à un plasma inductif (Inductively Coupled Plasma Mass Spectrometry, ICP-MS) permet de doser plusieurs éléments simultanément. Le plasma couplé par induction, comme dans le cas de l'ICP-AES (chapitre 2.3.1 plus haut), est obtenu par l'application d'un champ magnétique sur le gaz d'argon. La solution à analyser, séparée en de petites gouttelettes (aérosol) par un nébuliseur, est ensuite injectée dans le plasma où elle subit vaporisation, atomisation et ionisation. La spectrométrie de masse assure l'extraction des ions du plasma à travers une série de cônes dans un spectromètre de masse (aimant quadripolaire dans le cas du système analytique appliqué dans cette étude). Un quadripôle, constitué de 4 électrodes qui ont la forme de tiges hyperboliques disposées parallèlement les unes aux autres, assure la séparation des ions, en fonction de leur rapport masse sur charge. Le détecteur photoélectrique (le multiplicateur d'électrons) transforme les coups des ions en signal électrique. Plus les ions sont nombreux, plus le courant est important. La concentration d'isotope d'élément est déterminée selon la courbe d'étalonnage obtenue dans les mêmes conditions expérimentales à partir de solutions standards. Plusieurs éléments chimiques peuvent avoir la même masse et charge (on parle alors d'isobare): les interférences isobariques peuvent gêner l'analyse.

Dans notre étude, le système analytique Agilent 7500ce (GET, Toulouse) a été utilisé pour doser Au, Pt, Cu, Fe, Sn, Mo, Ti dans les solutions expérimentales. Les concentrations typiques dosées couvrent l'intervalle 1-500 ppb. Les étalons externes de ces métaux ont été préparés à partir de solutions d'Aldrich standardisées (1000±5 ppm) dans une matrice de HCl 0.5 wt% + HNO_3 1.5 wt%. Le standard interne (spike) d'indium et de rhénium a été ajouté dans les échantillons pour tenir compte de la variabilité du signal dans le temps. Les limites de détection sont estimées d'après trois analyses de la matrice (tableau 2.3).

Tableau 2.3. Les limites de détection des métaux par ICP-MS.

Elément	Isotopes dosés	Limite de détection, ppb	Concentrations dans les blancs, ppb	Interférences isobariques les plus gênantes
Au	197	0.03	≤ 0.36	
Pt	194, 195	0.02	bdl	
Sn	118, 120	0.02	0.03-2.2	
Mo	95, 97	0.02	bdl	$Ar^{40}Fe^{57}$
Cu	63	0.005	≤ 0.6	$Ti^{47}O^{16}$
	65			$Ti^{49}O^{16}$, $Ti^{48}O^{16}H^{1}$
Fe	56	0.002	2-4	$Ar^{40}O^{16}$
	57	0.2		$Ar^{40}O^{16}H^{1}$, $K^{41}O^{16}$
Ti	47, 49	0.02	≤ 0.6	$Si^{30}O^{16}H^{1}$

Un problème de lavage de la machine après un échantillon ou un standard concentré a été observé pour l'or. La figure 2.9 montre qu'au moins trois lavages sont nécessaires après le passage d'un échantillon pour que le signal de Au redescende au niveau de celui du blanc passé avant le standard, alors que les signaux des autres métaux redescendent au niveau du blanc dès le premier lavage. Une attention particulière a donc été portée au dosage de Au, en établissant une séquence d'échantillons dans un ordre croissante de concentration, en passant au moins 3 solutions de lavage après un standard et en choisissant le blanc le plus proche de l'échantillon dans la séquence d'analyse pour le calcul des concentrations.

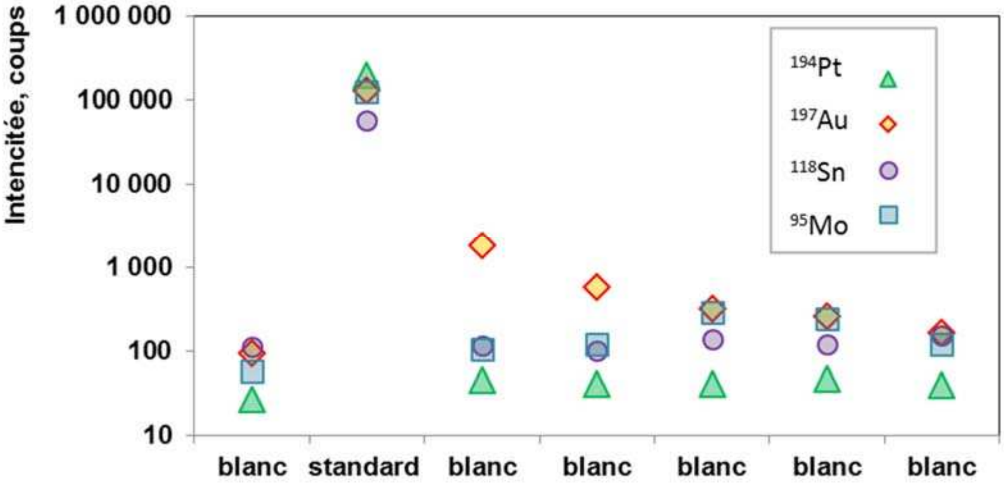

Fig. 2.9. L'efficacité du lavage de la machine pendant une analyse ICP-MS.

La correction des intensités des isotopes à mesurer dans les échantillons et les standards externes en utilisant le spike (standard interne) se fait avec la formule:

$$I_{\text{Me corr}} = \frac{I_{\text{Me}} \cdot I_{\text{InRe stand}} \cdot C_{\text{InRe sample}}}{I_{\text{InRe sample}} \cdot C_{\text{InRe stand}}} \tag{2.4}$$

où I_{Me} est l'intensité du signal de l'isotope à analyser dans l'échantillon, $I_{\text{InRe stand}}$ est l'intensité du signal de In (ou Re) dans le standard, $I_{\text{InRe sample}}$ est l'intensité du signal de In (Re) dans l'échantillon, $C_{\text{InRe sample}}$ est la concentration de In (Re) dans l'échantillon, $C_{\text{InRe stand}}$ est la concentration de In (Re) dans le standard. Cette correction, largement utilisée dans l'analyse par ICP-MS, pourrait cependant présenter les risques d'erreurs suivants: a) les concentrations de In et Re utilisées dans l'équation 2.4 pourraient être incorrectes dû à des erreurs de manipulation lors de l'ajout du spike dans les échantillons, b) les échantillons eux-mêmes pourraient contenir déjà In ou Re, c) une réponse différente de la machine aux isotopes légers et lourds (e.g., légers – Cu, Fe; lourds – Au, Pt), pourrait être mal corrigée par l'utilisation d'un spike de masse intermédiaire (In). Afin de vérifier l'importance des corrections de concentration en utilisant le spike, nous avons calculé les concentrations de Au, Pt, Sn, Mo dans 10 échantillons typiques avec ou sans la correction des intensités avec les standards internes ^{115}In et ^{187}Re. La différence entre les concentrations obtenues avec et sans la correction ^{115}In et ^{187}Re ne dépasse jamais 5% pour les métaux dosés (Fig. 2.10). La correction avec le standard interne n'est donc pas très utile dans notre cas. Les erreurs dues à la dilution et l'utilisation des matrices différentes sont du même ordre de grandeur, typiquement 10% de la valeur obtenue. Par conséquent, pour les calculs des concentrations de nos éléments par ICP-MS, nous nous sommes basés sur les standards externes de ces éléments sans aucune correction interne.

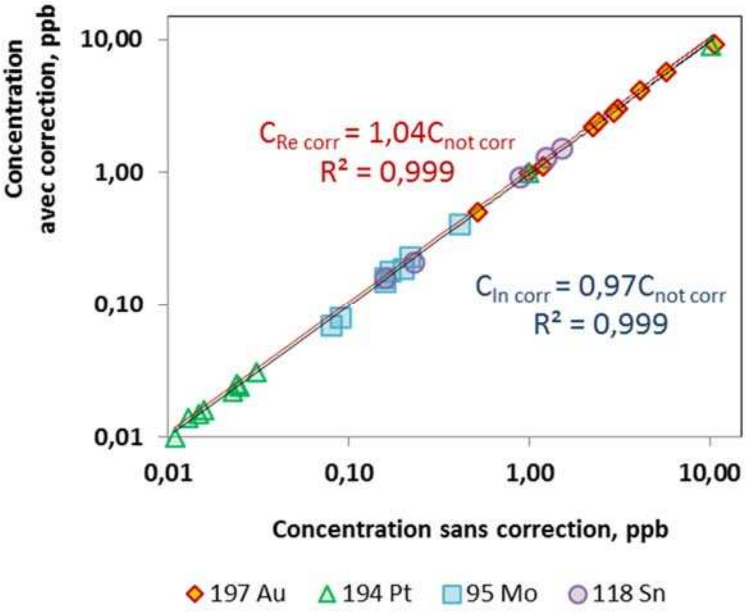

Fig. 2.10. Comparaison des concentrations des isotopes de Au, Pt, Sn et Mo (voir la légende) obtenues avec et sans les standards internes (In et Re) dans des solutions expérimentales représentatives. Les lignes droites représentent la corrélation linéaire entre les concentrations de tous les 4 isotopes calculées avec et sans chaque spike (^{187}Re – rouge, ^{115}In – bleu). Les pentes de ces courbes sont proches de 1.00 (±0.04) montrant ainsi que les corrections en utilisant les spikes sont mineures et peuvent donc être négligées.

En conclusion, les avantages de l'ICP-MS sont: a) une analyse multi élémentaire, b) des limites de détection bien plus basses que l'ICP-AES (jusqu'au niveau du ppt), c) une bonne linéarité du signal dans une large gamme de concentration (ppt-ppm), d) une quantité relativement faible (~5 mL) de la solution qui ne dépend pas beaucoup de nombre d'éléments à doser. Cependant, la forte sensitivité de la méthode induit les inconvénients suivants: a) l'intensité du signal dépend fortement de la matrice utilisée, b) une stabilité médiocre du signal dans le temps, surtout pour des matrices chargées (en sel ou soufre), c) des interférences isobariques entre l'isotope mesuré, l'argon et la matrice, d) un lavage délicat pour certains éléments (Au dans notre cas) – le signal des échantillons/standards de faibles concentrations peut être «contaminé» par des solutions plus concentrées qui les précédent dans la séquence d'analyse.

2.3.4. Colorimétrie de la silice par la réduction du complexe silicimolybdate

Le principe physique de la colorimétrie est similaire à celui de l'AAS (chapitre 2.3.2) et basé sur la relation de Bouguer-Lambert-Beer (Beer, 1852) (équation 2.2). La méthode de dosage consiste à envoyer un faisceau de lumière monochromatique au travers d'une cuve d'épaisseur (ℓ) contenant une solution colorée et à mesurer la lumière absorbée par la solution. On peut donc établir en utilisant des solutions standards une relation linéaire entre la densité optique et la concentration. Nous avons utilisé cette technique analytique pour le silicium parce que ce dernier se prête mal à l'AAS et l'ICP-AES en raison de sa nature réfractaire et à l'ICP-MS en raison de nombreuses interférences sur ses isotopes principaux (^{28}Si, ^{29}Si, ^{30}Si).

La méthode colorimétrique utilisée est celle de Mulin et Riley (1955) revue par Fanning et Pilson (1973). Elle implique la formation du complexe silici-12-molybdate jaune:

$$12\,[Mo_7O_{24}]^{6-} + 7\,Si(OH)_4^0 + 16\,H^+ \rightarrow 7\,[Si(Mo^{VI}_2O_7)_6]^{8-}\ \text{(jaune)} + 22\,H_2O \tag{2.5}$$

Le reste de l'acide molybdique qui n'a pas réagi avec la silice est éliminé par l'acide oxalique:

$$2\,[Mo_7O_{24}]^{6-} + 14\,C_2O_4^{2-} + 26\,H^+ \rightarrow 7\,Mo_2O_5(C_2O_4)_2^{2-} + 13\,H_2O \tag{2.6}$$

$$[Mo_7O_{24}]^{6-} + 7\,C_2O_4^{2-} + 6\,H^+ \rightarrow 7\,MoO_3(C_2O_4)^{2-} + 3\,H_2O \tag{2.7}$$

Ensuite le complexe jaune est réduit par l'acide ascorbique pour former un complexe bleu, qui appartient au groupe de polyanions nommés les 'bleus de molybdène':

$$C_6H_8O_6 - 2\bar{e} \leftrightarrow C_6H_6O_6 + 2\,H^+ \tag{2.8}$$

$$[Si(Mo^{VI}_2O_7)_6]^{8-}\ \text{(jaune)} + 4\,H^+ + 4\,\bar{e} \leftrightarrow [Si(Mo^{VI}_2O_7)_5(Mo^{IV}_2O_5)]^{8-}\ \text{(bleu)} + 2\,H_2O \tag{2.9}$$

Les 'bleus de molybdène' sont reliés par la structure commune du type Keggin (Keggin, 1934), qui consiste en un atome central (Si^{IV} dans notre cas) mis en cage par 12 unités MoO_6 octaédriques (Fig. 2.11).

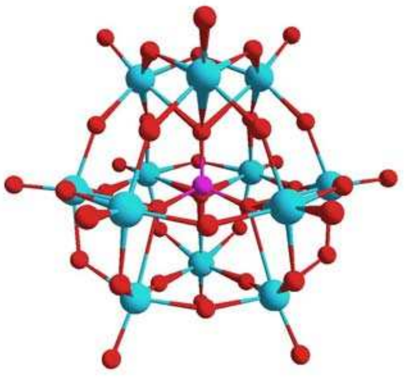

Fig. 2.11. La structure du type Keggin.

Le même principe peut être utilisé pour doser les éléments Al^{III}, P^{V}, B^{III}, As^{V}, Ge^{IV} qui forment des complexes similaires avec le molybdate. Les premières études sur ce type de complexes ont été faites à la fin du XVIII^ème^ siècle par les chimistes suédois Scheele et Berzelius. Les premiers observations d'«eaux bleues» naturelles avec du bleu de molybdène formé par oxydation de la molybdénite (MoS_2) ont été faites par des Amérindiens dans la Vallée des Dix Mille Fumées (Gouzerh and Che, 2006).

Dans notre travail, le dosage de la silice a été effectué au GET avec une chaîne automatique Autoanalyzer II Technicon en mode *flow-through*. L'intensité de la coloration de ce complexe bleu est mesurée à 660 nm. Nous avons utilisé les réactifs suivants: hepta-molybdate d'ammonium $(NH_4)_6Mo_7O_{24}\cdot 4H_2O$, acide oxalique et acide ascorbique. Les standards (1-10 ppm) ont été préparés par dilution (eau MQ) d'une solution-mère de Si (1000 ppm, 0.5 M NaOH, Merck). Les limites de détection et de quantification ont été déterminées d'après l'analyse de 6 blancs et sont respectivement 0.05 ppm et 0.16 ppm.

Le traitement de nos échantillons expérimentaux impose la présence des acides HNO_3 et HCl (voir plus haut). Nous avons donc étudié l'effet de cette matrice sur le dosage de Si. La gamme d'étalonnage a été créée dans une matrice de l'eau MQ. Avec cette gamme nous avons dosé des étalons préparés dans de l'eau MQ et une matrice 1 wt% HCl + 1 wt% HNO_3. La méthode utilisée donne des résultats similaires pour les étalons préparés avec l'eau, tandis qu'en présence de la matrice 1 wt% HCl + 1 wt% HNO_3 on analyse seulement la moitié du silicium (Fig. 2.12).

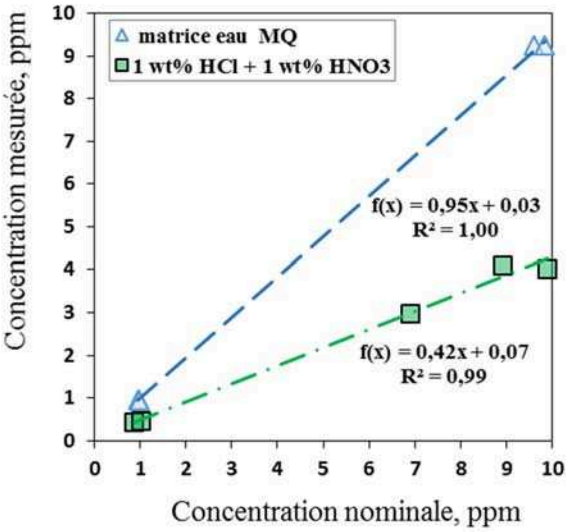

Fig. 2.12. L'influence de la matrice sur le dosage de la silice par colorimétrie.

Ce désaccord en milieu acide est probablement dû au fait que plus le milieu est acide, plus la formation du complexe jaune (réaction 2.5) est lente (Charlot, 1966). Une deuxième possibilité est la présence du Cl^- qui empêche la formation du complexe jaune (Charlot, 1966). Enfin, la capacité réductrice de l'acide ascorbique diminue en milieu très acide (réaction 2.8). Par conséquent, nous avons évité de doser la silice par cette méthode dans les échantillons acidifiés traités à l'eau régale.

En revanche, pour les échantillons prélevés dans de l'ammoniac, traités par du peroxyde d'hydrogène et diluées par de l'eau MQ, la méthode permet un dosage de Si correct.

2.3.5. Titrage des formes chimiques de soufre

Dans nos solutions expérimentales de haute température, le soufre se présente sous différentes formes chimiques: le sulfate, le sulfure et, éventuellement, le dioxide de soufre, le soufre moléculaire et les polysulfures. Ces formes de soufre ne peuvent pas être dosées par les méthodes décrites plus haut pour les métaux. En outre, elles sont très réactives et leurs concentrations absolues et proportions relatives évoluent rapidement avec la température. Par conséquent, lors du prélèvement du fluide, certaines de ces formes ont été piégées avec de l'iode ou de l'acétate de Cd et analysées par titrage comme décrit ci-dessous.

Le principe du titrage volumétrique consiste à ajouter un volume de solution de concentration connue (appelée titrant) afin de neutraliser une espèce contenue dans la solution inconnue (appelée analyte ou espèce titrée). Afin de déterminer le moment de neutralisation (appelé le point d'équivalence) un indicateur coloré est souvent utilisé. Dans le cas de l'iodometrie effectuée dans ce travail, la solution d'iode est l'analyte, la solution de thiosulfate de sodium est le titrant et la solution d'amidon sert d'indicateur.

Pour appliquer l'iodometrie aux solutions expérimentales, nous avons commencé les démarches analytiques dès le prélèvement. Le prélèvement a été effectué dans des solutions de concentrations connues d'iode acidifié ou d'acétate de cadmium en utilisant l'ampoule et la vanne de prélèvement connectées au réacteur de séparation de phases ou au réacteur à cellule flexible (chapitre 2.1 plus haut). La solution passe vite (premières secondes) du réacteur vers l'ampoule de prélèvement et réagi avec les réactifs presque instantanément.

Pour les solutions qui ont été prélevées dans la solution d'iode les réactions chimiques qui permettent l'analyse quantitative des formes « réduites » de soufre (le sulfure, le sulfite et les polysulfures) sont les suivantes (en milieu acide):

$$I_2 + H_2S \rightarrow 2\ I^- + S^0\downarrow + 2\ H^+ \qquad (2.10)$$

$$S_nS^{2-} + I_2 \rightarrow 2\ I^- + (n+1)\ S^0\downarrow \qquad (2.11)$$

$$SO_2 + I_2 + 2\ H_2O \rightarrow 2\ I^- + SO_4^{2-} + 4\ H^+ \qquad (2.12)$$

La quantité d'iode qui reste après l'interaction avec les espèces de soufre est titrée par $S_2O_3^{2-}$:

$$2\ S_2O_3^{2-} + I_2 \rightarrow S_4O_6^{2-} + 2\ I^- \qquad (2.13)$$

L'iode donne un composé bleu avec l'amidon. La limite de sensibilité de la couleur bleue est de 10^{-5} M de I_2 (Charlot, 1966). La disparition de la couleur bleue lors du titrage par thiosulfate signifie que la réaction 2.13 est complète.

Pour les solutions prélevées dans de l'acétate de cadmium, la réaction permettant l'analyse quantitative du sulfure est:

$$Cd(CH_3COO)_2 + H_2S \rightarrow CdS\downarrow + 2\ CH_3COOH \qquad (2.14)$$

Le précipité du CdS est séparé de la solution par centrifugation (3200 tours/s) et fait réagir en milieu très acide (10 pds % HCl) dans une ampoule en verre fermée avec un excès de solution d'iode acidifiée dont la concentration est connue. Cette réaction se passe en 2 étapes: d'abord le CdS se dissout rapidement en milieu d'acide chloridrique en libérant le H_2S selon la réaction 2.15.

$$CdS\downarrow + 2\ HCl \rightarrow H_2S + CdCl_2 \qquad (2.15)$$

Puis H_2S s'oxyde par I_2 en soufre selon la réaction 2.10. Le reste d'iode est titré par le thiosulfate selon la réaction 2.13.

Le titre de la solution de thiosulfate de sodium a été pris comme référence. La solution d'iode, qu'on ajoute dans l'ampoule ou dans le flacon avec le CdS, a été titrée trois fois par la solution de référence pour établir le titre de la solution d'iode $\mathrm{N}(\mathrm{I}_2)$ en Norm/kg:

$$\mathrm{N}(\mathrm{I}_2) = \frac{V_{thios} \cdot \mathrm{N}_{thios}}{m(I_2)} \qquad (2.16)$$

où V_{thios} est le volume de la solution du thiosulfate de sodium en ml (±0.05 mL), N_{thios} est le titre de la solution de thiosulfate en N/L, $\mathrm{m}(I_2)$ est la masse d'iode en g. La masse d'iode qui a réagi avec les formes réduites du soufre (réactions 2.10-2.12) ou le CdS (réaction 2.14), $\mathrm{m}(I_2)_{reacted\ with\ S}$, est calculée par différence entre la masse d'iode $\mathrm{m}(I_2)^0$ introduite dans l'ampoule de prélèvement (ou dans le flacon en verre avec le précipité de CdS) et la masse d'iode réagie avec la solution de thiosulfate (tous en g):

$$\mathrm{m}(I_2)_{reacted\ with\ S} = \mathrm{m}(I_2)^0 - \frac{V_{thios} \cdot \mathrm{N}_{thios}}{\mathrm{N}(I_2)} \qquad (2.17)$$

La concentration du soufre dans le fluide expérimental sous forme réduite, $\mathrm{m}(S)_{reduced}$, en mol/kg solution, ou sous forme de H_2S (d'après les réactions 2.10-2.12) est ensuite calculée comme:

$$\mathrm{m}(S)_{reduced} = \frac{\mathrm{m}(I_2)_{reacted\ with\ S} \cdot \mathrm{N}(\mathrm{I}_2)}{2 \cdot \mathrm{m}_{fluid}} \qquad (2.18)$$

où m_{fluid} est la masse du fluide expérimental (en g). Le coefficient 2 vient de la formule $N(I_2)=2 \cdot C(I_2)$ où $N(I_2)$ est la normalité d'iode en Norm/kg solution, et $C(I_2)$ est la concentration massique d'iode en mol/kg solution. La limite de détection pour cette méthode est 0.0005 mol S/kg solution (valeur estimée pour les «blancs»), tandis que le dosage quantitatif commence à partir de 0.002 mol S/kg solution avec une reproductibilité 10%. Pour les conditions typiques de dosage (~0.05 mol S/kg solution) la reproductibilité est de 5%.

2.3.6. *Chromatographie à haute performance en phase liquide (HPLC)*

La chromatographie à haute performance en phase liquide (l'abréviation anglaise HPLC, high performance liquid chromatography) est une technique basée sur la séparation des ions au travers d'une colonne d'échange chargée soit positivement (dans le cas de séparation des anions), soit négativement (dans le cas de séparation des cations). Les ions à doser s'adsorbent sur la colonne à différents niveaux, puis sont élués sous pression avec une solution «éluant» en fonction du temps. L'éluant sert à «chasser» les ions de l'échantillon qui sont absorbés à différents niveaux vers la sortie de la colonne. Il en résulte que les différents ions sortent à des moments différents. La vitesse du passage des ions à travers la colonne est différente en fonction de leur nature chimique et le temps de rétention est caractéristique pour chaque type d'ion. Après avoir été séparés, les différents constituants de l'échantillon pénètrent dans un suppresseur qui élimine les ions de l'éluant dont la conductivité est forte. Les ions de l'échantillon sont ensuite mesurés par conductimétrie (conductivité est mesurée en µS, micro-Siemens).

Cette méthode a été utilisée pour doser Cl^- et SO_4^{2-} (ce dernier correspond à la concentration de soufre totale après oxydation par H_2O_2, voir Fig. 2.4 et chapitre 2.2.2 plus haut). Dans notre étude, nous avons utilisé une chaîne Dionex ICS 2000, constituée d'une colonne de séparation (Dionex Ion Pac AS 18), d'un autosampleur, d'une pompe pour la circulation d'éluant, d'un suppresseur qui élimine l'éluant par un mécanisme d'électrolyse et d'une cellule de détection qui mesure la conductivité de la phase mobile. L'éluant utilisé est une solution de 30 mmol/L KOH avec un débit de 1 mL/min. La quantité de la solution d'échantillon nécessaire pour un dosage est de 200 µL. Un chromatogramme d'échantillon typique contenant le sulfate SO_4^{2-} (temps de rétention ~5.6 min) et le chlorure Cl^- (temps de rétention ~4.3 min) est donné sur la Fig 2.12. La gamme d'étalonnage de 1 à 50 ppm reste linéaire pour les anions Cl^- et SO_4^{2-}; elle permet de doser ces deux anions jusqu'à ~200 ppm (Fig. 2.14). Les limites de détection et de quantification pour le chlorure et le sulfate sont respectivement de 0.1 ppm et 0.3 ppm. La justesse du dosage est contrôlée par une solution standard certifiée, dosée comme un échantillon (ION-915, standard d'eau naturelle du Lac Supérieur, Canada).

Les solutions expérimentales qui ont été prélevées dans NH_4OH, traitées par H_2O_2 et diluées par MQ (Fig. 2.13) contiennent de faibles concentrations de NO_2^- et NO_3^- produites par oxydation partiels de NH_3, qui ne sont pas gênants et permettent donc d'effectuer l'analyse avec une reproductibilité de 2 à 5%. Par contre, dans les échantillons avec la matrice 0.5% pds HNO_3, la présence de l'ion nitrate (temps de rétention ~7.2 min) rend l'analyse du soufre impossible parce que dans ces conditions il n'y a plus de résolution des pics du nitrate et du sulfate. L'ion acétate (temps de rétention ~3.5 min; échantillons prélevés dans $Cd(CH_3COO)_2$) gêne l'analyse du chlorure – le pic du Cl^- se trouve sur la peinte du pic de l'acétate (Fig. 2.15). Une quantité importante de l'ion carbonate peut gêner l'analyse du Cl^- et du SO_4^{2-}(Fig. 2.16).

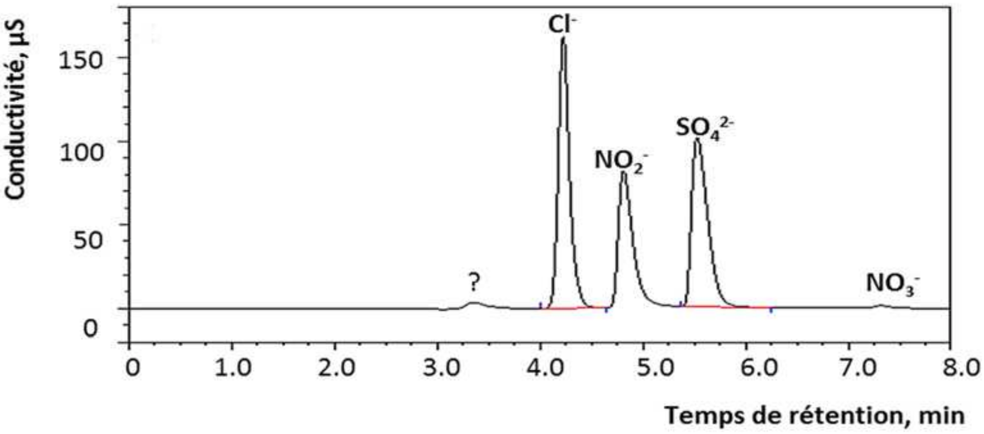

Fig. 2.13. Exemple d'un chromatogramme: l'intensité du signal des anions en fonction du temps de rétention, '?' – pic non-identifié, probablement l'ion acétate ou HOO^-.

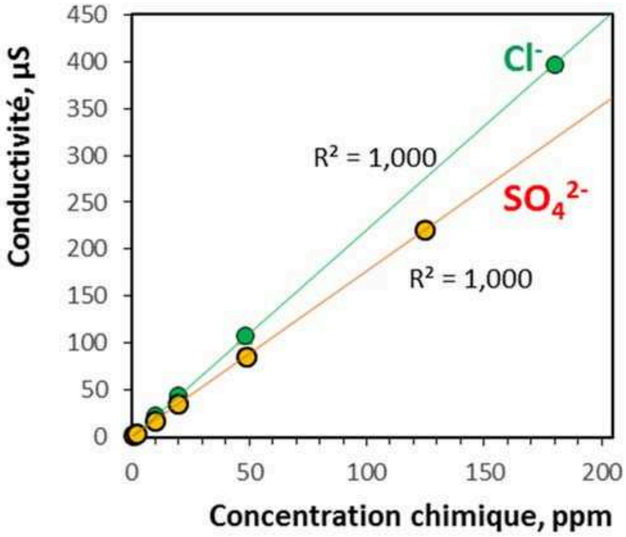

Fig. 2.14. Exemple de courbes d'étalonnage HPLC de Cl^- et SO_4^{2-}.

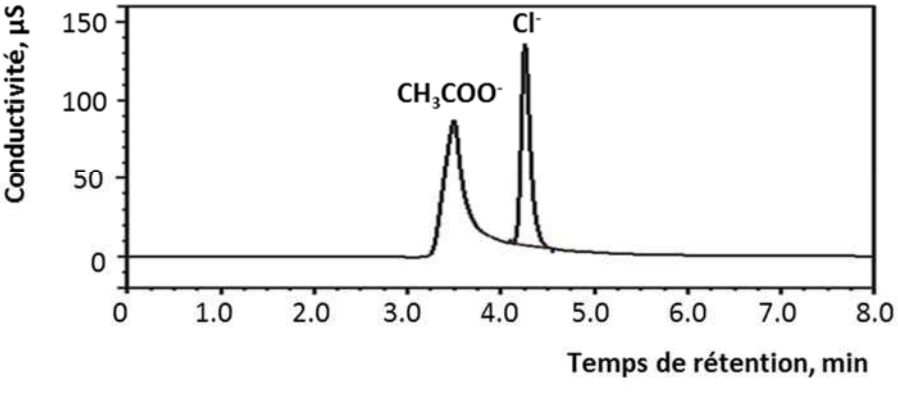

Fig. 2.15. Chromatogramme d'un échantillon contenant les ions acétate et chlorure.

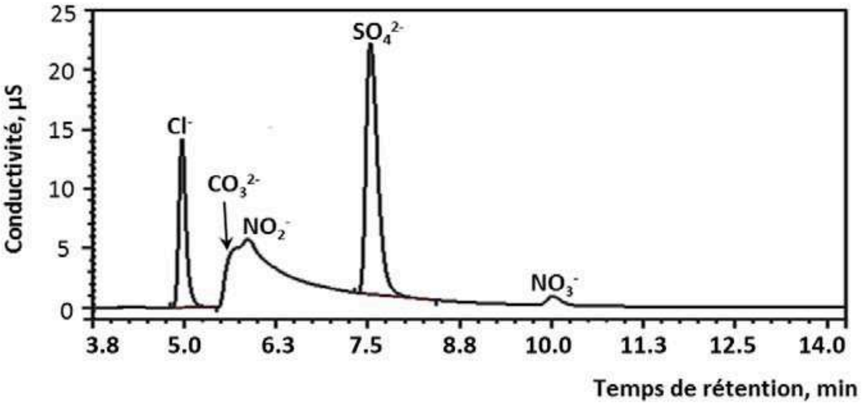

Fig. 2.16. Chromatogramme d'un échantillon, contenant une grande quantité d'ion carbonate (prélèvement du fluide contenant ~45 wt% de CO_2). La dérive entre le temps de rétention pour chlore et sulfate sur cette figure et les figures précédentes (2.13, 2.15) est due au changement de la colonne chromatographique. Le temps de rétention pour chaque anion et la résolution entre les pics est donc fonction non seulement de la concentration d'éluant, son débit, mais aussi des propriétés de la colonne, qui changent avec le temps d'utilisation.

2.3.7. Résumé des méthodes analytiques

Les caractéristiques métrologiques des méthodes d'analyses quantitatives décrites ci-dessus sont résumées dans le tableau 2.4.

Tableau 2.4. Caractéristiques métrologiques des analyses (voir Tableau 2.1-2.3 pour les détails).

Méthode, appareil	Eléments/ isotopes/ formes chimiques	Gamme de concentrations typique, ppb	Limite de détection, ppb	Quantité minimale de la solution, ml	Matrice	Remarques
ICP-AES Ultima 2 (Horiba Jobin Yvon)	Au	10-10000	1-2	30	HNO_3 1.5 wt%, HCl 0.5 wt%	
	Cu	10-100	1-2			
	Zn	7-450	2			
	Ti	30-750	1			
	Fe	30-4500	5			
	K	1000-10000	10			
ICP-MS Agilent 7500ce	^{197}Au	1-15	0.03	5	HNO_3 1.5 wt%, HCl 0.5 wt%	
	^{194}Pt ^{195}Pt	10-40	0.02			
	^{95}Mo ^{97}Mo	100-400	0.02			
	^{118}Sn ^{120}Sn	100-1500	0.02			
	^{63}Cu, ^{65}Cu	1-100	0.005			
	^{56}Fe, ^{57}Fe	30-100	0.02			
	^{47}Ti, ^{49}Ti	30-750	0.02			
Colorimétrie Autoanalyzer II Technicon	Si	1000-10000	50	2	MQ	ions gênants H^+, NO_3^-, Cl^-
AEFS et AAFS/ AAnalyst 400 (Perkin Elmer)	K	1000-10000	60	12	HNO_3 0.5 wt%	ion gênant Cl^-
	Sr	500-5000	50			
	Cs	1500-15000	70			
HPLC Dionex ICS 2000	Cl^- SO_4^{2-}	1000-50000	100	0.2	MQ	ions gênants NO_3^-, CO_3^{2-}, CH_3COO^-
Iodometrie	H_2S, HS^-, S_nS^{2-}, SO_2	60000-1500000	10 000	1	HCl 10 wt%	

2.4. Préparation et caractérisation des phases solides

Les minéraux suivants ont été utilisés dans notre étude pour tamponner le pH, la fugacité de soufre et d'oxygène: feldspath potassique (adulaire, JCPDS carte #31-966), muscovite (2M-type, #6-263), quartz (#33-1161,), andalousite (#39-376), pyrite (Alfa-Aesar, #42-1340), pyrrhotine (#29-724, Primorskiy kray, Dalnegorsk, Russia), magnétite (crédits A. Zotov, #19-0629) et hématite (Milhas, Haute-Garonne, Pyrénées, France). Les abréviations suivantes pour ces assemblages minéraux sont utilisées dans cette étude : PPM – pyrite, pyrrhotite, magnétite, PMH – pyrite, magnétite, hématite, QMK – quartz, muscovite, feldspath potassique, QMA – quartz, muscovite, andalousite. Ce tamponnage est nécessaire d'une part, pour assurer la stabilité des conditions pH, fO_2 et fS_2 lors des expériences de longue durée et, d'autre part, pour estimer plus précisément les valeurs de ces paramètres à partir des constantes bien connues des équilibres thermodynamiques suivantes:

$$FeS_{(cr)} + H_2S^0_{(aq)} = FeS_{2(cr)} + H_{2(g)} \text{ (PP)} \quad (2.19)$$

$$3FeS_{(cr)} + 4H_2O = Fe_3O_{4(cr)} + 2H_{2(g)} + 1.5S_{2(g)} \text{(PM)} \quad (2.20)$$

$$Fe_3O_{4(cr)} + 6H_2S^0_{(aq)} = 3FeS_{2(cr)} + 4H_2O + 2H_{2(g)} \text{ (MP)} \quad (2.21)$$

$$2Fe_3O_{4(cr)} + 0.5O_{2(g)} = 3Fe_2O_{3(cr)} \text{ (MH)} \quad (2.22)$$

$$Fe_2O_{3(cr)} + 4H_2S^0_{(aq)} = 2FeS_{2(cr)} + 3H_2O + H_{2(g)} \text{ (PH)} \quad (2.23)$$

$$KAl_3Si_3O_{12}H_{2(cr)} + 6SiO_{2(cr)} + 2K^+ = 3KAlSi_3O_{8(cr)} + 2H^+ \text{ (QMK)} \quad (2.24)$$

$$3Al_2SiO_{5(cr)} + 3SiO_{2(cr)} + 3H_2O + 2K^+ = 2KAl_3Si_3O_{12}H_{2(cr)} + 2H^+ \text{ (QMA)} \quad (2.25)$$

Les minéraux suivants des métaux d'intérêt économique Cu, Mo, Sn, Zn et Au ont été utilisés pour les mesures de solubilité dans les systèmes tamponnés: chalcopyrite $CuFeS_2$ (Messina Transvaal R.S.A., #37-0471), molybdénite MoS_2 (courtoisie de A. Zotov, #17-0744), cassitérite SnO_2 (courtoisie de P. Kartashov, Iultine, Chukotka, Russie, #41-1445), sphalérite ZnS (courtoisie de B. Tagirov, Santander, l'Espagne, #05-566), and gold métal foil (Heraeus, 99.999% purification). Avant les expériences, tous les minéraux (grains >50 µm) ont été triés à la main sous un binoculaire, lavés plusieurs fois avec de l'eau déminéralisée jusqu'à ce que le surnageant (constitué de fines particules) devienne transparent au bout de 2 minutes. L'absence d'impuretés a été vérifiée par diffraction des rayons X (XRD) et microscopie électronique à balayage (MEB).

Le sulfure de platine (II) (PtS, taille des cristaux <1 µm, #26-1302) a été synthétisé en autoclave en conditions hydrothermales à partir de poudres fines de Pt et S, puis pressé en pastilles pour les expériences de solubilité (voir les détails dans le chapitre 3, *annexe électronique EA1*). Une poudre de soufre natif (99.98%, Sigma-Aldrich, CAS 7704-34-9) a été utilisée pour un autre type d'expériences de solubilité de l'or, à la fois pour fournir les ligands (HS^- et S_3^-) et pour tamponner l'acidité et le potentiel redox via les équilibres hydrogène sulfate-sulfure d'hydrogène en solution (Jacquemet et al., 2014) selon les réactions suivantes :

$4S_{(cr)} + 4H_2O = 3H_2S^0_{(aq)} + SO_4^{2-} + 2H^+$ (2.26)

$H_2S^0_{(aq)} + 2O_{2(g)} = SO_4^{2-} + 2H^+$ (2.27)

$SO_4^{2-} + H^+ = HSO_4^-$ (2.28)

Après les expériences avec les tampons minéraux, les phases solides ont été examinées à l'aide de MEB et XRD. Les minéraux qui ont tamponné les systèmes expérimentaux sont toujours restés inchangés. Le seul changement entre les minéraux initiaux et les minéraux finaux a été enregistré après l'expérience #m23: la sphalérite (ZnS) initialement mise s'est transformée en cubanite ($CuFe_2S_3$ avec 1.7 wt% Zn). Par la suite, nous avons donc exclu le Zn de nos systèmes expérimentaux en présence du cuivre et du soufre.

2.5. Modélisation thermodynamique

Les solubilités des métaux obtenus dans cette étude ont été comparées avec les calculs d'équilibre chimique en utilisant les propriétés thermodynamiques des minéraux et des espèces aqueuses disponibles dans la littérature, combinées avec un modèle récent pour les fluides mixtes.

2.5.1. Modèle du solvant mixte H_2O-CO_2

L'énergie libre de Gibbs d'une espèce dissoute dans un fluide aqueux à une *T* et une *P* données est décrite par l'équation:

$$G_{i,TP} = \Delta G_i^0 + 2.3026RT\log a_i \quad (2.29)$$

où ΔG_i^o est l'énergie libre standard de Gibbs de l'espèce *i*, *R* est la constante de gas parfait, *T* est la température en Kelvin, et a_i est l'activité de l'espèce, qui se présente comme

$$a_i = \gamma_i \cdot m_i \quad (2.30)$$

où γ_i et m_i sont, respectivement, le coefficient d'activité et la molalité de l'espèce *i.* Lorsque l'espèce est transférée du fluide aqueux dans un fluide mixte CO_2-H_2O, deux changements fondamentaux ont lieu dans son énergie libre Gibbs ($\Delta G_{i,TP}$): la solvatation, appelée la contribution de Born (ΔG^o_{Born}) qui décrit les interactions de l'espèce avec les molécules du solvant, et une contribution électrostatique appelée Debye–Hückel (ΔG_{DH}), qui décrit les interactions des espèces ioniques entre elles:

$$\Delta G_{i,TP} = \Delta G^0_{Born} + \Delta G_{DH} \quad (2.31)$$

De grandes concentrations de CO_2 modifient les propriétés du solvant (eau) et donc la contribution de Born (solvatation) de l'espèce (Akinfiev and Zotov, 1999) qui est décrite par l'équation électrostatique de Born (1920):

$$\Delta G^0_{Born} = \omega_i \cdot \left(\frac{1}{\varepsilon_{mix}} - \frac{1}{\varepsilon_{water}} \right) \tag{2.32}$$

où ΔG^0_{Born} est le changement de l'énergie Gibbs standard de l'espèce, ω_i est le coefficient de Born de l'espèce, ε_{mix} est la constante diéléctrique du solvant mixte H_2O-CO_2 et ε_{water} est la constante diéléctrique de l'eau pure.

Le coefficient de Born classique est défini comme

$$\omega_i = \frac{N^\circ e^2 q_i^2}{2r_i} \tag{2.33}$$

où N° est le nombre d'Avogadro ($6.02252 \cdot 10^{23}$ mol^{-1}), e est la charge de l'électron ($4.80298 \cdot 10^{-10}$ esu), q_i est la charge électrique de l'ion et r_i est son rayon dit « électrostatique ». Cependant, compte tenu de la difficulté d'estimer directement le rayon électrostatique pour un complexe et l'ambiguïté du paramètre de Born classique pour des espèces neutres ($q_i = 0$), dans les modèles thermodynamiques utilisant ce paramètres (e.g., modèle HKF, voir plus bas), la valeur de ω est souvent déduit à l'aide de corrélations empiriques avec d'autres paramètres thermodynamiques ou par régression de données de solubilité ou de mesures directes de la capacité calorifique ou du volume de l'espèce dissoute en fonction de la température et pression (e.g., Sverjensky et al., 1997, 2014; Oelkers et al., 2009). Pour s'affranchir de ces ambigüités qui peuvent conduire à des valeurs de ω non-physiques (i.e., négatives pour les non-électrolytes volatils), dans notre modèle pour les fluides mixtes nous n'avons retenu que des valeurs positives bien contraintes pour certains espèces neutres comme $Si(OH)_4^0$, alors que celles de la plupart des complexes neutres des métaux ont été fixées à zéro (voir Tableau 2.5 plus bas).

La contribution Debye-Hückel (ΔG_{DH}), quant à elle, influe sur les coefficients d'activités de l'espèce dissoute en changeant les paramètres A et B de l'équation:

$$\log(\gamma_i) = -\frac{A q_i^2 \sqrt{I}}{1 + B a_i \sqrt{I}} \tag{2.34}$$

où q_i est la charge électrique de l'éspèce, a_i est la distance minimale entre deux espèces en solution (different du rayon electrostatique de l'equation 2.33); I est la force ionique de la solution, A et B sont les coefficients Debye-Hückel qui sont une fonction de la temperature, la constante diélectrique du fluide ε_{mix} et la densité.

Les propriétes volumetriques (la densite) et la constante diélectrique du fluide ont été calculées avec les équations de Redlich-Kwong (1949) et Kirkwood (1939), respectivement (voir Akinfiev and Zotov (1999) pour les details). Les coefficients d'activité des espèces neutres sont pris égaux à 1. Les contributions de Born et de Debye-Hückel ont été calculées pour chaque concentration de CO_2 en utilisant le code MIX-FL (Akinfiev and Zotov, 1999). Ensuite, l'énergie libre de Gibbs totale du système a été minimisée en utilisant la code HCh (Shvarov, 2008) et les molalités pour chaque espèce à l'équilibre ont été obtenues.

2.5.2. Principe de calcul d'équilibre chimique

Le code de calcul d'équilibre chimique HCh (Shvarov, 2008) est basé sur la minimisation de l'énergie libre du système:

$$\sum_i G_{i,TP} = \min \tag{2.35}$$

Le logiciel HCh est constitué de trois modules: UNITHERM, MAIN et GIBBS. Le module de calcul d'équilibre chimique *sensu stricto* GIBBS est associé à une base de données UNITHERM qui fournit les valeurs thermodynamiques pour les espèces aqueuses, solides et gaseuses; le module MAIN sert à créer un projet de calcul (description du système et des phases, liste des éléments et espèces et leurs concentrations initiales). L'utilisateur de HCh a l'accès aux programmes MAIN et UNITHERM (pour l'ajout et la correction des propriétés thermodynamiques dans la base de donnée) directement, mais n'a pas d'accès direct au code GIBBS. On peut en revanche accéder à ce dernier à l'aide de programmes/modules externes (voir plus bas et Shvarov, 2008).

Dans ce travail, le code MIX-FL et une macro écrite dans MS Excel ont été utilisés pour communiquer avec le programme HCh, tandis que les données calculées avec le MIX-FL sont introduites dans la macro manuellement, telles que la température, la pression, la concentration du CO_2, la salinité du fluide, les paramètres *A* et *B* de l'équation Debye-Hückel et le facteur de correction diélectrique:

$$\theta \equiv \left(\frac{1}{\varepsilon} - \frac{1}{\varepsilon_{H_2O}} \right) \cdot \frac{1}{2.303RT} \tag{2.36}$$

5.2.3. Propriétés thermodynamiques des espèces aqueuses

La bonne connaissance des énergies libres de Gibbs standard des espèces à une *T* et une *P* données (ΔG_i^o) est nécessaire pour mettre en application notre modèle. Ces données sont répertoriées sous forme de trois équations d'état différentes dans le programme UNITHERM: le modèle HKF (Helgeson–Kirkham–Flowers, 1981), le modèle RB (Ryzhenko-Bryzgalin, 1981, 1982) et le modèle AD basé sur de l'équation d'état d'Akinfiev et Diamond (2003).

Le modèle HKF révisé décrit l'énergie libre standard de Gibbs des espèces aqueuses en utilisant l'équation :

$$\begin{aligned} G(T,P) = {} & G_0 - S_0(T - T_0) + a_1(P - P_0) + a_2 \ln\frac{\psi + P}{\psi + P_0} + \frac{1}{T - \Theta}\left[a_3(P - P_0) + a_4 \ln\frac{\Psi + P}{\Psi + Po}\right] \\ & - c_1\left[T \ln\frac{T}{T_0} - T + T_0\right] - c_2\left[\frac{\Theta - T}{\Theta}\left(\frac{1}{T - \Theta} - \frac{1}{T - \Theta}\right) - \frac{T}{\Theta^2}\ln\frac{T_0(T - \Theta)}{T(T_0 - \Theta)}\right] \\ & + \omega_0\left(Z_0 + 1\right) + \omega_0 Y_0\left(T - T_0\right) - \omega\left(Z + 1\right) \end{aligned} \tag{2.37}$$

où G_0 et S_0 sont l'énergie libre de Gibbs et l'entropie standard molal de l'espèce sous conditions de référence, respectivement; a_1, a_2, a_3, a_4, c_1 et c_2 sont des constantes couramment appelées 'paramètres HKF', ψ et Θ sont les constantes du solvant (2600 bars et 228 K, respectivement) liées aux propriétés de l'eau, Z et Y sont des dérivés T-P non-linéaires de la constante diélectrique de l'eau, ω (paramètre Born) est une fonction T-P non-linéaire qui dépend de la taille de l'ion et de sa charge électrique, T et P sont la température (en K) et la pression (en bar), respectivement; l'indice 0 correspond aux conditions standards de référence (T_0=298.15K, P_0=1 bar). Ce modèle est très largement répandu et il existe actuellement des paramètres HKF fiables pour beaucoup de complexes des métaux en solution. Les avantages de ce modèle sont: a) une grande versatilité, compte tenu du grand nombre de paramètres ajustables pour chaque espèce ($G°$, $S°$, $a1$-4, $c1$-2 et ω), b) la possibilité d'utiliser des corrélations entre différents paramètres ajustables pour chaque type d'espèces en solution (e.g., anions et cations chargés +/-1, différents complexes de métaux; voir Sverjensky et al., 1997; Shvarov, 2015), c) l'applicabilité de ce modèle aux très hautes températures et pressions (jusqu'à 1200°C et 60 kbar) en utilisant la densité et la constante diélectrique de l'eau récemment révisées par Sverjensky et al. (2014). Les faiblesses de ce modèle sont: a) des incertitudes sur les paramètres HKF mal connues ou très souvent ignorées dans la plupart des travaux reportant ces paramètres, ce qui rend difficile d'estimer l'incertitude finale sur la valeur de G à haute T-P, b) les limitations fondamentales pour les complexes neutres et non-électrolytes volatils qui sont liées à l'utilisation du paramètre de Born qui, par définition, ne s'applique qu'à des ions ou complexes ayant une charge électrique et ne peut pas être négatif (voir équation 2.33 plus haut).

Le deuxième modèle thermodynamique, celui de Ryzhenko (1982) et Bryzgalin and Rafal'sky (1981), décrit les constantes de dissociation de complexes aqueux selon l'équation:

$$\mathrm{pK}(T,P) = 298.15/T \cdot \mathrm{pK}_{298} + \mathrm{f}\,(T,P) \cdot (\mathrm{zz/a})_{\mathrm{eff}} \tag{2.38}$$

où $\mathrm{pK} = -\log_{10}\mathrm{K}$, T est la température (en K), P est la pression (en bar), f (T,P) est la fonction indépendante d'espèce qui est dérivée à partir de la constante diélectrique de l'eau et la constante de dissociation de l'eau en fonction de T et P, $(\mathrm{zz/a})_{\mathrm{eff}}$ est une propriété du complexe, définie comme

$$(\mathrm{zz/a})_{\mathrm{eff}} = \mathrm{A} + \mathrm{B}/T \tag{2.39}$$

où A et B sont constantes, T est la température (en K).

Le gros avantage de ce modèle est sa simplicité (avec seulement 3 paramètres ajustables: pK, A et B) qui permet de générer des paramètres robustes à partir d'un petit nombre de données expérimentales de pK en fonction de *T* et *P*; par conséquent, l'extrapolation de telles données au-delà de la gamme *T-P* couverte par les mesures devient plus fiable. Cependant, comme tout autre modèle électrostatique, il pourrait présenter des faiblesses pour traiter des espèces neutres, volatils (appelés gaz-like comme H_2S, H_2, SO_2) ou des complexes à forte liaison covalente.

De telles espèces neutres et volatiles peuvent désormais être traitées en utilisant un modèle alternative récemment développé par Akinfiev et Diamond (2003). Dans le cadre de ce modèle, la fonction de l'énergie libre Gibbs de l'espèce aqueuse $g_{aq}{}^{0}(P,T)$ d'un non-électrolyte à T et P donnée est définie comme:

$$g_{aq}^{o}(T,P) = g_{g}^{o}(T) - RT\ln N_{w} + (1-\xi)RT\ln f_{1}^{o} + RT\xi\ln\left(\frac{\tilde{R}T}{M_{w}}\rho_{1}^{o}\right) + RT\rho_{1}^{o}\left[a + b\left(\frac{10^{3}}{T}\right)^{0.5}\right] \quad (2.40),$$

où $g_{g}^{o}(T)$ est la fonction de l'énergie libre de Gibbs de l'espèce en état de gaz idéal, M_w=18.0152 g mol^{-1}, N_w= 1000/$M_w$mol, f_1^o et ρ_1^o sont respectivement la fugacité (en bar) et la densité (en g cm^3) du solvant pur (H_2O) à *T* et *P* données, $R = 1.9872$ cal·mol^{-1}·K^{-1} et $\tilde{R} = 83.144$ cm^3·bar·mol·K^{-1} sont les constantes du gaz parfait et *a*, *b* et ξ sont des coefficients empiriques, indépendants de *T* et *P* et propres à chaque espèce. Ce modèle s'est montré très efficace pour décrire l'ensemble des données expérimentales (mesures Cp et V, coefficients de partage entre liquide et valeur, équilibres des assemblages des oxydes et sulfures de fer comme PPM et PHM) sur les espèces volatiles clés des fluides hydrothermaux et de nos systèmes expérimentaux comme H_2S, H_2, O_2, CO_2, SO_2. La grande force de ce modèle est qu'il est fondamentalement basé sur les propriétés des espèces gazeuses qui sont bien mieux connues que celles des espèces aqueuses, et sur la densité de l'eau qui est le paramètre le mieux connu pour ce solvant. Ceci offre la possibilité d'extrapolation robuste dans une large gamme de *T* et *P* et notamment pour les fluides et vapeurs hydrothermaux-magmatiques caractérisées par des hautes températures (>500°C) et faibles densités (<0.5 g/cm^3) (e.g., Pokrovski et Dubessy, 2015). La seule limitation de ce modèle est la nécessité de connaître la valeur *g°(T)* de l'espèce gazeuse correspondante, donnée qui n'est pas facilement disponible pour la plupart des complexes des métaux (chlorurés, sulfurés ou hydroxylés) qui existent en solution aqueuse (Akinfiev et al., 2015).

Le tableau 2.5 liste les sources de données et le type de modèle parmi les trois discutés ci-dessus que nous avons utilisés dans ce travail pour les complexes aqueux des métaux et les principaux composés volatils. Les propriétés thermodynamiques de la plupart des ions et pairs d'ions des constituants majeurs de nos fluides (Na, Cl) et des minéraux proviennent de la source de données SUPCRT (Johnson et al., 1992), basée sur le modèle HKF et complétée par plusieurs travaux récents (http://geopig.asu.edu/index.html#).

Table 2.5. Sources de données pour les complexes des métaux et volatils considérées dans ce travail.

Element	Complex	Model	Born parameter ω×10^{-5}, cal/mol	Références[a] pour ω	Références[a] pour $G^0{}_{TP}$
H, O, S	**H_2S**, SO_2, H_2, O_2	AD	0	ce travail	AD03
	HS^-	HKF	1.441	SH88	SH88
C	**CO_2,** CH_4	AD	0	ce travail	AD03
	HCO_3^-	HKF	1.273	Jo92	Jo92
	CO_3^{2-}	HKF	3.391	Jo92	Jo92
	CO	HKF	0	Jo92	Jo92
Si	SiO_2	HKF	0.13	Sh97	Sh97
	SiO_2	HKF	0.36	Sv14	Sv14
	Si_2O_4	HKF	0.10	Sv14	Sv14
	H_4SiO_4	HKF	0.087	St01	St01
Fe	**$FeCl_2^0$**	HKF	0	ce travail	Sv97
	$FeCl_4^{2-}$	RB	2.67	ce travail[b]	Te09
Cu	**$Cu(HS)^0$**	HKF	0	AZ10	AZ10
	$CuCl_2^-$	HKF	0.81	AZ10	AZ10
	$CuCl^0$	HKF	0	Br07	Br07
	$CuCl_2^-$	HKF	0.84	Br07	Br07
	$CuCl_3^{2-}$	HKF	2.37	Br07	Br07
	$CuCl^0$	HKF	0	Sv97	Sv97
	$CuCl_2^-$	HKF	1.22	Sv97	Sv97
	$CuCl_3^{2-}$	HKF	2.86	Sv97	Sv97
Au	**$Au(HS)^0$**	HKF	0	Po14	Gi98, BS96, SS04,
	$Au(HS)_2^-$	HKF	0.77	Po14	Ta05, AZ01, AZ10
	$Au(HS)S_3^-$	RB	0.77	ce travail[c]	Po15
	$AuOH^0$, $AuCl^0$	HKF	0	Po14	Po14
	$AuCl_2^-$	HKF	0.86	Po14	Po14
Mo	**$KHMoO_4^0$**	BR	0	ce travail	Ku85, Zo94
	$HMoO_4^-$	HKF	1.14	Sh97	MS10
	MoO_4^{2-}	HKF	3.08	Sh97	Sh97
	$H_2MoO_4^0$	HKF	0	ce travail	MS10
Sn	**$Sn(OH)_4^0$**	BR	0	ce travail	Ry97
	$Sn(OH)HCO_3^0$	BR	0	ce travail	ce travail
Zn	**$ZnCl_2^0$**, $Zn(HS)_2^0$	HKF	0	AT14	AT14
	$ZnCl^+$	HKF	0.53	AT14	AT14
	$ZnCl_3^-$	HKF	1.00	AT14	AT14
	$ZnCl_4^{2-}$	HKF	2.67	AT14	AT14
Pt	**$Pt(HS)_2^0$**	HKF	0	ce travail	ce travail
	$PtCl^+$	HKF	0.62	Ta15	Ta15
	$PtCl_2^0$	HKF	0	Ta15	Ta15
	$PtCl_3^-$	HKF	1.17	Ta15	Ta15
	$PtCl_4^{2-}$	HKF	2.70	Ta15	Ta15

[a] SH88 – Shock and Helgeson (1988), Jo92 – Johnson et al. (1992), AD03 – Akinfiev and Diamond (2003), Sv14 – Sverjensky et al. (2014), Sv97 –Sverjensky et al. (1997), Te09 – Testemale et al., (2009), St01 –Stefánsson (2001), Sh97 – Shock et al. (1997), AZ01 – Akinfiev and Zotov (2001), AZ10 – Akinfiev and Zotov (2010), Br07 – Bruger et al. (2007), Gi98 – Gibert et al. (1998), BS96 – Benning and Seward (1996), SS04 – Stefánsson and Seward (2004), Ta05 – Tagirov et al. (2005), Ta15 – Tagirov et al. (2015), MS10 – Minubaeva and Seward (2010), Ku85 – Kudrin et al. (1985), Zo94 – Zotov et al. (1994), Ry97 – Ryzhenko et al. (1997), AT14 – Akinfiev and Tagirov (2014), PW94 – Pan and Wood (1994), Po14 – Pokrovski et al., (2014), Po15 – Pokrovski et al. (2015).

[b] Paramètre Born de $FeCl_4^{2-}$ est supposé être égal à celui de $ZnCl_4^{2-}$

[c] Paramètre Born de $AuHSS_3^-$ est supposé être égal à celui de $Au(HS)_2^-$.

Les espèces dominantes de chaque élément dans nos systèmes expérimentaux sont marquées en gras.

RÉFÉRENCES

Akinfiev N.N. and Zotov A.V. (1999) Thermodynamic description of equilibria in mixed fluids (H_2O-non polar gas) over a wide range of temperature (25 to 700°C) and pressure (1 to 5000 bars*). Geochim. Cosmochim. Acta* **63**, 2025-2041.

Akinfiev N.N. and Zotov A.V. (2001) Thermodynamic description of chloride, hydrosulfide, and hydroxo complexes of Ag(I), Cu(I) and Au(I) at temperatures of 25-500°C and pressures of 1-2000 bar. *Geochem. Intern.* **39**, 990-1006.

Akinfiev N.N. and Diamond L.W. (2003) Thermodynamic description of aqueous nonelectrolytes at infinite dilution over a wide range of state parameters. *Geochim. Cosmochim. Acta* **67**, 613-629.

Akinfiev N.N. and Zotov A.V. (2010) Thermodynamic description of aqueous species in the system Cu-Ag-Au-S-O-H at temperatures of 0-600°C and pressures of 1-3000 bar. *Geochem. Intern.* **48**, 714-720.

Akinfiev N.N. and Tagirov B.R. (2014) Zn in hydrothermal systems: thermodynamic description of hydroxide, chloride, and hydrosulfide complexes. *Geochem. Intern.* **52**, 197-214.

Akinfiev N.N., Plyasunov A.V. and Pokrovski G.S. (2015) An equation of state for predicting the thermodynamic properties and vapor-liquid partitioning of aqueous $Ge(OH)_4$ in a wide range of water densities. *Fluid Phase Equilibria* **392**, 74-83.

Beaty R.P. and Kerber J.D. (1993) *Concepts, Instrumentation and Techniques in Atomic Absorption Spectrophotometry.* The Perkin-Elmer, Inc.: Shelton, CT.

Beer A. (1852) Bestimmung der Absorption des rothen Lichts in farbigen Flüssigkeiten, *Ann. der Phys. und Chem.*, **86**, 78-88.

Benning L.G. and Seward T.M. (1996) Hydrosulphide complexing of Au (I) in hydrothermal solutions from 150-400°C and 500-1500 bar. *Geochim. Cosmochim. Acta* **60**, 1849-1871.

Born Von M. (1920) Volumen und Hydratationswarme der Ionen. *Zeitschr. Physik* **1**, 45-48.

Brugger J., Etschmann B., Liu W., Testemale D., Hazemann J.-L., Emerich H., van Beek W. and Proux O. (2007) An XAS study of the chloride complexing of Cu (I) in brines. *Geochim. Cosmochim. Acta* **71**, 4920-4941.

Bryzgalin O.V. and Rafal'sky R.P. (1982) Estimation of instability constants for ore-element complexes at elevated temperatures. *Geochem. Intern.* **19**, 839-849.

Carré M., Excoffier S., and Mermet J.M. (1997) A study of relation between the limit of detection and the limit of quantification in inductively coupled plasma spectrochemistry. *Spectrochim. Acta Part B* **52,** 2043-2049.

Castet S. (1991) Solubilité de la boehmite et spéciation de l'aluminium dissous dans les solutions aqueuses à haute température. Détermination expérimentale et modélisation. *Thèse de l'Université Paul Sabatier, Toulouse.*

Charlot G. (1966) *Les Méthodes de la Chimie Analytique. Analyse Quantitative Minérale.* Masson et C^{ie}, Paris.

Fanning K.A. and Pilson M. E.Q. (1973) Spectrophotometric determination of dissolved silica in natural waters. *Analytical Chemistry* **45**, 136-140.

Gibert F., Pascal M.-L. and Pichavant M. (1998) Gold solubility and speciation in hydrothermal solutions: Experimental study of the stability of hydrosulfide complex of gold ($AuHS^0$) at 350 to 450°C and 500 bars. *Geochim. Cosmochim. Acta* **62**, 2931-2947.

Gouzerh P. and Che M. (2006) From Scheele and Berzelius to Müller. Polyoxometalates (POMs) revisited and the "missing link" between the bottom up and top down approaches. *L'actualité chimique*. *Recherche et Développement* **298**, 2-22.

Helgeson H.C., Kirkham D.H. and Flowers G.C. (1981) Theoretical prediction of thermodynamic behavior of aqueous electrolytes at high temperatures and pressures. IV. Calculation of activity coefficients, osmotic coefficients, and apparent molal and standard and relative partial molal properties to 5 kb and 600°C. *Am. J. Sci.* **281**, 1249-1516.

IUPAC Analytical Chemistry Division (1976), Nomenclature, Symbols, Units and their Usage in Spectrochemical Analysis – II. Data interpretation. *Pure and Appl. Chem.* **45**, 99-103.

Jacquemet N., Guillaume D., Zwick A. and Pokrovski G.S. (2014) In-situ Raman spectroscopy identification of the S_3^- ion in S-rich hydrothermal fluids from synthetic fluid inclusions. *Amer. Mineral.* **99**, 1109-1118.

Johnson J.W., Oelkers E.H. and Helgeson H.C. (1992) SUPCRT92: A software package for calculating the standard molal thermodynamic properties of minerals, gases, aqueous species, and reactions from 1 to 5000 bar and 0 to 1000°C. *Comput. and Geosci.* **18**, 899-947; updated version based on a series of subsequent papers reporting HKF parameters for most ions and aqueous complexes is available on line at http://geopig.asu.edu/index.html#.

Keggin J.F.(1934) The structure and formula of 12-phosphotungstic acid. *Proc. Roy. Soc. London A* **144,** 75-100.

Kirkwood J.G. (1939) The dielectric polarization of polar liquids. *J. Phys. Chem.* **7**, 911-919.

Kudrin A.V. (1985) The solubility of tugarinovite MoO_2 in aqueous solutions at elevated temperatures*.* *Geochem. Intern.* **22**, 126-138.

Minubaeva Z. and Seward T.M. (2010) Molybdic acid ionization under hydrothermal conditions to 300 °C. *Geochim. Cosmochim. Acta* **74**, 4365-4374.

Mullin J.B. and Riley J.P. (1955) The colorimetric determination of silicate with special reference to sea and natural waters. *Anal. Chim. Acta* **12**, 162-176.

Oelkers E.H., Bénézeth P. and Pokrovski G.S. (2009) Thermodynamic Databases for Water-Rock Interaction. *Rev. Miner. Geochem.* **70**, 1-46.

Pan P. and Wood S.A. (1994) Solubility of Pt and Pd sulfides and Au metal in aqueous bi-sulfide solutions. II. Results at 200 to 350°C and saturated vapor pressure. *Mineral. Deposita* **29**, 373-390.

Pokrovski G. (1996) Etude expérimentale du comportement du germanium, du silicium et de l'arsenic et de la complexation de l'aluminium avec la silice dans les solutions naturelles. *Thèse de l'Université Paul Sabatier, Toulouse.*

Pokrovski G.S., Borisova A.Yu. and Harrichoury J.-C. (2008) The effect of sulfur on vapor-liquid fractionation of metals in hydrothermal systems. *Earth Planet. Sci. Lett.* **266**, 345-362.

Pokrovski G.S., Akinfiev N.N., Borisova A.Y., Zotov A.V. and Kouzmanov K. (2014) Gold speciation and transport in geological fluids: insights from experiments and physical-chemical modelling. *Geol. Soc. Spec. Publ. London.* **402**, 9-70.

Pokrovski G.S. and Dubessy J. (2015) Stability and abundance of the trisulfur radical ion S_3^- in hydrothermal fluids. *Earth Planet. Sci. Lett.* **411**, 298-309.

Pokrovski G.S., Kokh M.A., Guillaume D., Borisova A.Y., Gisquet P., Hazemann J.-L., Lahera E., Del Net W., Proux O., Testemale D., Haigis V., Jonchière R., Seitsonen A.P., Ferlat G., Vuilleumier R., Saitta A.M., Boiron M.-C. and Dubessy J. (2015) Sulfur radical species form gold deposits on Earth. *Proc. Nat. Acad. Sci. USA* **112**, 44.

Redlich O. and Kwong (1949) On the thermodynamics of solutions. V. An equation of state. Fugacities of gaseous solutions. *Chem. Rev.* **44**, 233-244.

Ryzhenko B.N. (1981) *Equilibria in Hydrothermal Solutions.* Nauka, Moscow (in Russian).

Ryzhenko B.N., Shvarov Yu.V. and Kovalenko N.I. (1997) System Sn-Cl-F-C-S-H-O-Na. Thermodynamic component properties under conditions of the Earth's crust. *Geochem. Intern.* **11**, 1149-1153.

Saldi G. (2009) Les cinétiques de dissolution et précipitation de la magnésite aux conditions hydrothermales. *Thèse de l'Université Paul Sabatier, Toulouse.*

Saunier G. (2011) Etude expérimentale du fractionnement isotopique du fer aux conditions hydrothermales. *Thèse de l'Université Paul Sabatier, Toulouse.*

Seyfried W. E., Janecky D.R. and Berndt M. E. (1987) Rocking autoclaves for hydrothermal experiments II. The flexible reaction-cell system. *In Hydrothermal Experimental Techniques* (eds. G. C. Ulmer and H. L. Barnes). John Wiley & Sons, Inc., New York. pp. 216-239.

Shock E.L. and Helgeson H.C. (1988) Calculation of the thermodynamic and transport properties of aqueous species at high pressures and temperatures: correlation algorithms for ionic species and equation of state predictions to 5 kb and 1000°C. *Geochim. Cosmochim. Acta* **52**, 2009-2036.

Shock E.L., Sassani D.C., Willis M. and Sverjensky D.A. (1997) Inorganic species in geologic fluids: Correlation among standard molal thermodynamic properties of aqueous ions and hydroxide complexes. *Geochim. Cosmochim. Acta* **61**, 907-950.

Shvarov Y.V. (2008) HCh: new potentialities for the thermodynamic simulation of geochemical systems offered by Windows. *Geochem. Intern.* **46**, 834-839.

Shvarov Y.V. (2015) A suite of programs, OptimA, OptimB, OptimC, and OptimS compatible with the Unitherm database, for deriving the thermodynamic properties of aqueous species from solubility, potentiometry and spectroscopy measurements. *Appl. Geochem.* **55**, 17-27.

Stefánsson A. (2001) Dissolution of primary minerals of basalt in natural waters: I. Calculation of mineral solubilities from 0°C to 350°C. *Chem. Geol.* **172**, 225-250.

Stefánsson A. and Seward T.M. (2004) Gold (I) complexing in aqueous sulphide solutions to 500°C at 500 bar. *Geochim. Cosmochim. Acta* **68**, 4121-4143.

Sverjensky D.A., Shock E.L. and Helgeson H.C. (1997) Prediction of the thermodynamic properties of aqueous metal complexes to 1000°C and 5 kb. *Geochim. Cosmochim. Acta* **61**, 1359-1412.

Sverjensky A.D., Harrison B. and Azzolini D. (2014) Water in the deep Earth: The dielectric constant and the solubilities of quartz and corundum to 60 kb and 1200 °C. *Geochim. Cosmochim. Acta* **129**, 125-145.

Tagirov B.R., Salvi S., Schott J. and Baranova N.N. (2005) Experimental study of gold-hydrosulphide complexing in aqueous solutions at 350-500°C, 500 and 1000 bars using mineral buffers. *Geochim. Cosmochim. Acta* **69**, 2119-2132.

Tagirov B.R., Baranova N.N. and Bychkova Ya.V. (2015) Thermodynamic properties of platinum chloride complexes in aqueous solutions: derivation of consistent parameters from literature data and experiments on Pt(cr) solubility at 400-475°C and 1 kbar. *Geochem. Int.* **53**, 327-340.

Testemale D., Brugger J., Liu W., Etschmann B. and Hazemann J.-L. (2009) In-situ X-ray absorption study of Iron (II) speciation in brines up to supercritical conditions. *Chem. Geol.* **264**, 295-310.

Verdes G. (1990) Solubilité des hydroxydes d'aluminium entre 20 et 300°C. Propriétés thermodynamiques des principales espèces naturelles du système Al_2O_3-H_2O. *Thèse de l'Université Paul Sabatier, Toulouse.*

Zotov A., Kudrin A.V., Levin K.A., Shikina D. and Var'yash L. (1994) Experimental studies of the solubility and complexing of selected ore elements (Au, Ag, Cu, Mo, As, Sb, Hg) in aqueous solutions. In: *Fluids in the Crust: Equilibrium and Transport Properties* (eds. Shmulovich K.I., Yardley B.W.D., Gonchar G.G.). Chapman and Hall, London, pp. 97-136.

Chapitre 3. Rôle du CO_2 dans les transferts et le fractionnement des métaux d'intérêt économique par des fluides géologiques

3.1. Résumé en français de l'article: «The role of carbon dioxide in the transport and fractionation of metals by geological fluids» Maria A. Kokh, Nikolay N. Akinfiev, Gleb S. Pokrovski, Stefano Salvi and Damien Guillaume soumis à *Geochimica and Cosmochimica Acta* le 27 Octobre 2015

Bien que le dioxyde de carbone (CO_2) soit, après l'eau, le deuxième après l'eau composant majeur des fluides géologiques responsables de la formation des gisements, son effet sur le transport et la précipitation des métaux reste peu connu en raison d'un manque de données expérimentales et, par conséquent, de modèles physico-chimiques fiables capables de traiter des fluides riches en CO_2. Pour combler cette lacune, nous avons combiné des expériences de laboratoire avec des modélisations thermodynamiques afin de quantifier systématiquement le rôle du CO_2 sur la solubilité des métaux d'intérêt économique comme Fe, Cu, Zn, Au, Mo, Pt, Sn dans les conditions hydrothermales de formations de leurs gisements.

Les mesures de solubilité des minéraux majeurs de ces métaux (FeS_2, $CuFeS_2$, ZnS, Au, MoS_2, PtS, SnO_2) ont été effectuées en utilisant un réacteur équipée d'une cellule flexible en or ou en titane et d'un dispositif d'échantillonnage rapide, dans un fluide monophasé (CO_2-H_2O-KCl) à 350-450°C et 600-700 bar, tamponné par des sulfures (pyrite, pyrrhotite), et des oxydes de fer (magnétite, hématite) et des minéraux alcalino-alumino-silicates (andalousite, muscovite, feldspath potassique). Un autre type d'expériences a également été réalisé pour mesurer spécifiquement la solubilité d'or dans les fluides supercritiques CO_2-H_2O-S-NaOH riches en soufre (jusqu'à 3 wt%) à 450°C et 700 bars en utilisant des réacteurs à trempe.

Nos résultats montrent que les solubilités de Au, Mo, Pt, Cu soit diminuent légèrement (moins de 0.5-1.0 d'unité log), soit demeurent constantes lorsque ce que la teneur en CO_2 augmente, tandis que celles de Fe, Zn et Sn augmentent (> 1 unité logarithmique) avec l'augmentation de CO_2 dans le fluide de 0 à 50 wt%. Ces premières données directes ont été interprétées à l'aide d'un modèle thermodynamique qui ne nécessite pas de paramètres ajustables et qui est basé sur la constante diélectrique du solvant H_2O-CO_2 bien connue et le paramètre de solvatation de Born pour les espèces dominantes des métaux dans le fluide aqueux.

Nos prédictions à l'aide de ce modèle suggèrent que, dans un fluide supercritique du système CO_2-H_2O-S-sel, typique de gisements associés à des intrusions et de gisements Au orogéniques, en équilibre avec la pyrite et la chalcopyrite, le rapport Cu/Fe diminue de 2 ordres de grandeur avec l'augmentation de la teneur en CO_2 de 0 à 70 wt%. Cet effet surprenant est dû à la différence de solvatation des espèces dominantes de Cu ($CuCl_2^-$) et Fe ($FeCl_2^0$) en présence du CO_2. Nos résultats expliquent l'enrichissement en Fe et l'appauvrissement en Cu des gisements d'or métamorphiques formés par des fluides riches en CO_2. En revanche, le transport de l'or est défavorisée par la présence du CO_2 uniquement dans les fluides riches en soufre (> 0.5 wt% de S) où les espèces négativement chargées $Au(HS)_2^-$ et $Au(HS)S_3^-$ dominent, alors que le transport de Au n'est que faiblement affecté dans les fluides acides et pauvres en soufre (<0.1 wt% de S) où le complex neutre $Au(HS)^0$ domine. Ainsi, même à des teneurs en CO_2 très élevées (> 50% pds de CO_2), les fluides peuvent transporter l'or en quantités comparables à celles des fluides aqueux (jusqu'à plusieurs centaines de ppb Au). Dans les fluides des gisements porphyres Cu-Au-Mo, plus salins et riches en soufre, les solubilités de Fe et Cu évoluent d'une façon plus complexe en présence du CO_2, dictée par la fraction des espèces chargées vs espèces neutres ($FeCl_2^0$ vs $FeCl_4^{2-}$ and $CuCl_2^-$ vs $CuHS^0$). L'effet du CO_2 sur la mobilité de Pt et Mo qui forment respectivement des complexes de sulfurés et (oxy)hydroxylés, respectivement, est relativement faible dans la plupart des environnements géologiques. Parmi les éléments étudiés, l'étain (Sn) est le seul dont la solubilité puisse être favorisée à haute teneurs de CO_2 (> 20% en poids) en raison de la formation des complexes (bi)carbonatés.

Cette étude montre, pour la première fois, que, contrairement au paradigme actuel selon lequel le CO_2 est une molécule chimiquement peu réactive en phase fluide, la présence du CO_2 dans un fluide supercritique peut conduire à une mobilité élevée pour certains métaux et des fractionnements significatifs entre différents métaux, un effet important qui a été négligé jusqu'à présent.

The role of carbon dioxide in the transport and fractionation of metals by geological fluids

Maria A. Kokh [1]*, Nikolay N. Akinfiev [2], Gleb S. Pokrovski [1]*, Stefano Salvi [1], Damien Guillaume [1#]

[1] Groupe Métallogénie Expérimentale, Géosciences Environnement Toulouse (GET), UMR 5563, Observatoire Midi-Pyrénées, Université de Toulouse, Centre National de la Recherche Scientifique (CNRS), Institut de Recherche pour le Développement (IRD), 14 avenue Edouard Belin, F-31400 Toulouse, France

[2] Institute of Geology of Ore Deposits, Petrology, Mineralogy and Geochemistry (IGEM) Russian Academy of Sciences, Staromonetniy per., 35, 119017 Moscow, Russia

[#] Present address: LMV, UMR 6524 CNRS-UBP-UJM-IRD, Faculté des Sciences et Techniques, 23 rue du Dr. Paul Michelon, 42023 Saint Étienne, France.

* Corresponding authors: Phone: (33)-(0)5-61-33-26-18; fax: (33)-(0)5-61-33-25-60;

E-mail: maria.kokh@get.obs-mip.fr; gleb.pokrovski@get.obs-mip.fr

Submitted to Geochim. Cosmochim. Acta

27 Octobre 2015

Abstract

Although carbon dioxide is the second (after water) major component of crustal fluids responsible for ore deposit formation, its effect on transport and precipitation of metals remains largely unknown, due to a lack of direct experimental data and physical-chemical models for CO_2-rich fluids. To fill this gap, we combined laboratory experiments and thermodynamic modeling to systematically quantify the role played by CO_2 on the solubility of economically important metals such as Fe, Cu, Zn, Au, Mo, Pt, Sn under hydrothermal conditions. Solubility measurements of common ore minerals of these metals (FeS_2, $CuFeS_2$, ZnS, Au, MoS_2, PtS, SnO_2) were performed, using a flexible-cell reactor equipped with a rapid sampling device, in a homogeneous fluid (CO_2-H_2O-KCl) at 350-450°C and 600-700 bar, buffered with iron sulfide-oxide and alkali-aluminosilicate mineral assemblages. In addition, another type of experiments was conducted to measure gold solubility in more sulfur-rich supercritical CO_2-H_2O-S-NaOH fluids at 450°C and 700 bar using a batch reactor that allowed fluid quenching. Our results show that the solubilities of Au, Mo, Pt, Cu either decrease (within 0.5-1.0 log unit) or remain constant upon CO_2 increase, whereas those of Fe, Zn and Sn increase significantly (>1 log unit) with increasing CO_2 contents in the fluid from 0 to 50 wt%. These data were interpreted using a simple model that does not require adjustable parameters, and is based on the dielectric constant of the H_2O-CO_2 solvent and on the Born solvation parameter for the dominant metal-bearing species in an aqueous fluid. Our predictions using this model suggest that in a supercritical CO_2-H_2O-S-salt fluid typical of intrusion-related and orogenic Au deposits, in equilibrium with pyrite and chalcopyrite, the Cu/Fe ratio decreases by up to 2 orders of magnitude with an increase of CO_2 content from 0 to 70 wt%. This effect is due to the difference in solvation of the dominant species of Cu ($CuCl_2^-$) and Fe ($FeCl_2^0$) in the presence of CO_2. Our results explain the Fe enrichment and Cu depletion in metamorphic gold deposits formed by CO_2-rich fluids. The transport of gold is disfavored by the presence of CO_2 only in S-rich (> 0.5 wt% S) fluids in which Au forms the negatively charged $Au(HS)_2^-$ and $Au(HS)S_3^-$ complexes, in contrast, it is only weakly affected in S-poor (<0.1 wt% S) acidic-to-neutral fluids in which the uncharged $Au(HS)^0$ complex predominates. Thus, even at very high CO_2 contents (> 50 wt% CO_2), the capacity of such fluids of transporting gold (up to 100s ppb Au) remains comparable to that of aqueous fluids. In more saline oxidizing and S-rich fluids such as those in porphyry Cu-Au deposits, Fe and Cu solubilities in the presence of CO_2 evolve in a more complex fashion, depending of the predominance of changed vs neutral species ($FeCl_2^0$ vs $FeCl_4^{2-}$ and $CuCl_2^-$ vs $CuHS^0$). The effect of CO_2 on the mobility of Pt and Mo, metals that likely form hydrogen sulfide and oxy-hydroxide complexes, respectively, is expected to be weak in most settings. Among the studied elements, Sn is likely to be the only one whose solubility may be favored at high CO_2 content (> 20 wt%) due to direct bicarbonate complexing. This study demonstrates, for the first time, that, contrary to common belief, the presence of CO_2 in a supercritical fluid may lead to enhanced mobility of some metals and, in addition, to significant fractionations between different metals - an important effect that has been disregarded so far.

Key-words: carbon dioxide; metals; supercritical fluid; dielectric constant; orogenic deposits

1. INTRODUCTION

Almost all types of hydrothermal deposits of base and precious metals on Earth are characterized by the ubiquitous presence of CO_2, which is a major volatile in geological fluids and silicate melts. Analyses of fluid inclusions show that CO_2 concentrations in aqueous low-salinity fluids that formed intrusion-related and orogenic gold deposits in metamorphic belts attain more than 50 wt% (Boiron et al., 2003; Phillips and Evans, 2004; Garofalo et al., 2014), with some inclusions hosting almost pure CO_2 (> 95%) vapor or liquid phases (e.g., Schmidt Mumm et al., 1997). Carbon dioxide contents in saline fluids from magmatic-hydrothermal porphyry Cu-Mo-Au deposits amount to 10 wt% (~5 mol%) on average, locally attaining 20 wt% (Rusk et al., 2008, 2011). Carbon dioxide is also omnipresent in low-to-moderate temperature fluids from most epithermal and Carlin type Au deposits, attaining 5-10 wt% in some cases (e.g., Bodnar et al., 1985; Koděra et al., 2005; Catchpole et al., 2011).

Although direct analyses of metal concentrations in CO_2-rich fluid inclusions still remain scarce owing to analytical difficulties and lack of adequate internal standards (e.g., Hanley and Gladney, 2011; Rauchenstein-Martinek et al., 2014), there is growing evidence that the capacity of CO_2-rich fluids to transport some metals at high temperatures (*T*) and pressures (*P*) may be comparable to that of H_2O-dominated solutions. For example, 10s to 100s ppm Cu, Te, Ni, Bi and Pd were analyzed in CO_2-rich fluid inclusions from mafic pegmatites of the Lac des Iles Complex, Ontario, Canada (Hanley and Gladney, 2011), up to 5 ppm Au and 100s ppm Cu and As were found in CO_2-rich low-salinity fluid inclusions from the Sigma gold deposit, Val d'Or, Canada (Garofalo et al., 2014), and 10s to 100s ppm As in metamorphic vein systems of the Central Alps, also rich in CO_2 (Rauchenstein-Martinek et al., 2014). Very high Cu concentrations (0.1 to 3.4 wt%), were reported in CO_2/CH_4-rich fluid inclusions from the Fenghuangshan orogenic Cu-Fe-Au deposit, China (Lai and Chi, 2007). In spite of such wide occurrence and large abundance of CO_2 and of the observed metal enrichment in CO_2-rich fluids, the true role of CO_2 on metal transport and deposition remains one of the big enigmas of the geochemistry of ore deposits.

Carbon dioxide may affect metal behavior in hydrothermal fluids in different ways, both direct and indirect. First, CO_2 may act as a ligand forming carbonate and bicarbonate complexes with metals, a phenomenon known in low-temperature aqueous solution for some 'hard' metals (Ca, Sr, U, REE; Haas et al., 1995; references therein). However, direct carbonate complexes at elevated *T-P* have not been unambiguously demonstrated for most economic metals (Seward et al., 2014) whose speciation is dominated by Cl, HS or OH complexes in saline and S-bearing, slightly acidic to neutral hydrothermal fluids of magmatic or metamorphic origin (e.g., Seward and Barnes, 1997; Wood and Samson, 1998; Kouzmanov and Pokrovski, 2012; references therein). The abundance of carbonate complexes is furthermore limited by very low concentrations of the bicarbonate and carbonate ions in most high *T-P* fluids and vapors, in which molecular CO_2 largely dominates (Manning, 2013), and by low solubility of major carbonate minerals such as calcite and barite (e.g., Seward et al., 2014; references therein).

Second, CO_2 minor derivatives, such as CO, are known to form stable complexes with transition metals like Ni and Fe or platinum group elements (PGE) both in gas and solid phase; however this phenomenon, if it occurs in natural fluids, would be limited owing to the low abundance of CO (e.g., few ppm at redox conditions of the pyrite-pyrrhotite-magnetite mineral assemblage; Kokh, 2015) and the lack of any direct experimental evidence. Simple organic compounds such as carboxylic acids and their anions are also extremely rare in high-temperature fluids (>300°C) because they are thermodynamically unstable with respect to CO_2 and CH_4 (e.g., Shock and Koretsky, 1993). Furthermore, even if such organic ligands are more abundant in low-*T* sedimentary-basin fluids, they are usually unable to compete with chloride and hydroxide ligands for metals (Shock and Koretsky, 1993).

Third, an indirect effect of CO_2 that has been known for a long time, is to extend in *T-P*-compositional space the domain in which vapor-liquid unmixing and fluid boiling occur in CO_2-H_2O-salt systems, compared to H_2O-salt systems (Gibert et al., 1998; Lowenstern, 2001; Bakker, 2009). As a result, the presence of CO_2 increases the depth of vapor-liquid separation (e.g., Barton and Chou, 1993), which, in turn, may affect vapor-liquid partitioning of some metals (e.g., Heinrich, 2007; Pokrovski et al., 2013). Departure of CO_2 and accompanying volatiles (H_2S, HCl) into the vapor phase is known to decrease the acidity and sulfur ligand activity in the liquid phase, leading to metal precipitation (e.g., Drummond and Ohmoto, 1985; Spycher and Reed, 1989; Heinrich, 2007).

Finally, the most general effect of CO_2 as a relatively inert component, when it is present at high concentrations (>5 mol%), is to decrease water activity and the dielectric constant of the fluid (Walther and Orville, 1983; Walther and Schott, 1988). These changes may be accurately quantified using the well-known properties of CO_2-H_2O(-salt) systems and associated physical chemical models (Bowers and Helgeson, 1983; Duan, 1995; Akinfiev ans Zotov, 1999; Bakker, 2009). Because mineral solubility is largely driven by hydration, the decrease of water activity in the presence of CO_2 should lower the solute concentrations. Indeed, the solubility of most ionic compounds such as salts and oxides is negligibly low in pure CO_2 solvent even at high *T* and *P* (e.g., NaCl solubility in pure CO_2 at 500 bar and 400°C is ~10^{-8} mol%, Zakirov et al., 2007) whereas their solubility in pure water at similar conditions is many orders of magnitude greater (e.g., NaCl solubility in H_2O at 500 bar and 400°C is ~20 mol%, Driesner and Heinrich, 2007). This negative effect of CO_2 is observed in solubility experiments on quartz (e.g., Walther and Orville, 1983; Newton and Manning, 2001, 2009) and on simple chlorides (e.g., AgCl, Akinfiev and Zotov, 1999) and oxides (e.g., Sb_2O_3, Zotov et al., 2003) in supercritical H_2O-CO_2 fluid mixtures. These solubility data were interpreted using physical-chemical models based on the change, with addition of CO_2, of either water activity (hydration model, e.g., Walther and Orville, 1983; Newton and Manning, 2009) or solvent dielectric constant (electrostatic Born model, Walther and Schott, 1988; Dandurand and Schott, 1992; Gibert et al., 1992; Akinfiev and Zotov, 1999). In contrast, an opposite effect of CO_2, i.e., favoring solubility, was reported on iron oxides in CO_2-HCl-NaCl-H_2O mixtures at 500-600°C and 2 kbar (Tagirov and Korzhinsky, 2001a,b); however it is difficult to interpret these limited data because of uncertain Fe speciation at such conditions. The enhanced solubility of some organic thiol-bearing compounds in supercritical CO_2 vapor is a property used in ingeneering for extracting gold and other metals from organic-bearing aqueous solution (e.g., Glennon et al., 1999; Erkey, 2000; Yang et al., 2010). By analogy, it has been hypothesized that Au and Cu complexes with sulfide ligands might also be stabilized in CO_2-rich vapor in natural hydrothermal systems (e.g., Pokrovski et al., 2008), but so far no experimental verification exists.

As a conclusion, no direct experimental data on the solubility of ore minerals (sulfides and oxides) of most base and precious metals in supercritical water-carbon dioxide mixtures are available to date, and the current models for mixed fluids discussed above have not been applied to multicomponent H_2O–CO_2–S–Cl fluid-mineral systems, typical of natural high-temperature environments. To fill this gap, in this study we conducted systematic measurements of major ore minerals of economically critical metals (Fe, Cu, Zn, Au, Pt, Mo and Sn) in model supercritical H_2O-CO_2 fluids containing salt and sulfur and in the presence of sulfide, oxide, and silicate minerals commonly found in a large variety of mineralized systems, from magmatic to epithermal. We used a simple electrostatic model, parameterized based on the data obtained, to predict ore mineral solubility and metal ratios in CO_2-rich fluids from typical crustal settings. Our results show that, contrary to the common belief, CO_2 may have a contrasting effect on the transport of different metals by geological fluids and thus control metal signatures in certain types of ore deposits.

2. MATERIALS AND METHODS

2.1. Solid phases

The following natural minerals were used in our study to buffer the fluid acidity (pH) and oxygen and sulfur fugacity: K-feldspar (adularia, JCPDS card number 31-966), muscovite (2M-type, 6-263), quartz (33-1161), andalusite (39-376), pyrite (Alfa-Aesar, 42-1340), pyrrhotite (29-724, Primorskiy Kray, Dalnegorsk, Russia), magnetite (courtesy of A. Zotov, 19-0629) and hematite (Milhas, Haute-Garonne, Pyrénées, France). The following abbreviations for these mineral buffers are used in the text: PPM – pyrite, pyrrhotite, magnetite; PMH – pyrite, magnetite, hematite; QMK – quartz, muscovite, K-feldspar; QMA – quartz, muscovite, andalusite.

The following natural ore minerals were used for solubility measurements in the buffered experimental systems: chalcopyrite (Messina, Transvaal, South Africa, 37-0471), molybdenite (courtesy of A. Zotov, 17-0744), cassiterite (Iultine, Chukotka, Russia, 41-1445), sphalerite (Santander, Spain, 05-566), and gold metal foil (Heraeus, 99.999% purity). Before experiments, all mineral grains (size >50 μm) were handpicked under a binocular microscope and washed several times with deionized water until the supernatant fluid became clear within 2 to 3 min. The absence of impurities and other phases was checked by X-ray diffraction (XRD) and scanning electron microscopy (SEM). Platinum sulfide (PtS, synthetic, crystal size <1 μm, 26-1302) was hydrothermally synthesized from Pt and S, and pressed into pellets for solubility experiments (see EA1 for details). Sulfur powder (99.98%, Sigma-Aldrich) was used for another type of gold solubility experiments, both to supply ligands (HS^- and S_3^-) and to buffer acidity and redox potential via (hydrogen)sulfate-hydrogen sulfide equilibria in solution (Jacquemet et al., 2014).

2.2. Experimental Setup

2.2.1. Flexible-cell reactor with rapid sampling

The solubility of the minerals described above was investigated in the system H_2O-CO_2-S-KCl in the temperature range 350-450°C and the pressure range 650-750 bar (Tables 1-3), using a hydrothermal reactor (Coretest® type) equipped with a rapid sampling device and a flexible titanium or gold inner cell (initial cell volume ~150-200 cm^3), in which the solids and experimental solutions are loaded. The cell is placed into a large volume (~1200 cm^3) high-pressure vessel, made of stainless steel (type 316 SS), and filled with water as a pressure medium (Fig. 1), which, in turn, is placed into a rocking furnace (Rosenbauer et al., 1993). The furnace is heated by electrical resistances with temperature control within 1°C. A gas-driven pump was used for delivery of water into the vessel to regulate the pressure during the experiment. A back-pressure regulator served to release water from the pressure vessel during heating or during injection of CO_2 or aqueous solution into the flexible cell (see below). The reactor is equipped with a sampling titanium tube attached to two high-pressure titanium valves with ceramic stems and a rigid titanium ampoule, tightly assembled to the second valve, for taking samples (Fig. 1). Opening the two valves leads to almost instantaneous (within <1 s) transfer into the ampoule of a portion of the liquid or vapor phase pushed by the internal pressure in the reactor. This design avoids any mineral precipitation or volatile degassing (see Pokrovski et al., 2008 for details), which would have inevitably occurred in S- and CO_2-rich systems during traditional sampling procedures (e.g., Gibert et al., 1998; Tagirov et al., 1995).

Both gold and titanium cells are equipped with a Ti head, a sealing ring, and a Ti 2-µm frit filter. All titanium parts were washed with concentrated HNO_3 and deionized water, and passivated by heating at 400°C in air overnight to create a titanium oxide layer, which is far more resistive to chemical corrosion and eventual hydrogen diffusion than non-passivated Ti metal. The gold cell was cleaned with HNO_3 and H_2O and annealed at 350°C for 2h to allow for a greater malleability and deformation during the experiment. The cell was loaded with ~20 g of solid phases together with a 0.1 *m* KCl aqueous solution, prepared using doubly deionized water. The solution mass (~50-100 g) was adjusted, according to the injected CO_2 quantity (see below), to be in the allowable range of expansion or compression, which is between 60 and 90% of the initial volume for both types of cell, to avoid cell explosion or irrecoverable deformation (Seyfried et al., 1987, 1993). The cell volume at the experimental *T-P* was calculated using the fluid composition and mass and the densities of the H_2O-CO_2±KCl system (Bakker et al., 2009). Before loading into the pressure vessel, the cell was checked for leaks using an overpressure of 2 bars of nitrogen gas. More details about cell design and handling are given elsewhere (Seyfried et al., 1987; Tagirov et al., 2005).

Liquid CO_2 (Air Liquide, 99.999% purity) was introduced into the loaded cell under pressure via the sampling tube either before heating or during the experiment, using a calibrated capstan pump (total volume =12 cm^3). The slightly cooled pump (10-15°C) was filled by liquid CO_2 from a commercial bottle (which was at ambient temperature, 20-30°C), and the injected CO_2 quantity was calculated using the density of pure CO_2 at the injection *T-P* and the volume change of the pump. These injected quantities were in good agreement with the CO_2 concentrations measured in high *T-P* samples by weight loss upon complete degassing of the sampling ampoule, indicating that no CO_2 escape or consumption via carbonate formation occurred during most experiments (except #m24 and #m25, for which we detected a leak at the end of the run).

To further check for the cell integrity in some experiments, a CsCl tracer dissolved in water (~100 ppm Cs) was introduced into the external vessel, but no Cs was detected in the fluid sampled from the cell during the experiment, demonstrating the absence of any fluid exchange between the external pressure medium and the experimental fluid in the cell. Note that the use of Sr as a leak tracer (e.g., Tagirov et al., 2005) is not recommended in the presence of CO_2 because of $SrCO_3$ formation as detected by SEM in some preliminary runs (#m24 and #m25) that showed Ti cell leak after the experiment.

2.2.2. Batch reactor with quenching

Another type of solubility experiments was conducted for gold in the system Au-H_2O-CO_2-S-NaOH at 450°C and 600 bar (Table 4), using batch reactor vessels made of a titanium-based alloy (grade VT-8, volume ~20 cm^3). Details about the reactor handling are given elsewhere (e.g. Pokrovski et al., 2002). The vessel was loaded with weighed amounts of 0.1 *m* NaOH aqueous solution, native sulfur powder, then cooled down using liquid nitrogen, and a weighed CO_2 solid piece (dry ice, Air Liquide, 99.9% purity) was rapidly loaded over the frozen solution. A weighed piece of gold foil was attached to the reactor cover. Multiple vessels were introduced together into a temperature-controlled oven (±1°C); the pressure was estimated at the run temperature using the PVTX properties of H_2O-CO_2 fluids and assuming that the relatively small amounts of NaOH and S (<0.05 mol%) do not significantly change these properties. At the end of the experiment, the autoclave was cooled in cold water for 20 min, unloaded, and washed with hot aqua regia to remove all Au that was dissolved in the experiment but precipitated on reactor walls upon cooling.

2.3. Analytical methods

In experiments with the flexible-cell equipment, multiple samples of fluid (usually 3 to 4) were directly taken into different aqueous matrixes (I_2, NH_3, $Cd(CH_3COO)_2$) placed in the sampling ampoule to allow for trapping, preservation and analyses of the different forms of sulfur, bulk metal concentrations and CO_2 (see Pokrovski et al., 2008, and Kokh, 2015 for details). Carbon dioxide in all condensates trapped in the sampling ampoule was quantified by weight loss after complete gentle degassing of the ampoule. This procedure was found to be accurate within better than ±0.3 wt% and ±1.5 wt%, respectively for the lowest (~5 wt%) and highest (50 wt%) CO_2 contents in this study. Concentrations of K, Fe, Ti, Cu, Mo, Sn, Pt, and Au were determined by Inductively Coupled Plasma Mass Spectrometry (ICP-MS) and/or Inductively Coupled Plasma Atomic Emission Spectrometry (ICP-AES) and, selectively, by flame Atomic Absorption Spectrometry (AAS), depending on the element and concentrations, and after the sample treatment with aqua regia in a clean room. The protocol consists of i) gentle evaporation of the sample on hot plate (60-80°C) in a cleaned Teflon vial (Savilex ®), ii) reaction of the residue with 2 g of hot aqua regia in the closed vial (at 120°C for 2h), followed by iii) gentle evaporation to 0.2-0.3 g solution (60-70°C), and iv) dilution of the remaining solution by ultra-pure doubly-distilled 0.5 wt% HCl-1.5wt% HNO_3 in water. This treatment ensures complete conversion of Au and Pt into very soluble $AuCl_4^-$ and $PtCl_4^{2-}$ which are infinitely stable in dilute aqueous solution; whereas all other attempts of sample conservation (e.g., acidification with strong acids or bases) led to systematic loss of Au and Pt from the solution. The aqua-regia treatment is less critical for other metals that are more soluble, but was found to yield very stable samples, with no loss of any of the metal in any step of evaporation or further conservation prior to analyses.

Total chloride was quantified as the Cl^- ion by high-pressure liquid chromatography (HPLC) in non-acid-treated water-diluted samples. The concentrations of silica, which cannot be preserved during the aqua-regia treatment owing to the formation of volatile $SiCl_4$, were measured in water-diluted samples by colorimetry using the molybdate blue method (Fanning and Pilson, 1973). Total dissolved sulfur was analyzed by ICP-AES ion after complete oxidation to sulfate in NH_3-H_2O_2 solutions. Total reduced sulfur (H_2S, S_n^{2-}, SO_2) was quantified by iodometric titration. Hydrogen sulfide (H_2S/HS^-) was separated from the other sulfur forms by precipitation as Cd sulfide followed by iodometric titration. More details about the methods, concentrations, detection limits and matrixes are reported in Table EA2.

2.4. Thermodynamic data sources and models

The results of solubility measurements obtained in this study were critically evaluated by comparing them with chemical equilibrium calculations using thermodynamic properties of minerals and aqueous species available in the literature, combined with a recent model for mixed fluids (Akinfiev and Zotov, 1999). The data sources and approaches are briefly discussed below.

2.4.1. Data sources

The thermodynamic properties of the minerals used in this study, aqueous volatile nonelectrolyte species (CO_2, H_2S, SO_2, O_2, H_2), and major cations, anions, and their ion pairs (e.g., HS^-, HCO_3^-, HSO_4^-, S_3^-, Na^+, K^+, Cl^-, KCl^0) were taken from the SUPCRT92 database (Johnson et al., 1992), complemented with more recent thermodynamic data (e.g. Plyasunov and Shock, 2001; Akinfiev and Diamond, 2003; Pokrovski and Dubessy, 2015). Stability constants for aqueous metal complexes (or, alternatively, their standard molal Gibbs free energies at given T and P) were chosen from recent compilations based on large amount of experimental solubility studies (e.g. Akinfiev and Zotov, 2010; Pokrovski et al., 2014; Sverjensky et al., 2014). These constants are described within thermodynamic models such as HKF (Helgeson, Kirkham, Flowers, 1981) and RB (Ryzhenko, 1981; Bryzgalin and Rafal'skiy, 1982). The currently available thermodynamic parameters for Si, base metals such as Fe, Zn, Cu, and gold allow accurate solubility predictions (within one order of magnitude) in aqueous solution at the conditions of our study. In contrast, available data for Mo, Sn and Pt are far more discrepant and their dominant species are poorly known (see section 4 for discussion). In the present study, we chose the thermodynamic data sources cited in Table 5 for all metals, for comparison with our solubility measurements.

2.4.2. Electrostatic model

To interpret our measurements in CO_2-rich fluids, we used an electrostatic model, developed in the classical studies of H. Helgeson, J. Schott and their coworkers (Helgeson and Kirkham, 1976; Walther and Schott, 1988), modified by Akinfiev and Zotov (1999). The Gibbs free energy of an ion or a molecule dissolved in an aqueous fluid phase at a given T and P is defined as follows:

$$G_{i,TP} = G_i^0 + 2.3026RT\log a_i \tag{1}$$

where $G_{i,TP}$ is the standard molal Gibbs free energy of the species *i* at given *T-P*, *R* is the ideal gas constant, *T* is the absolute temperature (K), and a_i is the species activity defined as the product of the species molality and its activity coefficient:

$$a_i = \gamma_i \cdot m_i \tag{2}$$

When this species is transferred from the aqueous to a mixed CO_2-H_2O fluid, there is a change in two fundamental contributions to its Gibbs free energy ($\Delta G_{i,TP}$): a solvation part, so called Born contribution to the standard molal Gibbs free energy (ΔG^o_{Born}), arising from interactions of the species with the solvent molecules, and the electrostatic Debye–Hückel contribution (ΔG_{DH}) originating from interactions between ions themselves depending on their concentrations:

$$\Delta G_{i,TP} = \Delta G^0_{Born} + \Delta G_{DH} \tag{3}$$

The solvation contribution ΔG^0_{Born} is treated by the Born equation (1920):

$$\Delta G^0_{Born} = \omega_i \cdot \left(\frac{1}{\varepsilon_{mix}} - \frac{1}{\varepsilon_{water}} \right) \tag{4}$$

where ω_i is the species solvation Born parameter from the HKF model, and the ε_{mix} and ε_{water} are the dielectric constant of the H_2O-CO_2 fluid and pure water, respectively. The electrostatic contribution for charged species ΔG_{DH} corresponds to the activity coefficient (γ_i) calculated using the Debye-Hückel equation:

$$\log(\gamma_i) = -\frac{Aq_i^2\sqrt{I}}{1 + Br_i\sqrt{I}} \tag{5}$$

where q_i and r_i are, respectively, the electric charge of *i*-th species and the distance of the closest approach for the species, *I* – ionic strength of the solution, and *A* and *B* are Debye-Hückel coefficients that are functions of temperature, the fluid dielectric constant ε_{mix}, and density. We adopted a value of r_i of 4.5 Å for all charged species, for consistency. The activity coefficients of neutral species are assumed to be 1.

Volumetric properties of the H_2O-CO_2 supercritical fluid were calculated using Redlich-Kwong (1949) equation of state, with the CO_2 parameters adopted from Holloway (1981), and those for H_2O – computed using the multiparametric equation of Hill (1990). Such a method allows for keeping the accuracy of multiparametric equation, while using the formalism of the Redlich-Kwong description. Dielectric properties of pure water were computed using the empirical equation given by Archer and Wang (1990), while calculation of dielectric permittivity of the binary mixture was based on the assumption of additive contribution to the polarizability of polar and non-polar components. This assumption leads to a modified Kirkwood (1939) equation suited for the mixture. The details of the employed approach and its validation are given in Akinfiev and Zotov (1999). The solvation and Debye-Hückel contributions were calculated for each CO_2 composition using the MIX-FL code (Akinfiev, 1997); then the total Gibbs free energy of the system was minimized ($\sum_i G_{i,TP} = \min$) using the HCh computer code (Shvarov, 2008) and the equilibrium molality of each species (Eqn. 1 and 2) is obtained.

2.4.3. Standard states

In our thermodynamic model, standard and reference state conventions correspond to those of the revised HKF model (Shock et al., 1997). The standard Gibbs free energy and the Born parameter of H^+ are equal to 0 at any T, P and CO_2 content. The standard states for the solid phases and H_2O are unit activity for the pure phase at all T and P. The activity of water in a mixed fluid is assumed to be equal to its mole fraction. At each CO_2-H_2O composition, the standard state convention for dissolved species corresponds to unit activity coefficient for a hypothetical one molal solution whose behavior is ideal (Akinfiev and Zotov, 1999). Consequently, at a given CO_2-H_2O composition, the change in species solvation energy from pure water to a mixed fluid (Eqn. 4) is ascribed to the standard Gibbs free energy of the species and the only correction for non-ideality is the Debye-Hückel equation (5). This convention is different from that usually adopted for mixed fluids (e.g., Walther and Schott, 1988), which ascribes the change in solvation energy (Eqn. 4) to the activity coefficient of the species relative to pure water. Although both types of standardization are thermodynamically allowed, the main advantage of our standard state convention is the ability to directly calculate mineral-fluid multicomponent equilibria using the HCh package and the related Unitherm database for minerals and aqueous species compatible with the HKF model (Shvarov, 2008, 2015). Note that the final result of these calculations is *equilibrium molalities* of the species, which are independent of the choice of standard states.

2.4.4. Model limitations

This model has several general thermodynamic simplifications, which have however a weak impact at the conditions of our study. First, short-range interactions between the aqueous species and the surrounding solvent molecules were not taken into account both because they cannot be reliably predicted at our conditions (Akinfiev and Zotov, 1999) and because the electrostatic interactions (Eqn. 4) are expected to largely dominate at high temperature (Helgeson et al., 1981). Second, the Born parameter (ω) is assumed to be independent of temperature, because its change is rather small at fluid densities above 0.4-0.5 g/cm^3 according to the HKF model as compared to the uncertainties related to the reported values at 25°C and 1 bar. Third, the water activity in mixed fluid was assumed to be equal to its mole fraction, which is a reasonable assumption for our supercritical high-temperature and moderate-pressure H_2O-CO_2 mixtures (Perfetti et al., 2008); in addition, H_2O activity does not directly affect the reactions involving the majority of oxide, chloride and sulfide aqueous species considered in this study. Because of the limited experimental dataset obtained in this study, no attempt was done to derive new Born coefficients or to improve these model imperfections, which would necessitate more systematic studies in simplified systems.

As such, this simple model does not require any adjustable parameter if standard Gibbs free energies of aqueous species at given *T-P* and their Born parameters are known. The G_i^o values are calculated using stability constants from references reported in Table 5 (most of them use the HKF or RB models), while all ω_i values for aqueous species are taken according to the HKF model from sources cited in Table 5. The only correction made for G_i^0 of certain elements was for the mismatch between measured and calculated solubilities in CO_2-free fluids using the data sources from Table 5 (see section 4 below).

3. RESULTS

The resulting element concentrations in the fluid are expressed in molality *m* (number of moles of the element or compound per kg of water), for consistency with the thermodynamic model described above. The experimental data are reported in Tables 1-3 for multicomponent experiments using flexible cell reactors at 350-450°C and 570-780 bar (runs #m19, #m23, #m24, #m25, #m30) and in Table 4 for experiments on gold solubility in batch reactors at 450°C and 600 bar.

The measured concentrations of total sulfur, reduced sulfur and H_2S in runs buffered by iron sulfide and oxide minerals were always the same within errors, demonstrating that the dominant sulfur species is H_2S and that other sulfur forms (e.g. SO_2, SO_4^{2-}) are minor. The concentration of H_2S increases with temperature from 0.005 *m* (at 350°C) to 0.05 *m* (at 450°C), and is independent of CO_2 content. The measured values are in excellent agreement with calculated H_2S concentrations using the thermodynamic properties chosen in this study (Akinfiev and Diamond, 2003) and assuming equilibrium with the PPM (Fig. 2) or PMH (not shown) buffers. This agreement strongly suggests that sulfur fugacity (and, by inference, redox) buffering occurs in our experiments.

Chloride concentrations are constant within the data scatter in most experiments and correspond to injected quantities in runs where aqueous KCl solution was introduced into the cell during the experiment (e.g., #m19 and #m30). Potassium concentrations usually show a decrease (up to two-three times) with increasing CO_2 content, which reflects the reaction with alkali silicate minerals (muscovite and feldspar) induced by pH change in the fluid in response to CO_2 injection. At constant CO_2, potassium concentrations attain a steady state after two days from the injection, indicating that fluid equilibrium with the silicate minerals is rapidly attained, in agreement with previous studies (Gibert et al., 1998; Tagirov et al., 2005).

Measured metal concentrations are plotted as a function of CO_2 in Fig. 3 for two representative experiments (#m19 and #m30). The concentrations are stable within analytical errors at each injected CO_2 (#m30) or KCl (#m19) content, suggesting that steady state is attained within less than 3 days. Because of experimental difficulties and time limitations, no attempt has been done in this study to approach steady state concentrations from supersaturated solutions to check for reversibility, which is an additional criterion of equilibrium. Nevertheless, we believe that our steady-state concentrations reached from the under-saturated solutions correspond to equilibrium with the different metal-bearing phases, because of the known high reactivity of most sulfide phases and metallic gold in Cl- and S-bearing hydrothermal fluids above 350°C shown in many previous studies (Hemley et al., 1992; Seyfried and Ding, 1993; Tagirov et al., 2005; Pokrovski et al. 2008, 2015).

It can be seen in Fig. 3 that different metals behave differently in the presence of CO_2. For example, while the solubility of quartz decreases as expected (e.g., Walther and Orville, 1983; Newton and Manning, 2000), that of SnO_2, ZnS and FeS_2 increases by one order of magnitude when CO_2 attains 50 wt% (~20 *m*). The concentrations of Cu and Pt remain constant whereas those of Mo decrease slightly at low CO_2 content and remain almost constant at higher CO_2 content. Gold solubility trends are different depending on the system: with the PPM-QMK buffer, Au decreases at first and then slightly increases at high CO_2 contents, whereas with PHM-QMA buffer, it increases slightly with addition of CO_2. In batch-reactor experiments with aqueous sulfide and sulfate as the redox and pH buffer (Table 4), addition of CO_2 to 10 *m* leads to a decrease in gold concentration, which becomes constant at higher CO_2 contents.

4. DISCUSSION

4.1. Major ligands

To interpret such variable trends, we used the Akinfiev and Zotov (1999) model described in section 2.4, which is based on metal speciation in the aqueous phase and changes in the H_2O-CO_2 solvent electrostatic properties in the presence of CO_2. In this model, CO_2 and its anionic counterparts (HCO_3^-, CO_3^{2-}) and other C forms (CH_4, CO, small organic compounds like carboxylic acids and their anions) were considered as solutes with the corresponding Born parameter taken according to the HKF model for charged species and assumed to be equal to zero for all neutral species. Note that the calculated equilibrium concentrations of (bi)carbonate ions do not exceed 10^{-10} *m* (ppt level) at highest CO_2 concentrations (10-50 wt%), those of carboxylates are at ppt-to-ppb levels, and those of CH_4 and CO amount to a few ppb and few ppm, respectively. Thus, it is highly unlikely that these compounds could significantly bind metals in our systems dominated by chloride, sulfide or hydroxide ligands.

The main tendency in element speciation is to favor the stability of uncharged species at the expense of ions and charged complexes with increasing CO_2 concentration in the fluid. This is illustrated in Fig. 4, which shows the calculated distribution of K and Cl species as a function of CO_2 concentration. It can be seen that while K^+ and Cl^- ions are the dominant species in aqueous solution, the fraction of their ion pair KCl^0 grows with CO_2 rise to 5 *m* and attains >95% at CO_2 concentration from 5 to at least 20 *m* CO_2. This strong change in the availability of the Cl^- ligand within a narrow range of CO_2 affects the solubility trends of metals that dominantly form chloride complexes (e.g., Fe and Cu). Below we discuss the each metal speciation in aqueous solution and we compare measured solubilities with thermodynamic predictions using the model adopted in this study. The results are illustrated in Figs. 4 to 14.

4.2. Silica

Measured silica solubility in aqueous fluid is in excellent agreement with calculated solubilities of quartz using the thermodynamic properties of silicic acid from different data sources (Fig. 5A). Most data sources (e.g., Shock et al., 1997; Stefánsson et al., 2001; references therein) postulate monomeric silicic acid ($Si(OH)_4$ or SiO_2) as the only species in equilibrium with quartz at our experimental conditions. In contrast, a recent study of Sverjensky et al. (2014) reinterpreted silica speciation as a sum of SiO_2 and its dimer, $Si_2O(OH)_6$ (or Si_2O_4), based on quartz solubility and Raman spectroscopy measurements at high *P* and *T* (≥4 kbar, ≥400°C), coupled with monomer-dimer equilibrium measurements at ambient conditions (see Sverjensky et al., 2014 for details). The revised silica speciation is in agreement with previous data sources and predicts quartz solubility identical to the measured value in our aqueous solutions. With increasing CO_2 fraction, the calculated solubility using the standard Gibbs free energy and Born parameters from any of the three references discussed above shows identical values, which decrease with CO_2, again, in good agreement with our measurements. Note that according to the Sverjensky et al. (2014) speciation model, the dimer, having a close-to-zero value of ω (0.10×10^5 cal/mol), is the solubility controlling species over the whole range of CO_2 contents; conversely, the monomer, which has a larger positive value of ω (0.36×10^5 cal/mol), becomes minor at CO_2 contents above ~5 *m* (Fig. 5B). If the Sverjensky et al. (2014) speciation model for silica is correct at moderate pressures (<1 kbar), our predictions imply that polymeric silica species would be greatly favored in CO_2-rich fluids, and such fluids would be capable of transporting significant amounts of Si.

4.3. Iron

Iron solubilities measured in aqueous and mixed fluid in equilibrium with the PPM or PMH assemblage were interpreted using the thermodynamic properties of iron dichloride complex $FeCl_2^0$ (Fig. 6A-C), based on a large number of experimental data, which were described by Sverjensky et al. (1997) using the HKF model. Another iron complex, tetrachloride ($FeCl_4^{2-}$), suggested by Testemale et al. (2009), was also added to our model with a Born parameter (2.5×10^5 cal/mol) adopted by analogy with $ZnCl_4^{2-}$ for which HKF parameters are available (Akinfiev and Tagirov, 2014). The solubility of iron increases with increasing salt content in the experimental system, in perfect agreement with the predominance of these two chloride complexes (Fig. 6A-C). The iron tetrachloride complex, found to be significant in aqueous solution at salinities above 0.1 *m* KCl (Fig. 6C), sharply decreases with increasing CO_2 content, and becomes negligible (≤1% of total iron) above 5 *m* CO_2. In contrast, the neutral $FeCl_2^0$ increases from 0 to 3 *m* CO_2, and exhibits a constant concentration at higher CO_2. This trend follows the abundance of KCl^0 (Fig. 4) and thus reflects interplay between the decreasing availability of the Cl^- ligand and growing thermodynamic stability (i.e., formation constant) of $FeCl_2^0$ with increasing CO_2 content.

4.4. Zinc

Zinc concentrations were measured in equilibrium with ZnS in one experiment (#m19, PMH and QMA buffers, Table 3); they increase by almost an order of magnitude when increasing CO_2 content from 3 to 20 *m* (Fig. 7). Our data in CO_2-poor solution (3 *m*; no data are available in CO_2-free solutions) are in reasonable agreement (within a factor of 2) with the thermodynamic predictions of sphalerite solubility using the extensive recent compilation of Zn chloride, (hydrogen)sulfide and hydroxide complexes of Akinfiev and Tagirov (2014). These calculations predict three zinc chloride species, $ZnCl_2$, $ZnCl_3^-$, $ZnCl_4^{2-}$, in roughly comparable fractions at CO_2 ≤ 5 *m*. As in the case of Fe, at higher CO_2 the two charged species become negligible at the expense of the neutral dichloride complex, which accounts well for the observed solubility trend up to 20 *m* CO_2. Although our few measured solubility data points in such CO_2-rich fluids are somewhat higher (by factor of ~3) than these predictions, this small difference is likely to be within the uncertainties of the thermodynamic HKF-model coefficients for $ZnCl_2$, which have been not evaluated in Akinfiev and Tagirov's (2014) study.

4.5. Copper

Copper solubility measured in aqueous solution is in excellent agreement with calculated values in equilibrium with chalcopyrite, using the thermodynamic properties of the dominant copper dichloride $CuCl_2^-$ and mono-hydrosulfide $CuHS^0$ given in Akinfiev and Zotov (2010), whereas the concentrations of other copper complexes suggested in the literature ($CuCl^0$, $CuCl_3^{2-}$ and $Cu(HS)_2^-$) are negligible ($<10^{-7}$ *m*). Thermodynamic data for the same copper complexes obtained from older major sources, i.e., Brugger et al. (2007) and Sverjensky et al. (1997), respectively, predict copper solubilities that are one and two orders of magnitude lower than our measured values (Fig. 8). Consequently, we adopted the Akinfiev and Zotov (2010) set of values of Gibbs free energy and Born coefficient (Table 5) for these complexes for describing copper solubility trends with variable CO_2 content. Within the data scatter, copper solubility does not show any dependence on CO_2 in the low-salinity fluids examined in this study (Fig. 8 and 9). Measured total copper concentrations over the whole CO_2 (0-20 *m*) and KCl (0.01-0.30 *m*) range are described by $CuHS^0$ and $CuCl_2^-$, the latter species increasing with the KCl content, at constant CO_2 (Fig. 9). The neutral $CuHS^0$ is independent of CO_2 content whereas the charged $CuCl_2^-$, predominant at KCl >0.05 *m*, exhibits a weak maximum at 2-3 *m* CO_2 (Fig. 9B,C), and then steadily decreases with further CO_2 rise. A similar maximum in calculated $AgCl_2^-$ concentration was predicted for AgCl(s) solubility in H_2O-CO_2-NaCl supercritical fluids at 400°C and 600-1000 bar (Akinfiev and Zotov, 1999). As in the case of $FeCl_2^0$ shown above, this trend is due to the sharp change in Cl^- ligand concentration with increasing CO_2 up to 3 *m* (Fig. 4).

4.6. Gold

Gold solubility measured in silicate and iron oxide/sulfide buffered solutions shows a significant scatter of data points (within at least 0.5 log unit), mostly due to intrinsic experimental and analytical difficulties in measuring ppb-level Au concentrations in high *T-P* fluids. Our data in both buffer systems (QMK+PPM and QMA+PMH; Fig.10) are reasonably well described by the mono-hydrosulfide complex $AuHS^0$, within the variation of its Gibbs free energy among the major available experimental or theoretical data sets (see Table 5 for references). Other gold complexes ($Au(HS)_2^-$, $AuCl_2^-$, $AuCl^0$, and $AuOH^0$) from most data sources available, are relatively minor at our experimental conditions. As for Fe and Cu, the major tendency with increasing CO_2 is a weakening of the stability of charged species ($AuCl_2^-$ and $Au(HS)_2^-$), which become negligible at elevated CO_2 contents ($<10^{-8}$ *m* Au at CO_2 above 5-10 *m*).

Additional experiments performed in batch autoclaves in a more sulfur-rich system (Au-CO_2-H_2O, 1 *m* S, 0.1 *m* NaOH, Table 4) at 450°C and 600 bar show measured gold solubility in CO_2-free fluid (32 ppm Au) identical to that predicted using the thermodynamic properties of the gold-trisulfur ion complex $Au(HS)S_3^-$, a species only recently recognized in S-rich fluids

(Pokrovski et al., 2015). Conversely, the solubility predicted using traditional Au complexes with HS^- and OH^- ligands is at least 1 log unit lower at our experimental conditions (Fig. 11). With addition of CO_2, the calculated concentration of the charged $Au(HS)_2^-$ and $Au(HS)S_3^-$ species decreases sharply and, above ~5 *m* CO_2, the neutral $AuHS^0$ is predicted to become the solubility controlling species, matching within errors the measured gold concentrations in the H_2O-CO_2 fluid.

4.7. Platinum

Platinum concentrations measured in experiments #m30 and #m19 is between 0.5 and 5 ppb Pt, independently of CO_2 content (Fig. 12). These values are at least three orders of magnitude higher than predictions using the thermodynamic properties of Pt-Cl complexes from a recent compilation of Tagirov et al. (2015), suggesting that such complexes are definitely not the species controlling PtS solubility in our H_2S-bearing, Cl-poor experiments. Our data would be more consistent with the predominance of uncharged hydrogen sulfide species such as $Pt(HS)_2^0$ whose concentration is expected to be independent of CO_2. However, the available thermodynamic data for this complex are limited, to the best of our knowledge, to the single study of Pan and Wood (1994) who reported stability constants for $Pt(HS)_2^0$ between 250-350°C and saturated vapor pressure (P_{sat}). We extrapolated these constants within the framework of the RB model using the OptimC program (Shvarov, 2015) to our experimental *T-P* conditions and found that they yield PtS solubilities in CO_2-free aqueous fluid two orders of magnitude higher than our measured values. Not being able to evaluate either the uncertainties associated with these predictions or those of the original experimental data points of Pan and Wood (1994), we have corrected the $Pt(HS)_2^0$ solubility constant to match our measured solubility in aqueous fluid:

$$PtS(s) + H_2S = Pt(HS)_2^0 \qquad \log K_{450°C,\,675bar} = -6.8 \pm 0.5 \qquad (6)$$

It can be seen in Fig.12 that the whole set of our data in H_2O-CO_2 fluids is accurately described using this new constant and a Born parameter of 0 for $Pt(HS)_2^0$. Noteworthy is that the predicted Pt tri-chloride complex is at least three log units lower in concentration, passing through a weak maximum at CO_2 ~3 *m*, and steadily decreasing at higher CO_2 content. This behavior is similar to that of $CuCl_2^-$, $AuCl_2^-$, and $ZnCl_3^-$ (see above).

4.8. Tin

Tin concentrations measured at 450°C and 570-680 bar (#m23 and #m30 with the QMK and PPM buffers) is constant at CO_2 contents <3 *m*, then increases by more than one order of magnitude in the CO_2 range 3–20 *m* (Fig. 13), but is independent of Cl concentration at constant CO_2 (Table 2). This pattern suggests *i)* possible formation of carbonate complexes in CO_2 rich fluids, and *ii)* absence of significant chloride complexing. Thermodynamic calculations of Sn speciation in aqueous 0.1 *m* KCl solution at our experimental conditions in equilibrium with cassiterite, using one of the most complete databases of stability constants of Sn-OH-Cl-(H)CO_3 complexes (Ryzhenko et al., 1997), predict that $Sn(OH)_4^0$ is by far the dominant species with concentrations ~10 times higher than our experimental value at CO_2-free conditions (Fig. 13A). We note, however, that uncertainties associated with such predictions may be quite large, if one considers the data scatter in the rare experimental studies compiled by Ryzhenko et al. (1997). Consequently, we corrected the stability constant of $Sn(OH)_4^0$to match our experimental values in CO_2-poor solutions:

$$SnO_2(s) + 2\ H_2O = Sn(OH)_4^0 \qquad \log K_{450°C,\ 675bar} = -5.8\pm0.5 \qquad (7)$$

Our model for CO_2 fluids using this new constant and a value of ω of 0 for $Sn(OH)^0{}_4$ shows that its concentration is independent of CO_2 (Fig. 13B). Therefore, to account for the increase in solubility at high CO_2, we tentatively added a bicarbonate complex, according to the simplest ligand exchange reaction:

$$Sn(OH)_4^0 + HCO_3^- = SnHCO_3(OH)_3^- + OH^-, \qquad \log K_{450°C,\ 675bar} = -0.8\pm0.5 \qquad (8)$$

According to the value obtained, which is referred to pure water at infinite dilution, the affinity of HCO_3^- for Sn(IV) is lower than that of OH^-. Thus significant carbonate complexing for Sn may only occur in CO_2-rich and/or less acidic fluids in which bicarbonate ions are more abundant. Furthermore, we cannot completely exclude carbonate complex stoichiometries other than that of reaction (8), nor the existence of complexes with other carbon forms such as CO- a possibility that still awaits experimental verification. Thus, among the metals investigated in this study, tin is the only one that is likely to form weak (bi)carbonate complexes in CO_2-rich fluids at our experimental conditions; however, more systematic measurements are required to validate this conclusion.

4.9. Molybdenum

Molybdenum concentrations in equilibrium with molybdenite (MoS_2), measured in the PPM and QMK buffered runs, decrease slightly from 0 to 3 *m* CO_2 and remain constant within error up to 20 *m* CO_2. They are also weakly dependent of KCl concentration, increasing by a factor of 2 between 0.1 *m* KCl and 0.3 *m* KCl at constant CO_2 (Table 2). These trends point to *i)* the absence of carbonate complexes, and *ii)* a likely predominance of neutral species with K^+ and/or Cl^- ligands. Such speciation is confirmed by thermodynamic calculations in equilibrium with molybdenite, suggesting that the hydrogen molybdate ion $HMoO_4^-$ and its ion pair with K^+ $KHMoO_4^0$ are dominant at our experimental conditions, and may account for the measured solubilities within an order of magnitude, depending on the data source chosen (Fig. 14). Similarly to the charged species of other metals, $HMoO_4^-$ decreases with increasing CO_2 concentration in favor of its neutral ion pair $KHMoO_4^0$. The best description of the whole set of experimental data points was achieved with $HMoO_4^-$ from Shock et al. (1997) and $KHMoO_4^0$ with the following reaction constant, adjusted to match our experimental solubility in CO_2-free solution:

$HMoO_4^- + K^+ = KHMoO_4^0$ $\log K_{450°C,\,675bar} = 2.2 \pm 0.3$ (9).

This value overlaps within errors with that of Zotov et al. (1994), whose experimental data between 300 and 450°C at 500 bar were regressed in our study using the RB model to extrapolate to the experimental pressure: $\log K_{450°C,\,675bar} = 3.3 \pm 0.7$. We are not aware of other data sources for this ion pair. Note that the stability constants of $HMoO_4^-$ are also quite uncertain and the differences in its predicted concentration vary over at least 1 order of magnitude among the available sources (Fig. 14). We do not have evidence from our data that Cl- and S-type complexes would be significant at our conditions.

4.10. Common features for different metals

The above analysis reveals a number of common physical-chemical controls that CO_2 exerts on metal solubility in hydrothermal fluids. First, all electrically charged species having large Born parameter (ω) values are disfavored even at moderate CO_2 contents (3-5 *m*). In contrast, neutral species with small positive ω values that are well constrained (e.g., for silica, arsenic), or zero values (e.g., chloride and sulfide complexes, for which there is no sufficient solubility data nor direct C_p and V measurements for a more accurate derivation of the Born parameter), are far less sensitive to the presence of CO_2. This implies that CO_2-rich hydrothermal fluids may transport these metals in comparable amounts as aqueous fluids. The results also indicate that, in the presence of CO_2, the higher the value of the Born parameter, the larger a negative effect is produced on the species concentration. Second, there is no evidence for direct carbonate complexing for most metals, at least at the conditions of the present study, with a possible exception of Sn. In conclusion, despite the great variety of complex types for different metals (chloride, sulfide, carbonate or hydroxide), our electrostatic model accounts satisfactorily for their solubility in a wide range of CO_2 contents.

5. GEOLOGICAL APPLICATIONS

The findings of our study may have far-reaching implications for modelling transport and fractionation by geological fluids. The strength of our model is that it does not require adjustable parameters, and that it is based on the accurately predictable change of the dielectric constant in the mixed fluid and on the knowledge of the metal speciation in aqueous solution. Consequently, this model may be applied beyond the range of conditions covered by our experiments. Contrary to common belief that the presence of CO_2 has a negative effect on mineral solubility, our results show that CO_2 may lead to contrasting mobility for different metals and large variations of their ratios between aqueous and CO_2-rich fluids.

This is illustrated in Fig. 15 and 16, which show solubilities of pyrite, chalcopyrite and native gold, calculated for H_2O-CO_2 low-salinity fluids at contrasting redox conditions and sulfur concentrations (f_{O_2} of the PPM and graphite redox buffers; sulfur concentrations of 0.1 and 1 wt% S) encompassing the range of environments for orogenic Au deposit formation (Ridley and Diamond, 2000; Tomkins, 2010). The fluid is assumed to be buffered with the quartz-muscovite-(K)feldspar mineral assemblage and contain 7 wt% salt (NaCl+KCl). It can be seen that, even though both copper and iron form predominantly chloride complexes in these fluids, they exhibit different solubility trends above 20 wt% CO_2. This is because the negatively charged $CuCl_2^-$ is disfavored in a CO_2-rich fluid of low dielectric constant compared to the uncharged $FeCl_2^0$ species (Fig. 15A, 16A). As a result, the corresponding Cu/Fe ratio in the fluid decreases by one to two orders of magnitude when the CO_2 content increases from 0 to ~60 wt% (Fig. 15b, 16b). This finding provides an elegant and simple explanation as to why most orogenic gold deposits formed by CO_2-rich fluids are enriched in iron sulfide minerals (pyrite, pyrrhotite, arsenopyrite), but contain very little copper (Goldfarb et al., 2005). Part of Fe in orogenic deposits also comes from surrounding rocks (Pitcairn, 2014), and thus may be efficiently remobilized at local scale by CO_2-rich fluids. Thus, along with other possible factors affecting metal ratios in orogenic deposits (e.g. specific metal source such as pyrite, redox potential, efficiency of metal precipitation, Tomkins, 2010; Large et al., 2011; Pitcairn et al., 2014; Zhong et al., in press), the presence of CO_2 could significantly contribute to selective metal enrichment or depletion.

The solubility of gold in a hydrothermal fluid may also be affected by CO_2 concentration, depending on Au speciation. In H_2S-rich reducing environments, Au solubility in the form of its dominant species in solution, $Au(HS)_2^-$, decreases significantly with increasing CO_2, following the common trend for charged species (Fig. 16); in S-poor environments, Au is in the form of neutral $Au(HS)^0$ and its solubility is almost unaffected (Fig. 15). Interestingly, in terms of absolute Au concentrations, the capacity of CO_2-rich fluids to carry gold is similar in a wide range of S content and redox potential, amounting to ~100 ppb Au at >50 wt% CO_2 under the conditions considered here (Fig. 15 and 16). It follows that CO_2-dominated fluids still have capacities of transporting Au at concentrations 100 times higher than the average abundance of Au in common rocks (~1 ppb). The fact that our data do not show a negative effect of CO_2 on Au solubility in near-neutral S-poor fluids, may account for the association of gold with vein quartz hosting fluid inclusions with >80 wt% CO_2 observed in many orogenic Au deposits, particularly in Precambrian terrains such as in West Africa (e.g., Schmidt Mumm et al., 1997), which so far has remained unexplained. In contrast, in H_2O-dominated fluids, Au solubility is strongly sulfur-dependent (200 ppb at 0.1 wt%

S, Fig. 15, vs 2 000 ppb at 1 wt% S, Fig. 16), and thus changes in S concentration (e.g., metamorphic S liberation or sulfidation of Fe-rich rocks) will lead to large variations in Au mobility in such fluids.

Although not covered by our experiments, As and Sb, which form soluble neutral hydroxide complexes (Pokrovski et al., 1996, 2006) with slightly positive values of the Born parameter (ω $As(OH)_3$ ~ 0.12×10^5 cal/mol, Perfetti et al., 2008; ω $Sb(OH)_3$ ~ 0.05×10^5 cal/mol, Zotov et al., 2003), are expected to be little affected by CO_2 and thus be very mobile in CO_2-rich fluids. This reasoning is in agreement with natural observations of As and Sb enrichment in many orogenic and associated deposits (Boiron et al., 2003; Pitcairn et al., 2014; Velásquez et al., 2014) and direct analyses of elevated As and Sb concentrations in fluid inclusions from orogenic deposits (Garofalo et al., 2014; Rauchenstein-Martinek et al., 2014; Salvi et al., 2015). Noteworthy is that supercritical CO_2-dominated fluids also have significant capacities for carrying silica (e.g., 100s ppm Si at 50 wt% CO_2 in Fig. 5), which is the primary gangue mineral in orogenic Au deposits and the main host of CO_2-rich inclusions. Thus, the geochemical signature of most orogenic and associated deposits enriched in Fe, Au, As and some other metalloids is in line with the potentially large capacities of CO_2-rich fluids to transport these metals revealed in this study for the first time.

The effect of CO_2 on metal transport in oxidizing S-rich saline fluids typical of porphyry Cu-Au-Mo and associated deposits may be different because of the different metal speciation. This is illustrated in Fig. 17, which shows Cu, Fe, Au solubilities calculated at 500°C and 1 kbar in a model fluid representative of those generated by magma degassing in major porphyry deposits (10 wt% NaCl and 1 wt% S, $H_2S:SO_2 = 1$; e.g., Heinrich, 2005; Kouzmanov and Pokrovski, 2012). In such fluids, Fe, Cu and Au form predominantly negatively charged chloride (Fe and Cu) and hydrogen sulfide or trisulfur ion complexes (Au), which are not favored by CO_2. As a result, the presence of CO_2 will lower their solubilities across the CO_2 range reported in this type of deposits (up to ~20 wt%; Rusk et al., 2008). Note, however, that this effect is much stronger for Fe and Cu than for Au in S-rich fluids that are still capable of transporting ~10 ppm Au on average, in the range of typical CO_2 contents of such fluids (marked by a grayed area in Fig. 17). In contrast to orogenic systems, porphyry fluids exhibit much larger variations in composition, temperature and pressure during their evolution (Sillitoe, 2010; Kouzmanov and Pokrovski, 2012). As a result, the effect of CO_2 on metal solubility and element ratios is overlapped with many other factors such as magma composition and evolution at depth, a particular *T-P* path of the ascending hydrothermal fluid undergoing vapor-brine immiscibility phenomena, or selective mobilization of Au by specific sulfur ligands such as the trisulfur ion (e.g., Murakami et al., 2010; Wilkinson, 2013; Pokrovski et al., 2015).

The interpretation of the effect of CO_2 on the mobility of other metals considered in this study such as Pt, Mo, Sn, Zn is less straightforward because of large uncertainties associated with their speciation in aqueous solution and the small amount of pioneering experimental data obtained in this study. Based on the dataset available, it is expected that Pt and Mo, which form predominantly neutral sulfide and hydroxide species, respectively, will be little affected by CO_2 in most geological settings. As for Sn, (bi)carbonate complexes at high CO_2 content might form, thus increasing tin mobility. Zinc is expected to be controlled by chloride complexes, both neutral and charged similar to Fe(II), whose fraction strongly depends on the chloride content. Furthermore, with high salt concentrations in the fluid phase, the presence of CO_2 will significantly widen the immiscibility domain in *T-P*-composition space, yielding CO_2-rich vapors and salt-rich aqueous liquids of contrasting compositions. Metal speciation and partitioning in such phases are virtually unknown, and direct experimental data are required to fill this gap.

6. CONCLUDING REMARKS

The key points of this study are the following.

We have obtained first direct experimental data on the solubility of Fe, Cu, Zn, Sn, Mo, Pt, and Au in supercritical CO_2-rich (up to 50 wt%), sulfur- and salt-bearing fluids typical of hydrothermal ore deposits. Contrary to common knowledge, presence of CO_2 does not necessarily reduce the metal transporting potential of a fluid. Rather, metals solubilities as a function of CO_2 exhibit different trends depending on the metal identity, S and Cl concentration and the resulting chemical speciation.

These new data are interpreted using a simple electrostatic model, which does not require “adjustable” parameters, and is based on the change of the dielectric constant in the mixed fluid and the stability of the dominant metal complexes in aqueous fluid. Whatever the identity of the ligand (HS^-, S_3^-, Cl^-, OH^-), the key tendency is favoring the stability of uncharged complexes with increasing CO_2 fraction. This leads to contrasting solubility trends for metals whose speciation is dominated either by neutral or charged species, depending on the metal identity and solution composition. For comparison, traditional thermodynamic modeling, employed so far, based on aqueous fluid properties and ignoring changes of solvation properties in the presence of CO_2, postulates the constancy of all these species concentrations with addition of CO_2.

Our model suggests that the presence of large amounts of CO_2 (20-70 wt%) in typical orogenic fluids leads to the fluid being enriched in Fe compared to Cu, whereas Au solubility is significantly weakened in S-rich fluids, but it is only weakly affected in S-poor fluids. Our predictions are in agreement with the large abundance of Fe (pyrite) and low contents of Cu in most orogenic gold deposits. For comparison, in magmatic-hydrothermal fluids typical of porphyry Cu-Au-Mo deposits, with generally low CO_2 contents (<20 wt%), metal fractionation induced by CO_2 is weaker and may be obscured by other multiple factors related to magma and fluid evolution.

The other metals studied (Pt, Sn, Mo, Zn) show less contrasting trends with CO_2, with solubilities either being roughly constant or moderately increasing with CO_2 content in the systems investigated. Accurate interpretation of these trends will require a far better knowledge of the metal speciation in aqueous fluids. It seems likely that none of the studied metals (with possible exception of Sn) form significant (bi)carbonate complexes in supercritical hydrothermal fluids.

It cannot be excluded that other minor C-bearing ligands such as CO and small organic compounds may selectively bind some metals in specific environments in which such form may be sufficiently abundant (e.g., strongly reducing conditions, very high pressures). This hypothesis requires experimental confirmation. Similarly, the role of CH_4, which is also an abundant volatile in reduced metamorphic environments, requires further studies. Finally, another important aspect unknown so far is the effect of CO_2 (and, potentially, CH_4) on vapor-liquid fractionation of metals, which is a subject of our on-going research.

Acknowledgments

This work was funded by the French National Research Agency (Grant SOUMET, ANR-2011-Blanc SIMI 5-6 009), the University of Toulouse (Grant CO2MET), the Institut des Sciences de l'Univers of the Centre National de la Recherche Scientifique (Grants ORPY-CESSUR and S3MIF-PNP). M.A.K. acknowledges support from the University of Toulouse (PhD fellowship of the Ministère de l'Education Nationale, de l'Enseignement Supérieur et de la Recherche (MENESR), awarded by the President of the University of Toulouse). We thank P. Gisquet, A. Castillo, S. Mounic, Ph. Besson, C. Causserand, A. Lanzanova, F. Candaudap, J. Chmeleff, M. Henry, J. Prunier, T. Aigouy, M. Thibaut for their professional help with tough hydrothermal experiments and interminable chemical analyses. We are grateful to J. Schott, P. Bénézeth, A. Zotov, and D. Grichuk for fascinating discussions about CO_2 fluids.

REFERENCES

Akinfiev N.N. (1997) Thermodynamic description of H_2O-gas binary systems by means of Redlich-Kwong equation over a wide range of parameters of state. *Geochem. Intern.* **35**, 188-196.

Akinfiev N. and Zotov A. (1999) Thermodynamic description of equilibria in mixed fluids (H_2O-non polar gas) over a wide range of temperature (25 to 700°C) and pressure (1 to 5000 bars*). Geochim. Cosmochim. Acta* **63**, 2025-2041.

Akinfiev N.N. and Diamond L.W. (2003) Thermodynamic description of aqueous nonelectrolytes at infinite dilution over a wide range of state parameters. *Geochim. Cosmochim. Acta* **67**, 613-629.

Akinfiev N.N. and Zotov A.V. (2010) Thermodynamic description of aqueous species in the system Cu-Ag-Au-S-O-H at temperatures of 0-600°C and pressures of 1-3000 bar. *Geochem. Intern.* **48**, 714-720.

Akinfiev N.N. and Tagirov B.R. (2014) Zn in hydrothermal systems: thermodynamic description of hydroxide, chloride, and hydrosulfide complexes. *Geochem. Intern.* **52**, 197-214.

Archer D.G. and Wang P. (1990) The dielectric constant of water and Debye-Hückel-limiting law slopes. *J. Phys. Chem.* **19**, 371-411.

Bakker R. J. (2009) Package FLUIDS. Part 3: correlations between equations of state, thermodynamics and fluid inclusions. *Geofluids* **9**, 63-74.

Barton P.B. and Chou I.-M. (1993) Refinement of the evaluation of the role of CO_2 in modifying estimates of the pressure of epithermal mineralization. *Econ. Geol.* **88,** 873-884.

Benning L.G. and Seward T.M. (1996) Hydrosulphide complexing of Au(I) in hydrothermal solutions from 150-400°C and 500-1500 bar. *Geochim. Cosmochim. Acta* **60**, 1849-1871.

Bodnar R.J., Reynolds T.J. and Kuehn C.A. (1985) Fluid-inclusion systematics in epithermal systems. *Rev. Econ. Geol.* **2**, 73-97.

Boiron M.-C., Cathelineau M., Banks D., Fourcade S. and Vallance J. (2003) Mixing of metamorphic and surficial fluids during the uplift of the Hercynian upper crust: consequences for gold deposition. *Chem. Geol.* **194**, 119-141.

Born Von M. (1920) Volumen und Hydratationswarme der Ionen. *Zeitschr. Physik* **1**, 45-48.

Bowers T.S. and Helgeson H.C. (1983) Calculation of the thermodynamic and geochemical consequences of nonideal mixing in the system H_2O-CO_2-NaCl on phase relations in geologic systems: Equation of state for H_2O-CO_2-NaCI fluids at high pressures and temperatures. *Geochim. Cosmochim. Acta* **47**, 1247-1275.

Brugger J., Etschmann B., Liu W., Testemale D., Hazemann J.-L., Emerich H., van Beek W. and Proux O. (2007) An XAS study of the chloride complexing of Cu(I) in brines. *Geochim. Cosmochim. Acta* **71**, 4920-4941.

Bryzgalin O.V. and Rafal'sky R.P. (1982) Estimation of instability constants for ore-element complexes at elevated temperatures. *Geochem. Intern.* **19**, 839-849.

Catchpole H., Kouzmanov K., Fontboté L., Guillong M. and Heinrich C. A. (2011). Fluid evolution in zoned Cordilleran polymetallic veins — Insights from microthermometry and LA-ICP-MS of fluid inclusions. *Chem. Geol.* **281**, 293-304.

Dandurand J.-L. and Schott J. (1992) Prediction of ion association in mixed-crustal fluids. *J. of Phys. Chem.* **96**, 7770-7777.

Driesner T. and Heinrich C. (2007) The system H_2O-NaCl. Part I: Correlation formulae for phase relations in temperature-pressure-composition space from 0 to 1000°C, 0 to 5000 bar, and 0 to 1 XNaCl. *Geochim. Cosmochim. Acta* **71**, 4880-4901.

Drummond S.E. and Ohmoto H. (1985) Chemical evolution and mineral deposition in boiling hydrothermal systems. *Econ. Geol.* **80**, 126-147.

Duan Z., Moller N. and Weare J. (1995) Equation of state for NaCl–H_2O–CO_2 system – prediction of phase equilibria and volumetric properties. *Geochim. Cosmochim. Acta* **59**, 2869–2882.

Erkey C. (2000) Supercritical carbon dioxide extraction of metals from aqueous solutions: a review. *J. of Supercrit Fluids* **17**, 259-287.

Fanning K.A. and Pilson M. E.Q. (1973) Spectrophotometric determination of dissolved silica in natural waters. *Analytical Chemistry* **45**, 136-140.

Garofalo P.S., Ficker M.B., Gunther D., Bersani D. and Lottici P.P. (2014) Physical-chemical properties and metal budget of Au-transporting hydrothermal fluids in orogenic deposits. *Geol. Soc., London, Special Publications* **402**, 71-102.

Gibert F., Moine B., Schott J. and Dandurand J-L. (1992) Modeling of the transport and deposition of tungsten in the scheelite-bearing calc-silicate gneisses of the Montagne Noire, France. *Contrib. Mineral. Petrol.* **112**, 371-384.

Gibert F., Pascal M.-L. and Pichavant M. (1998) Gold solubility and speciation in hydrothermal solutions: Experimental study of the stability of hydrosulfide complex of gold ($AuHS^0$) at 350 to 450°C and 500 bars. *Geochim. Cosmochim. Acta* **62**, 2931-2947.

Gibert F., Guillaume D. and Laporte D. (1998) Importance of fluid immiscibility in the H_2O -NaCl - CO_2 system and selective CO_2 entrapment in granulites: experimental phase diagram at 5-7 kbar, 900°C and wetting textures. *Eur. J. Mineral.* **10**, 1109-1123.

Glennon J.D., Harris S.J., Walker A., McSweeney C.C. and O'Connell M. (1999) Carrying gold in supercritical CO_2. *Gold Bulletin* **32**, 52-58.

Goldfarb R.J., Baker T., Dubé B., Groves D.I., Hart C.J.R. and Gosselin P. (2005) Distribution, character and genesis of gold deposits in metamorphic terranes. Society of Economic Geologists, Inc. *Econ. Geol. 100th Anniversary Volume,* 407-450.

Haas J.R., Shock E.L. and Sassani D.S. (1995) Rare earth elements in hydrothermal systems: Estimates of standard partial molal thermodynamic properties of aqueous complexes of the rare earth elements at high pressures and temperatures. *Geochim. Cosmichim. Acta* **59**, 4329-4350.

Hanley J. J. and Gladney E. R. (2011) The presence of carbonic-dominant volatiles during the crystallization of sulfide-bearing mafic pegmatites in the North Roby zone, Lac des Iles Complex, Ontario. *Econ. Geol.* **106**, 33-54.

Heinrich C.A. (2005) The physical and chemical evolution of low-salinity magmatic fluids at the porphyry to epithermal transition: A thermodynamic study. *Miner. Deposita* **39**, 864-889.

Heinrich C.A. (2007) Fluid-fluid interactions in magmatic hydrothermal ore formation. *Rev. Mineral. Geochem.* **65**, 363-387.

Helgeson H.C. and Kirkham (1976) Theoretical prediction of the thermodynamic properties of aqueous electrolytes at high pressures and temperatures. III. Equation of state for aqueous species at infinite dilution. *Amer. J. Sci.* **276**, 97-240.

Helgeson H.C., Kirkham D.H. and Flowers G.C. (1981) Theoretical prediction of thermodynamic behavior of aqueous electrolytes at high temperatures and pressures. IV. Calculation of activity coefficients, osmotic coefficients, and apparent molal and standard and relative partial molal properties to 5 kb and 600°C. *Am.J.Sci.* **281**, 1249-1516.

Hemley J.J., Cygan G.L., Fein J.B., Robinson G.R. and d'Angelo W.M. (1992) Hydrothermal ore-forming processes in the light of studies in rock-buffered systems: I. Iron-Copper-Zinc-Lead sulfide solubility relations. *Econ. Geol.* **87**, 1-21.

Hill P.G. (1990) A unified fundamental equation for the thermodynamic properties of H_2O. *J. Phys. Chem.* **19**, 1233-1274.

Holloway J.R. (1981) Compositions and volumes of supercritical fluids in the Earth's crust. In *Fluid Inclusions Application to Petrology. Short course handbook* (eds. Hollister L.S. and Crawford M.L.), Mineralogical Association of Canada. pp. 13-35.

Jacquemet N., Guillaume D., Zwick A. and Pokrovski G.S. (2014) In-situ Raman spectroscopy identification of the S_3^- ion in S-rich hydrothermal fluids from synthetic fluid inclusions. *Amer. Mineral.* **99**, 1109-1118.

Johnson J.W., Oelkers E.H. and Helgeson H.C. (1992) SUPCRT92: A software package for calculating the standard molal thermodynamic properties of minerals, gases, aqueous species, and reactions from 1 to 5000 bar and 0 to 1000°C. *Computers and Geosci* **18**, 899-947; updated version based on a series of subsequent papers reporting HKF parameters for most ions and aqueous complexes is available on line at http://geopig.asu.edu/index.html#.

Kirkwood J.G. (1939) The dielectric polarization of polar liquids. *J. Phys. Chem.* **7**, 911-919.

Koděra P., Lexa J., Rankin A.H. and Fallick AE (2005) Epithermal gold veins in a caldera setting: Banská Hodruša, Slovakia. *Mineral. Deposita* **39**, 921–943.

Kokh M.A. (2016) Rôle du CO_2 dans les transferts des métaux d'intérêt économiques par les fluides géologiques. PhD thesis, University of Toulouse.

Kouzmanov K. and Pokrovski G.S. (2012) Hydrothermal controls on metal distribution in Cu(-Au-Mo) porphyry systems. In: Geology and Genesis of Geology and Genesis of Major Copper Deposits and Districts of the World: A Tribute to Richard H. Sillitoe (eds. J.W. Hedenquist, M. Harris, and F. Camus). *Soc. of Econ. Geol. Special Publication*, **16**, 573-618.

Kudrin A.V. (1985) The solubility of tugarinovite MoO_2 in aqueous solutions at elevated temperatures. *Geochem. Intern.* **22**, 126-138.

Lai J. and Chi G. (2007) CO_2-rich fluid inclusions with chalcopyrite daughter mineral from the Fenghuangshan Cu–Fe–Au deposit, China: implications for metal transport in vapor. *Mineral. Deposita* **42**, 293-299.

Large R.R., Bull S.W. and Maslennikov V.V. (2011) A carbonaceous sedimentary source-rock model for Carlin-type and orogenic gold deposits. *Econ. Geol.* **106**, 331-358.

Lowenstern J.B. (2001) Carbon dioxide in magmas and implications for hydrothermal systems. *Mineral. Deposita* **36**, 490-502.

Manning C.E., Shock E.L. and Sverjensky D.A. (2013) The chemistry of carbon in aqueous fluids at crustal and upper-mantle conditions: experimental and theoretical constraints. *Rev. Mineral. Geochem.* **75**, 109–148.

Minubaeva Z. and Seward T.M. (2010) Molybdic acid ionization under hydrothermal conditions to 300 °C. *Geochim. Cosmochim. Acta* **74**, 4365-4374.

Murakami H., Seo J.H. and Heinrich C.A. (2010) The relation between Cu/Au ratio and formation depth of porphyry-style Cu-Au±Mo deposits. *Mineral. Deposita* **45**, 11-21.

Newton R.C. and Manning C.E. (2000) Quartz solubility in H_2O-NaCl and H_2O-CO_2 solutions at deep crust-upper mantle pressures and temperatures: 2-15 kbar and 500-900°C. *Geochim. Cosmochim. Acta* **64**, 2993-3005.

Newton R.C. and Manning C.E. (2009) Hydration state and activity of aqueous silica in H_2O-CO_2 fluids at high pressure and temperature. *Amer. Mineral.* **94**, 1287-1290.

Pan P. and Wood S.A. (1994) Solubility of Pt and Pd sulfides and Au metal in aqueous bi-sulfide solutions. II. Results at 200 to 350°C and saturated vapor pressure. *Mineral. Deposita* **29**, 373-390.

Perfetti E., Thiery R. and Dubessy J. (2008) Equation of state taking into account dipolar interactions and association by hydrogen bonding: II-Modelling liquid–vapour equilibria in the H_2O–H_2S, H_2O–CH_4 and H_2O–CO_2 systems. *Chem. Geol.* **251**, 50-57.

Phillips G. N. and Evans K. A. (2004) Role of CO_2 in the formation of gold deposits. *Nature* **429**, 860-863.

Pitcairn I.K., Craw D. and Teagle D.A.H. (2014) The gold conveyor belt: Large-scale gold mobility in an active orogen. *Ore Geol. Rev.* **62**, 129-142.

Plyasunov A.V. and Shock E.L. (2001) Correlation strategy for determining the parameters of the revised Helgeson-Kirkham-Flowers model for aqueous nonelectrolytes. *Geochim. Cosmochim. Acta* **65**, 3879-3900.

Pokrovski G.S., Gout R., Zotov A., Schott J. and Harrichoury J.-C. (1996) Thermodynamic properties and stoichiometry of the arsenic (III) hydroxide complexes at hydrothermal conditions. *Geochim. Cosmochim. Acta* **60**, 737-749.

Pokrovski G. S., Kara S. and Roux J. (2002) Stability and solubility of arsenopyrite, FeAsS, in crustal fluids. *Geochim. Cosmochim. Acta* **66**, 2361-2378.

Pokrovski G.S., Borisova A.Y. and Harrichoury J.-C. (2008). The effect of sulfur on vapor-liquid fractionation of metals in hydrothermal systems. *Earth Planet. Sci. Lett.* **266**, 345-362.

Pokrovski G.S., Borisova A.Y. and Bychkov A.Y. (2013) Speciation and transport of metals and metalloids in geological vapors. *Rev. Mineral. Geochem.* **76**, 165-218.

Pokrovski G.S., Akinfiev N.N., Borisova A.Y., Zotov A.V. and Kouzmanov K. (2014) Gold speciation and transport in geological fluids: insights from experiments and physical-chemical modelling. *Geol. Soc., London, Spec. Publ.* **402**, 9-70.

Pokrovski G.S. and Dubessy J. (2015) Stability and abundance of the trisulfur radical ion S_3^- in hydrothermal fluids. *Earth Planet. Sci. Lett.* **411**, 298-309.

Pokrovski G.S., Kokh M.A., Guillaume D., Borisova A.Y., Gisquet P., Hazemann J.-L., Lahera E., Del Net W., Proux O., Testemale D., Haigis V., Jonchière R., Seitsonen A.P., Ferlat G., Vuilleumier R., Saitta A.M., Boiron M.-C. and Dubessy J. (2015) Sulfur radical species form gold deposits on Earth. *Proc. Nat. Acad. Sci. USA* **112**, 44.

Rauchenstein-Martinek K., Wagner T., Walle M. and Heinrich C.A. (2014) Gold concentrations in metamorphic fluids: A LA-ICPMS study of fluid inclusions from the Alpine orogenic belt. *Chem. Geol.* **385**, 70–83.

Ridley J.R. and Diamond L.W. (2000) Fluid chemistry of orogenic lode gold deposits and implications for genetic models. *Rev. Econ. Geol.* **13**, 141-162.

Rosenbauer R.J., Bischoff J.L. and Potter J.M. (1993) A flexible Au-Ir cell with quick assembly for hydrothermal experiments. *Amer. Mineral.* **78**, 1286-1289.

Rusk B.G., Reed M.H. and Dilles J.H. (2008) Fluid inclusion evidence for magmatic-hydrothermal fluid evolution in the porphyry copper-molybdenum deposit at Butte, Montana. *Econ. Geol.* **103**, 307-334.

Rusk B., Emsbo P., Hammersli J., Hofstra A., Hunt A., Landis G. and Rye R. (2011) Origin and composition of fluids that form giant porphyry Cu (Mo–Au) deposits. In: *Proc. of the 11th Biennial SGA Meeting.* Antafogasta, Chile, 414–416.

Ryzhenko B.N. (1981) *Equilibria in Hydrothermal Solutions.* Nauka, Moscow (in Russian).

Ryzhenko B.N., Shvarov Yu.V. and Kovalenko N.I. (1997) System Sn-Cl-F-C-S-H-O-Na. Thermodynamic component properties under conditions of the Earth's crust. *Geochem. Intern.* **11**, 1149-1153.

Salvi S., Béziat D. and Siebenaller L. (2015) Sulphide microchemistry variations in West African gold deposits.

Metallogenesis, Tectonics and Surface Evolution of the West African Craton – Senegal Conference. Dacar, Senegal. Available online at http://www.tectonique.net/Dakar2015/WAXI2-talk salvi.pdf

Seward T. M. and Barnes H. L. (1997) Metal transport by hydrothermal ore fluids. In: Barnes, H. L. (ed.) Geochemistry of Hydrothermal ore Deposits. 3rd edn. Wiley and Sons, New York, 435-486.

Seward T.M., Williams-Jones A.E. and Migdisov A.A. (2014) The chemistry of metal transport and deposition by ore-forming hydrothermal fluids. In: *Treatise on Geochemistry*, 2nd Edition, Chap. **13.2**, 29-57.

Seyfried W. E., Janecky D.R. and Berndt M. E. (1987) Rocking autoclaves for hydrothermal experiments II. The flexible reaction-cell system. *In Hydrothermal Experimental Techniques* (eds. G. C. Ulmer and H. L. Barnes). John Wiley & Sons, Inc., New York. pp. 216-239.

Seyfried W.E. and Ding K. (1993) The effect of redox on the relative solubilities of copper and iron in Cl-bearing aqueous fluids at elevated temperatures and pressures: An experimental study with application to subseafloor hydrothermal systems. *Geochim. Cosmochim. Acta* **57**, 1905-1917.

Schmidt Mumm A., Oberthür T., Vetter U. and Blenkinsop T.G. (1997) High CO_2 content of fluid inclusions in gold mineralisations in the Ashanti Belt, Ghana: a new category of ore forming fluids. *Mineral. Deposita* **32**, 107-118.

Shock E.L. and Koretsky C.M. (1993) Metal-organic complexes in geological processes: calculation of standard partial molal thermodynalmic properties of aqueous acetate complexes at high pressures and temperatures. *Geochim. Cosmochim. Acta* **57**, 4899-4922.

Shock E.L., Sassani D.C., Willis M. and Sverjensky D.A. (1997) Inorganic species in geologic fluids: Correlation among standard molal thermodynamic properties of aqueous ions and hydroxide complexes. *Geochim. Cosmochim. Acta* **61**, 907-950.

Shvarov Y.V. (2008) HCh: new potentialities for the thermodynamic simulation of geochemical systems offered by Windows. *Geochem. Intern.* **46**, 834-839.

Shvarov Y.V. (2015) A suite of programs, OptimA, OptimB, OptimC, and OptimS compatible with the Unitherm database, for deriving the thermodynamic properties of aqueous species from solubility, potentiometry and spectroscopy measurements. *Appl. Geochem.* **55**, 17-27.

Sillitoe R.H. (2010) Porphyry copper systems. *Econ. Geol.* **105**, 43-41.

Spycher N.F. and Reed M.H. (1989). Evolution of a Broadlands-type epithermal ore fluid along alternative P-T paths: Implications for the transport and deposition of base, precious, and volatile metals. *Econ. Geol.* **84**, 328-359.

Stefánsson A. (2001) Dissolution of primary minerals of basalt in natural waters: I. Calculation of mineral solubilities from 0°C to 350°C. *Chem. Geol.* **172**, 225-250.

Stefánsson A. and Seward T.M. (2004) Gold(I) complexing in aqueous sulphide solutions to 500°C at 500 bar. *Geochim. Cosmochim. Acta* **68**, 4121-4143.

Sverjensky D.A., Shock E.L. and Helgeson H.C. (1997) Prediction of the thermodynamic properties of aqueous metal complexes to 1000°C and 5 kb. *Geochim. Cosmochim. Acta* **61**, 1359-1412.

Sverjensky A.D., Harrison B. and Azzolini D. (2014) Water in the deep Earth: The dielectric constant and the solubilities of quartz and corundum to 60 kb and 1200 °C. *Geochim. Cosmochim. Acta* **129**, 125-145.

Tagirov B.R. and Korzhinsky M.A. (2001a) An experimental study of iron(II) complexing in H_2O-HCl-NaCl(-CO_2) fluids at temperarure of 500°C and pressure of 1 kbar. *Geokhimia* **2***,* 228-231 (in Russian).

Tagirov B.R. and Korzhinsky M.A. (2001b) Speciation of iron(II) in H_2O-HCl(-CO_2) fluid at 500-600˚C and pressures of 2 kbar. *Geokhimia* **9***,* 943-950 (in Russian).

Tagirov B.R., Salvi S., Schott J. and Baranova N.N. (2005) Experimental study of gold-hydrosulphide complexing in aqueous solutions at 350-500°C, 500 and 1000 bars using mineral buffers. *Geochim. Cosmochim. Acta* **69**, 2119-2132.

Tagirov B.R., Baranova N.N. and Bychkova Ya.V. (2015) Thermodynamic properties of platinum chloride complexes in aqueous solutions: derivation of consistent parameters from literature data and experiments on Pt(cr) solubility at 400-475°C and 1 kbar. *Geochem. Int.* **53**, 327-340.

Testemale D., Brugger J., Liu W., Etschmann B. and Hazemann J.-L. (2009) In-situ X-ray absorption study of Iron (II) speciation in brines up to supercritical conditions. *Chem. Geol.* **264**, 295-310.

Tomkins A.G. (2010) Windows of metamorphic sulfur liberation in the crust: Implications for gold deposit genesis. *Geochim. Cosmochim. Acta* **74**, 3246-3259.

Velásquez G., Béziat D., Salvi S., Siebenaller L., Borisova A.Y., Pokrovski G.S. and de Parseval P. (2014) Formation and deformation of pyrite and implications for gold mineralization in the El Callao District, Venezuela. *Econ. Geol.* **109**, 457-486.

Walther J. J. and Orville P. M. (1983) The extraction-quench technique for determination of the thermodynamic properties of solute complexes: application to quartz solubility in fluid mixtures. *Amer. Mineral.* **68**, 731–741.

Walther J.V. and Schott J. (1988) The dielectric constant approach to speciation and ion pairing at high temperature and pressure. *Nature* **332**, 635-638.

Wilkinson J.J. (2013) Triggers for the formation of porphyry ore deposits in magmatic arcs. *Nat. Geosci.* **6**, 917-925.

Wood S.A., Pan P., Zhang Y. and Mucci A. (1994) The solubility of Pt and Pd sulfide and Au in bisulfide solutions. I. Results at 25-90°C and 1 bar pressure. *Mineral. Deposita* **29**, 309-317.

Wood S.A. and Samson I.M. (1998) Solubility of ore minerals and complexation of ore metals in hydrothermal solutions. *Rev. Econ. Geol.* **10**, 33-80.

Yang Z., Yang X., Xu Z. and Yang N. (2010). Molecular simulations of structures and solvation free energies of passivated gold nanoparticles in supercritical CO_2. *J. Chem. Phys.* **133**, 094702.

Zakirov I.V., Stretenskaja N.G., Aranovich L.Y. and Volchenkova V.A. (2007) Solubility of NaCl in CO_2 at high pressure and temperature: first experimental measurements. *Geochim. Cosmochim. Acta* **71**, 4251-4255.

Zhong R., Brugger J., Tomkins A.G., Cheng Y. and Li W. (2015) Fate of gold and base metals during metamorphic devolatilization of a pelite. *Geochim. Cosmochim. Acta,* in press.

Zotov A., Kudrin A.V., Levin K.A., Shikina D. and Var'yash L. (1994) Experimental studies of the solubility and complexing of selected ore elements (Au, Ag, Cu, Mo, As, Sb, Hg) in aqueous solutions. In: *Fluids in the Crust: Equilibrium and Transport Properties* (eds. Shmulovich K.I., Yardley B.W.D., Gonchar G.G,). Chapman and Hall, London, pp. 97-136.

Zotov A., Shikina N.D. and Akinfiev N.N. (2003) Thermodynamic properties of the Sb(III) hydroxide complex $Sb(OH)_{3(aq)}$ at hydrothermal conditions. *Geochim. Cosmochim. Acta,* **67**, 1821-1836.

Table 1. Fluid composition measured in three experimental runs **(#m23, m24, m25)** in the system CO_2-H_2O-KCl-QMK-PPM-Au-$CuFeS_2$-MoS_2-PtS-SnO_2-ZnS at the indicated *T-P* conditions using titanium flexible cell reactor. The initial aqueous solution in each run contains 0.10 *m* KCl.

Duration, days	**T, °C**	**P, bar**	**CO_2, wt% fluid**	**K**	**Cl**	**S_{tot}**	**S_{red}**	**H_2S**	**Si**	**Cu**	**Fe**	**Ti**	**Zn**	**Sr**	**Au**	**Pt**	**Sn**	**Mo**
				mol/kg water					**ppm ^{a}**						**ppb ^{a}**			
experiment #m23																		
3	350	603	0	0.087	0.090	0.0043	0.005 ^{b}	0.0021	573	0.45	5.7±0.1	25	1.0±0.1	5.2	322±30	2.4±0.1	11±4	30±1
7	350	609	0	0.085	0.089	0.0040	0.005 ^{b}	0.0047	526	0.24	9.6±0.1	32	1.0±0.1	4.8	130±32	2.5±0.1	≤11	13±1
12	350	597	0	0.094	0.094	0.0037	0.005 ^{b}	0.0045	723	0.26	3.6±0.1	19	0.5±0.1	7.1	41±19	0.8±0.1	≤5	12±1
17	350	610	0	0.088	0.092	0.0042	0.005 ^{b}	0.0033	569	0.05	3.6±0.1	33	0.4±0.1	3.5	296±19	2.3±0.1	≤5	8±1
2	450	640	0	0.085	0.091	0.035	0.032	0.026	677	1.55	44±1	6.0	14±1	1.2	283±14	4.3±0.2	43±7	31±2
6	450	626	0	0.082	0.084	0.036	0.034	0.030	706	1.13	68±1	13	18±1	1.0	225±7	1.2±0.1	82±4	20±4
10	450	630	0	0.079	0.059	0.028	0.032	0.033	730	1.17	68±1	20	25±1	0.9	758 ±89	3.0±0.1	150±5	30±3
14	450	625	0	0.073	0.064	0.028	0.033	0.034	684	1.06	58±1	15	20±1	0.5	242±14	1.4±0.1	129±4	19±4
experiment #m24																		
1	450	667	7.7±1.6	0.020	0.024	- ^{c}	0.046	0.023	695	0.02	4.0±0.1	- ^{c}	-	<2	20±5	0.5±0.1	<55	22±1
6	450	645	6.0±0.5	0.016	0.017	-	0.044	0.028	590	0.15	4.5±0.1	-	-	<2	45±5	0.1±0.1	<60	10±2
10	450	625	4.5±0.3	0.015	0.013	0.054	0.045	0.029	563	0.47	4.1±0.1	-	-	<6	*30 000* ^{d}	*88* ^{d}	<65	40±2
Injection of KCl-H_2O (1.000 m)																		
14	450	635	5.8±1.6	0.141	0.140	0.042	0.041	-	597	2.56	193±5	-	-	<4	*7 000* ^{d}	1.8 ^{d}	250±55	36±1
27	450	622	2.3±0.4	0.052	0.054	0.035	0.042	0.031	589	1.30	70±5	-	-	<2	230±10	1.8±0.2	<55	34±1
33	450	608	2.0±0.3	0.036	0.037	0.036	0.040	0.027	635	0.65	25±5	-	-	<2	137±1	3.0±0.2	<70	20±2
experiment #m25																		
Injection of CO_2 at 25°C																		
0.5	450	660	22±?	0.026	0.021	*0.031* ^{e}	0.059	-	314	0.68	21±1	-	-	<2	125±15	1.4±0.1	<40	14±4
3	450	680	16±1	0.026	0.026	*0.036* ^{e}	0.063	0.019	*625* ^{f}	0.24	63±1	-	-	<2	275±90	3.2±1.3	<35	6±2
7 ^{g}	*450*	*657*	*9±1*	*0.008*	*0.009*	*0.031*	*0.054*	*0.037*	*427*	*0.12*	*4.0±0.3*	-	-	-	*1 800*	*17±1*	*<47*	*14±5*
10 ^{g}	*450*	*630*	*7±1*	*0.008*	*0.008*	*0.040*	*0.051*	*0.029*	*460*	*0.09*	*2.0±0.3*	-	-	-	*4 500*	*33±1*	*<48*	*9±3*
typical error (unless indicated)	±2	±10		±10%	±10%	±10%	±10%	±20%	±10%	±10%		±10%		±6%				

a – reported concentration values are for an aqueous CO_2-free fluid; b – uncertainty ±15%, c – '-' means not measured or not applicable; d – contamination during sampling; e – poor analysis; f – evaporation of analyzed sample; g – cell leak, numbers are italized.

Table 2. Fluid composition measured in the system CO_2-H_2O-KCl-QMK-PPM-Au-$CuFeS_2$-MoS_2-PtS-SnO_2 at the indicated *T-P* conditions (experiment #m30) using a gold flexible cell reactor. The initial aqueous solution contains 0.10 *m* KCl.

Duration, days	T, °C	P, bar	CO_2, wt% fluid	K	Cl	S_{tot}	S_{red}	H_2S	Si	Cu	Fe	Ti	Au	Pt	Sn	Mo
				mol/kg water					ppm [a]				ppb [a]			
6	350	568	0	0.103	0.092	0.0058	0.005 [b]	0.0012	740±10	0.21±0.02	0.50±0.05	10	27±5	1.6±0.5	21±1	175±15
9	350	593	0	0.113	0.096	0.0060	0.005 [b]	0.0033	790±10	0.24±0.02	1.1±0.5	20	32±5	3.5±0.6	50±1	200±20
12	350	601	0	0.101	0.090	0.0046	0.004 [b]	0.0035	720±70	0.03±0.01	0.8±0.5	2.6	28±5	0.35±0.15	8±7	160±10
4	400	669	0	0.109	0.095	0.0235	0.0122 [b]	0.0086	1100±110	0.15±0.02	1.0	5	27±5	4.0±0.4	13±1	60±5
8	400	638	0	0.105	0.086	0.0119	0.0104 [b]	0.0097	775±85	0.37±0.04	7.6	28	50±5	1.0±0.1	26±1	45±5
2	450	689	0	0.094	0.084	0.056	0.030	0.022	970±30	2.0±0.6	70	23	220±10	3.0±0.1	189±60	55±5
6	450	675	0	0.097	0.090	0.042	0.028	0.022	1090±110	2.3±0.6	95	15	150±50	0.7±0.5	120±40	35±5
Injection of CO_2																
3	450	670	11.2	0.083	0.080	*0.031* [c]	0.019	0.034	515±20	2.1±0.2	220	3	60±5	0.2±0.1	150±10	12±1
8	450	663	11.0	0.085	0.081	0.045	0.026	0.023	490±45	1.8±0.2	290	45	50±5	3±1	175±20	12±1
Injection of CO_2																
5	450	675	25.0	0.069	0.079	0.057	0.027	0.016	240±25	4.1±0.5	690	20	72±5	6.0±3.0	540±10	30±5
9	450	669	24.3	0.057	0.071	0.057	0.027	- [d]	180±15	2.2±0.3	600	43	19±5	0.3±0.1	620±20	9±2
12	450	677	24.8	0.061	0.080	0.035	0.030	0.024	215±20	3.8±0.5	700	9.0	25±5	0.5±0.3	930±30	9±1
Injection of CO_2																
3	450	688	46.2	0.025	*0.055* [c]	0.082	0.019	0.014	90±20	2.9±1.0	500	130	21±5	1.1±0.1	1120±50	17±5
6	450	668	44.1	0.027	*0.071* [c]	0.083	0.021	- [d]	80±10	8.9±1.8	730	30	38±10	1.5±0.3	3590±20	15±5
9	450	676	43.1	0.020	*0.064* [c]	0.063	0.015	0.017	85±25	4.0±1.2	555	160	60±20	1.3±1.2	2940±30	13±5
Injection of KCl-H_2O (0.451 m)																
4	450	688	24.6	0.290	0.285	0.056	0.019	0.030	260±30	12.5±8.5	1 180	65	125±65	4±3	3440±2360	65±35
7	450	670	20.1	0.298	0.303	0.015 [e]	0.056 [e]	0.025 [e]	150±15	6.6±1.6	1 740 [b]	25	50±15	0.5±0.1	1760±340	25±10
Injection of KCl-H_2O (0.310 m)																
4	450	692	9.9	0.279	0.303	0.029	0.018	0.037	145±15	13.3±1.3	990	30	120±60	1.2±0.3	2100±100	35±15
8	450	680	10.3	0.285	0.300	0.031	0.020	0.017	340±80	6.8±0.7	1 270	10	75±5	0.3±0.2	1570±100	20±10
error	±2	±10	±1.5	±10%	±10%	±10%	±10%	±25%			±10%	±45%				

a – reported values are for an aqueous CO_2-free fluid; b – uncertainty ±20%; c – numbers in italic are uncertain because of poor analysis; d – '-' means not measured; e – boiling during sampling yielding inaccurate S analysis.

Table 3. Fluid composition measured in the system CO_2-H_2O-KCl-QMA-PMH-Au-$CuFeS_2$-ZnS at the indicated *T-P* conditions using a titanium flexible cell reactor (experiment #m19). The initial aqueous solution composition is 0.107 *m* KCl.

Duration, days	T, °C	P, bar	CO_2, wt% fluid	K	Cl	S_{tot}	S_{red}	H_2S ^{a}	Si	Cu	Fe	Zn	Ti	Au	Pt	Al
				mol/kg water					ppm ^{b}					ppb ^{b}		
Injection of CO_2 at 25°C																
3	450	780	46.2	0.044	-^{c}	*0.030* ^{d}	0.041	0.025	141	*11.7±5*^{d}	228±10	690±82	6.0	*573±200* ^{d}	*4.0±2.0* ^{d}	82±10
7	450	730	49.3	0.032	-	-	0.054	0.036	158	3.3±0.3	345±10	650±15	8.5	*271±100* ^{d}	1.3±0.2	95±15
11	450	734	46.4	0.029	-	*0.025* ^{d}	0.052	0.039	153	3.1±0.3	413±20	610±10	22.0	211±30	2.3±0.2	98±20
Injection of KCl-H_2O (0.107 m)																
3	450	735	18.7	0.078	-	-	0.028	-	369	4.5±0.3	172±10	229±5	12.0	152±20	0.4±0.1	144±20
7	450	735	19.2	0.073	-	-	0.030	0.027	423	6.8±0.3	229±15	234±10	8.8	206±30	0.5±0.2	163±30
10	450	726	19.7	0.070	-	-	0.024	0.027	304	6.5±0.3	264±10	275±20	11.0	86±15	1.4±0.2	158±50
Injection of KCl-H_2O (0.107 m)																
4	450	735	6.6	0.089	-	-	0.026	0.019	590	4.8±0.2	86±5	96±7	23.0	42±15	0.8±0.4	166±30
8	450	736	6.9	0.088	-	-	0.029	0.020	569	5.2±0.2	114±5	130±5	25.0	43±10	0.7±0.1	155±20
error	±2	±10	±0.5	±10%	-	±30%	±10%	±25%	±10%	±25%						

a – H_2S concentrations may be underestimated due to incomplete precipitation of CdS in H_2O-CO_2 solutions; b - reported values are for an aqueous CO_2-free fluid; c '-' means not measured; d – numbers in italic are uncertain because of possible contamination or poor analysis.

Table 4. Gold dissolved concentration measured in the system Au-CO_2-S-NaOH-H_2O at 450°C and 600±50 bar, using a batch reactor with quench.

Autoclave		**Initial load**			**Weight loss**		**System composition**			**Gold concentration** [a]	
№	**volume (cm^3)**	**CO_2, g**	**0.1 m NaOH aq soln, g**	**S, g**	**Au, before exp., g**	**Au, after exp., g**	**CO_2, wt.%**	**CO_2, mol/kg water**	**S, mol/kg water**	**Au ppb**	**Au mol/kg water**
3	21.12	0	10.140	0.320	0.3148[b]	0.3144[b]	0	0	0.99	32400[b]	1.71E-04
1	21.26	0.93	8.345	0.272	0.0786	0.0786	9.7	2.5	1.02	3990	2.32E-05
2	22.66	2.60	6.022	0.196	0.0522	0.0522	29.5	9.9	1.02	520	3.88E-06
101	19.58	3.69	3.525	0.114	0.0594	0.0594	50.3	23.9	1.01	271	2.87E-06
103	20.50	3.50	3.700	0.120	0.0607	0.0607	47.8	21.6	1.02	973	9.82E-06
3	21.12	5.49	2.314	0.074	0.0509	0.0509	69.7	54.1	1.00	525	9.12E-06

a - reported values (ICP-AES data) are calculated for an aqueous CO_2-free fluid; b – in agreement with weight loss of gold (error 15%)

Table 5. Metal aqueous complexes considered in this study to describe the solubility of minerals.

Element	Complexes	Born parameter $\omega * 10^{-5}$, cal/mol	References[a] for ω	Reference[a] for G^0_{TP}
Si	SiO_2	0.13	Sh97	Sh97
	SiO_2	0.36	Sv14	Sv14
	Si_2O_4	0.10	Sv14	Sv14
	H_4SiO_4	0.087	St01	St01
Fe	$\mathbf{FeCl_2^0}$	0	this study[b]	Sv97
	$FeCl_4^{2-}$	2.67	this study[c]	Te09
Cu	$\mathbf{Cu(HS)^0}$	0	AZ10	AZ10
	$\mathbf{CuCl_2^-}$	0.81	AZ10	AZ10
	$CuCl^0$	0	Br07	Br07
	$CuCl_2^-$	0.84	Br07	Br07
	$CuCl_3^{2-}$	2.37	Br07	Br07
	$CuCl^0$	0	Sv97	Sv97
	$CuCl_2^-$	1.22	Sv97	Sv97
	$CuCl_3^{2-}$	2.86	Sv97	Sv97
Au	$\mathbf{Au(HS)^0}$	0	Po14	Gi98, BS96, SS04,
	$\mathbf{Au(HS)_2^-}$	0.77	Po14	Ta05, AZ01, AZ10
	$\mathbf{Au(HS)S_3^-}$	0.77	this study[d]	Po15
	$AuOH$	0	Po14	Po14
	$AuCl_2^-$	0.86	Po14	Po14
	$AuCl^0$	0	Po14	Po14
Mo	$\mathbf{KHMoO_4^0}$	0	this study[b]	Ku85, Zo94
	MoO_4^{2-}	3.08	Sh97	Sh97
	$\mathbf{HMoO_4^-}$	1.14	Sh97	MS10
	$H_2MoO_4^0$	0	this study[b]	MS10
Sn	$\mathbf{Sn(OH)_4^0}$	0	this study[b]	Ry97
	$Sn(OH)HCO_3^0$	0	this study[b]	this study
Zn	$\mathbf{ZnCl_2^0}$	0	AT14	AT14
	$ZnCl^+$	0.53	AT14	AT14
	$ZnCl_3^-$	1.00	AT14	AT14
	$ZnCl_4^{2-}$	2.67	AT14	AT14
	$Zn(HS)_2^0$	0	AT14	AT14
Pt	$\mathbf{Pt(HS)_2^0}$	0	this study[b]	this study
	$PtCl^+$	0.62	Ta15	Ta15
	$PtCl_2^0$	0	Ta15	Ta15
	$PtCl_3^-$	1.17	Ta15	Ta15
	$PtCl_4^{2-}$	2.70	Ta15	Ta15

[a] Sv14 – Sverjensky et al. (2014), Sv97 –Sverjensky et al. (1997), Te09 – Testemale et al., (2009), St01 –Stefánsson (2001), Sh97 – Shock et al. (1997), AZ01 – Akinfiev and Zotov (2001), AZ10 – Akinfiev and Zotov (2010), Br07 – Bruger et al. (2007), Gi98 – Gibert et al. (1998), BS96 – Benning and Seward (1996), SS04 – Stefánsson and Seward (2004), Ta05 – Tagirov et al. (2005), Ta15 – Tagirov et al. (2015), MS10 – Minubaeva and Seward (2010), Ku85 – Kudrin et al. (1985), Zo94 – Zotov et al. (1994), Ry97 – Ryzhenko et al. (1997), AT14 – Akinfiev and Tagirov (2014), PW94 – Pan and Wood (1994), Po14 – Pokrovski et al., (2014), Po15 – Pokrovski et al. (2015, in press).

[b] Born parameter for these uncharged complexes was set to zero.

[c] Born parameter of $FeCl_4^{2-}$ was assumed equal to that of $ZnCl_4^{2-}$.

[d] Born parameter of $AuHSS_3^-$ was assumed equal to that of $Au(HS)_2^-$.

The dominant species of each element are shown in bold.

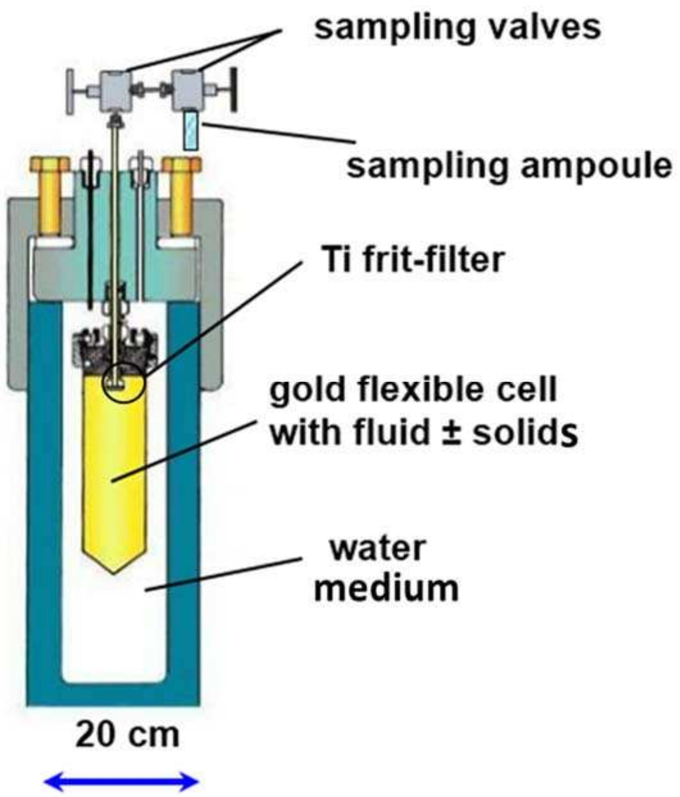

Fig.1. Schematic drawing of the Coretest hydrothermal reactor equipped with a gold flexible cell and an ultra-fast sampling device, used in this study for solubility measurements.

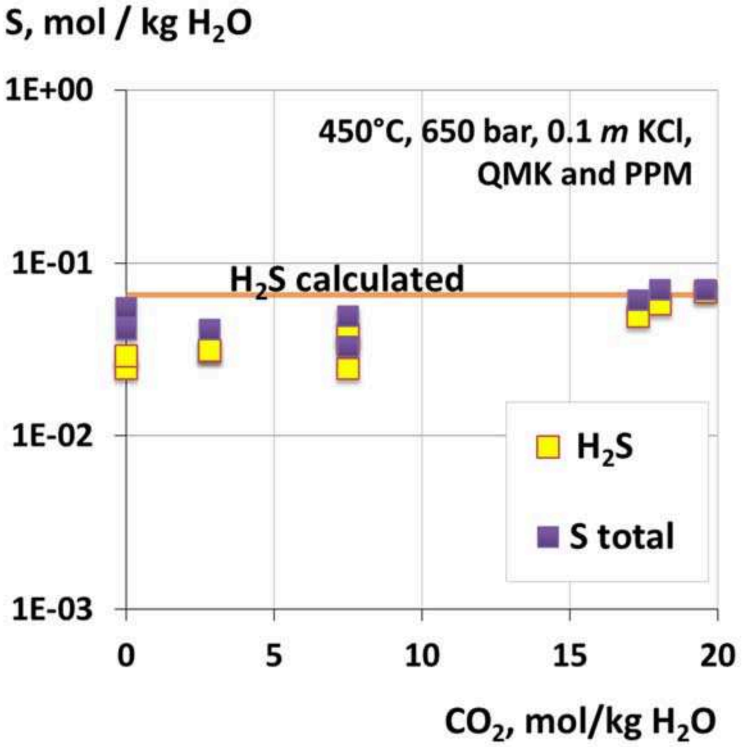

Fig. 2. Total sulfur and H_2S concentrations in supercritical H_2O-CO_2 fluids with 0.1 *m* KCl as a function of CO_2 content at 450°C and 650 bar, and in the presence of the mineral buffers QMK and PPM. The symbols stand for measured values, whereas the curve is equilibrium solubility calculated using the Akinfiev and Diamond model (2003) for H_2S thermodynamic properties.

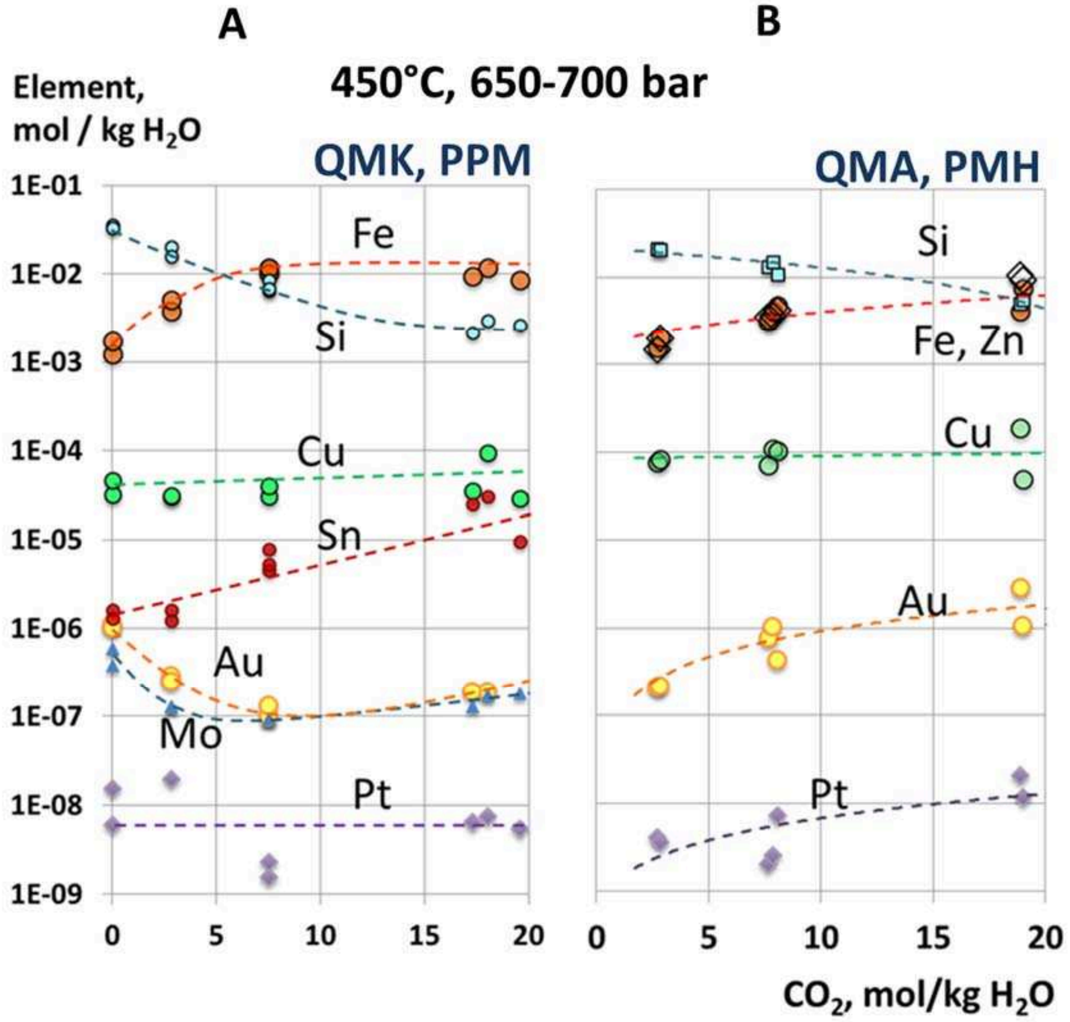

Fig. 3. Solubility of metals in supercritical H_2O-CO_2 fluids with 0.1 *m* KCl as a function of CO_2 content at 450°C and 650-750 bar, and in the presence of the mineral buffers QMK and PPM (A) and QMA and PMH (B) (see section 2.1 for abbreviations and the identity of minerals). Symbols show measured solubilities for the indicated elements, whereas dashed curves are least-square fits drawn to highlight solubility trends. Analytical error bars ou datapoints are comparable to the symbol size.

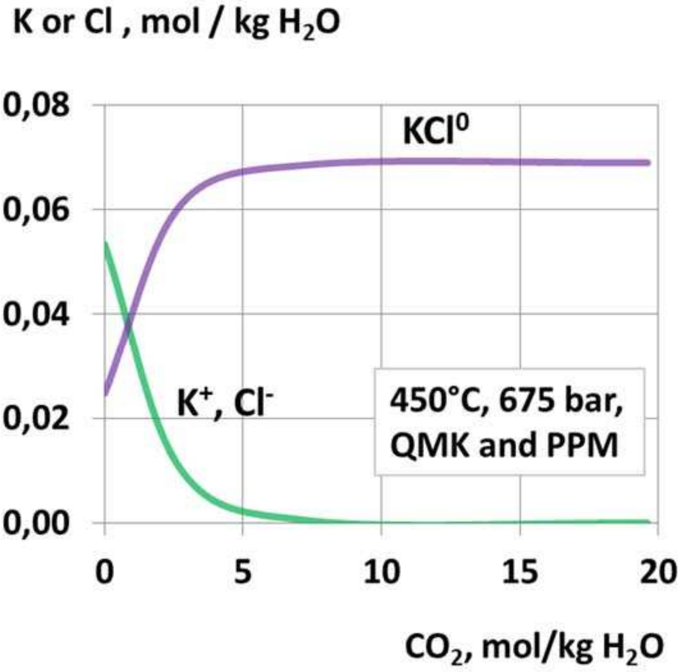

Fig. 4. Calculated distribution of potassium and chlorine species in 0.1 *m* KCl as a function of CO_2 content at 450°C, 675 bar, and in the presence of the mineral buffers QMK and PPM.

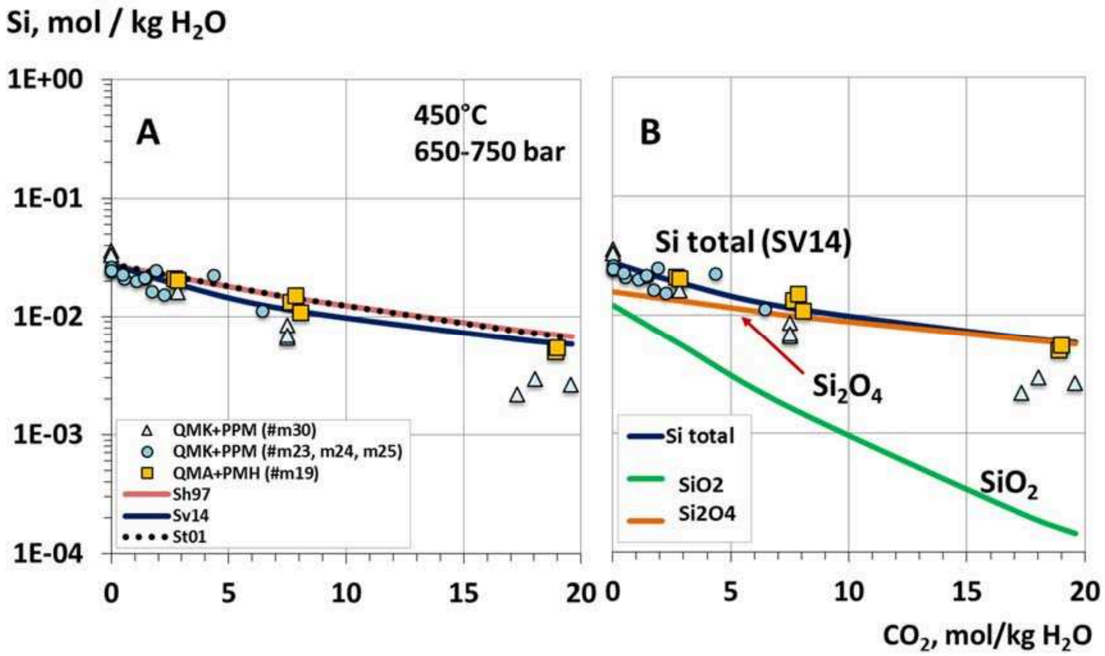

Fig. 5. (A) Solubility of quartz measured in supercritical H_2O-CO_2 fluids with 0.01-0.3 *m* KCl as a function of CO_2 content at 450°C and 650-750 bar, and in the presence of the mineral buffers QMK and PPM or QMA and PMH. Symbols stand for measured solubilities, whereas curves show calculated solubilities of SiO_2 using thermodynamic properties of silicic acid from Shock et al. (1997), Stefánsson et al. (2001) and Sverjensky (2014). (B) Calculated speciation of quartz in supercritical H_2O-CO_2 fluids with 0.01-0.3 *m* KCl and PPM and QMK buffers as a function of CO_2 content using thermodynamic properties of Sverjensky (2014). Symbols stand for measured solubilities, whereas curves show calculated species concentrations and their sum. The variations of pressure (±50 bar) among the experimental runs do not affect significantly the calculated solubility values.

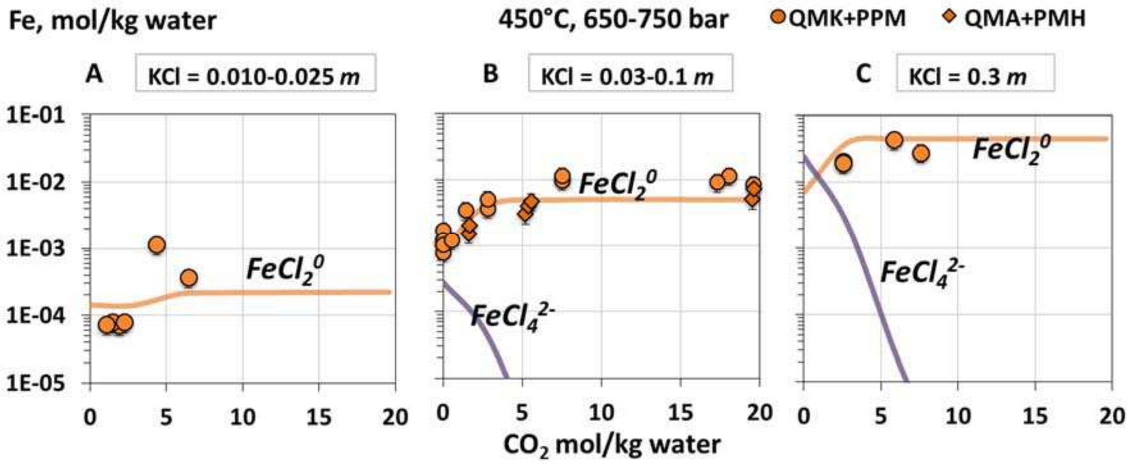

Fig. 6. Solubility of Fe in equilibrium with pyrite in supercritical H_2O-CO_2 fluids with 0.01-0.3 *m* KCl as a function of CO_2 content at 450°C and 650-750 bar, and in the presence of the mineral buffers QMK and PPM (runs #m23, 24, 25, 30) and QMA and PMH (#m19). Symbols stand for measured solubilities, whereas curves are calculated solubilities using the model developed in this study. Gibbs free energy and ω values of Fe chloride species are from Table 5.

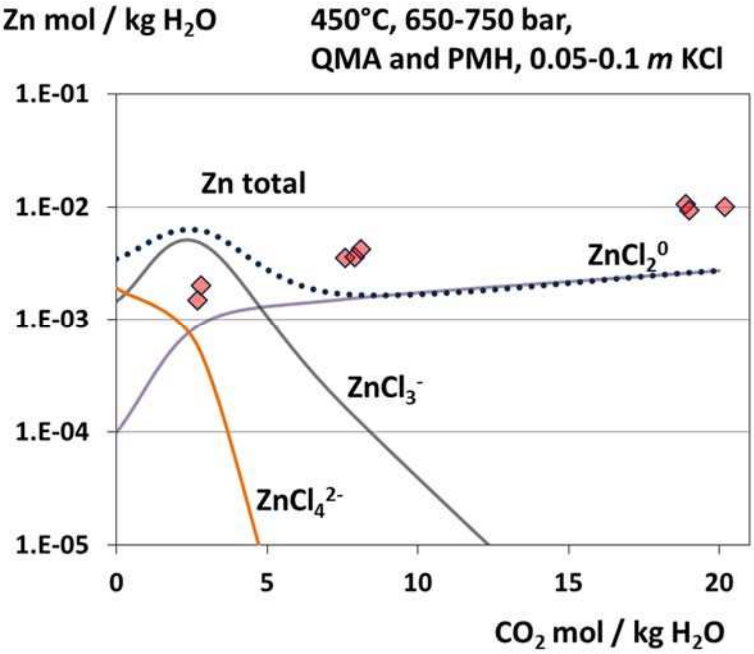

Fig. 7. Solubility of sphalerite in supercritical H_2O-CO_2 fluids with 0.05-0.1 *m* KCl as a function of CO_2 content at 450°C and 650-750 bar, and in the presence of the QMA and PMH buffers (#m19). Symbols stand for measured solubilities, whereas curves are calculated solubilities using thermodynamic data for the indicated zinc chloride complexes from Akinfiev and Tagirov (2014). Concentration of Zn sulfide complexes are below 10^{-5} *m*.

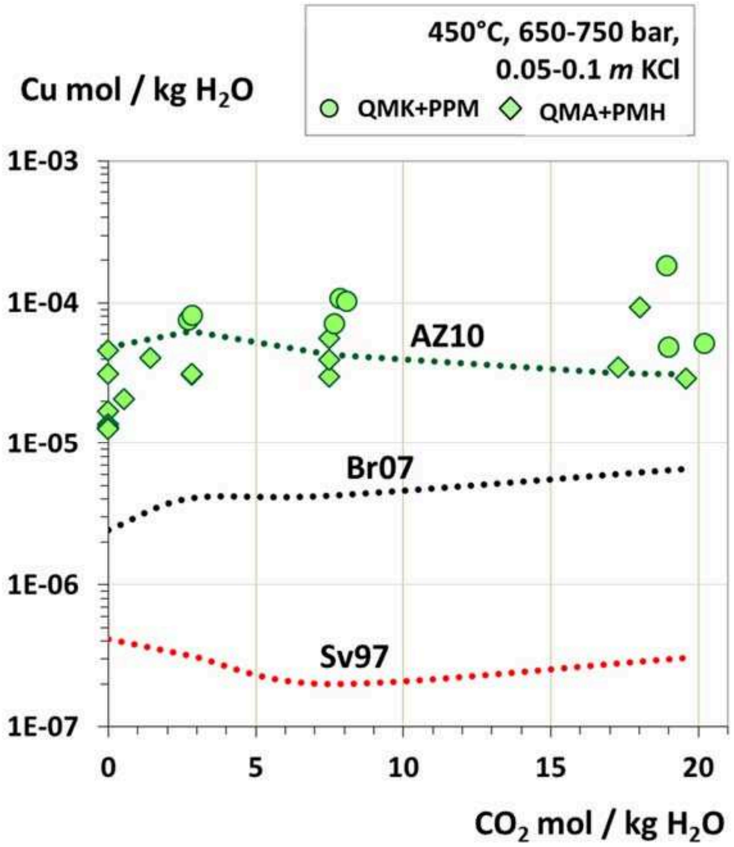

Fig. 8. Comparison of the measured Cu solubilities, in equilibrium with chalcopyrite, at 450°C and 650-750 bar in supercritical H_2O-CO_2 fluids with 0.05-0.1 *m* KCl and in the presence of the indicated mineral buffers, as a function of CO_2 content. Predicted chalcopyrite solubilities were calculated using thermodynamic properties of Cu-Cl and Cu-HS complexes from different sources (see section 4 for discussion and Table 5 for full references).

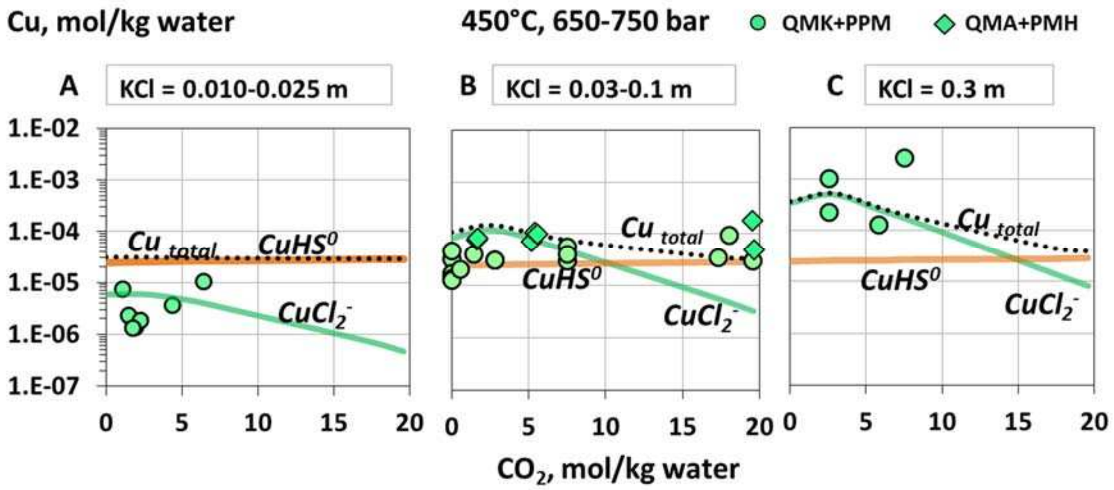

Fig. 9. Solubility of Cu in equilibrium with chalcopyrite in supercritical H_2O-CO_2 fluids with 0.01-0.1 *m* KCl as a function of CO_2 content at 450°C and 650-750 bar, and in the presence of the mineral buffers QMK and PPM (#m23, 24, 25, 30) and QMA and PMH (#m19). Symbols stand for measured solubilities, whereas curves are calculated solubilities (for the system PPM/QMK) using Akinfiev and Zotov's (2010) thermodynamic data for Cu aqueous species. The Gibbs free energy of $CuCl_2^-$ was slightly adjusted (≤5 kJ) to match our experimental data in CO_2-free solution.

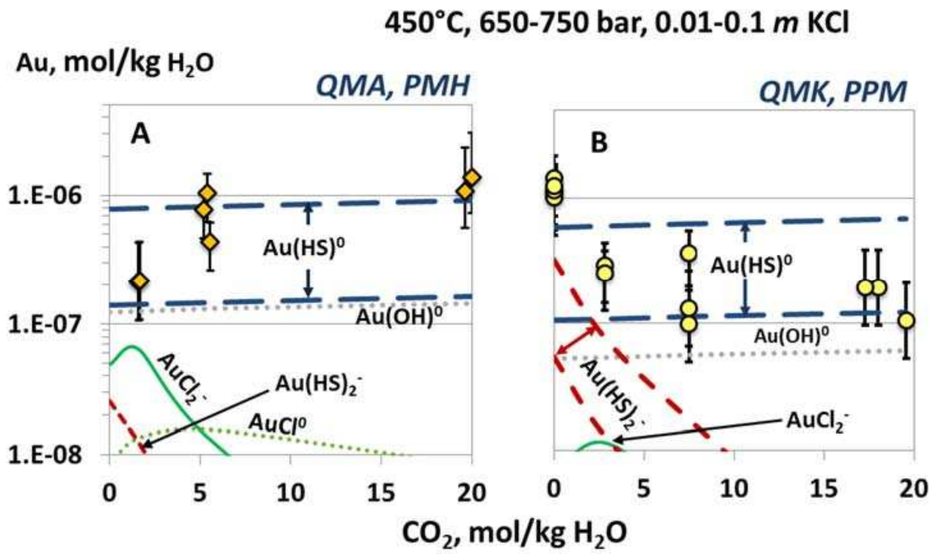

Fig. 10. Solubility of Au in supercritical H_2O-CO_2 fluids with 0.01-0.10 *m* KCl as a function of CO_2 content at 450°C and 650-750 bar, and in the presence of the mineral buffers QMA and PMH (A) and QMK and PPM (B). Symbols stand for measured solubilities; curves are calculated solubilities using available thermodynamic data. Dashed lines represent reasonable interval of uncertainty in the thermodynamic properties for $AuHS^0$ and $Au(HS)_2^-$ (see Table 5 for references).

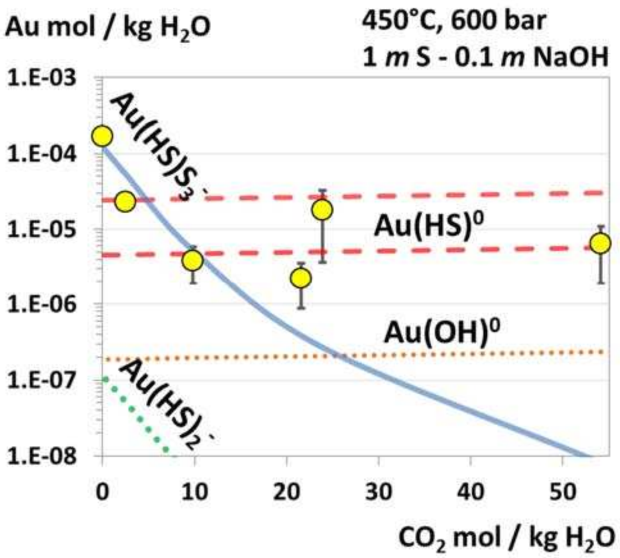

Fig. 11. Solubility of gold in supercritical H_2O-CO_2 fluids with 0.1 *m* NaOH and 1 *m* S as a function of CO_2 content at 450°C and 600 bar. Symbols stand for measured solubilities in batch reactors; curves are calculated solubilities using available thermodynamic data. Dashed lines represent reasonable interval of uncertainty in the thermodynamic properties for $Au(HS)^0$ (see Table 5 for references).

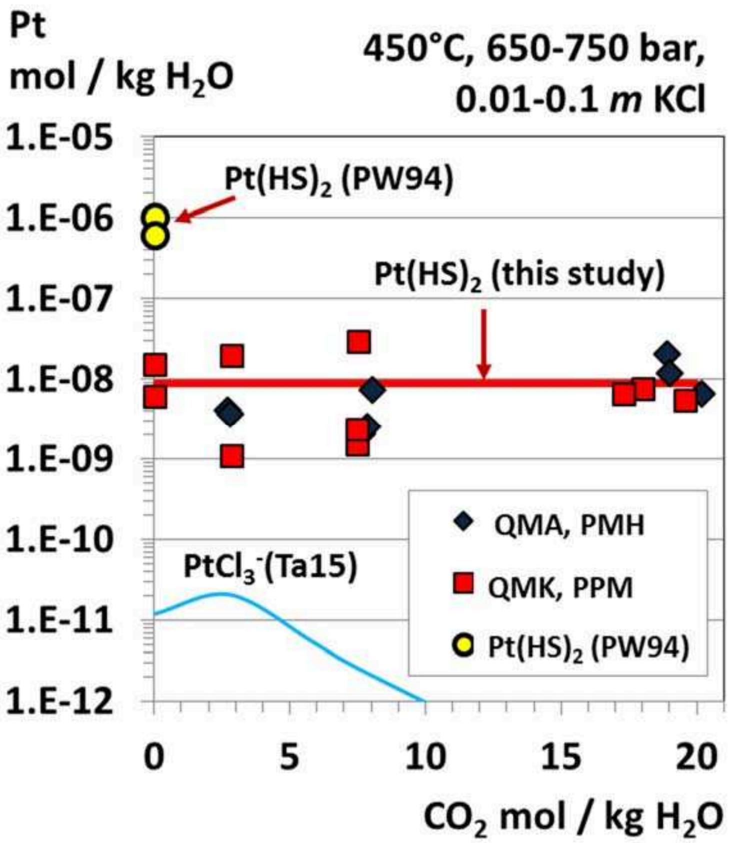

Fig. 12. Solubility of PtS in supercritical H_2O-CO_2 fluids at 450°C and 650-750 bar with 0.01-0.1 *m* KCl as a function of CO_2 content, and in the presence of the mineral buffers QMK and PPM (#m30) and QMA and PMH (#m19). Symbols stand for measured solubilities in this study. The circles (PW94) represent the extrapolated solubility using the stability constants of Pan and Wood (1994). The thick (red) curve is calculated solubility using the stability constant of $Pt(HS)_2$ derived in this study (reaction 6); for comparison, the thin (blue) curve shows calculated concentration of $PtCl_3^-$ according to Tagirov et al. (2015).

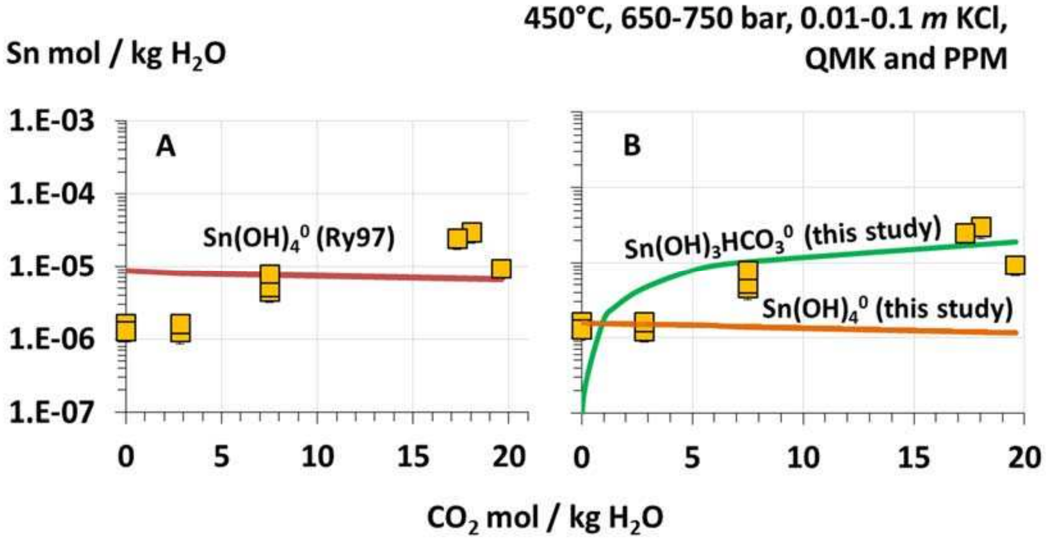

Fig. 13. Solubility of SnO_2 in supercritical H_2O-CO_2 fluids with 0.01-0.10 *m* KCl as a function of CO_2 content at 450°C and 650-750 bar and in the presence of the mineral buffers QMK and PPM. Symbols stand for measured solubilities; curves are calculated solubilities using available thermodynamic data (e.g., Ry97; see Table 5 for full reference) or those derived in this study (see section 4).

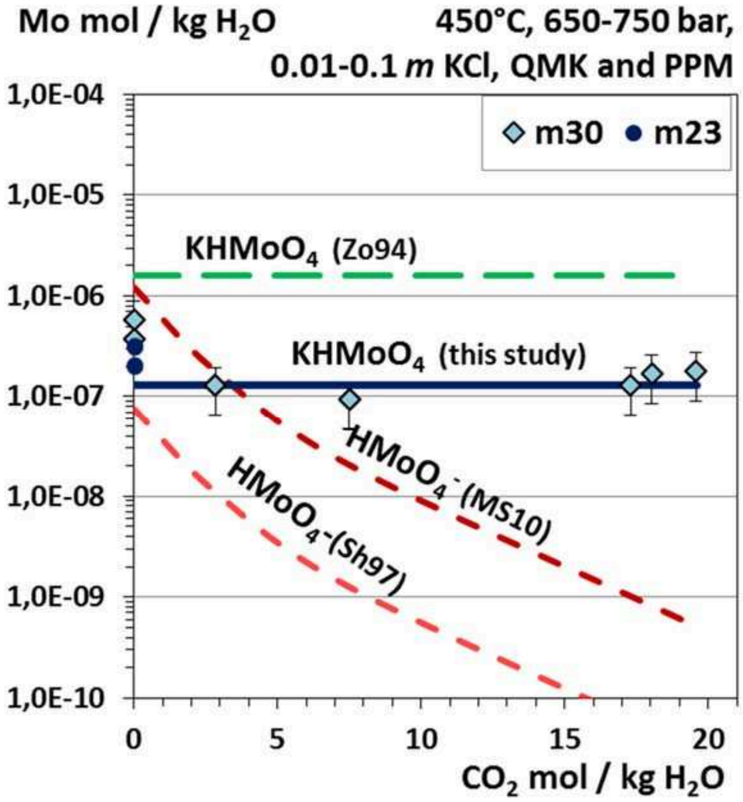

Fig. 14. Solubility of MoS_2 in supercritical H_2O-CO_2 fluids with 0.01-0.10 *m* KCl as a function of CO_2 content at 450°C and 650-750 bar, and in the presence of the mineral buffers QMK and PPM. Symbols stand for measured solubilities; curves are calculated solubilities using available thermodynamic data (see Table 5 for full references). Concentrations of other Mo species such as $H_2MoO_4^0$ and MoO_4^{2-} are less than 10^{-10} *m*, according to available thermodynamic data sources.

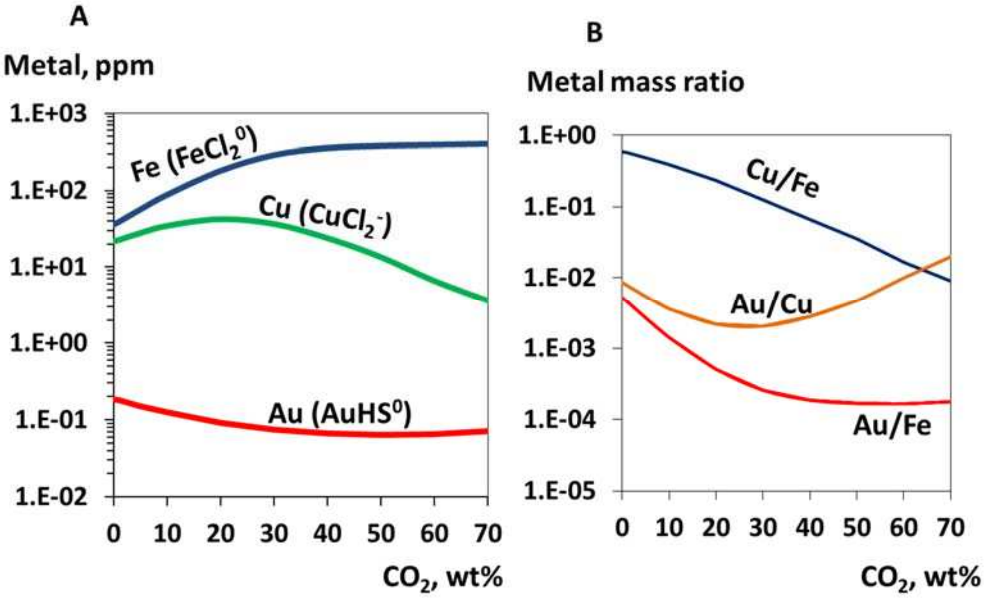

Fig. 15. Solubility of pyrite, chalcopyrite and native gold in supercritical fluids at 450°C and 2 kbar with 7 wt% (NaCl + KCl), as a function of CO_2 content (A), and the corresponding metal ratios in the fluid (B), predicted using the model parameterized in this study. The dominant metal species are indicated in (A). Redox and acidity conditions are buffered by the QMK and PPM assemblages (H_2S ~0.1 wt%). These conditions simulate relatively oxidizing and S-poor (<0.1 wt% S) fluids, typical of orogenic Au deposits, and, possibly, some deep porphyry and volcanic massive sulfide Cu-Fe-Au deposits.

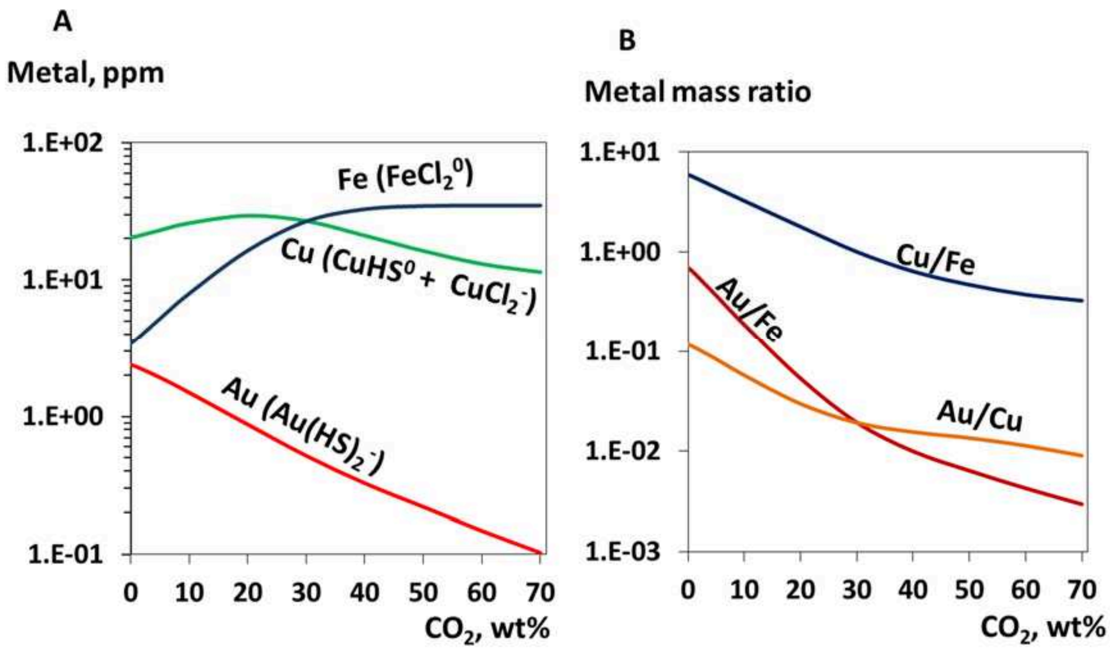

Fig. 16. Solubility of pyrite, chalcopyrite and native gold in supercritical fluids at 450°C and 2 kbar with 7 wt % (NaCl + KCl) and 1 wt% S, in equilibrium with graphite, as a function of CO_2 content (A), and the corresponding metal ratios in the fluid (B), predicted using the model from this study. The dominant metal species are indicated in (A). The fluid is assumed to be in equilibrium with the QMK assemblage. Oxygen fugacity is buffered by the graphite-CH_4-CO_2 equilibrium, which roughly corresponds to that of the quartz-fayalite-magnetite mineral buffer. These conditions simulate highly reducing and H_2S-rich fluids, such as produced during metamorphism of carboniferous shales hosting some orogenic gold deposits.

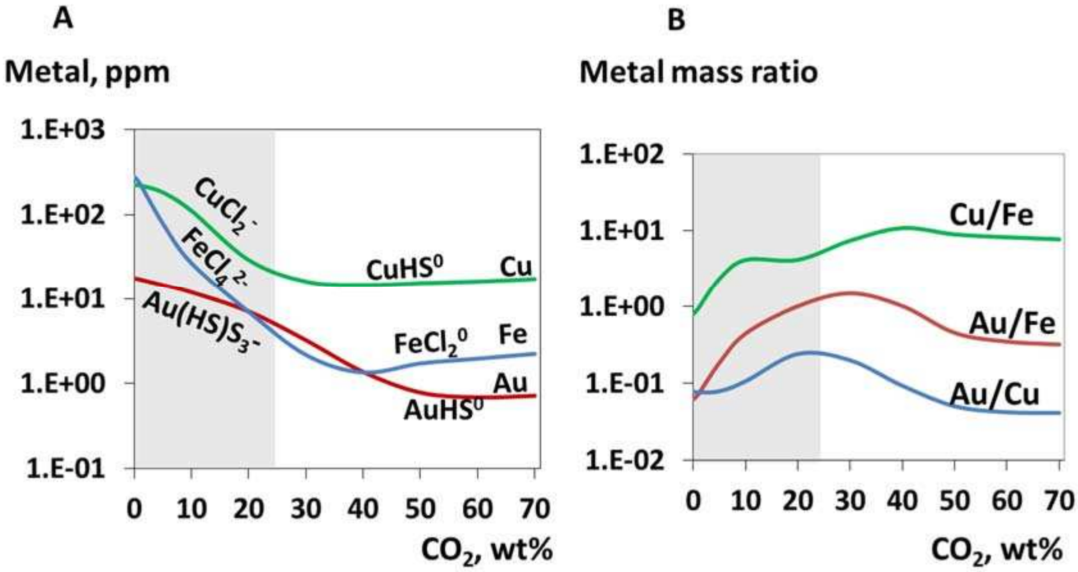

Fig. 17. Solubility of pyrite, chalcopyrite and native gold in supercritical fluids at 500°C and 1 kbar with 10 wt% NaCl and 1 wt% S (H_2S:SO_2 = 1) as a function of CO_2 content (A), and the corresponding metal ratios in the fluid (B), predicted using the model of this study. The dominant metal species are indicated in (A). Redox and acidity conditions are controlled by the QMK or QAK buffers (muscovite transforms into andalusite at 40 wt% CO_2). These conditions simulate the oxidizing S-rich fluids of magmatic origin from typical porphyry Cu-Au deposits. The gray region denotes the maximal range of CO_2 contents reported in such deposits.

Electronic annex EA1: Hydrothermal synthesis of PtS

Hydrothermal synthesis of platinum (II) sulfide (PtS) was performed in a titanium reactor at 450±5°C and 500±20 bar by reacting a fine powder of platinum metal and an aqueous solution of S + NaOH. We used titanium autoclaves (total volume ~20 cm3; grade alloy VT-8, described in main text), which were cleaned with 5 wt. % HNO_3 and passivated with 1 wt. % HNO_3 at 400°C and 500 bar for 48 hours. Temperature during the synthesis was controlled by an electrically heated oven. Pressure was estimated from the degree of the reactor filling with the solution (which is equivalent to the density) and using the PVT properties of the H_2O-NaCl-H_2S system (the SOWAT software for NaCl-H_2O, Driesner, T. and Heinrich, C., 2007), and Redlich-Kwong equation of state for H_2O-H_2S (Mix-Fluid software, Akinfiev, 1997, Akinfiev and Zotov, 1999)., which was used as an approximation of the experimental system in the absence of direct volumetric data or models for H_2O-S-NaOH system.

The HCh software package (Shvarov, 2008) was used to choose the optimal conditions for PtS synthesis, which occurs via the reaction: $Pt + H_2S = PtS + H_2$
It was found that PtS stable in near-neutral to basic solutions, while another Pt sulfide, PtS2 in acidic solutions, therefore, to avoid the formation of PtS_2, moderate amount of NaOH was added (0.1M NaOH).

The following reagents were used: platinum black powder ≤20 micron (≥ 99.97% trace metals basis, Sigma-Aldrich, CAS 7440-06-4; surface area ≥25 m^2/g), sulfur powder (99.98%, Sigma-Aldrich, CAS 7704-34-9), and 0.1 M NaOH in deionized water. A weight of 2.173 g of platinum powder and 0.411 g of sulfur powder was placed in the autoclave, together with 8.583 g of aqueous 0.1M NaOH solution. The autoclave was then closed and placed vertically in an oven (temperature gradient <3°C over the reactor height). The run duration was 11 days. Sometimes the autoclave was taken out of the furnace and shaken by hand.

The reactor was cooled by water during 30 min. The autoclave was opened and washed with deionized water to collect the solution and solid suspension. The beaker containing the wash solution was set aside to allow the solid particles to settle down during the period from 4 to 20 h. The remaining supernatant containing the finest particles was rejected, and the precipitate was kept for further treatment. Finally, the precipitate was washed in ethanol, centrifuged, and dried at 90°C for 12 hours in an oven.

SEM-EDS analyses revealed no differences between the sizes of the particles of platinum sulfide in the samples taken after 4 and 20 h of settling. The average particle size is 0.2 microns for both samples (Fig. EA1). Differences are observed only in the size of agglomerates, in which the particles stick together. Chemical composition of these samples corresponded to Pt:S = 1:1 stoichiometry. The synthesized solid was characterized by XRD analyses, which showed a well crystalline PtS (JCPDS card # 18-0972), without any other detectable impurity. The synthesized PtS powder was pressed into pellets and used in solubility experiments.

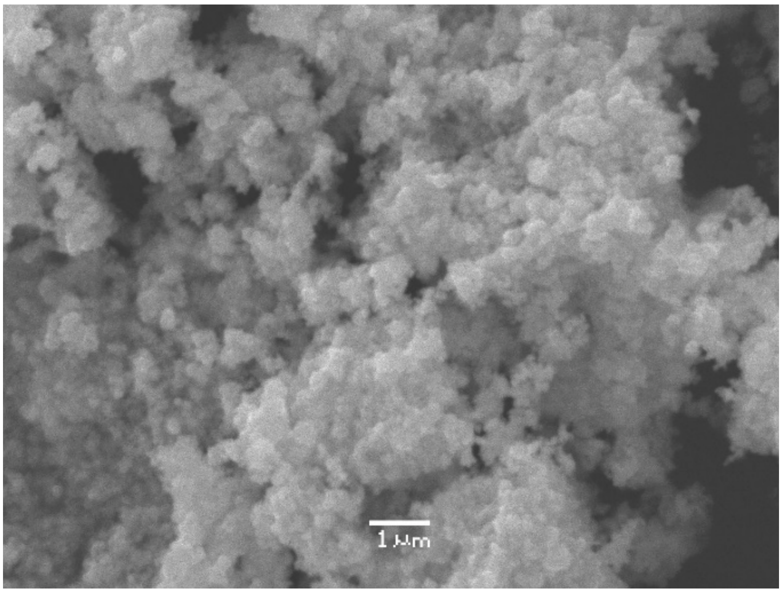

Fig. EA1. Scanning electron microscope photography (secondary electrons) of the synthesized PtS, sample after 4 hours of settling.

Electronic annex EA2: Table. Details of experimental solutions analyses.

Method	Elements/ isotopes/ species	Typical concentration range, ppb	Detection limit, ppb	Matrix composition
ICP-AES	Au	10 - 10 000	1-2	HNO_3 1.5 wt%,
	Cu	10 - 100	1-2	HCl 0.5 wt%
	Zn	7 - 450	2	
	Ti	30 - 750	1	
	Fe	30 - 4 500	5	
	K	10 - 100	10	
	S	1 000 - 10 000	50	
ICP-MS	^{197}Au	1 - 15	0.03	HNO_3 1.5 wt%,
	^{194}Pt ^{195}Pt	10 - 40	0.02	HCl 0.5 wt%
	^{95}Mo ^{97}Mo	100 - 400	0.02	
	^{118}Sn ^{120}Sn	100 - 1 500	0.02	
	^{63}Cu, ^{65}Cu	1 - 100	0.005	
	^{56}Fe, ^{57}Fe	30 - 100	0.02	
	^{47}Ti, ^{49}Ti	30 - 750	0.02	
Colorimetry	Si	1 000 -10 000	50	water
AAS	K	1 000 - 10 000	60	HNO_3 0.5 wt%
HPLC	Cl^-	1 000 - 50 000	100	water
	SO_4^{2-}	1 000 - 50 000	100	water
Iodometric titration	H_2S, HS^-, S_nS^{2-}, SO_2	60 000 - 1 500 000	10 000	HCl 10 wt%

Chapitre 4. L’effet du CO_2 et du soufre sur le fractionnement liquide-vapeur des métaux dans les systèmes hydrothermaux

4.1. Résumé de l'article: «Combined effect of carbon dioxide and sulfur on vapor-liquid partitioning of metals in hydrothermal systems» Kokh M.A., Lopez M., Gisquet P., Lanzanova A., Candaudap F., Besson Ph. and Pokrovski G.S soumis à *Geochimica and Cosmochimica Acta.*

Il est bien connu que la présence du CO_2 dans le système eau-sel favorise les phénomènes d'ébullition et de démixtion qui se passent couramment lors de l'évolution des fluides dans la croute terrestre, et que ce phénomène peut conduire à la formation des dépôts métallifères. Cependant, l'effet du CO_2 lui-même sur le comportement et le partage des métaux entre les phases liquide et vapeur dans ces systèmes demeure quasiment inconnu, faute de données expérimentales directes.

En utilisant des réacteurs hydrothermaux à séparation de phase que nous avons mis au point, nous avons effectué les premières expériences directes pour quantifier l'influence du CO_2 sur la distribution des différents métaux. Ces expériences ont été conduites dans le système modèle eau-sel-soufre-CO_2 à 350°C et des pressions de CO_2 allant jusqu'à ~100 bars, soit les conditions typiques de formation des dépôts de métaux en contexte magmatique-hydrothermal et métamorphique. En outre, en utilisant des cellules capillaires, nous avons effectué des mesures par spectroscopie Raman in-situ sur ces systèmes à deux phases dans des conditions similaires, pour déterminer la spéciation du soufre et du carbone dans la phase liquide et vapeur. Le système aqueux sans soufre contient NaCl, KCl et HCl (~15 wt% en sel) avec des teneurs plus faibles de $FeCl_2$, CuCl, Na_2MoO_4, du minéral SnO_2 (cassitérite) et de l'or Au et du platine Pt métals et un excès de magnétite et hématite pour tamponner la fugacité d'oxygène. Le système avec soufre contient KCl, HCl et $K_2S_2O_3$ avec les minéraux suivants: FeS_2 (pyrite), $CuFeS_2$ (chalcopyrite), MoS_2 (molybdénite), SnO_2 (cassitérite) et Au métal ainsi que un mélange de PtS_2 avec PtS, synthétisé à partir de poudres fines de Pt et S pressées en pastilles. Les fugacités de soufre et d'oxygène et l'acidité sont contrôlées par les équilibres entre le (bi)sulfate et le sulfure d'hydrogène en solution.

Les résultats montrent que, dans les systèmes sans soufre, dans une large gamme de concentration de CO_2 allant de 0 à 50 pds % en phase vapeur, les coefficients de partage vapeur-liquide des métaux ($K_{v/l} = C_{vap} / C_{liq}$, où C est la concentration massique du métal dans la phase vapeur ou liquide) sont dans les gammes suivantes: 10^{-6} à 10^{-5} pour Mo, 10^{-4} à 10^{-3} pour Na, K, Cu, Fe, Zn, Au, 10^{-3} à 10^{-2} pour Si et 10^{-4} à 10^{-1} pour Pt. Avec l'augmentation de CO_2 de 0 à 50 wt%, ces valeurs diminuent légèrement pour Fe, Cu et Si (moins d'un demi ordre de grandeur), restent constantes dans les limites des incertitudes pour Na, K et Zn, ou augmentent de ~ 0.5 et 2 ordres de grandeur, respectivement pour Au et Pt. Dans les systèmes riches en soufre, avec des teneurs de H_2S de 0.1 à 1.0 wt% dans la phase vapeur, les valeurs de $K_{v/l}$ de Cu, Fe, Mo et Au sont dans la gamme de 0.01 à 0.1, celles de Pt de 0.5 à 2, et celles des métaux alcalins sont similaires dans les deux systèmes, avec et sans soufre. Dans le système soufré, les coefficiants de partage d'aucun des métaux étudiés ne sont influencés par la présence du CO_2 (jusqu'à 50 wt% dans la phase vapeur).

Nos données confirment l'augmentation de la volatilité des métaux en présence du soufre réduit (H_2S) pour les métaux chalcophiles tels que Au, Pt, Mo et, dans une moindre mesure, Cu et Fe, ce qui a été déjà rapporté dans des études précédentes des systèmes eau-sels sans CO_2. En revanche, nos données révèlent un effet direct faible ou négligeable de CO_2 sur la distribution entre les phases vapeur et liquide des métaux étudiés. La seule exception est le platine dans le système eau-sels-CO_2 sans soufre, dont le coefficient de partage vapeur-liquide est largement augmenté (jusqu'à 2 ordres de grandeur par rapport à un système sans CO_2) en présence du CO_2, probablement en raison de la formation de complexes chlorures-carbonyles volatils, connus pour ce métal en conditions ambiantes.

Outre le platine qui nécessite une étude plus systématique aux hautes températures et pressions, notre travail démontre que la présence du CO_2 affecte l'évolution du fluide et le fractionnement des métaux principalement de manière indirecte, par l'extension du domaine d'immiscibilité vapeur-liquide à des températures et pressions plus élevées par rapport à un système H_2O-S-sel. Ceci engendre un fractionnement plus efficace des métaux chalcophiles (Au, Pt, Mo, ± Cu) dans la phase vapeur et la concentration des métaux alcalins et de base (Na, K, Fe, ± Cu) dans le liquide riche en sel. Cette séparation précoce vapeur-liquide en présence de CO_2 va à la fois augmenter la profondeur du dépôt de minerais et affecter la zonation verticale des métaux dans les systèmes hydrothermaux. Ces phénomènes doivent être pris en compte dans l'exploration des gisements.

Combined effect of carbon dioxide and sulfur on vapor-liquid partitioning of metals in hydrothermal systems

Maria A. Kokh, Mathieu Lopez, Pascal Gisquet, Aurélie Lanzanova, Frédéric Candaudap, Philippe Besson, Gleb S. Pokrovski*

Groupe Métallogénie Expérimentale, Géosciences Environnement Toulouse (GET), UMR 5563, Observatoire Midi-Pyrénées, Université de Toulouse, Centre National de la Recherche Scientifique (CNRS), Institut de Recherche pour le Développement (IRD), 14 avenue Edouard Belin, F-31400 Toulouse, France

* Corresponding author: phone: (33)-(0)5-61-33-26-18; fax: (33)-(0)5-61-33-25-60;

e-mail: gleb.pokrovski@get-obs-mip.fr; glebounet@gmail.com

Submitted to Geochimica et Cosmochimica Acta

21 December 2015

Abstract

Although CO_2 is a ubiquitous volatile in geological fluids and vapors, its effect on metal vapor-liquid fractionation during fluid boiling and immiscibility phenomena in the Earth's crust remains virtually unknown. Here we conducted first experiments to quantify the influence of CO_2 on the partitioning of different metals in model water+salt+sulfur+CO_2 systems at 350°C and CO_2 pressures up to 100 bar, which are typical conditions of formation of many hydrothermal ore deposits. In addition, we performed in situ Raman spectroscopy measurements on these two-phase systems at similar conditions, to determine sulfur and carbon speciation in the liquid and vapor phases. Results show that, in S-free systems and across a CO_2 concentration range of 0–50 wt% in the vapor phase, the absolute vapor-liquid partitioning coefficients of metals ($K_{vap/liq} = C_{vap}/C_{liq}$, where C is the mass concentration of the metal in the corresponding vapor and liquid phase) are in the range 10^{-6}–10^{-5} for Mo; 10^{-4}–10^{-3} for Na, K, Cu, Fe, Zn, Au; 10^{-3}–10^{-2} for Si; and 10^{-4}–10^{-1} for Pt. With increasing CO_2 from 0 to 50 wt%, $K_{vap/liq}$ values decrease for Fe, Cu and Si (by less than one order of magnitude), remain constant within errors (±0.2 log unit) for Na, K and Zn, and increase by 0.5 and 2 orders of magnitude, respectively for Au and Pt. The negative effect of CO_2 on the partitioning of some metals is due to weakening of hydration of chloride complexes of some metals (Cu, Fe) in the vapor phase and/or salting-in effects in the liquid phase (Si), whereas both phenomena are negligible for complexes of other metals (Na, K, Zn, Mo). The only exception is Pt (and in a lesser extent Au), which partitions significantly more to the vapor of S-free systems in the presence of CO_2, likely due to formation of volatile carbonyl (CO) complexes. In the S-bearing system, with H_2S content of 0.1–1.0 wt% in the vapor, $K_{vap/liq}$ values of Cu, Fe, Mo, and Au are in the range 0.01–0.1, those of Pt 0.5–2.0, those of alkali metals are similar to the S-free system, and the partitioning of none of the studied metals is influenced by the presence of CO_2 (up to 50 wt% in the vapor). Our data thus confirm the large enhancement of volatility in the presence of reduced sulfur (H_2S) due to formation of sulfide complexes for chalcophile metals such as Au, Pt, Mo and, to a lesser extent, Cu and Fe, as reported in previous studies of CO_2-free water-salt systems. The negligible effect of CO_2 on vapor-liquid partitioning of the studied metals in S-bearing systems is due to the lack of hydration of metal sulfide species making them little sensitive to changes in water activity and solvation properties of CO_2-H_2O vapor. Thus, CO_2 is expected to exert an indirect impact on fluid evolution and metal fractionation, by extending vapor-liquid immiscibility to higher temperatures and pressures or depth compared to a CO_2-free H_2O-S-salt system. The deeper vapor-liquid separation, in particular in S-bearing systems, will cause more efficient partitioning of chalcophile metals (Au, Pt, Mo, ±Cu) into the vapor phase and concentration of alkali and base metals and chloride (Cl, Na, K, Fe, ±Cu) into the salt-rich liquid phase. In addition, irrespective of the presence of sulfur, an expansion of the immiscibility domain to higher temperature and pressure conditions in the presence of CO_2 will also increase the depth of ore deposition and affect the vertical metal zonation in hydrothermal systems.

Key-words: Carbon dioxide; sulfur; metals; fluid; vapor; vapor-liquid partitioning; immiscibility.

1. INTRODUCTION

Fluid boiling and vapor-liquid immiscibility are ubiquitous phenomena occurring during the formation of most magmatic-hydrothermal and metamorphic ore deposits, as well as in active volcanic-geothermal systems on Earth. These phenomena are controlled by the physical-chemical properties of geological fluids containing water, salts and volatiles (e.g., S, C) that allow for the coexistence of the vapor and liquid phases across the wide range of temperatures (T), pressures (P), and fluid compositions of the Earth's crust (e.g., Hedenquist and Lowenstern, 1994; Barnes, 1997; Heinrich, 2007). Fluid immiscibility has two fundamental effects on the fate of metals that are carried by the fluid. First, it is known to induce precipitation of some metals from the liquid phase owing to enhanced metal concentration and changes in the acidity, redox, and ligand content in the residual liquid as a result of the removal of volatile components (H_2S, H_2, HCl, CO_2) into the vapor (e.g., White, 1973; Spycher and Reed, 1989; Drummond and Ohmoto, 1985). Second, it may cause metal re-distribution between the two phases, with selective partitioning of some metals (e.g., Au, Pt ±Cu) into the vapor (e.g., Heinrich et al., 1992, 1999; Pokrovski et al., 2005, 2008; Seo and Heinrich, 2013). The goal of this study is to better understand the role of CO_2, the most common volatile in geological fluids, on metal behavior during immiscibility processes.

Fluid inclusions from a variety of mineralized systems, from magmatic to epithermal, record the ubiquitous presence of CO_2 in fluids, which underwent boiling/unmixing phenomena presumably leading to ore deposition. For example, these data show that CO_2 concentrations in fluids that formed metamorphic Au and skarn Cu-Au deposits, and mafic pegmatite-hosted Cu-PGE deposits often attain 40-50 wt% and, locally, more than 95 wt% CO_2 in vapor or liquid phases observed in fluid inclusions (Schmidt Mumm et al., 1997; Boiron et al., 2003; Phillips and Evans, 2004; Hanley and Gladney, 2011; Garofalo et al., 2014). Fluids of magmatic-hydrothermal porphyry Cu-Au-Mo deposits show up to 10-20 wt% CO_2 (Rusk et al., 2008, 2011), and those of epithermal Au-Ag-Cu and Carlin-type Au deposits systematically contain 1-10 wt% CO_2 (e.g., Bodnar et al., 1985; Koděra et al., 2005; Catchpole et al., 2011). Fluids and vapors enriched in CO_2 in these environments can carry significant concentrations of metals such as As, Cu, Au, Pd, reaching 10s to 100s ppm, as shown by the rapidly growing body of fluid inclusion compositional data (e.g., Hanley and Gladney, 2011; Garofalo et al., 2014; Rauchenstein-Martinek et al., 2014). Furthermore, these fluid-inclusion records show that metal deposition is systematically related to fluid boiling or unmixing phenomena, leading to the formation of CO_2-rich vapor phases. Nevertheless, despite the ubiquitous presence of CO_2 in hydrothermal systems, its fundamental role on metal behavior during fluid evolution remains largely unknown or, to the least, controversial.

On one hand, it is well known that the fluid immiscibility domain in the water(-salt) system is largely extended in *T-P* space in the presence of CO_2 (e.g., Takenouchi and Kennedy, 1964; Bowers and Helgeson, 1983; Lowenstern, 2001; Bakker, 2009). In this process, CO_2 is usually considered as an inert component, following the very low capacity of CO_2-dominated, as compared to H_2O-dominated supercritical fluids or vapors to solubilize ionic compounds such as salts (e.g., NaCl; Zakirov et al., 2007) and metal oxides (e.g., SiO_2, Newton and Manning, 2009; references therein), whose solubility is driven by hydration (e.g., Pokrovski et al., 2013). On the other hand, supercritical (>31°C) CO_2 is also known as an efficient solvent for certain organic compounds and thiol and phosphoryl complexes of metals, a property used in industry for purification of organics and metal extraction from aqueous solution (e.g., Glennon et al., 1999; Erkey, 2000; Yang et al., 2010). It remains hypothetical, however, whether a similar solvation phenomenon may operate in natural vapor-liquid systems for metals forming sulfide complexes (e.g., Pokrovski et al., 2008). Compared to water-salt-sulfur vapor-liquid and fluid-melt systems, for which a large amount of experimental data and robust models on vapor-liquid partitioning of various metals has been acquired in the past 10 years (see Simon and Ripley, 2011; Pokrovski et al., 2013 for recent reviews), there are only few direct data on metal vapor-liquid partitioning in the presence of CO_2. For example, Webster et al. (1989) reported partitioning coefficients of a large set of lithophile elements (ranging from Li to U) between a fluid and a topaz rhyolite melt at 800-950°C and 2 kbar systematically decreased by a factor of 5–10 with increasing CO_2 content to ~50 mol% in the fluid. More recently, Tattich et al. (2015) measured Cu distribution in a S-free felsic melt-brine-vapor system at 900°C and 1 kbar in the presence of up to 40 mol% CO_2 in the vapor, and detected a moderate decrease (by a factor of <5) in Cu vapor-brine and fluid-melt partitioning coefficients with increasing CO_2 content. Rempel et al. (2008) studied vapor-liquid distribution of Na, Cu, Zn and Fe between a dilute aqueous solution and a CO_2 vapor at 60°C and up to 160 bar, at conditions relevant to CO_2 geological storage, and did not detect any effect of CO_2 within the data scatter. In between these contrasting *T-P* regimes of sedimentary and magmatic settings, lies a vast domain of hydrothermal vapor-liquid systems, which have not been covered yet by direct experimental work.

To fill this gap, in this study we carried out first direct measurements of the vapor-liquid partitioning of a large set of metals (Na, K, Fe, Cu, Zn, Si, Sn, Au, and Pt) in the water-salt(-sulfur) systems in the presence of CO_2 at 350°C, which is the typical temperature of fluid boiling and vapor-liquid separation phenomena in most types of ore deposits in the Earth's crust. Our results show that the presence of CO_2 may exert contrasting effects on vapor-liquid distribution of metals, depending on the element nature and speciation, and the concentration of reduced sulfur (H_2S) in the system. Furthermore, our findings point that CO_2-rich and H_2S-bearing vapors have significant capacities, comparable to those of water-dominated systems, to transport S-loving metals.

2. MATERIALS AND METHODS

2.1. Experimental systems and conditions

In the face of the extremely variable and complex chemistry of high-temperature brine-vapor systems, in particular in the presence of sulfur and CO_2, this exploratory experimental study was primarily designed to identify major trends in the vapor-liquid partitioning of different economically important metals as a function of CO_2 and sulfur contents in the system. No attempt has been done to derive the exact stoichiometry and thermodynamic properties of particular metal complexes in the vapor phase.

Multi-element experiments were performed in a specially designed batch reactors (see below) at 350°C and at the two-phase vapor-liquid equilibrium curve of two types of systems, S-free and S-bearing. The S-free system H_2O-KCl-NaCl-HCl contains minor amounts of soluble $FeCl_2$, $ZnCl_2$ and CuCl and Na_2MoO_4 and an excess of solid phases of SnO_2 and metallic Au and Pt (Table 1). Oxygen fugacity (f_{O_2}) and solution acidity (pH) were imposed, respectively, by an excess of magnetite-hematite mineral assemblage and by addition of HCl. The S-bearing system H_2O-KCl-$K_2S_2O_3$-HCl contains an excess of sulfide, oxide or native minerals such as FeS_2, $CuFeS_2$, native Au, PtS_2, MoS_2, and SnO_2 (Table 2). Details about the sources and compositions of the solids used are reported in Kokh (2016). Potassium was preferred to sodium as salt content because of higher solubility of K_2SO_4 than Na_2SO_4 at elevated temperatures (Pokrovski and Dubessy, 2015). Both S-free and S-bearing experimental systems represent a good proxy for natural fluids in arc-related magmatic–hydrothermal systems hosting porphyry Cu-Au-Mo deposits, which are characterized by acidic pH and the coexistence of sulfate-sulfide and magnetite-magnetite minerals (Einaudi et al., 2003; Kouzmanov and Pokrovski, 2012). Furthermore, the S-bearing system imposes sulfur balance through breakdown of thiosulfate to sulfate and sulfide that enables f_{O_2} and pH buffering via sulfide-sulfate and sulfate-hydrogen sulfate equilibria (Jacquemet et al., 2014; Pokrovski and Dubessy, 2015), which may be quantified using thermodynamic modeling (see below).

Pure CO_2 (99.999 %) was periodically injected in the reactor during the course of experiments via a high-pressure calibrated manual pump. Metal concentrations in the liquid phase are controlled by dissolution of oxide, sulfide or native metal solids, which may be rather sluggish at moderate temperatures (<400°C). Consequently, caution was taken when comparing the measured liquid-phase concentrations in short runs (<1 week) with those from thermodynamic predictions of fluid-mineral equilibria. In contrast, vapor-liquid equilibrium for all studied metals, carbon and sulfur species is expected to be attained within a few hours after the temperature-pressure stabilization. This was demonstrated by the constancy of the vapor-liquid partition coefficients in subsequent samples versus time and agrees with the rapid vapor-liquid equilibration reported in many previous studies both in S-free and S-bearing systems using similar experimental designs (e.g., Hovey et al., 1990; Pokrovski et al., 2002, 2005, 2008; Shmulovich et al., 2002; Foustoukos and Seyfried, 2007a; Liebscher, 2007; Pester et al., 2015). Thus, it is believed that the vapor-liquid partition data obtained in our experiments may be interpreted using equilibrium thermodynamics.

2.2. Hydrothermal reactor and experimental procedure

Sulfur- and CO_2-rich vapor-liquid multi-component systems at elevated temperatures and pressures represent a formidable experimental and analytical challenge for accurate measurement of metal concentrations. The major difficulties are i) the low concentrations of some poorly soluble metals (e.g., Sn, Mo, Pt, Au) in both phases requiring very sensitive analytical techniques and accurate sample preservation and treatment, ii) the frequent precipitation during sampling of sulfur and metal sulfides, which are poorly soluble at low temperatures, and iii) a risk of contamination during sampling or quenching of the vapor-phase samples of generally low metal concentrations (ppb to ppm) by the highly concentrated brine (hundreds to thousands ppm).

To overcome these intrinsic difficulties, we used a modified version of the hydrothermal reactor used earlier (Pokrovski et al., 2008), equipped with two sampling lines for ultra-rapid multiple extractions of coexisting vapor and liquid phases, independently during the experimental run. Each line consists of a 2-µm Ti frit-filter fixed in the head and bottom of the reactor, high-pressure (HP) titanium capillary (6.35 and 1.80 mm of external and internal diameter, respectively), two HP titanium valves (Top Industrie) and a rigid titanium ampoule (~3 cm^3 internal volume) tightly attached to the second valve via a Teflon seal (Fig. 1). Opening the two valves leads to almost instantaneous (<1 s) transfer of a portion of the liquid or vapor phase pushed by the internal pressure from the reactor into the ampoule. The fast fluid sampling efficiently precludes any precipitation inherent to sulfide systems during the fluid transfer from the hot reactor to ambient conditions. Subsequently, the second valve with the ampoule is disconnected, cooled down, weighed, and the condensate from the ampoule analyzed for metals, sulfur, chloride and CO_2 (see section 2.3). The sampling ampoule was always found to be full of condensate demonstrating that no degassing, boiling or loss occurs during sampling of both liquid and vapor, and that the complete transfer of the dissolved content was achieved. Furthermore, because the fluid extraction is conducted under pressure, it allows accurate sampling and quantification of CO_2 and volatile sulfur (H_2S), which have tendency to escape from solution if sampled under atmospheric pressure.

Two lines allowing subsequent extractions of each phase (Fig. 1) were assembled to a large-volume (~400 cm^3) titanium (Ti grade 2) reactor, capable of operating up to 370°C and 500 bar. The use of two independent vapor and liquid sampling lines avoids any contamination of the low-concentrated vapor (typically 1-100 ppb of metal) by the highly concentrated liquid (10-1000 ppm). The autoclave was loaded with experimental solution and solids and placed in a vertical furnace (~80 cm height) whose temperature was maintained within ±0.2°C by two electrical heating resistances independently regulated by a Eurotherm programmer and K-type thermocouples. The temperature gradients were less than 5°C across the reactor length (~30 cm). Pressure was measured periodically through the vapor sampling line using commercial pressure transducers calibrated against the saturated pressure of pure water vapor. Experiments were started in the two-phase domain with sufficient quantities of the liquid and vapor phase formed at the experimental temperature (typically 80-120 and 20-30 g, respectively); this allows multiple samples of both phases. During each sampling session, the vapor was sampled first followed by the liquid. Pressure decrease induced by extraction of a vapor portion typically was less than 2-3 bars, which is too small to affect significantly the metal, salt, and volatile concentrations in the coexisting liquid. Consequently, each vapor-liquid pair may be considered as isobaric.

2.3. Chemical analyses of metals, sulfur, and CO_2

The chemical complexity of the multi-element experimental systems, and instability of the extracted condensates yielding rapid precipitation of poorly soluble metal sulfides, gold and sulfur at ambient temperature, required combination of various treatment procedures and analyses for quantifying solute concentrations. Multiple samples (usually 3 to 4) of vapor and liquid were directly taken into different aqueous matrixes (I_2, NH_3, HCl, Cd-acetate) placed in the sampling ampoule to allow for trapping, preservation and analyses of the different forms of sulfur, bulk metal concentrations and CO_2 (see Kokh, 2016 for details). Briefly, concentrations of K, Fe, Ti, Cu, Mo, Sn, Pt, and Au were determined by Inductively Coupled Plasma Mass Spectrometry (ICP-MS) and/or Inductively Coupled Plasma Atomic Emission Spectrometry (ICP-AES) and, selectively, by flame Atomic Absorption Spectrometry (AAS), after the sample treatment with aqua regia. Total chloride was quantified (as the Cl^- ion) by high-pressure liquid chromatography (HPLC). Total dissolved sulfur was analyzed by both ICP-AES and HPLC (as the SO_4^{2-} ion) after complete oxidation to sulfate in NH_3-H_2O_2 solutions. Both methods for S showed an agreement within 10% of the total concentration value. Total reduced sulfur (dominant hydrogen sulfide, and potentially sulfite and polysulfides) was quantified by iodometric titration. Hydrogen sulfide (H_2S/HS^-) was separated from the other sulfur forms by precipitation as Cd sulfide followed by iodometric titration. Carbon dioxide in condensates trapped in the sampling ampoule was quantified by weight loss after complete gentle degassing of the ampoule. This procedure was found to be accurate within better than ±0.1 wt% for the CO_2 contents in this study.

2.4. Raman spectroscopy measurements

To verify the validity of our analytical protocols for sulfur and CO_2 in sampled condensates and to check for the presence of sulfur or carbon species (e.g., S_8, COS, CO, SO_2, S_3^-) that are not directly detected by the available analytical techniques, we used in situ Raman spectroscopy on two model H_2O-$K_2S_2O_3$-HCl±CO_2 systems closely matching the compositions of our hydrothermal reactor experiments. The aqueous solution and CO_2 were loaded in a round cross-section silica-fused capillary tubing (of 323 µm external and 100 µm internal diameter) using the recently developed protocols (Caumon et al., 2013; Dargent et al., 2013) The capillary that contains an aqueous solution and a vapor phase is sealed with oxygen-hydrocarbon flame at both ends, and brought to the desired temperature (350°C) on a heating stage (CAP-500 Linkam®). Raman spectra were obtained at the GeoRessources Laboratory (Nancy, France) with a LabRam HR spectrometer (Jobin Yvon Horiba®), using 457.9 nm Ar^+ laser excitation (~1-2 µm spot size on the sample), from the liquid and vapor phases in a backscattering geometry using an Olympus ×20 objective, a 1800 lines/mm grating, an entrance slit of 200 µm, and a confocal hole of 500 µm (spectral resolution ~3-5 cm^{-1}). The spectrometer was calibrated using the Raman stretching vibrations of a Si wafer (520.7 cm^{-1} at 20°C), and oxygen (1555 cm^{-1}) and nitrogen (2331 cm^{-1}) gas from the air (Dubessy et al., 2012). Because of the absence of standards for each sulfur and carbon species closely matching the experimental solutions, quantification of the species concentrations is not possible; the spectra were only used for identification purposes and comparisons of relative abundances of some dominant species based on their peak areas (e.g., SO_4^{2-} vs HSO_4^-; H_2S(vap) vs H_2S(aq)).

2.5. Thermodynamic calculations

Metal, sulfur and carbon chemical speciation and solubility were simulated via equilibrium thermodynamic calculations and compared with experimental data. Modeling was performed using the HCh software package (Shvarov, 2008) based on the minimization of the Gibbs free energy in multicomponent and multiphase systems. Due to limitations of the HCh application to aqueous vapor-liquid systems, the absence of accurate PVTX properties of the H_2O-NaCl-KCl-$KHSO_4$-H_2S-CO_2 two-phase systems, and the lack of thermodynamic data on vapor-liquid partitioning of volatiles and vapor-phase species of metals, no quantitative calculations of vapor-liquid equilibria could be done. In contrast, solid-liquid equilibria can be modelled using the salt and volatile (CO_2, H_2S) contents directly measured in our experiments.

The sources of thermodynamic properties of the system constituents are detailed elsewhere (Pokrovski and Dubessy, 2015; Pokrovski et al., 2015; Kokh et al., 2016), and only briefly overviewed below. The thermodynamic properties of the major fluid constituents and most aqueous carbon and sulfur species were taken from the updated SUPCRT database (Johnson et al., 1992; Sverjensky et al., 1997), complemented by more recent data for some ion pairs, polysulfides, and neutral volatile sulfur species (Akinfiev and Diamond, 2003; Pokrovski and Dubessy, 2015; references therein). Activity coefficients (γ_i) of charged species in aqueous solution were calculated using the extended Debye-Hückel equation; those for neutral species (except for silicic acid, see below) were assumed to be equal to 1 owing to a lack of Setchenov coefficients for such species in high-temperature brines (Pokrovski et al., 2008).

Stability constants for aqueous Fe chloride species were taken from Sverjensky et al. (1997) and Testemale et al. (2009), Cu and Au species (with chloride, hydroxide, hydrogen sulfide, and trisulfur ion ligands) from Akinfiev and

Zotov (2010) and Pokrovski et al. (2015), respectively. These compilations are based on extensive experimental data; they are in reasonable agreement with other recent sets of HKF parameters for some of those species (e.g., Brugger et al., 2007; Rauchenstein-Martinek et al., 2014). Other Au species with hydrogen sulfide ligands tentatively suggested in acidic S-rich solutions such as $Au(HS)H_2S^0$ (Pokrovski et al., 2009a; references therein) and $Au(HS)(H_2S)_3{}^0$ (Loucks and Mavrogenes, 1999) were not included in the modeling due to large inconsistencies in the data.

Thermodynamic properties for the Pt^{2+} cation and Pt^{II} chloride ($PtCl_{1\text{-}4}$) complexes were taken from the recent compilation of literature data by Tagirov et al. (2015) complemented by their own Pt solubility measurements at 400-475°C and 1 kbar, whereas hydroxide ($Pt(OH)_{1\text{-}2}$) and sulfate ($Pt(SO_4)_{1\text{-}3}$) complexes were adopted according to the HKF model predictions of Sassani and Shock (1998) based on ambient temperature data. Both data sources are in reasonable agreement with independent earlier estimations of Wood et al. (1992). Stability constants for Pt hydrogen sulfide complexes with a tentative stoichiometry $Pt(HS)_2{}^0$ were adopted from Pan and Wood (1994) and Wood et al. (1994) and regressed using the Ryzhenko-Bryzgalin model (Shvarov, 2015).

Thermodynamic data for aqueous Mo are rare and far less consistent than those for Fe, Cu and Au. In this study, we chose the HKF set of parameters for $MoO_4{}^{2-}$ from Shock et al. (1997), its protonation constants with formation of $HMoO_4{}^-$ and $H_2MoO_4{}^0$ from Minubaeva and Seward (2010), and those for the $KHMoO_4{}^0$ ion pair from Zotov et al. (1995). Although alternative speciation schemes for Mo were proposed in saline (NaCl, KCl) aqueous fluids and HCl vapors (e.g., Ulrich and Mavrogenes, 2007; Rempel et al., 2008), with the formation of oxy-chlorides (e.g., MoO_2Cl_2, MoO_2Cl^+) rather than alkali metal ion pairs, the data are either very scattered or beyond our investigated *T-P* range. The effect of reduced sulfur on Mo speciation remains unclear according to the few available studies; for example Zotov et al. (1995) did not detect sulfide complexes in H_2S-bearing solutions at 350-450°C, whereas Zhang et al. (2012) suggested Mo oxy-sulfide-alkali complexes at 600-800°C in fluids buffered by iron sulfide mineral assemblages. In view of such discrepancies, we ignored both chloride and sulfide complexes in the modeling. Our calculations suggest that $HMoO_4{}^-$ ion pairs with K^+ or Na^+ to be the dominant species in the liquid phase of our experiments.

Thermodynamic properties of dissolved silicic acid, $Si(OH)_4{}^0$ or $SiO_2{}^0$ (which are equivalent thermodynamic notations for H_2O-dominated solutions) and its dimer, $Si_2O_4{}^0$ or $Si_2O(OH)_6{}^0$, were taken from Sverjensky et al. (2014); they predict about 65% of total dissolved silica in equilibrium with quartz to be in the form of monomer at our conditions. Older thermodynamic data sets for silicic acid (e.g., Jonhson et al., 1992; Stefánsson, 2001) that are based on a similar quartz solubility experimental data set but ignore the dimer species, predict identical total Si concentrations (within ±0.05 log units) in equilibrium with quartz in pure water. Setchenov coefficients for dissolved silica available in NaCl-KCl solutions (Foustoukous and Seyfried, 2007b; references therein) imply slightly higher (by about 0.1 log unit) solubilities compared to pure water at our experimental conditions.

Thermodynamic data on aqueous Sn(II) and Sn(IV) species such as chlorides, hydroxides, hydroxy-chlorides, and (bi)carbonates in a wide range of *T-P* were adopted from the compilation of Ryzhenko et al. (1997), which is likely to be the most complete one and globally consistent with earlier estimations for selected species within more limited *T-P* ranges (e.g., Jackson and Helgeson, 1985; Heinrich, 1990; references therein). The available thermodynamic data suggest that $Sn(OH)_4{}^0$ is by far the dominant species in the liquid phase, but its absolute concentrations in equilibrium with cassiterite may have uncertainties of 1 to 2 log units. (Bi)carbonate species of Sn are predicted to be negligible in our CO_2-bearing solutions.

Thermodynamic properties for ideal gas carbon and sulfur species (CO_2, CO, CH_4, HCl, H_2S, SO_2, $S_{2\text{-}8}$, $H_2S_{2\text{-}6}$) and major sulfide and oxide minerals were adopted from well-known published compilations (e.g., Naumov et al., 1974; Robie and Hemingway, 1995; Chase, 1998). Variations of their standard Gibbs free energies between different original sources are too small (less than a few kJ/mol) to affect significantly the volatile species vapor-liquid distribution and mineral solubility in the liquid phase. No attempt was done to directly model metal speciation in the vapor phase because of the extreme scarcity of available thermodynamic data and the absence of adequate models, in particular in CO_2-rich systems. However, some qualitative conclusions about major ligands complexing metals in the vapor phase will be done based on trends in vapor-liquid partition coefficients and the simulated species distribution and amounts in the liquid phase.

3. RESULTS

3.1. Liquid-phase solubility and speciation of metals and volatiles

3.1.1. Sulfur-free system

Alkali metals (K and Na), base metals (Zn, Cu and Mo), and chloride in the S-free experiments show a steady increase in their liquid-phase concentrations relative to the initially loaded solution (~50% of the value by the last sampling session), in agreement with elemental partitioning into the liquid phase whose volume decreases at each sampling, and as controlled by mass balance of the water content in a close reactor. This trend also indicates that the liquid remains under-saturated with respect to any solid phase of these elements.

Iron concentrations increase by almost a factor of two with increasing total salinity from the beginning to the end of the sample series (Table 1; Fig. 2a), in quantitative agreement with the concentrations predicted from equilibrium with the hematite-magnetite (HM) assemblage, using the stability constants of Fe(II) chloride complexes selected above (section 2.5; Fig. EA1). Noteworthy, if equilibrium is assumed only with hematite which is a mineral more reactive than magnetite at moderate temperatures (e.g., Saunier et al., 2011), the predicted Fe concentrations in our acidic solutions differ by less than 30% of the value (Fig. EA1). This difference is within the uncertainties of the thermodynamic constants themselves, and thus is not big enough to be conclusive as to the establishment or not of redox equilibrium between iron oxide minerals and aqueous solution in this run.

Gold concentrations vary from 6-7 ppm in CO_2-free liquid-phase samples to 0.4-0.7 ppm in CO_2-rich samples. In contrast, assuming equilibrium with Au metal and an oxygen fugacity value buffered by Fe_2O_3-Fe_3O_4, thermodynamic calculations predict Au concentrations of 2 to 3 log units lower (~0.02 ppm, Fig. EA1) with $Au(OH)^0$ and $AuCl_2^-$ as the dominant species according to the reactions:

$$Au_{(s)} + 2\ Cl^- + H^+ + 0.25\ O_2 = AuCl_2^- + 0.5\ H_2O \quad (1)$$

$$Au_{(s)} + 0.5\ H_2O + 0.25\ O_2 = Au(OH)^0 \quad (2)$$

The differences among the major thermodynamic data sources for these Au complexes (e.g., Stefánsson and Seward, 2003; Pokrovski et al., 2014; Rauchenstein-Martinek, 2014) are too small to account for this discrepancy. Inclusion of additional species such as gold chloride alkali metal ion pairs evoked from molecular dynamics simulations ($NaAuCl_2$ and $KAuCl_2$, Mei et al., 2014) increases the predicted solubility by only a factor of 2. The potential presence of carbonate or other C-bearing complexes of Au (even though unlikely from a chemical point of view), should further increase its solubility, which disagrees with the decrease with addition of CO_2 observed experimentally (Fig. EA1). Thus, the most plausible explanation for the elevated measured Au concentrations and for their decrease in the course of the experiment is incomplete redox buffering by the HM assemblage that did not allow attainment of equilibrium between Fe_2O_3 and Fe_3O_4 within the limited time (few weeks) of our moderate-temperature runs. This hypothesis is confirmed by thermodynamic calculations performed omitting magnetite from the system, which predicted an f_{O2} value several orders of magnitude higher than that of HM, and ~10s ppm of Au in the fluid, which is close to the Au concentrations measured in the first samples (Fig. EA1). With time, this oxygen was progressively consumed by magnetite leading to the observed decrease in Au solubility. Note, however, that sluggishness of mineral redox reactions in this experiment has no consequences for the interpretation of vapor-liquid partitioning as this is much faster and thus very likely corresponds to equilibrium at each sampling point (see section 2.1).

Platinum liquid-phase concentrations decrease from ~200 to ~1 ppb with time, similarly to Au, while equilibrium thermodynamic calculations assuming f_{O2} buffering by HM yield ~1 ppb in the form of $PtCl_3^-$, independently of the CO_2 content. As for gold, this pattern may be plausibly explained by a deficiency of the HM redox equilibrium at early stages of the experiment with elevated f_{O2}, resulting in high Pt solubility according to the reaction:

$$Pt(s) + 3Cl^- + 2H^+ + 0.5\ O_2 = PtCl_3^- + H_2O \qquad (3)$$

It was only after 1–2 weeks of the run that Pt solubility seemed to have approached the predicted equilibrium values (Fig. EA1). Note, however, that the predicted Pt concentrations may have uncertainties of 1 to 2 log units due to discrepancies among the scant available data on Pt-Cl stability constants (see Tagirov et al., 2015, and section 2.5), so that the agreement may be fortuitous.

Silica experimental concentrations measured in the liquid phase are identical (within <0.05 log units) to those predicted in pure water in equilibrium with quartz and using the thermodynamic data for $Si(OH)_4$ and its dimer. The effect of salinity (NaCl-KCl) at our experimental compositions that may be estimated using reported Setchenov coefficients for aqueous silica is within 0.1 log unit of the total Si concentration (Fig. EA1).

Tin measured concentrations are from <1 to ~5 ppb, while the calculated values in equilibrium with cassiterite suggest ~5 ppm in the form of $Sn(OH)_4^0$ as the dominant complex (Fig. EA1). This three-log-unit difference may be due to i) the lack of thermodynamic data on aqueous Sn species (see section 2.5) and/or ii) the slow dissolution kinetics of well-crystallized cassiterite in aqueous solution at moderate temperature (350°C) that may not have allowed attainment of mineral-solution equilibrium within duration of the run.

3.1.2. Sulfur-bearing system

Major constituents. The liquid-phase composition is dominated by K, Cl, and sulfate whose measured concentrations in the sampled solutions are in good agreement with those calculated using mass balance relationships considering the initial quantities of KCl and $K_2S_2O_3$ and the masses of the liquid and vapor phases at the experimental *T-P* conditions. These concentrations increase slightly in successive sampling sessions (Table 2), according to the decrease of the mass of the liquid phase in the reactor and reflecting the negligible volatility of KCl and $KHSO_4$. Hydrogen sulfide concentrations (equivalent to sulfur in reduced form) are typically 10 times less those of total S (dominated by sulfate) and systematically decrease in subsequent samples, owing both to the increasing amount of H_2S-enriched vapor compared to liquid, and H_2S extraction from the system by vapor sampling. This pattern is in agreement with Raman spectroscopic measurements, which indicate sulfate (975 cm^{-1}) and hydrogensulfate (1054 cm^{-1}) as the dominant S species in the liquid, with only minor amounts of H_2S (2580 cm^{-1}) present (Fig. 3). The SO_4^{2-}/HSO_4^- peak ratio derived from these spectra (~3) is equivalent to the concentration ratio $[SO_4^{2-} + KSO_4^-]/[HSO_4^- + KHSO_4^0]$, based on the similarity of the Raman cross-sections of sulfate and hydrogen sulfate and the negligible (within the spectral resolution) influence of alkali ion pairs on the Raman signal (Pokrovski and Dubessy, 2015). This concentration ratio is in agreement with that calculated using the thermodynamic data discussed in section 2.5, and corresponds to an equilibrium pH of 5.0±0.3 at 350°C and pressures of 150-250 bar. Note that the concentrations of CO_2 in the aqueous liquid are only a few wt% (3-6 wt%) and do not significantly affect the speciation of other constituents of the aqueous solution. No other S- and C-bearing species were detected in the liquid phase by in situ Raman spectroscopy (Fig. 3). Because H_2S exhibits the largest changes among the major compounds in the samples, and because it is a main controlling factor of sulfide mineral solubility, it is convenient to discuss metal solubility and speciation in the liquid phase in terms of H_2S rather than CO_2 or salinity, which change little (Fig. 4a, b).

Iron and copper concentrations vary between ~1 and ~20 ppm and both show a systematic decrease with increasing H_2S in the liquid phase (Fig. EA2). The negative correlation with H_2S is in qualitative agreement with the following solubility-controlling reactions in the liquid phase:

$$FeS_2(s) + 2H^+ + 0.5H_2 + 2Cl^- = FeCl_2^0 + 2H_2S \quad (4a)$$

$$FeS_2(s) + 2H^+ + 0.5H_2 + 4Cl^- = FeCl_4^{2-} + 2H_2S \quad (4b)$$

$$CuFeS_2(s) + 3H^+ + 0.5H_2 + 4Cl^- = CuCl_2^- + FeCl_2^0 + 2H_2S \quad (5)$$

Equilibrium Fe and Cu concentrations may be estimated from the stability constants of reactions (4a, b) and (5) generated from the available thermodynamic data (section 2.5), and predicted pH (5.0±0.3) and H_2 concentrations (~10^{-5} m), which are almost constant in our H_2S-SO_4^{2-}-HSO_4^- buffered system in subsequent samples. The estimated values match the measured values within 0.5 log unit for Fe and 1.5 log unit for Cu. This may be regarded as a reasonable agreement, taking into account the errors of H_2S analyses and pH estimations, the uncertainties of the available stability constant values, and the potentially incomplete attainment of the mineral-fluid equilibrium at 350°C at the low solid:solution ratios of our experiments (<1:50). Furthermore, at higher H_2S concentrations (>0.04 m) a significant contribution of hydrogensulfide complexes of these metals cannot be excluded.

Gold measured concentrations are between 0.5 and 10 ppm and show a rough positive correlation with reduced sulfur in the liquid phase (Fig. EA2), in agreement with formation of hydrogen sulfide and trisulfur ion complexes according to the reactions:

$$Au(s) + H_2S = Au(HS)^0 + 0.5H_2 \quad (6a)$$

$$Au(s) + 2H_2S = Au(HS)_2^- + H^+ + 0.5H_2 \quad (6b)$$

$$Au(s) + H_2S + S_3^- = Au(HS)S_3^- + 0.5H_2 \quad (6c)$$

Gold concentrations in equilibrium with Au metal calculated using the thermodynamic data for these complexes (section 2.5) match within errors (±0.5 log unit) those measured in the liquid phase, further confirming the H_2S control on Au solubility.

Platinum concentrations do not show systematic changes with H_2S, CO_2 or salt content in the liquid (Fig. 4a, EA2), in agreement with the following solubility reaction for $PtS_{2(s)}$ which is the thermodynamically stable Pt-bearing phase at our conditions:

$$PtS_{2(s)} + H_2 = Pt(HS)_2^0 \quad (7)$$

Absolute Pt concentrations calculated according to Wood's studies are about 2 orders of magnitude higher than measured ones; this difference is likely to reflect the large uncertainties associated with the available thermodynamic properties of $Pt(HS)_2^0$.

Molybdenum concentrations measured in the liquid phase are higher in H_2S-rich samples than in H_2S-poor samples (Fig. 4a). Calculated solubility of MoS_2 using the data for oxy-hydroxide complexes chosen in this study (section 2.5) matches pretty well (within ±0.2 log unit) the measured values at low H_2S (<0.03m) whereas at higher H_2S underestimates the experimental concentrations by about one log unit (Fig. EA2). This difference may point to the presence of additional complexes in S-rich solutions (e.g., oxy-sulfides) not included in the thermodynamic modeling, but more systematic measurements are required to fully account for the observed discrepancies.

Tin measured concentrations are close to the analytical detection limit, which is 3-5 ppb, and do not show any trends. Calculated values assuming the dominant hydroxide species $Sn(OH)_4^0$ are, however, 100-1000 times higher. Like in the S-free experiments (section 3.1.1), this discrepancy may reflect both uncertainties of the thermodynamic data and a lack of solution equilibrium with small amounts of crystalline cassiterite.

3.2. Vapor-phase concentrations and vapor-liquid partitioning of metals and volatiles

Vapor-liquid partition coefficients of each metal and volatile compound measured in this study are expressed, for consistency, as the ratio between the metal bulk concentrations per unit mass of the corresponding vapor or liquid phase (including CO_2):

$$K_{\mathrm{vap/liq}} = C_{\mathrm{vap}}/C_{\mathrm{liq}} \qquad (8)$$

These coefficients ere generated from the concentrations measured in the CO_2-degassed sampled condensates of the vapor and liquid phase, which were recalculated to account for the presence of CO_2 in the corresponding phase at the experimental conditions (Tables 1 and 2). The uncertainties on each reported value primarily depend on the metal concentration in both phases; they are typically of ±0.2 log unit for major elements (Cl, K, Na, Si, ±Fe, ±Cu), ±0.3 to 0.5 log unit for trace metals (Au, Mo, Pt), and might attain more than ±1 log unit for tin.

3.2.1. Sulfur-free system

Carbon dioxide is the major constituent of the vapor phase, along with H_2O, in the S-free experimental runs, and accounts for more than 50 wt% of vapor, with $K_{\mathrm{vap/liq}}$ values decreasing from ~35 to ~13 with increasing salinity of the liquid phase during successive sampling (Table 1). The third most abundant component is Cl, with 100s ppm and $K_{\mathrm{vap/liq}}$ values decreasing from ~0.01 to ~0.002 with increasing CO_2 content. Total chloride concentrations analyzed by HPLC are in good agreement with those calculated from the measured pH values (pH 1.7-2.3) in the CO_2-degassed vapor condensates, assuming that $[H^+] \approx [Cl^-]$ because HCl is almost completely dissociated at room temperature (Supplementary Table EA1). Because the metallic elements are ~100 times less abundant than Cl in those condensates (see below), the cation-anion charge and mass balance constraints suggest that HCl is by far the dominant Cl-bearing compound in the vapor phase at the experimental temperature of 350°C.

Metal concentrations in the vapor phase are highly variable (Fig. 2b), ranging from ~0.02 ppb (Pt) or few ppb (Au, Sn) to 100s ppb (Cu, Mo, Zn) or 1000s ppb (Na, K, Fe, Si), with the corresponding $K_{\mathrm{vap/liq}}$ values ranging between 10^{-5} and 10^{-3} for most metals with two exceptions and ~10^{-2} for silica, with weak-to-nil trends as a function of CO_2 and salinity (Fig. 5-7). One of the two exceptions is Pt that shows an increase of almost two orders of magnitude (from 10^{-3} to 10^{-1}) of its partition coefficient with increasing vapor-phase CO_2 content to 50 wt% (Fig. 7). The other exception is Sn (not shown), which indicates surprisingly high $K_{\mathrm{vap/liq}}$ values, in favor of the vapor in the few samples where it was detectable (Table 1); however these values should be taken with caution as they are derived from Sn concentrations close to the detection limits in both liquid and vapor phases. The vapor-liquid partitioning trends are discussed in sections 4.1 and 4.2.

3.2.2. Sulfur-bearing system

Major volatile compounds. The aqueous vapor phase of S-bearing experimental runs is enriched in CO_2 and H_2S, typically by a factor of 5 to 15 compared to the coexisting liquid in terms of $K_{\mathrm{vap/liq}}$ (Table 2). Concentrations of total sulfur, reduced sulfur, and H_2S in the vapor are identical within the analytical errors, indicating that H_2S is by far the major sulfur species. This is also confirmed by in situ Raman spectroscopy, which only detected the presence of H_2O (~3630 cm^{-1}), H_2S (2601 cm^{-1}) and CO_2 (Fermi dyad 1387 and 1284 cm^{-1} and corresponding harmonics) in the vapor phase (Fig. 3). Vapor-liquid partition coefficients (on mass basis, Table 2) for H_2S do not show systematic trends, whereas those for CO_2 increase slightly (<2 times) with increasing total pressure and salinity of the liquid phase. *Potassium and Cl* partition largely in favor of the liquid (Fig. 5), with $K_{\mathrm{vap/liq}}$ of 10^{-4} and 10^{-3}, respectively, and without any systematic trends. This behavior is similar to what was observed in the S-free system (section 3.2.1), thus showing no effect of sulfur, CO_2 or nature of salts, at least for the experimental compositions studied.

Metal vapor-phase concentrations and vapor-liquid partition coefficients exhibit large variations in amplitude and trends and, for some of the metals, significant differences with the S-free system (Fig. 5-9). *Both Fe and Cu* show $K_{\mathrm{vap/liq}}$ values typically in the range ~0.01-0.1, which is 2 log units higher than in the S-free system (Fig. 6); they generally increase with increasing H_2S concentration (Fig. 8), independently of P_{CO2} (suspiciously high Fe concentrations, of ~5 ppm, and the resulting $K_{\mathrm{vap/liq}}$ values (~0.7) found in the first S-rich vapor sample might be due to contamination from the sampling tubing and valves and thus should be regarded with care). *Gold and Mo* show $K_{\mathrm{vap/liq}}$ values between 0.01 and 0.1 independently of CO_2 and S contents, which is ~2 to 4 log units higher than in the S-free system (Fig. 7 and 9). *Platinum* appears to be the most volatile of the metals in the presence of sulfur, with absolute $K_{\mathrm{vap/liq}}$ values up to ~3 in favor of the vapor and independent, within the data scatter, of CO_2 and S concentrations (Fig. 7 and 9). *Tin* concentrations in the vapor phase are below the detection limit (<5 ppb) in the majority of samples. Thus, the major difference between the S-free and S-bearing system with similar CO_2 content is the enhanced volatility of Fe, Cu, Au, Pt, and Mo in the presence of reduced sulfur.

4. DISCUSSION

4.1. Comparison with published data on vapor-liquid partitioning

4.1.1. CO_2 and H_2S

To allow a comparison with literature data for volatile components, the partition coefficients of CO_2 and H_2S between vapor and liquid measured in this study were expressed in terms of the conventional Henry constant:

$$K_h = P_i(\text{bar}) / m_i(\text{mol/kg } H_2O) \qquad (9),$$

where P_i is the partial pressure of H_2S or CO_2, which is by definition is the product of the total pressure and mole fraction of the volatile component in the vapor phase ($P_i = P_{tot} \times X_i$), and m_i is the molality of the dissolved volatile in the aqueous liquid phase (Tables 3 and 4).

Values of K_h for CO_2 obtained in the S-free system at 350°C in equilibrium with a ~1m (NaCl+KCl) solution are higher (K_h ~100) than most data and models for the pure water-CO_2 system (K_h ~30-50, e.g., Unitherm database; Shvarov, 2008), but the rare experimental data available in NaCl-H_2O-CO_2 systems (e.g., Ellis and Golding, 1963) do report K_h values close to ours at similar salinities, consistent with moderate "salting out" effects for CO_2 in electrolyte solutions. In the S-bearing KCl-$KHSO_4$ solutions of similar total salinity, the K_h values for CO_2 measured in this study are about 2 times lower compared to the S-free NaCl-KCl solutions, but yet remain within the scatter of the existing data. Because of the very small H_2S concentrations compared to those of CO_2 in our runs (H_2S:CO_2 ~1:100), it is very unlikely that the presence of H_2S may cause the differences observed between the S-free and S-bearing systems. Therefore, the variations between our S-free (NaCl-KCl dominated) and S-bearing (KCl-K_2SO_4 dominated) systems for $K_h(CO_2)$ are likely to be due to combined effects of the different nature of the salt (sulfate vs chloride and K versus Na).

The values of the Henry constants for H_2S measured in our KCl-$KHSO_4$-bearing runs are very close to the thermodynamic predictions of K_h (H_2S) in pure water (e.g., Akinfiev and Diamond, 2003; references therein), and in NaCl-bearing solutions at 350°C (e.g., Suleimenov and Krupp, 1994). They do not show any discernable systematics as a function of CO_2 contents, in agreement with the weak H_2S-CO_2 interactions in the low-density vapor phase (Perfetti et al., 2008).

4.1.2. Alkali (Na and K) and base (Fe, Zn, Cu) metals

Because of the absence of published data of vapor-liquid partitioning of metals in CO_2-bearing systems at hydrothermal conditions, this and following subsections (4.1.2-4.1.5) will discuss CO_2-free water-salt(-sulfur) systems; then the effect of CO_2 on metal partitioning will be evaluated based on the results of the present study (section 4.2).

The vapor-liquid partitioning of alkali (Na and K) and base (Fe, Zn, Cu) metals measured in this study at 350°C in S-free NaCl-KCl-water systems (typical $K_{vap/liq}$ ~10^{-3} – 10^{-4}) is in agreement with the large amount of data for these metals obtained by different hydrothermal techniques in CO_2-free systems (e.g., see Pokrovski et al., 2013 for a recent review). Partitioning of potassium is not affected by the presence of reduced sulfur. In contrast, $K_{vap/liq}$ values of Fe and Cu are 1 to 2 orders of magnitude higher in the presence of ~0.1m S in the vapor. The absolute $K_{vap/liq}$ (Cu) values and their evolution with H_2S are in excellent agreement with most published data for hydrothermal conditions, i.e., from 300 to 500°C (Pokrovski et al., 2008; Rempel et al., 2012). The elevated $K_{vap/liq}$ (Fe) values obtained in the H_2S-bearing system at 350°C are also comparable with existing data at the same temperature in a thioacetamide system of similar acidity (pH~4.5) and H_2S content (Pokrovski et al., 2008). Copper $K_{vap/liq}$ values are positively correlated with H_2S content in the vapor phase up to ~0.1m H_2S, but are independent of H_2S at higher concentration (Fig. 8b). Iron $K_{vap/liq}$ values are more scattered, but still indicate a roughly similar tendency (Fig. 8a). Because the speciation of both metals in the salt-rich liquid phase at low-to-moderate H_2S concentrations is controlled by chloride complexes as shown above (section 3.1), the positive $K_{vap/liq}$ – H_2S correlation may be explained by formation of dominantly sulfide complexes in the vapor phase, e.g., according to the following reactions involving H_2S and assuming the segregation of electrically uncharged complexes in the low-density vapor:

$FeCl_2(aq) + 2H_2S(vap) = Fe(HS)_2^0(vap) + 2HCl(vap)$ (10a)

$CuCl_2^-(aq)+ H^+(aq) + H_2S(vap) = Cu(HS)^0(vap) + 2HCl(vap)$ (10b)

At higher H_2S concentrations (>0.2 m H_2S in vapor, which corresponds to >0.03 m H_2S in liquid of CO_2-free samples, Table 2), sulfide complexes, which are generally more volatile than chlorides (Pokrovski et al., 2008), may represent a significant fraction of total dissolved metal in the liquid phase, and thus become the volatility-controlling species as described by the tentative reactions:

$Fe(HS)_2^0(aq) = Fe(HS)_2^0(vap)$ (11a)

$Cu(HS)^0(aq) = Cu(HS)^0(vap)$ (11b)

Thus, the change in the liquid-phase speciation of Cu and Fe at high H_2S content might explain the lack of dependence of $K_{vap/liq}$ on H_2S (see also discussion in Pokrovski et al., 2008).

4.1.3. Molybdenum

In the S-free runs, molybdenum exhibits the lowest partition coefficients among the studied metals ($K_{vap/liq}$ ~10^{-5}; Fig. 7c). These values are comparable with those reported in CO_2-free systems for analogous nonvolatile oxy-hydroxide anions and their ion pairs (e.g., $H_2AsO_3^-$, $H_2AsO_4^-$, HSO_4^-, $NaHSO_4^0$; Pokrovski et al., 2002; Palmer et al., 2004; Pokrovski, 2010). In contrast, our values for Mo are four orders of magnitude lower than those reported by Rempel et al. (2008) for $(NH_3)_2MoO_4$

aqueous solutions at 350°C and saturated vapor pressure. The reasons for this discrepancy may be multiple. First, thermodynamic predictions (section 2.5) suggest $HMoO_4^-$ and $(K,Na)HMoO_4^0$ as the dominant species in the liquid phase in Rempel's and our experimental systems, respectively; thus the presence of large amounts of KCl (and NaCl) in our experiment favors alkali ion pairs with the molybdate ion, which would preferentially partition into the saline liquid phase. Second, large analytical uncertainties, close to absolute concentration values themselves related to the chemical analyses of Mo in vapor condensates in the experiments of Rempel et al. (see their Table 5) imply a corresponding uncertainty in their reported $K_{vap/liq}$ values of at least 1 to 2 orders of magnitude, which hampers unambiguous comparisons. Third, the experimental procedure in Rempel et al.'s study, which involved entrapment of the vapor condensates in an inner cell inserted in the reactor, might lead to an overestimation of vapor-liquid partitioning coefficients as pointed out by the authors for the $NaCl-H_2O$ system. Their protocol contrasts with our experiments in which both the liquid and vapor were sampled separately via distinct and clean extraction lines and analyzed by very sensitive techniques (ICPMS). Acquisition of more systematic data on Mo partitioning using variable techniques is thus required to resolve these discrepancies.

In the S-bearing system, $K_{vap/liq}$(Mo) values (~0.1; Fig. 7c) measured in this study, to our knowledge for the first time, are 4 log units greater than those in the S-free experiments of similar salinity, pH, and CO_2 content, suggesting that highly volatile sulfide complexes form in the vapor phase. The absence of $K_{vap/liq}$(Mo) – H_2S dependence in S-bearing experiments implies that similar S-bearing species form in the liquid phase as well. This H_2S-dominated Mo speciation would also be in agreement with the much higher MoS_2(s) solubilities measured in the liquid phase of our experiments at high H_2S (Fig. EA2) than those predicted using the available thermodynamics for $HMoO_4^-$ and its K^+ ion pairs (section 3.1). The enhanced volatility of S-bearing species compared to oxy-hydroxides or chlorides, found for Mo in this study, is in agreement with the general tendencies of vapor-liquid partitioning for other S-loving metals that form highly volatile sulfur-bearing species (e.g., Cu, Au, Fe; see Pokrovski et al., 2008 for detailed discussions).

4.1.4. Gold and platinum

Gold and platinum in the CO_2-free vapor phase of our *S-free experiments* are at 0.1-1.0 ppb concentration levels, resulting in $K_{vap/liq}$ values of 10^{-4}–10^{-3} (Fig. 7a, b). These values are in good agreement with the few available data at higher temperatures (450°C) in NaCl brine – vapor systems and with the density model predictions for Au partitioning (Pokrovski et al., 2005). No published data are available for Pt in chloride-bearing S-free systems, and our first results indicate a similar volatility for both metals whose liquid-phase speciation is dominated by negatively charged chloride species ($AuCl_2^-$ and $PtCl_3^-$, see section 3.1).

In contrast, in the CO_2-free *S-bearing experiment*, Au volatility is higher by 1 to 2 orders of magnitude, and that of Pt by almost 4 orders of magnitude, with absolute vapor-liquid partitioning values in favor of the vapor ($K_{vap/liq}$(Pt) >1). This enhancement clearly demonstrates the formation of volatile S-bearing complexes by both metals. The constancy of $K_{vap/liq}$ values across the wide range of H_2S contents in the vapor (0.03-0.7 m H_2S, Fig. 9a, b), may be interpreted by vapor-liquid equilibrium between dominant species of similar stoichiometry and S ligation number both in liquid and vapor phase according to the following hypothetical reactions, and assuming the predominance of uncharged species in the low-density vapor:

$Au(HS)_2^-(liq) + H^+(liq) = Au(HS)H_2S^0(vap)$ (12a)

$Au(HS)^0(liq) = Au(HS)^0(vap)$ (12b)

$Pt(HS)_2^0(liq) = Pt(HS)_2^0(vap)$ (13)

This interpretation is consistent with Au (and by analogy Pt) coordination by H_2S/HS^- ligands (e.g., Pokrovski et al., 2009a) and the previous measurements in similar S-rich systems for Au at 350°C (Pokrovski et al., 2008) that reported $K_{vap/liq}$(Au) values identical to those of the present study (0.01-0.1). At higher T (450-800°C), the published $K_{vap/liq}$ (Au) values are ~1 log unit higher on average (0.1-1.0), but vary depending on liquid-phase pH, salinity and S content of the system (Pokrovski et al., 2013; references therein). The few $K_{vap/liq}$ (Pt) data points reported in the literature at 450 and 500°C (Pokrovski et al., 2008) are comparable, within ±0.5 log unit, to those found in this study. Thus, of all metals studied, Pt appears to be the most volatile one in the presence of reduced sulfur in a wide range of temperatures and pressures.

4.1.5. Silica and tin

Silica vapor-liquid partition coefficients measured in the CO_2-free NaCl-KCl system are close to 0.01. They are identical within errors to those measured at 350°C in water-salt systems of similar salinity, both S-free and S-bearing ($K_{vap/liq}$(Si) = 0.02±0.01; Pokrovski et al., 2005, 2008). The available data and recent models for vapor-liquid partitioning of $Si(OH)_4$ in pure water report somewhat higher $K_{vap/liq}$(Si) values (0.04±0.01; e.g. Akinfiev et al., 2015 and references therein). This difference is due to a combination of factors such as the lower water vapor pressures in equilibrium with a salt-bearing aqueous liquid (e.g., ~140 vs 165 bar between our experiments and pure water) and enhanced salting-in effects in the salt-bearing solutions, both lowering silica partitioning into the vapor phase.

Tin concentrations were found to be close to (S-free system) or below (S-bearing system) the analytical detection limit (<1-5 ppb, depending of the sample) in the majority of vapor-phase condensates. The few values of $K_{vap/liq}$ that may tentatively be generated from the highest concentrations (Table 1 and 2) are above unity, suggesting an elevated volatility of the neutral hydroxide species $Sn(OH)_4^0$, which is dominant in the liquid phase (section 3.1). Although these values are highly uncertain, they are in line with those for other neutral hydroxide species studied so far, such as $As(OH)_3^0$, $Si(OH)_4^0$, $Ge(OH)_4^0$, $Ga(OH)_3^0$ that generally show higher vapor/liquid partitioning coefficients (0.01-0.1 at 350°C) compared to those of base metal chlorides (e.g., Pokrovski et al., 2002, Nekrasov et al., 2013; Akinfiev et al., 2015).

4.2. Effect of CO_2 on vapor-liquid partitioning of metals

4.2.1. Sulfur-free system

In CO_2-bearing experiments, for the S-free salt-bearing system, three groups of elements may be identified according to their partitioning trends as a function of CO_2.

Alkali metals (*K, Na), zinc, and molybdenum* show $K_{vap/liq}$ values that are constant within the data scatter over the studied range of P_{CO2} (from 0 to ~90 bars, X_{CO_2} up to ~0.35). This trend is consistent with the absence of complexes with (bi)carbonate ligands, and the negligible solubility of ionic salts of these metals in CO_2 vapor (e.g., Zakirov et al., 2007). Thus, CO_2 appears as an inert compound and the vapor-liquid partitioning of these metals is controlled by the density (or pressure) of saturated water vapor, which is roughly constant in our experiments (P_{H2O} ~140 bar) because buffered by equilibrium with aqueous liquid.

The second group of elements includes Si, Cl, Fe and Cu (and tentatively Sn). They show a decrease (by a factor of ~2 for Si and Sn and ~10 for the other elements) of their $K_{vap/liq}$ values over the studied P_{CO2} range. The reasons for such behavior may be different depending on the metal. *For Si,* it is likely due to small salting-in effects with increasing salt content in solution in subsequent samples, an affect known for silicic acid in electrolyte solutions (e.g., Newton and Manning, 2000). Tentatively, a similar salting-in control may hold *for Sn* as it forms analogous tetra-hydroxide species. *For Cl*, the dominant vapor-phase species is by far HCl^0 (section 3.1). Thus at the run temperature, Cl partitioning is controlled by the equilibrium $H^+(aq) + Cl^-(aq) = HCl^0(vap)$. Thermodynamic calculations show that both H^+ and Cl^- concentrations (or activities) vary little in the liquid phase in the presence of dissolved CO_2 (whose concentration does not exceed 1.1 m). Therefore, the decrease of $K_{vap/liq}$ (Cl) with increasing CO_2 content in the system is likely to reflect the decreasing stability of HCl itself in the vapor phase in the presence of CO_2. At the macroscopic level, this decrease may be explained by the lowering of the dielectric constant of the vapor in the presence of CO_2, similarly to the effect of CO_2 on the stability of polar and/or electrically charged species in supercritical H_2O-CO_2 fluids (Akinfiev and Zotov, 1999; Kokh et al., 2016). At the molecular level, the effect of CO_2 would be to destabilize the hydration shell of the polar HCl molecule in the vapor (e.g., Liu et al., 2015). *For Cu and Fe,* the dominant species in the vapor are neutral chloride complexes, presumably $CuCl^0$

and $FeCl_2^0$, hydrated to some extend by water molecules. Therefore, a similar weakening of their hydration shells may be expected in the presence of CO_2 to explain the lowering of their $K_{vap/liq}$ values relative to the CO_2-free aqueous system. In such a system, both Cu and Fe vapor-liquid partitioning was shown to be unaffected by the presence of HCl (Pokrovski et al., 2005). It follows that complexes containing HCl as ligand are not expected for these metals, and thus the decrease of their $K_{vap/liq}$ values with CO_2 is not related to the change of HCl concentration in the vapor described above (Fig. 5a). Thus, the particular molecular configuration (dipole moment of the complex, stability and structure of its hydration shell) of Cu and Fe chloride species in the vapor, compared to their Na, K and Zn analogs, may be responsible for the different trends of $K_{vap/liq}$ for the two groups of metals as a function of CO_2. The moderate decrease of Cu partitioning as a function of CO_2 found in this study is similar to that reported in experiments at magmatic conditions (800°C and 1 kbar) between the aqueous vapor and brine phase in a comparable CO_2 concentration range (Tattitch et al., 2015).

The third group of elements is represented by Au and Pt, which show a trend of increasing $K_{vap/liq}$ with CO_2 content, by half an order (Au) and two orders (Pt) of magnitude, even though the data scatter is quite large (Fig. 7a, b). If our measurements are correct, this is a surprising finding, which contrasts with the other metals for which the stability of chloride or hydroxide species has a tendency to weaken in the CO_2-rich vapor, as shown above. Direct CO_2 or carbonate complexes for Au and Pt, which are both extremely soft metals, are very unlikely (e.g., Barnes, 1997), and we do not have any evidence for such species from the solubility measurements in the liquid phase (this study) or supercritical fluid (Kokh et al., 2016). Thus, the only explanation that we could find at present is the formation of stable gaseous complexes with CO, which is known to have a high chemical affinity for transition metals, including Pt and Au (e.g., Cotton et al., 1999); in addition, a variety of Au and Pt halogen carbonyl complexes is reported in the chemical literature, at least at ambient conditions (e.g., $AuCl(CO)$, $PtCl_2(CO)_2$, Belli Dell'Amico et al., 2010; references therein). Furthermore, according to thermodynamic calculations, the concentrations of CO amount up to 10^{-4} m in the vapor phase, which is several orders of magnitude higher than those of Au and Pt themselves, thus favoring complexing. This effect of CO on noble metal volatility is a new feature that requires a more systematic investigation at hydrothermal conditions.

4.2.2. Sulfur-bearing system

In the presence of reduced sulfur (H_2S), no obvious trends with CO_2 could be detected within errors for any of the investigated elements. Potential trends might be, at least partly, obscured by the data scatter intrinsic to the sulfur-bearing system, which is far more analytically and experimentally challenging than that without sulfur discussed above. Nonetheless, the different nature of the dominant S-bearing versus Cl/OH-bearing complexes of metals may provide an adequate qualitative interpretation of the observed trends. In addition, for those elements that form the same dominant species in the S-free and S-bearing systems of this study (e.g., alkali metals and chlorine), differences in liquid-phase acidity (pH) and salt nature and concentration may also contribute to the differences observed between the two systems.

Potassium does not show any change in its partition coefficients with addition of CO_2, a behavior similar to the S-free system. The absolute $K_{vap/liq}$ values in the S-bearing system is slightly higher, on average within a factor of 2, than in the absence of sulfur; this is likely to reflect the differences in the solution compositions between the two systems (e.g., higher total K content in the liquid phase of the S-bearing experiments and the presence of K_2SO_4 and $KHSO_4$ electrolytes, which may have a different volatility than KCl). *Chloride* partitioning is also independent of CO_2 content but the scatter of data points is large because of the low absolute Cl concentrations in the vapor (~10s ppm). This contrasts with the more acidic S-free system (calculated $pH_{350°C}$ ~4.4) whose Cl vapor-phase content, dominated by HCl^0(vap), is 5-10 times higher and $K_{vap/liq}$ shows a decrease with increasing CO_2 fraction (Fig. 5a). This difference is likely due to the lesser abundance of HCl^0 (vap) in the S-bearing and less acidic run (calculated $pH_{350°C}$ ~5.0) which makes the effect of CO_2 less pronounced.

The speciation of the other studied metals, *Fe, Cu, Mo, Au and Pt*, in the presence of reduced sulfur in the vapor in our experiments is dominated by sulfide complexes as shown by their partitioning coefficients 1 to 4 orders of magnitude higher than those in S-free systems at the same salinity and CO_2 content (sections 3.2 and 4.1). Although the exact stoichiometry and structure of these vapor species are still unknown, they are expected from general chemistry to have stronger covalent metal-sulfide bonds and weaker dipole moments compared to complexes with Cl and OH ligands that are characterized by ionic-type bonds and thus a more enhanced polarity (Barnes, 1997; Wood and Samson, 1998). As a result, S species of metals are generally less hydrated by solvent water molecules than their OH and Cl counterparts, both in the liquid and vapor phase (e.g., Pokrovski et al., 2008). This is in agreement with the much higher volatility of sulfide-type species and the absence of water density control on their vapor-liquid partition coefficients (Pokrovski et al., 2005, 2013). The few direct structural data obtained using in situ X-ray absorption spectroscopy and molecular modeling in dense aqueous solution demonstrate that Au and Cu are linearly coordinated by two HS/H_2S ligands in the 1st shell, with no water molecules at distances less than 3 Å from the metal atom (Pokrovski et al., 2009a, 2015; Etschmann et al., 2010; Mei et al., 2013). If similar species form in the vapor phase, they should be only very weakly hydrated by water molecules. In contrast, chloride species of these and other metals (e.g., $(H_2O)CuCl^0$, $(H_2O)AuCl^0$, $(H_2O)_4FeCl_2^0$) in dense aqueous liquid, similar to those expected in the vapor phase in S-free systems, are known to have closely bound water molecules in the 1st coordination shell (e.g., Pokrovski et al., 2009b; Testemale et al., 2009), and thus exhibit much stronger hydration. CO_2 molecules may partly break or dilute such hydration environment, leading to a decrease in the stability of hydrated species and their partition coefficients. Same analogies may hold for other metals (Pt, Mo) even though their exact speciation and structure are still poorly known both in liquid and vapor. Thus, the generally low sensitivity of sulfide species to the solvent environment (H_2O vs CO_2) explains well the lack of an effect of CO_2 on their vapor-liquid partitioning. A more quantitative interpretation of the role of CO_2 on species stability and hydration structures would require a combination of solubility/partitioning measurements with in situ spectroscopy and molecular modeling approaches.

5. GEOLOGICAL SIGNIFICANCE

Our new vapor-liquid partitioning measurements, performed for a large set of metals, offer insights into the combined effect of CO_2 and sulfur on metal behavior at typical *T-P* conditions of fluid boiling, recorded in a great majority of hydrothermal ore deposits.

First, our data support previous findings indicating that reduced sulfur is the key compound controlling vapor-liquid fractionation of chalcophile metals (Cu, Mo, Au, Pt) over a wide range of magmatic-hydrothermal conditions, as shown by analyses of natural fluid inclusions and laboratory experiments in model systems (e.g., Heinrich, 2007; Simon and Ripley, 2011; Kouzmanov and Pokrovski, 2012; Pokrovski et al., 2013, for recent reviews). Specifically, the presence of H_2S enhances partitioning of these metals into the vapor phase in the following order of increasing difference between S-free and S-bearing systems: Cu<Au<Mo≈Pt. At 350°C, which is a common temperature of fluid boiling in different types of ore deposits ranging from magmatic porphyry to epithermal (e.g., Heinrich, 2007), at sulfur contents of 0.1–1.0 wt% S, absolute vapor-liquid partitioning coefficients for Cu, Mo and Au are of the order of 0.01–0.1. These values imply that extraction of half of the total metal content into the vapor phase would require boiling of at least 90% of the initial fluid. Consequently, for typical vapor/brine mass ratios between 4 and 9 as in most porphyry systems (e.g., Hedenquist et al., 1998; Lerchbaumer and Audétat, 2013) and even lower ratios in epithermal or orogenic deposits (Heinrich et al., 2007; Garofalo et al., 2014), the liquid (brine) phase would still remain the dominant transporting medium for these metals. Upon boiling, the growth of metal concentration in the liquid, together with the increase of its pH following the departure of acidic volatiles (HCl, CO_2, H_2S) into the vapor, are all well-known factors that can cause metal precipitation from the liquid (e.g., Drummond and Ohmoto, 1985). An exception from the list of chalcophile elements is platinum, which shows $K_{vap/liq}$ values above 1 (i.e., in favor of the vapor), implying a major role of the H_2S-enriched vapor phase in Pt transport even at epithermal conditions. In contrast, boiling of S-poor fluids will cause a negligible partitioning into the vapor of all metals

whose typical $K_{vap/liq}$ values are less than 0.001 at temperatures of epithermal settings (<300-350°C). In contrast, at higher temperatures of vapor-brine immiscibility such as occurring in some porphyry deposits (>400-450°C), vapor-liquid partitioning of Cu ($K_{vap/liq}$ ~0.1) and, particularly, of Au and Pt ($K_{vap/liq}$ ~1 to 10), in the presence of sulfur is at least one order of magnitude higher than that at 350°C (Pokrovski et al., 2008, Kouzmanov and Pokrovski, 2012; references therein); consequently, the vapor phase may play a dominant role in the transport of these metals at such conditions.

Second, our first measurements in CO_2-rich vapor-liquid systems demonstrate that the effect of CO_2 on vapor-liquid partitioning is primarily controlled by the reduced sulfur content of the system. In S-poor systems, the presence of CO_2 is unfavorable for Cu and Fe partitioning into the vapor, lowering $K_{vap/liq}$ values by up to 10 times with 50 wt% CO_2 in the vapor. For metals such as Si, Mo, K, Na, Zn (and likely Sn), the effect of CO_2 is almost negligible. Thus, the metal transporting potential of such vapors, which is generally weak for these metals at S-poor conditions in CO_2-free aqueous systems, will not be favored by the presence of CO_2. In contrast, partitioning of Pt (and, in lesser extent, Au) into the vapor may be enhanced by the presence of even minor amounts of carbon monoxide; this effect would be stronger under reducing conditions, which favor CO abundance. In S-rich systems, the effect of CO_2 (and CO) is negligible for all studied metals including Au and Pt, in the face of the dominant sulfur control on the partitioning as discussed above. Thus, at least at the conditions covered by our study, CO_2 itself neither acts as a direct ligand for the metals nor does it favor specific solvation of inorganic metal complexes. Nevertheless, specific solvation by CO_2 cannot be fully excluded for some organic-sulfur metal species at the lower temperatures of CO_2 geological storage, following the analogy with the well-known enhanced solvation affinity of supercritical CO_2 for certain organic compounds and thiol and phosphoryl organometallic complexes (e.g., Glennon et al., 1999; Erkey, 2000).

Third, our study implies that the effect of CO_2 on the behavior of most metals in vapor-liquid systems at hydrothermal conditions is mostly indirect, i.e., the presence of CO_2 would extend the vapor-liquid immiscibility domain and thus increase the temperature and pressure (or depth) of vapor-liquid separation, compared to an aqueous saline fluid free of CO_2, as shown by available data in the H_2O-NaCl-CO_2 system (e.g., Duan et al., 1995; Bakker, 2009). As a numerical example, illustrated in Fig. 10, the presence of only 5 mol% CO_2 (~10 wt%) in a single-phase aqueous fluid with 10 wt% NaCl, ascending along a typical geothermal gradient within the potassic alteration zone of a magmatic-arc-hosted porphyry system (~50°C/km; Sillitoe, 2010; Richards, 2011), will raise the temperature and pressure of fluid unmixing from 350°C and 150 bar (CO_2-free), corresponding to 0.6 km lithostatic depth, to 450°C and ~350 bar (CO_2-bearing), corresponding to ~2.6 km depth. Considering the typical vapor-liquid partition coefficients for Cu and Au at these two respective *T-P* points ($K_{vap/liq}$ 0.01 (Cu), 0.05 (Au) at 350°C, this study, and 0.1 (Cu), 1.0 (Au) at 450°C, Pokrovski et al., 2013), in the presence of 0.5 wt% S in the vapor (which is a typical concentration analyzed in fluid inclusions from porphyry deposits, Kouzmanov and Pokrovski, 2012), the capacity of the vapor phase to transport these metals will increase in the presence of CO_2 by a factor of 10 to 100 (depending on the extent of boiling). This effect should be taken into account in genetic models of ore deposit formation. In addition, the early vapor-brine separation induced by CO_2 may also cause precipitation of a portion of the metal from the liquid phase at greater depth than expected if CO_2 is ignored; this effect of CO_2 may directly impact exploration strategies.

6. CONCLUSIONS

The key points of this study are the following:

The first set of direct data was generated on vapor-liquid partitioning for a large panel of metals of different chemical nature, in the H_2O-salt-sulfur-CO_2 system along two-phase vapor-liquid equilibrium at temperatures (350°C), pressures (130-270 bar), and vapor compositions (S up to ~3 wt%, CO_2 up to 50 wt% in the vapor) typical of those occurring during fluid boiling and vapor-liquid immiscibility phenomena in many hydrothermal ore deposits.

Our data in the S-free and CO_2-free system yield absolute vapor-liquid partitioning coefficients ($K_{\mathrm{vap/liq}}$) largely in favor of the liquid and increasing over the range 10^{-5}–10^{-2} in the order Mo < Na, K < Zn, Fe, Cu, Au, Pt < Si(<Sn). In the presence of 0.1 to 1 wt% H_2S in the vapor phase, vapor-liquid partitioning of Mo, Au, Pt is enhanced by 2 to 4 orders of magnitude, that of Cu and Fe by about 1 to 2 orders of magnitude, whereas that of alkali metals is unaffected. These findings are in good agreement with published experimental and natural fluid inclusion data, and confirm the key role of reduced sulfur on vapor-liquid fractionation of most chalcophilic metals.

The effect of CO_2 on vapor-liquid partitioning of metals in S-free systems is to slightly decrease the volatility of Fe and Cu (within <1 log unit at 50 wt% CO_2 in the vapor phase), while that of other metals (Zn, Mo, Si, K, Na, Sn) is almost unaffected. In contrast, the presence of minor amounts of CO seems to enhance Au and Pt partitioning into the vapor by 1 to 2 orders of magnitude, an effect that requires further investigation. In S-bearing systems, no influence of CO_2 on vapor-liquid partitioning could be detected within errors for all metals, attesting the dominant control of H_2S on metal volatility, and the absence of specific solvation or direct complexation by CO_2.

Thus, the major effect of CO_2 on metal vapor-liquid fractionation, at least under the conditions of our study, is mostly indirect and consists of extending the vapor-liquid immiscibility domain to higher *T*-*P* conditions, compared to a CO_2-free system. This widening of the immiscibility gap, particularly in the presence of reduced sulfur in the system, causes enhanced partitioning of sulfur-loving metals (Au, Pt, ±Mo) into the vapor phase, and concentration of alkali and base metals (Na, K, ±Fe, ±Cu) and chloride into the salt-rich liquid phase. As a result, the presence of CO_2 in the fluid can affect both the depth of ore deposition and the vertical metal zonation in hydrothermal systems.

Acknowledgments

This work was funded by the French National Research Agency (grant SOUMET ANR-2011-Blanc SIMI 5-6 009), University of Toulouse (grant CO_2MET), Institute Carnot (grant ISIFoR), and the Institut des Sciences de l'Univers of the Centre National de la Recherche Scientifique (grants ORPY-CESSUR and S3MIF-PNP). M.A.K. acknowledges support from the University of Toulouse (PhD fellowship of the Ministère de l'Education Nationale, de l'Enseignement Supérieur et de la Recherche (MENESR), awarded by the President of the University of Toulouse). We thank A. Castillo, S. Mounic, C. Causserand, M. Henry, J. Prunier, T. Aigouy, and M. Thibaut for their professional help with tough hydrothermal experiments and interminable chemical analyses. We are grateful to J. Dubessy for the help with Raman spectroscopy experiments, N. Akinfiev and Y. Shvarov for advice on thermodynamic modeling, B. Ryzhenko for sharing thermodynamic data on Sn species, S. Salvi for comments and corrections on the manuscript, and J. Schott, P. Bénézeth, A.V. Zotov, D.V. Grichuk, S. Salvi and D. Beziat for fascinating discussions about CO_2 fluids.

Supplementary electronic data:

Supplementary Table EA1; Supplementary Figures EA1 and EA2

REFERENCES

Akinfiev N.N. and Diamond L.W. (2003) Thermodynamic description of aqueous nonelectrolytes at infinite dilution over a wide range of state parameters. *Geochim. Cosmochim. Acta* **67**, 613-629.

Akinfiev N. and Zotov A. (1999) Thermodynamic description of equilibria in mixed fluids (H_2O-non polar gas) over a wide range of temperature (25 to 700°C) and pressure (1 to 5000 bars*). Geochim. Cosmochim. Acta* **63**, 2025-2041.

Akinfiev N.N. and Zotov A.V. (2010) Thermodynamic description of aqueous species in the system Cu-Ag-Au-S-O-H at temperatures of 0-600°C and pressures of 1-3000 bar. *Geochem. Intern.* **48**, 714-720.

Akinfiev N.N., Plyasunov A.V. and Pokrovski G.S. (2015) An equation of state for predicting the thermodynamic properties and vapour-liquid partitioning of aqueous $Ge(OH)_4$ in a wide range of water densities. *Fluid Phase Equil.* **392**, 74-83.

Bakker R. J. (2009) Package FLUIDS. Part 3: correlations between equations of state, thermodynamics and fluid inclusions. *Geofluids* **9**, 63-74.

Barnes H.L. (1997) *Geochemistry of Hydrothermal Ore Deposits*, Wiley, New York.

Barton P.B. and Chou I.-M. (1993) Refinement of the evaluation of the role of CO_2 in modifying estimates of the pressure of epithermal mineralization. *Econ. Geol.* **88,** 873-884.

Belli Dell'Amico D., Labella L., Marchetti F. and Samaritani S. (2010) Halo-carbonyl complexes of palladium, platinum and gold. *Coor. Chem. Rev*. **254**, 635-645.

Bodnar R.J., Reynolds T.J. and Kuehn C.A. (1985) Fluid-inclusion systematics in epithermal systems. *Rev. Econ. Geol*. **2**, 73-97.

Boiron M.-C., Cathelineau M., Banks D., Fourcade S. and Vallance J. (2003) Mixing of metamorphic and surficial fluids during the uplift of the Hercynian upper crust: consequences for gold deposition. *Chem. Geol.* **194**, 119-141.

Bowers T. S and Helgeson H. C. (1983) Calculation of the thermodynamic and geochemical consequences of nonideal mixing in the system H_2O-CO_2-NaCl on phase relations in geologic systems: Equation of state for H_2O-CO_2-NaCI fluids at high pressures and temperatures. *Geochim. Cosmochim. Acta* **47**, 1247-1275.

Brugger J., Etschmann B., Liu W., Testemale D., Hazemann J.-L., Emerich H., van Beek W. and Proux O. (2007) An XAS study of the chloride complexing of Cu(I) in brines. *Geochim. Cosmochim. Acta* **71**, 4920-4941.

Catchpole H., Kouzmanov K., Fontboté L., Guillong M. and Heinrich C.A. (2011) Fluid evolution in zoned Cordilleran polymetallic veins — Insights from microthermometry and LA-ICP-MS of fluid inclusions. *Chem. Geol.* **281**, 293-304.

Caumon M.-C., Dubessy J., Robert P. and Tarantola A. (2013) Fused silica capillary capsules (FSCCs) as reference synthetic aqueous fluid inclusions to determine chlorinity by Raman spectroscopy. *Eur. J. Miner*. **25**, 755-763.

Chase M.W. Jr. (1998) NIST-JANAF Thermochemical Tables, Fourth Edition, *J. Phys. Chem. Ref. Data*, Monograph No. 9; available at http://webbook.nist.gov/chemistry.

Cotton F.A., Wilkinson G., Murillo C.A. and Bochmann M. (1999) *Advanced Inorganic Chemistry* (6th Edition, Wiley, Chichester).

Dargent M., Dubessy J., Truche L., Bazarkina E.F., Nguyen-Trung C. and Robert P. (2013) Experimental study of uranyl(VI) chloride complex formation in acidic LiCl aqueous solutions under hydrothermal conditions (T = 21°C–350 °C, Psat) using Raman spectroscopy. *Eur. J. Miner*. **25**, 765-775.

Drummond S.E. and Ohmoto H. (1985) Chemical evolution and mineral deposition in boiling hydrothermal systems. *Econ. Geol*. **80**, 126-147.

Duan Z., Moller N. and Weare J. (1995) Equation of state for NaCl-H_2O-CO_2 system - prediction of phase equilibria and volumetric properties. *Geochim. Cosmochim. Acta* **59**, 2869-2882.

Dubessy J., Caumon M.-C., Rull F. and Sharma S. (2012) Instrumentation in Raman spectroscopy: elementary theory and practice, in: Dubessy, J., Caumon, M.-C., Rull, F. (Eds.), *Raman Spectroscopy Applied to Earth Sciences and Cultural Heritage*, EMU Notes in Mineralogy, vol. 12, European Mineralogical Union and the Mineralogical Society of Great Britain & Ireland, London, pp. 83–165.

Einaudi M.T., Hedenquist J.W. and Inan E.E. (2003) Sulfidation state of fluids in active and extinct hydrothermal systems: Transitions from porphyry to epithermal environments. *Soc. Econ. Geol. Spec. Pub*. **10**, 285–313.

Ellis A.J. and Golding R.M. (1963). The solubility of carbon dioxide above 100 degrees C in water and in sodium chloride solutions. *Amer. J. Sci.* **261**, 47-60.

Erkey C. (2000) Supercritical carbon dioxide extraction of metals from aqueous solutions: a review. *J. Supercrit. Fluids* **17**, 259-287.

Etschmann B.E., Liu W., Testemale D., Müller H., Rae N.A., Proux O., Hazemann J-L. and Brugger J. (2010) An in situ XAS study of copper(I) transport as hydrosulfide complexes in hydrothermal solutions (25-592°C, 180-600 bar): Speciation and solubility in vapor and liquid phases. *Geochim. Cosmochim. Acta* **74**, 4723-4739.

Foustoukos D.I. and Seyfried W.E. Jr. (2007a) Trace element partitioning between vapor, brine and halite under extreme phase separation conditions. *Geochim. Cosmochim. Acta* **71**, 2056-2071.

Foustoukos D.I. and Seyfried W.E. Jr. (2007b) Quartz solubility in the two-phase and critical region of the NaCl-KCl-H_2O system: Implications for submarine hydrothermal vent systems at 9°50'N East Pacific Rise. *Geochim. Cosmochim. Acta* **71**, 186-201.

Garofalo P.S., Ficker M.B., Gunther D., Bersani D. and Lottici P.P. (2014) Physical-chemical properties and metal budget of Au-transporting hydrothermal fluids in orogenic deposits. *Geol. Soc. London Spec. Publ.* **402**, 71-102.

Glennon J.D., Harris S.J., Walker A., McSweeney C.C. and O'Connell M. (1999) Carrying gold in supercritical CO_2. *Gold Bull.* **32**, 52-58.

Haas J.R., Shock E.L. and Sassani D.S. (1995) Rare earth elements in hydrothermal systems: Estimates of standard partial molal thermodynamic properties of aqueous complexes of the rare earth elements at high pressures and temperatures. *Geochim. Cosmochim. Acta* **59**, 4329-4350.

Hanley J. J. and Gladney E. R. (2011) The presence of carbonic-dominant volatiles during the crystallization of sulfide-bearing mafic pegmatites in the North Roby zone, Lac des Iles Complex, Ontario. *Econ. Geol.* **106**, 33-54.

Hedenquist J.W. and Lowenstern J.B. (1994) The role of magmas in the formation of hydrothermal ore deposits. *Nature* **370**, 519–527.

Hedenquist J.W., Arribas A. Jr. and Reynolds T.J. (1998) Evolution of an intrusion-centered hydrothermal system: Far Southeast-Lepanto porphyry and epithermal Cu-Au deposits, Philippines. *Econ. Geol*. **93**, 373–404

Heinrich C.A. (1990) The chemistry of hydrothermal tin(-tungsten) ore deposition. *Econ. Geol*. **85**, 457-481.

Heinrich C.A. (2007) Fluid-fluid interactions in magmatic hydrothermal ore formation. *Rev. Mineral. Geochem.* **65**, 363-387.

Heinrich C.A., Ryan C.G., Mernagh T.P. and Eadington P.J. (1992) Segregation of ore metals between magmatic brine and vapor - a fluid inclusion study using PIXE microanalysis. *Econ. Geol*. **87**, 1566–1583.

Heinrich C.A., Günther D., Audédat A., Ulrich T. and Frischknecht R. (1999) Metal fractionation between magmatic brine and vapour, and the link between porphyry-style and epithermal Cu-Au deposits. *Geology* **27**, 755-758

Hovey J.K., Pitzer K.S., Tanger IV J.C., Bischoff J.L. and Rosenbauer R.J. (1990) Vapor-liquid phase equilibria of potassium chloride-water mixtures: Equation-of-state representation for KCl-H_2O and NaCl-H_2O. *J. Phys. Chem.* **94**, 1175-1179.

Jackson K.J. and Helgeson H.C. (1990) Chemical and thermodynamic constraints on the hydrothermal transport and deposition of tin: I. Calculation of the solubility of cassiterite at high pressures and temperatures. *Geochim. Cosmochim. Acta* **49**, 1-22.

Jacquemet N., Guillaume D., Zwick A. and Pokrovski G.S. (2014) In situ Raman spectroscopy identification of the S_3^- ion in S-rich hydrothermal fluids from synthetic fluid inclusions. *Amer. Miner.* **99**, 1109-1118.

Johnson J.W., Oelkers E.H. and Helgeson H.C. (1992) SUPCRT92: A software package for calculating the standard molal thermodynamic properties of minerals, gases, aqueous species, and reactions from 1 to 5000 bar and 0 to 1000°C. *Comput. Geosci.* **18**, 899-947; updated version based on a series of subsequent papers reporting HKF parameters for most ions and aqueous complexes is available on line at http://geopig.asu.edu/index.html#.

Koděra P., Lexa J., Rankin A.H. and Fallick AE (2005) Epithermal gold veins in a caldera setting: Banská Hodruša, Slovakia. *Mineral. Deposita* **39**, 921–943.

Kokh M.A. (2016) Role of CO_2 in the transfer of economic metals by geological fluids. *PhD thesis*, University of Toulouse, 205 pp.

Kokh M.A., Akinfiev N.N., Pokrovski G.S., Salvi S. and Guillaume D. (2016) The role of carbon dioxide in the transport and fractionation of metals by geological fluids. *Geochim. Cosmochim. Acta* (submitted October 2015).

Kouzmanov K. and Pokrovski G.S. (2012) Hydrothermal controls on metal distribution in Cu(-Au-Mo) porphyry systems. In: Geology and Genesis of Geology and Genesis of Major Copper Deposits and Districts of the World: A Tribute to Richard H. Sillitoe (eds. J.W. Hedenquist, M. Harris, and F. Camus). *Soc. Econ. Geol. Spec. Pub.* **16**, 573-618.

Lerchbaumer L. and Audétat A. (2012) High Cu concentrations in vapor-type fluid inclusions: An artifact? *Geochim. Cosmochim. Acta* **88**, 255-274.

Liebscher A. (2007) Experimental studies in model fluid systems. *Rev. Miner. Geochem*. **65**, 15-47.

Liu W., Mei Y., Brugger J., Migdisov A. and Williams-Jones A. (2015) Speciation and solubility of gold in CO_2-HCl-H_2O fluids: MD simulations and solubility experiments. *Goldschmidt Abstracts*, p. 1893.

Loucks R.R. and Mavrogenes J.A. (1999) Gold solubility in supercritical hydrothermal brines measured in synthetic fluid inclusions. *Science* **284**, 2159-2163.

Lowenstern J.B. (2001) Carbon dioxide in magmas and implications for hydrothermal systems. *Mineral. Deposita* **36**, 490-502.

Mei Y., Sherman D.M., Liu W. and Brugger J. (2013) Complexation of gold in S_3^--rich hydrothermal fluids: Evidence from ab-initio molecular dynamics simulations. *Chem. Geol.* **347**, 34-42.

Mei Y., Liu W., Sherman D.M. and Brugger J. (2014) Metal complexation and ion hydration in low density hydrothermal fluids: Ab initio molecular dynamics simulation of Cu(I) and Au(I) in chloride solutions (25–1000°C, 1–5000 bar). *Geochim. Cosmochim. Acta* **131**, 196–212.

Minubaeva Z. and Seward T.M. (2010) Molybdic acid ionization under hydrothermal conditions to 300 °C. *Geochim. Cosmochim. Acta* **74**, 4365-4374.

Naumov G.B., Ryzhenko B.N. and Khodakovsky I.L. (1974) *Handbook of Thermodynamic Data*, U.S. Geological Survey.

Nekrasov S.Y., Migdisov A.A., Williams-Jones A.E. and Bychkov A.Y. (2013) An experimental study of the solubility of gallium(III) oxide in HCl-bearing water vapour. *Geochim. Cosmochim. Acta* **119**, 137–148.

Newton R.C. and Manning C.E. (2000) Quartz solubility in H_2O-NaCl and H_2O-CO_2 solutions at deep crust-upper mantle pressures and temperatures: 2-15 kbar and 500-900°C. *Geochim. Cosmochim. Acta* **64**, 2993-3005.

Newton R.C. and Manning C.E. (2009) Hydration state and activity of aqueous silica in H_2O-CO_2 fluids at high pressure and temperature. *Amer. Mineral.* **94**, 1287-1290.

Palmer D.A., Simonson J.M. and Jensen J.P. (2004) Partitioning of electrolytes to steam and their solubilities in steam. In: *Aqueous Systems at Elevated Temperatures and Pressures* (eds. Palmer D.A., Fernàndez-Prini R., and Harvey A.H.), Elsevier, New York, pp. 409–439.

Pan P. and Wood S.A. (1994) Solubility of Pt and Pd sulfides and Au metal in aqueous bi-sulfide solutions. II. Results at 200 to 350°C and saturated vapor pressure. *Mineral. Deposita* **29**, 373-390.

Perfetti E., Thiery R. and Dubessy J. (2008) Equation of state taking into account dipolar interactions and association by hydrogen bonding: II-Modelling liquid–vapour equilibria in the H_2O–H_2S, H_2O–CH_4 and H_2O–CO_2 systems. *Chem. Geol.* **251**, 50-57.

Pester N.J., Ding K. and Seyfried W.E. Jr. (2015) Vapor-liquid partitioning of alkaline earth and transition metals in NaCl-dominated hydrothermal fluids: An experimental study from 360 to 465 °C, near-critical to halite saturated conditions. *Geochim. Cosmochim. Acta* **168**, 111-132.

Phillips G. N. and Evans K. A. (2004) Role of CO_2 in the formation of gold deposits. *Nature* **429**, 860-863.

Pokrovski G.S. (2010) Enhanced vapor-phase transport of tin in hydrothermal systems or experimental artifacts? *J. Volcanol. Geotherm. Res.* **194**, 63-66.

Pokrovski G.S. and Dubessy J. (2015) Stability and abundance of the trisulfur radical ion S_3^- in hydrothermal fluids. *Earth Planet. Sci. Lett.* **411**, 298-309.

Pokrovski G.S., Zakirov I.V., Roux J., Testemale D., Hazemann J-L., Bychkov A.Y. and Golikova G.V. (2002) Experimental study of arsenic speciation in vapor phase to 500°C: Implications for As transport and fractionation in low-density crustal fluids and volcanic gases. *Geochim. Cosmochim. Acta* **66**, 3453-3480.

Pokrovski G.S., Roux J. and Harrichoury J-C. (2005) Fluid density control on vapor-liquid partitioning of metals in hydrothermal systems. *Geology* **33**, 657-660.

Pokrovski G.S., Borisova A.Y. and Harrichoury J-C. (2008) The effect of sulfur on vapor-liquid fractionation of metals in hydrothermal systems. *Earth Planet. Sci. Lett.* **266**, 345-362.

Pokrovski G.S., Tagirov B.R., Schott J., Hazemann J-L. and Proux O. (2009a) A new view on gold speciation in sulfur-bearing hydrothermal fluids from in situ X-ray absorption spectroscopy and quantum-chemical modelling. *Geochim. Cosmochim. Acta* **73**, 5406-5427.

Pokrovski G.S., Tagirov B.R., Schott J., Bazarkina E.F., Hazemann J-L. and Proux O. (2009b) An in situ X-ray absorption spectroscopy study of gold-chloride complexing in hydrothermal fluids. *Chem. Geol.* **259**, 17-29.

Pokrovski G.S., Borisova A.Y. and Bychkov A.Y. (2013) Speciation and transport of metals and metalloids in geological vapors. *Rev. Mineral. Geochem.* **76**, 165-218.

Pokrovski G.S., Akinfiev N.N., Borisova A.Y., Zotov A.V. and Kouzmanov K. (2014) Gold speciation and transport in geological fluids: insights from experiments and physical-chemical modelling. *Geol. Soc. London Spec. Publ.* **402**, 9-70. doi: 10.1144/SP402.4

Pokrovski G.S., Kokh M.A., Guillaume D., Borisova A.Y., Gisquet P., Hazemann J.-L., Lahera E., Del Net W., Proux O., Testemale D., Haigis V., Jonchière R., Seitsonen, A.P., Ferlat G., Vuilleumier R., Saitta A.M., Boiron M.-C. and Dubessy J. (2015) Sulfur radical species form gold deposits on Earth. *Proc. Nat. Acad. Sci USA* **112**, 13484-13489.

Rauchenstein-Martinek K., Wagner T., Walle M. and Heinrich C.A. (2014) Gold concentrations in metamorphic fluids: A LA-ICPMS study of fluid inclusions from the Alpine orogenic belt. *Chem. Geol.* **385**, 70–83.

Rempel K.U., Williams-Jones A.E. and Migdisov A.A. (2009) The partitioning of molybdenum (VI) between aqueous liquid and vapour at temperatures up to 370°C. *Geochim. Cosmochim. Acta* **73**, 3381-3392.

Rempel K.U., Liesbcher A., Heinrich W. and Schettler G. (2011) An experimental investigation of trace element dissolution in carbon dioxide: Applications to the geological storage of CO_2. *Chem. Geol.* **289**, 224–234.

Rempel K.U., Liebscher A., Meixner A., Romer R.L. and Heinrich W. (2012) An experimental study of the elemental and isotopic fractionation of copper between aqueous vapour and liquid to 450°C and 400 bar in the CuCl-NaCl-H_2O and CuCl-NaHS-NaCl-H_2O systems. *Geochim. Cosmochim. Acta* **94**, 199-216.

Richards J.P. (2011) Magmatic to hydrothermal metal fluxes in convergent and collided margins. *Ore Geol. Rev.* **40**, 1-26.

Robie R.A. and Hemingway B.S. (1995) Thermodynamic properties of minerals and related substances at 298.15 K and 1 bar (10^5 Pascals) pressure and at higher temperatures. *U.S. Geol. Survey Bull.* No. 2131, 461p.

Rusk B.G., Reed M.H. and Dilles J.H. (2008) Fluid inclusion evidence for magmatic-hydrothermal fluid evolution in the porphyry copper-molybdenum deposit at Butte, Montana. *Econ. Geol.* **103**, 307-334.

Rusk B., Emsbo P., Hammersli J., Hofstra A., Hunt A., Landis G. and Rye R. (2011) Origin and composition of fluids that form giant porphyry Cu (Mo–Au) deposits. In: *Proc. 11th Biennial SGA Meeting,* Antafogasta, Chile, 414–416.

Ryzhenko B.N., Shvarov Y.V. and Kovalenko N.I. (1997) System Sn-Cl-F-C-S-H-O-Na. Thermodynamic component properties under conditions of the Earth's crust. *Geochem. Int.* **11**, 1149-1153.

Saunier G., Pokrovski G.S. and Poitrasson F. (2011). First experimental determination of iron isotope fractionation between hematite and aqueous solution at hydrothermal conditions. *Geochim. Cosmochim. Acta* **75**, 6629-6654.

Schmidt Mumm A., Oberthür T., Vetter U. and Blenkinsop T.G. (1997) High CO2 content of fluid inclusions in gold mineralisations in the Ashanti Belt, Ghana: a new category of ore forming fluids. *Miner. Deposita* **32**, 107-118.

Seo J.H. and Heinrich C.A. (2013) Selective copper diffusion into quartz-hosted vapour inclusions: Evidence from other host minerals, driving forces, and consequences for Cu-Au ore formation. *Geochim. Cosmochim. Acta* **113**, 60-69.

Shmulovich K., Heinrich W., Möller P. and Dulski P. (2002) Experimental determination of REE fractionation between liquid and vapour in the systems NaCl-H_2O and $CaCl_2$-H_2O up to 450°C. *Contrib. Mineral. Petrol.* **44**, 257-273.

Shock E.L., Sassani D.C., Willis M. and Sverjensky D.A. (1997) Inorganic species in geologic fluids: Correlation among standard molal thermodynamic properties of aqueous ions and hydroxide complexes. *Geochim. Cosmochim. Acta* **61**, 907-950.

Shvarov Y.V. (2008) HCh: New potentialities for the thermodynamic simulation of geochemical systems offered by windows. *Geochem. Int.* **46**(8), 834-839.

Shvarov Y.V. (2015) A suite of programs, OptimA, OptimB, OptimC, and OptimS compatible with the Unitherm database, for deriving the thermodynamic properties of aqueous species from solubility, potentiometry and spectroscopy measurements. *Appl. Geochem.* **55**, 17-27.

Sillitoe R.H. (2010) Porphyry copper systems. *Econ. Geol.* **105**, 3-41.

Simon A.C. and Ripley E.M. (2011). The role of magmatic sulfur in the formation of ore deposits. In: *Sulfur in Magmas and Melts* (eds. Behrens H. and Webster J.D.), *Rev. Miner. Geochem.* **73**, 513- 578.

Spycher N.F. and Reed M.H. (1989) Evolution of a Broadlands-type epithermal ore fluid along alternative P-T paths: Implication for the transport and deposition of base, precious and volatile metals. *Econ. Geol.* **84**, 328-359.

Stefánsson A. (2001) Dissolution of primary minerals of basalt in natural waters: I. Calculation of mineral solubilities from 0°C to 350°C. *Chem. Geol.* **172**, 225-250.

Suleimenov O.M. and Krupp R.E. (1994) Solubility of hydrogen sulfide in pure water and in NaCl solutions, from 20 to 320°C and at saturation pressures. *Geochim. Cosmochim. Acta* **58**, 2433-2444.

Sverjensky D.A., Shock E.L. and Helgeson H.C. (1997) Prediction of the thermodynamic properties of aqueous metal complexes to 1000°C and 5 kb. *Geochim. Cosmochim. Acta* **61**, 1359-1412.

Sverjensky A.D., Harrison B. and Azzolini D. (2014) Water in the deep Earth: The dielectric constant and the solubilities of quartz and corundum to 60 kb and 1200 °C. *Geochim. Cosmochim. Acta* **129**, 125-145.

Tagirov B.R., Baranova N.N. and Bychkova Y.V. (2015) Thermodynamic properties of platinum chloride complexes in aqueous solutions: derivation of consistent parameters from literature data and experiments on Pt(cr) solubility at 400-475°C and 1 kbar. *Geochem. Int.* **53**, 327-340.

Takenouchi S. and Kennedy G.C. (1964) The binary system H_2O-CO_2 at high temperatures and pressures. *Amer. J. Sci.* **262**, 1055-1074.

Tattitch B.C., Candela P.A., Piccoli P.M. and Bodnar R.J. (2015) Copper partitioning between felsic melt and H_2O-CO_2 bearing saline fluids. *Geochim. Cosmochim. Acta* **148**, 81-99.

Testemale D., Brugger J., Liu W., Etschmann B. and Hazemann J.-L. (2009) In-situ X-ray absorption study of Iron (II) speciation in brines up to supercritical conditions. *Chem. Geol.* **264**, 295-310.

Ulrich T. and Mavrogenes J. (2008) An experimental study of the solubility of molybdenum in H2O and KCl-H2O solutions from 500°C to 800°C and 150 to 300 MPa. *Geochim. Cosmochim. Acta* **72**, 2316-2330.

Webster J.D., Holloway J.R. and Hervig R.L. (1989) Partitioning of lithophile trace elements between H_2O and H_2O+CO_2 fluids and topaz rhyolite melt. *Econ. Geol.* **84**, 116-134.

White D.E. (1973) Characteristics of geothermal resources In: *Geothermal Energy* (eds. Pernger P. and Otte C.), Stanford Univ Press, pp. 69-95.

Wood S.A., Mountain B.W. and Pan P. (1992) The aqueous geochemistry of platinum, palladium and gold: recent experimental constraints and a re-evaluation of theoretical predictions. *Can. Miner*. **30**, 955-982.

Wood S.A., Pan P., Zhang Y. and Mucci A. (1994) The solubility of Pt and Pd sulfide and Au in bisulfide solutions. I. Results at 25-90°C and 1 bar pressure. *Mineral. Deposita* **29**, 309-317.

Wood S.A. and Samson I.M. (1998) Solubility of ore minerals and complexation of ore metals in hydrothermal solutions. *Rev. Econ. Geol.* **10**, 33-80.

Yang Z., Yang X., Xu Z. and Yang N. (2010). Molecular simulations of structures and solvation free energies of passivated gold nanoparticles in supercritical CO_2. *J. Chem. Phys.* **133**, 094702.

Zakirov I.V., Stretenskaja N.G., Aranovich L.Y. and Volchenkova V.A. (2007) Solubility of NaCl in CO_2 at high pressure and temperature: first experimental measurements. *Geochim. Cosmochim. Acta* **71**, 4251-4255.

Zhang L., Audétat A. and Dolejs D. (2012) Solubility of molybdenite (MoS_2) in aqueous fluids at 600-800°C, 200 MPa: a synthetic fluid inclusions study. *Geochim. Cosmochim. Acta* **77**, 175-185.

Zotov A., Kudrin A.V., Levin K.A., Shikina D. and Var'yash L. (1995) Experimental studies of the solubility and complexing of selected ore elements (Au, Ag, Cu, Mo, As, Sb, Hg) in aqueous solutions. In: *Fluids in the Crust*: *Equilibrium and Transport Properties* (eds. Shmulovich K.I., Yardley B.W.D., Gonchar G.G,). Chapman and Hall, London, pp. 97-136.

Table 1. Metal and volatile concentrations in the coexisting vapor and liquid phases and the corresponding vapor-liquid partition coefficients at 350°C at saturated vapor pressure in the S-free system (experiment #m31) [a].

Sample number	**1**	**2**	**3**	**4**	**5**	**6**
Temperature, °C	349	348	349	349	349	349
Pressure, bar	144.4	138.8	175.2	173.6	231.9	229.4
Duration, days	2	4	7	10	14	16
Vapor						
pH of condensate [b]	1.7	1.8	2.0	2.1	2.4	2.3
CO_2, wt%	0	0	23.65	29.41	56.71	56.56
Cl, ppm	696	522	325	208	103	95
Na, ppm	1.47	1.83	2.58	1.72	2.49	1.89
K, ppm	1.60	1.72	2.54	1.57	2.62	1.75
Si, ppm	2.81	3.87	3.57	2.60	2.35	1.43
Zn, ppm	0.10	0.18	0.11	0.06	0.22	0.13
Cu, ppm	0.55	0.30	0.31	0.19	0.215	0.22
Fe, ppm	1.79	0.45	0.52	0.23	0.15	0.13
Mo, ppm	0.0035	0.0042	0.018	0.0038	0.010	0.020
Sn, ppm	0.033	0.011	0.0061	0.0022	0.0018	0.0021
Pt, ppm	0.000053	0.000071	0.000075	0.000024	0.000047	0.000035
Au, ppm	0.0023	0.00043	0.0015	0.00068	0.00020	0.00052
Liquid						
pH of condensate [b]	1.7	2.5	2.7	2.6	2.7	3.5
CO_2, wt%	0	0	0.84	0.84	2.70	4.13
Cl, ppm	40605	44268	46896	51321	58363	60219
Na, ppm	12937	13907	14857	16136	17931	18893
K, ppm	20435	21880	23175	25176	27823	29582
Si, ppm	249	335	371	390	382	373
Zn, ppm	671	717	778	849	969	1010
Cu, ppm	704	759	809	885	1005	1073
Fe, ppm	1558	1666	1871	2131	2457	2621
Mo, ppm	1002	1071.8	1108	1194	1330	1366
Sn, ppm	0.0051	0.0028	<0.001	0.0016	<0.001	<0.001
Pt, ppm	0.22	0.11	0.0024	0.0088	0.00078	0.00081
Au, ppm	5.98	7.36	1.47	1.17	0.38	0.68
$Log_{10}K$ vapor/liquid						
CO2	NA	NA	1.45	1.54	1.32	1.14
Cl	-1.77	-1.93	-2.16	-2.39	-2.75	-2.80
Na	-3.94	-3.88	-3.76	-3.97	-3.86	-4.00
K	-4.11	-4.10	-3.96	-4.21	-4.03	-4.23
Si	-1.95	-1.94	-2.02	-2.18	-2.21	-2.42
Zn	-3.83	-3.59	-3.84	-4.13	-3.63	-3.90
Cu	-3.11	-3.40	-3.42	-3.68	-3.67	-3.68
Fe	-2.94	-3.57	-3.56	-3.97	-4.23	-4.29
Mo	-5.46	-5.41	-4.80	-5.50	-5.10	-4.83
Sn	0.81	0.58	NA	0.13	NA	NA
Pt	-3.62	-3.20	-1.51	-2.56	-1.22	-1.37
Au	-3.42	-4.24	-3.00	-3.24	-3.27	-3.12

[a] Initial system composition: aqueous solution 0.5m NaCl - 0.5m KCl – 0.1m HCl - 0.01m $ZnCl_2$ - 0.01m CuCl - 0.01m Na_2MoO_4; solid phases in excess: SnO_2, SiO_2, Fe_2O_3, Fe_3O_4, Pt, Au.

[b] pH of sampled CO_2-degassed condensate at ambient *T* and *P*.

NA = not applicable because of below-detection-limit concentrations.

Table 2. Metal and volatile concentrations in the coexisting vapor and liquid phases and the corresponding vapor-liquid partition coefficients at 350°C at saturated vapor pressure in the S-bearing system (experiment #m28) [a].

sample number	**1**	**2**	**3**	**4**	**5**	**6**	**7**
Temperature, ˚C	347	346	349	349	351	349	349
Pressure, bars	148.0	143.0	151.0	217.0	220.0	270.0	246.0
Duration, days	2	7	7	15	21	28	31
Vapor							
CO_2, wt% vapor	0	0	0	45.10	40.10	51.30	50.60
H_2S, mol/kg	ND	0.032	0.61	0.11	ND	ND	ND
S total, mol/kg	0.59	0.044	0.70	0.11	0.11	0.038	0.080
S reduced, mol/kg	0.46	0.039	0.69	0.18	0.14	0.090	0.079
Cl, ppm	159.5	131.2	33.0	106.4	31.9	46.1	39.0
K, ppm	16.0	21.5	22.3	12.9	14.5	23.1	13.3
Cu, ppm	0.46	0.056	0.40	0.44	0.18	0.066	0.047
Fe, ppm	5.25	0.69	0.73	0.25	1.32	0.20	0.12
Mo, ppm	0.013	0.0097	0.0072	0.0023	0.0073	0.0028	0.0037
Sn, ppm [b]	0.0014	<0.006	<0.007	0.00023	<0.007	<0.010	<0.016
Pt, ppm	0.00074	0.00014	0.00078	0.00023	0.00046	0.00072	0.00033
Au, ppm [c]	0.049	0.011	0.097	0.21	0.048	0.056	0.057
Liquid							
CO_2, wt% liquid	0	0	0	6.40	4.20	3.50	3.00
H_2S, mol/kg	ND	≤0.004	0.047	0.012	ND	ND	ND
S total, mol/kg	0.23	0.23	0.34	0.28	0.32	0.28	0.28
S reduced, mol/kg	0.034	0.0060	0.048	0.024	0.016	0.018	0.011
Cl, ppm	41122	43958	39350	38995	45376	48212	47503
K, ppm	58647	58647	58256	60602	68422	71940	74286
Cu, ppm	2.8	25.4	1.3	3.2	7.2	6.7	8.3
Fe, ppm	7.6	16.3	5.6	8.6	11.7	12.1	12.8
Mo, ppm	0.26	0.10	0.10	0.032	0.083	0.056	0.057
Sn, ppm [b]	0.0063	0.0045	0.0018	0.00049	0.016	0.0036	<0.006
Pt, ppm	0.00058	0.00014	0.00024	0.00013	0.00043	0.0017	0.00020
Au, ppm	10.6	1.51	4.51	0.95	0.96	4.52	0.57
$\log_{10}K$ vapor/liquid							
CO2				0.85	0.98	1.17	1.23
S reduced	1.13	0.81	1.16	0.86	0.93	0.70	0.86
Cl	-2.41	-2.53	-3.08	-2.56	-3.15	-3.02	-3.09
K	-3.56	-3.44	-3.42	-3.67	-3.67	-3.49	-3.75
Cu	-0.77	-2.65	-0.51	-0.86	-1.60	-2.01	-2.25
Fe	*-0.16*	-1.37	-0.89	-1.54	-0.95	-1.77	-2.02
Mo	-1.31	-0.99	-1.15	-1.14	-1.06	-1.31	-1.19
Sn	0.64	NA	NA	0.33	NA	NA	NA
Pt	0.10	0.00	0.51	0.23	0.03	-0.38	0.22
Au	-2.33	-2.16	-1.67	-0.65	-1.30	-1.91	-1.00

[a] The first experiment was stopped after sample 2. Initial system composition for samples 1 and 2: aqueous solution 0.97m KCl – 0.08m HCl - 0.15m $K_2S_2O_3$; solid phases in excess: SnO_2, SiO_2, FeS_2, $CuFeS_2$, MoS_2, PtS_2, Au. Then a new experiment was started from sample 3. Initial system composition for samples 3 to 7: aqueous solution 1.00m KCl – 0.10m HCl - 0.20m $K_2S_2O_3$; solid phases in excess: SnO_2, SiO_2, FeS_2, $CuFeS_2$, MoS_2, PtS_2, Au.

[b] most Sn analyses are close to the detection limit, which varies from one sample to another.

[c] error on Au vapor-phase concentrations is ±40% of the value.

NA = not applicable because of below-detection-limit concentrations.

ND = not determined.

Table 3. Vapor-liquid partitioning and apparent Henry constants of **CO_2** at 350°C derived in this study.

Sample number	P total, bar	CO_2 vap, wt%	CO_2 liq, wt%	X CO_2 vap	P CO_2 vap, bar	m CO_2 liq, mol/kg H_2O	Total salinity, wt%	K_h CO_2
28_4	217.0	45.1	6.40	0.252	54.6	1.78	12.1	30.6
28_5	220.0	40.1	4.20	0.215	47.4	1.16	13.6	40.8
28_6	270.0	51.3	3.50	0.301	81.3	0.97	14.3	84.1
28_6	246.0	50.6	3.00	0.296	72.7	0.83	14.9	87.6
31_3	175.2	23.7	0.84	0.113	35.2	0.21	9.0	93.2
31_4	173.6	29.4	0.84	0.146	33.6	0.21	9.8	119.1
31_5	231.9	56.7	2.70	0.349	91.9	0.71	11.0	114.6
31_6	229.4	56.6	4.13	0.348	89.4	1.10	11.5	72.2
error	*±1.0*	*±0.1*	*±0.10*					*±5.0*

Table 4. Vapor-liquid partitioning and apparent Henry constants of **H_2S** at 350°C derived in this study.

Sample number	P total, bar	H_2S vap, mol/kg	H_2S liq, mol/kg	X H_2S vap	P H_2S vap, bar	m H_2S liq, mol/kg H_2O	Total salinity, wt%	K_h H_2S
28_1	148	0.46	0.034	0.0083	1.22	0.039	11.6	31.8
28_2	143	0.039	0.0060	0.00070	0.10	0.0068	11.5	14.8
28_3	151	0.69	0.048	0.012	1.84	0.054	11.6	33.9
28_4	217	0.18	0.024	0.0043	0.93	0.029	12.1	31.5
28_5	220	0.14	0.016	0.0032	0.71	0.019	13.6	36.4
28_6	270	0.090	0.018	0.0023	0.63	0.022	14.3	28.6
28_7	246	0.079	0.011	0.0020	0.50	0.013	14.9	37.2
error	*±1*	*±10%*	*±10%*					*±5.0*

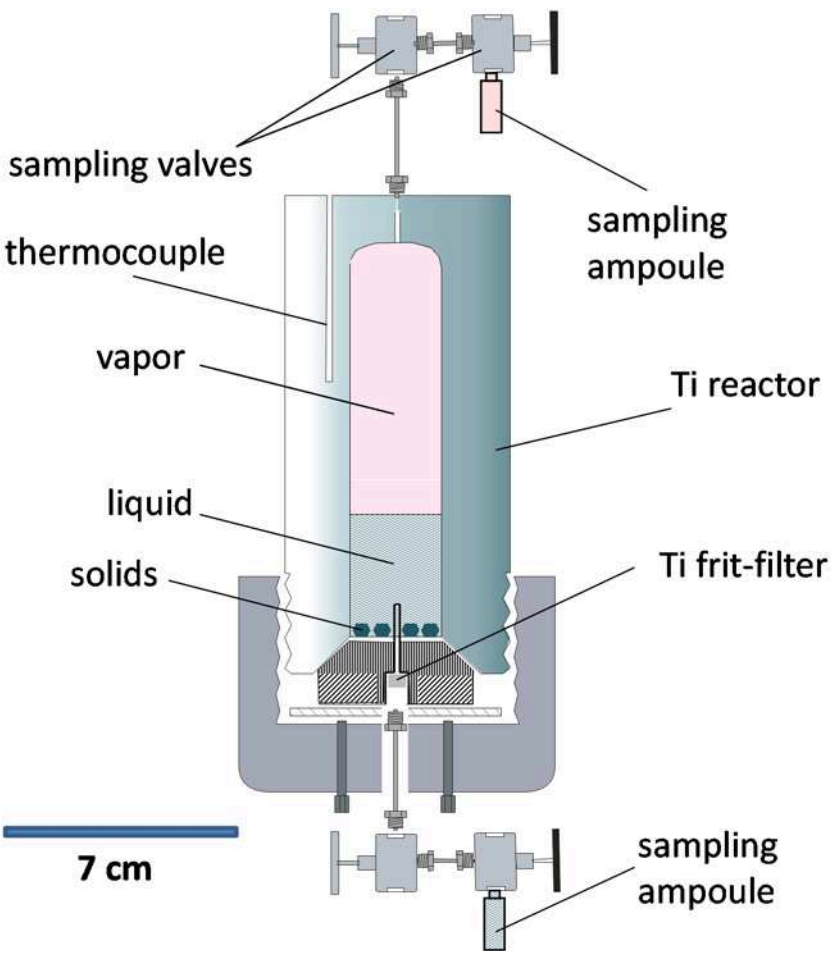

Fig. 1. Schematic drawing of the titanium reactor used in this study for vapor-liquid partitioning measurements.

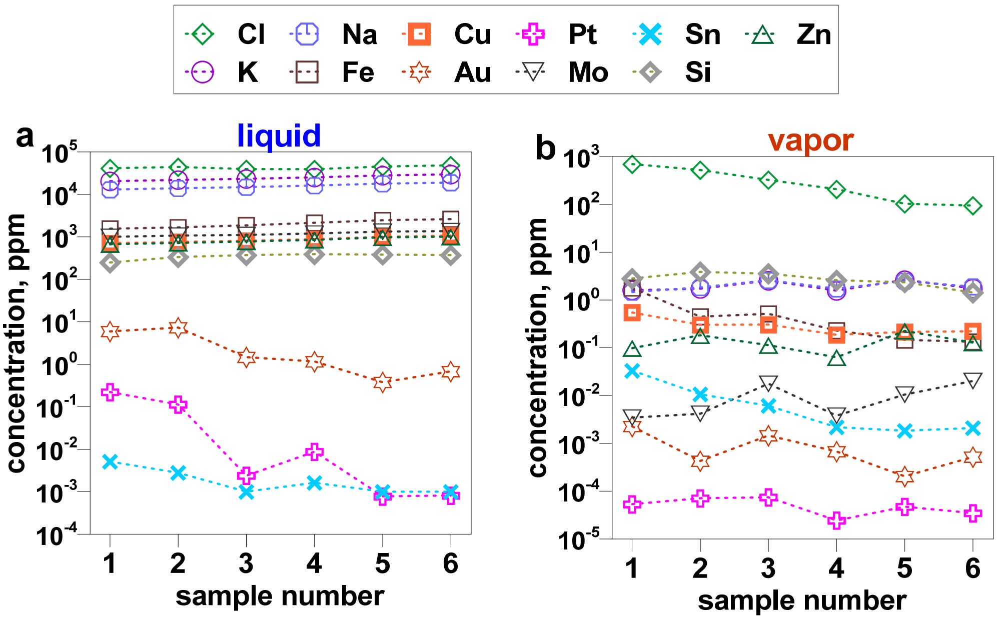

Fig. 2. Evolution of the concentrations of the indicated chemical elements in the coexisting liquid (a) and vapor (b) phases as a function of sampling number for the S-free experiment #m31. Analytical errors are less than the symbol size (except for Sn for which most data points correspond to the limit of detection). Dashed lines connecting the data points are drawn to guide the eye.

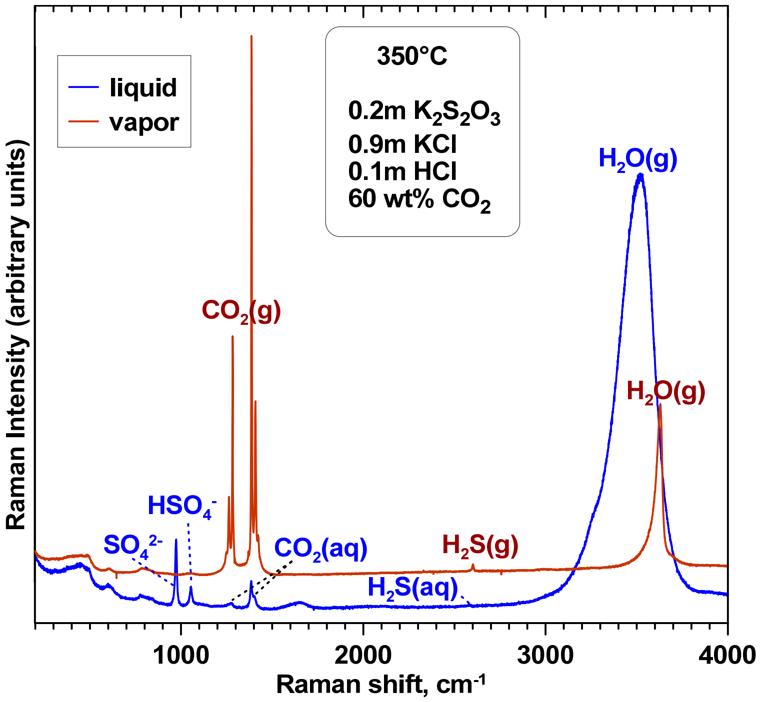

Fig. 3. Raman spectra, at 457.93 nm excitation, of the coexisting liquid and vapor phases at 350°C in the system of the total indicated composition similar to that used in S-bearing experiment #m28. Spectra are normalized to an acquisition time of 20 s. The detected aqueous and vapor S- and C-bearing species are shown. No S or C forms other than (bi)sulfate, hydrogen sulfide and carbon dioxide were detected.

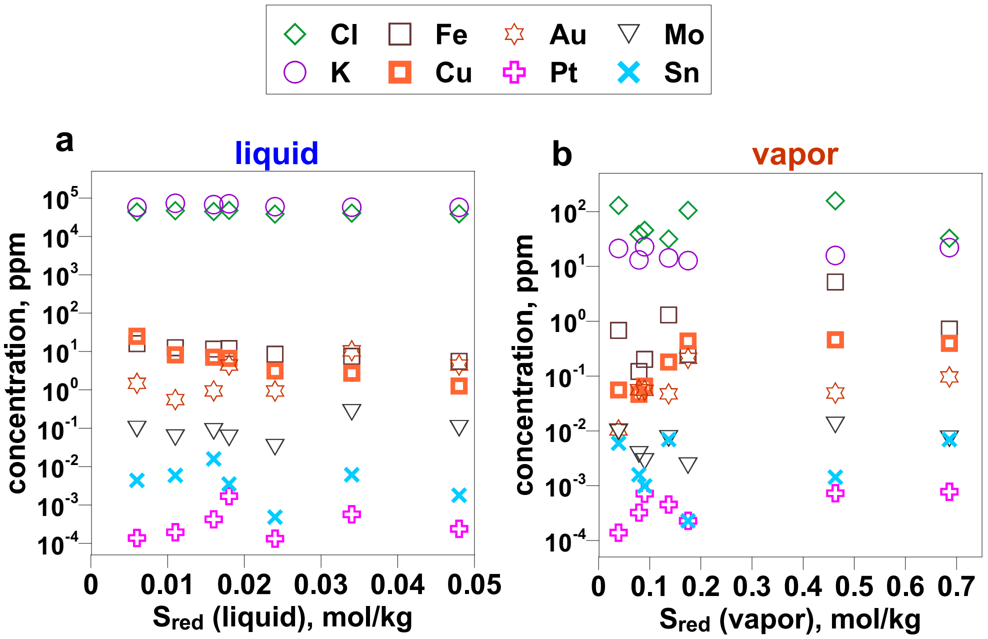

Fig. 4. Evolution of the concentrations of the indicated chemical elements in the coexisting liquid (a) and vapor (b) phases as a function of reduced sulfur concentration in the corresponding phase for the S-bearing experiment #m28. Analytical errors are less than the symbol size (except for Sn for which most data points in the vapor phase correspond to the limit of detection).

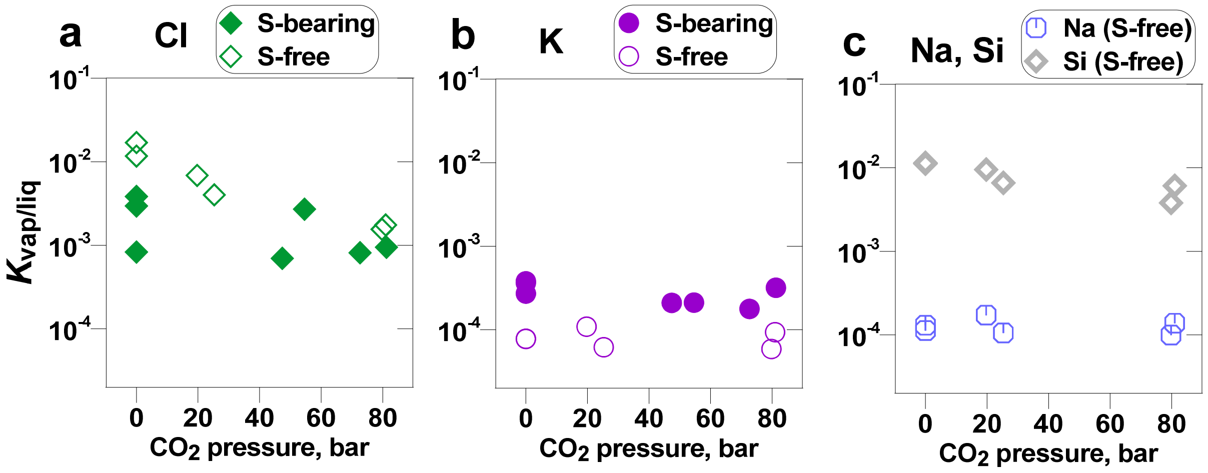

Fig. 5. Bulk vapor-liquid partition coefficients (defined by equation 8) for Cl, K, Na and Si as a function of CO_2 pressure in the S-free (#m31) and S-bearing (#m28) systems. Error bards of individual data points are comparable to the symbol size.

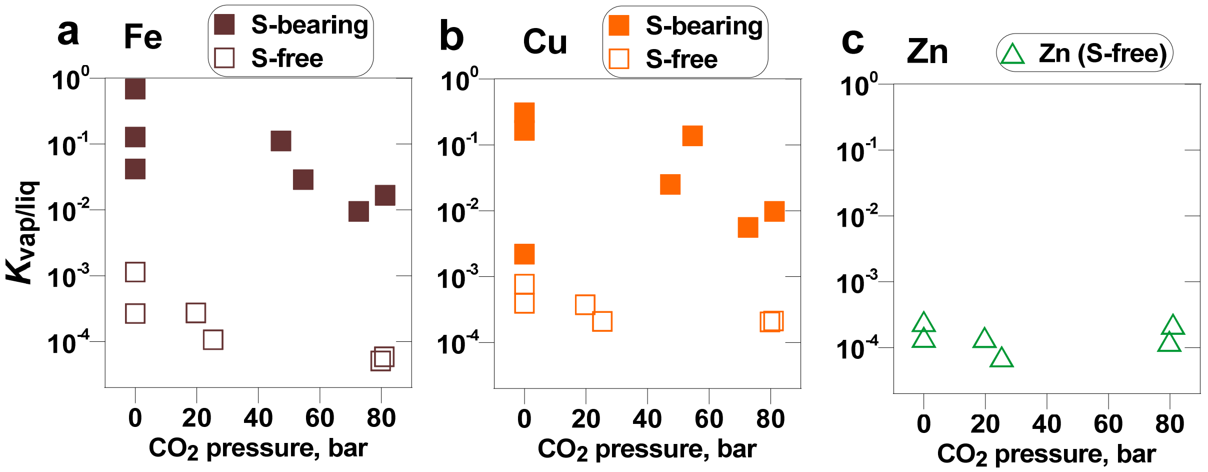

Fig. 6. Bulk vapor-liquid partition coefficients for Fe, Cu and Zn as a function of CO_2 pressure in the S-free (#m31) and S-bearing (#m28) systems.

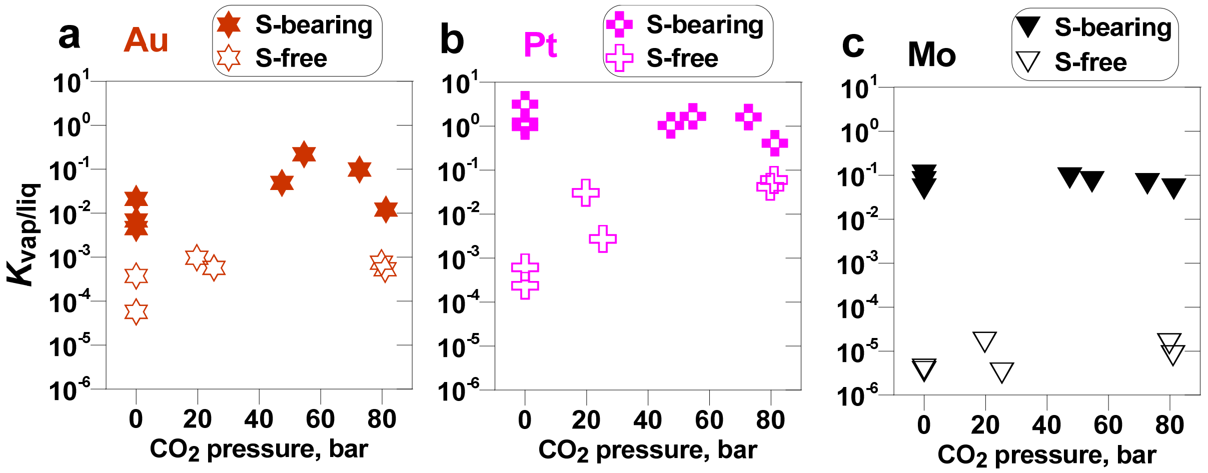

Fig. 7. Bulk vapor-liquid partition coefficients for Au, Pt and Mo as a function of CO_2 pressure in the S-free (#m31) and S-bearing (#m28) systems.

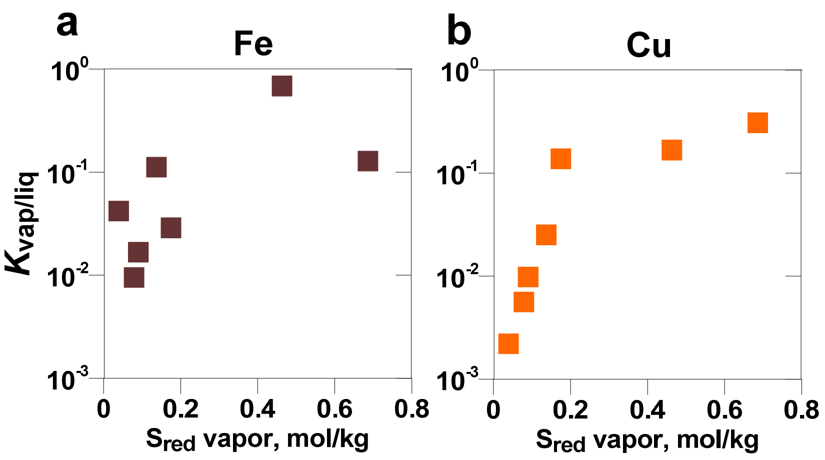

Fig. 8. Bulk vapor-liquid partition coefficients of Fe and Cu as a function of reduced sulfur concentration in the vapor phase (experiment #m28).

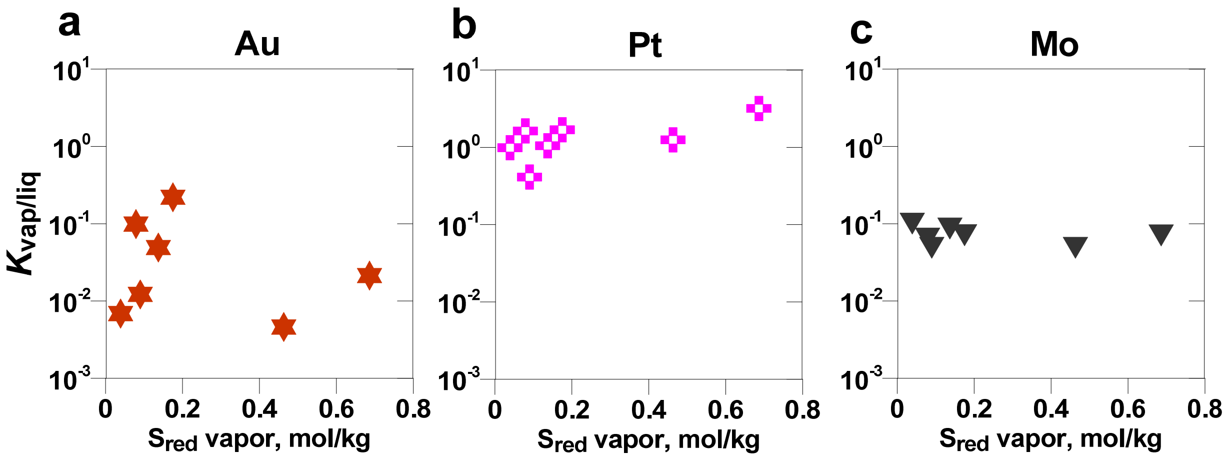

Fig. 9. Bulk vapor-liquid partition coefficients of Au, Pt and Mo as a function of reduced sulfur concentration in the vapor phase (experiment #m28).

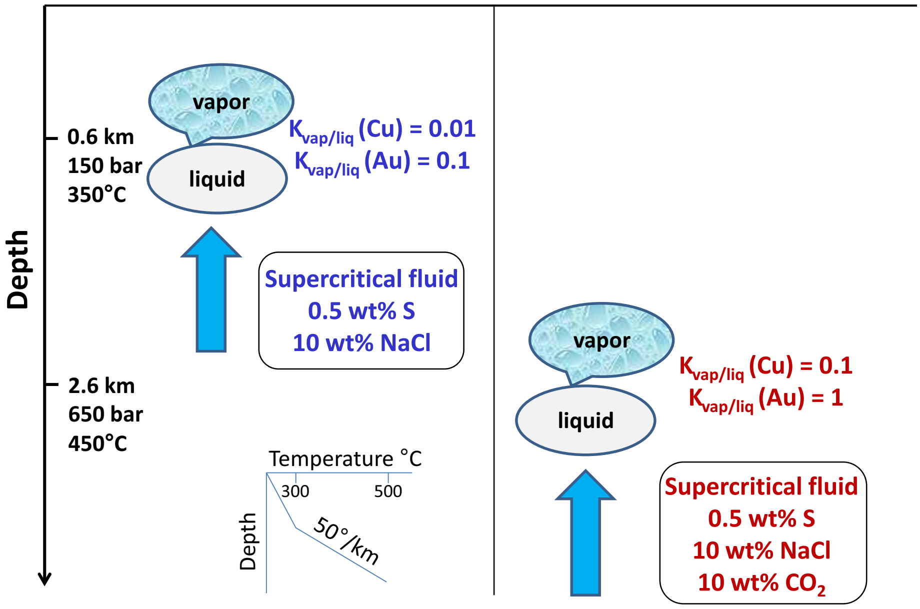

Fig. 10. Schematic illustration of the effect of CO_2 on the *T*-*P*-depth conditions and vapor-liquid partitioning of Cu and Au during an immiscibility phenomenon for a supercritical aqueous salt- and sulfur-bearing fluid, typical of porphyry-epithermal settings (see section 5).

Supplementary Electronic Annex (EA)

Supplementary Table EA1. Values of pH measured in vapor-phase condensates at ambient conditions in S-free experiment #m31 and the corresponding total Cl concentrations.

Sample number	pH (20°C)[a]	Cl from pH, ppm [b]	Cl from HPLC, ppm [c]
1	1.678	744	695
2	1.814	544	522
3	1.952	395	425
4	2.089	288	294
5	2.388	145	238
6	2.318	170	217

[a] measured using a combination glass electrode calibrated on H^+ activity scale using the NIST phthalate (pH = 4.00), phosphate (pH = 6.88) and borate (pH = 9.20) aqueous buffers.

[b] calculated from the measured pH and assuming that $[H^+] = [Cl^-]$ and that HCl^0, which is the major volatile Cl form in the experiment, is fully dissociated at ambient conditions. The contribution of metal chloride vapor-phase species to the total Cl content is less than 5 ppm (Table 1 of main text).

[c] measured in vapor-phase condensates as Cl^- by High Pressure Liquid Chromatography (HPLC).

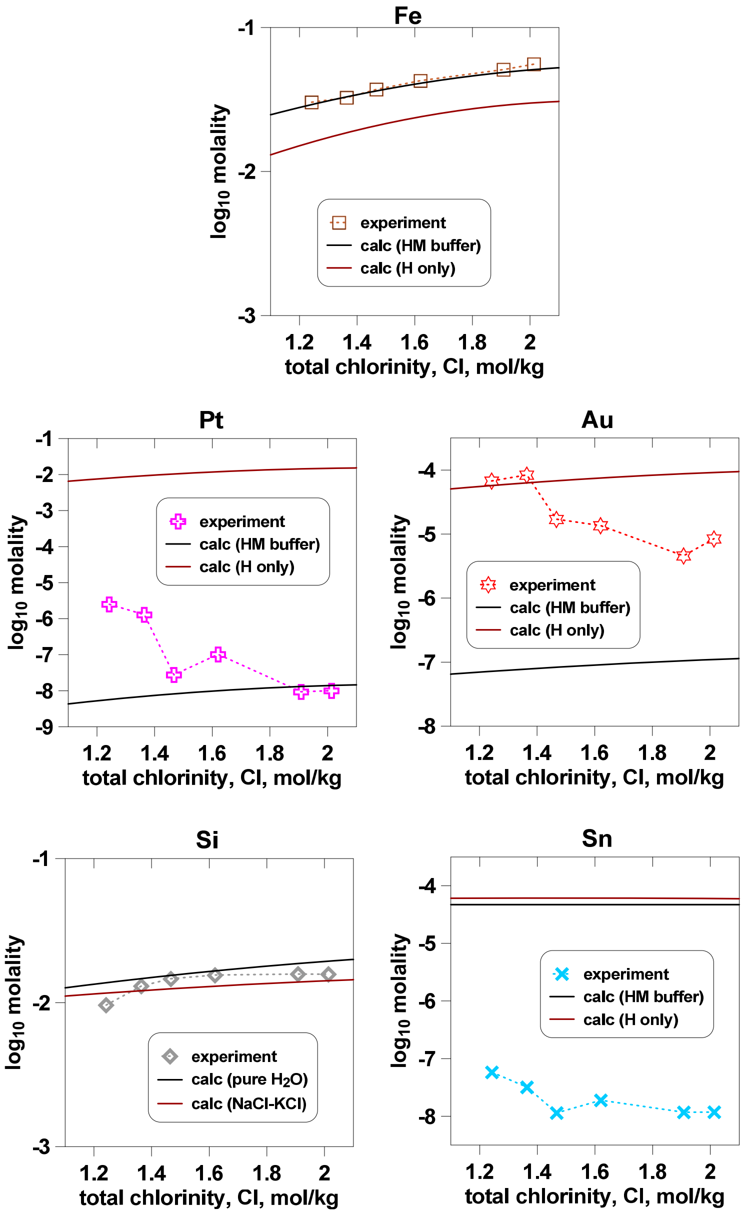

Supplementary Figure EA1. Comparisons between the measured Fe, Pt, Au, Si, and Sn concentrations (symbols) in the liquid phase of the S-free experiment (#m31) and calculated solubilities of Fe_2O_3, Pt metal, Au metal, SnO_2, and quartz in solution using the available thermodynamic data (discussed in section 2.5 of main text) and assuming either equilibrium with the hematite-magnetite mineral assemblage (HM buffer, black curve) or with hematite only (H only, brick-red curve). For silica, there is no effect of redox buffer on the solubility; the calculated concentrations are for pure water (black curve) and H_2O-KCl-NaCl solutions using published Sechenov coefficients for dissolved silica (brick-red curve). The total chlorinity increase in the subsequent samples is owing to the change in mass balance between vapor and liquid upon sampling. The total duration of the experiment (between the lowest and highest salinity data point) is 16 days.

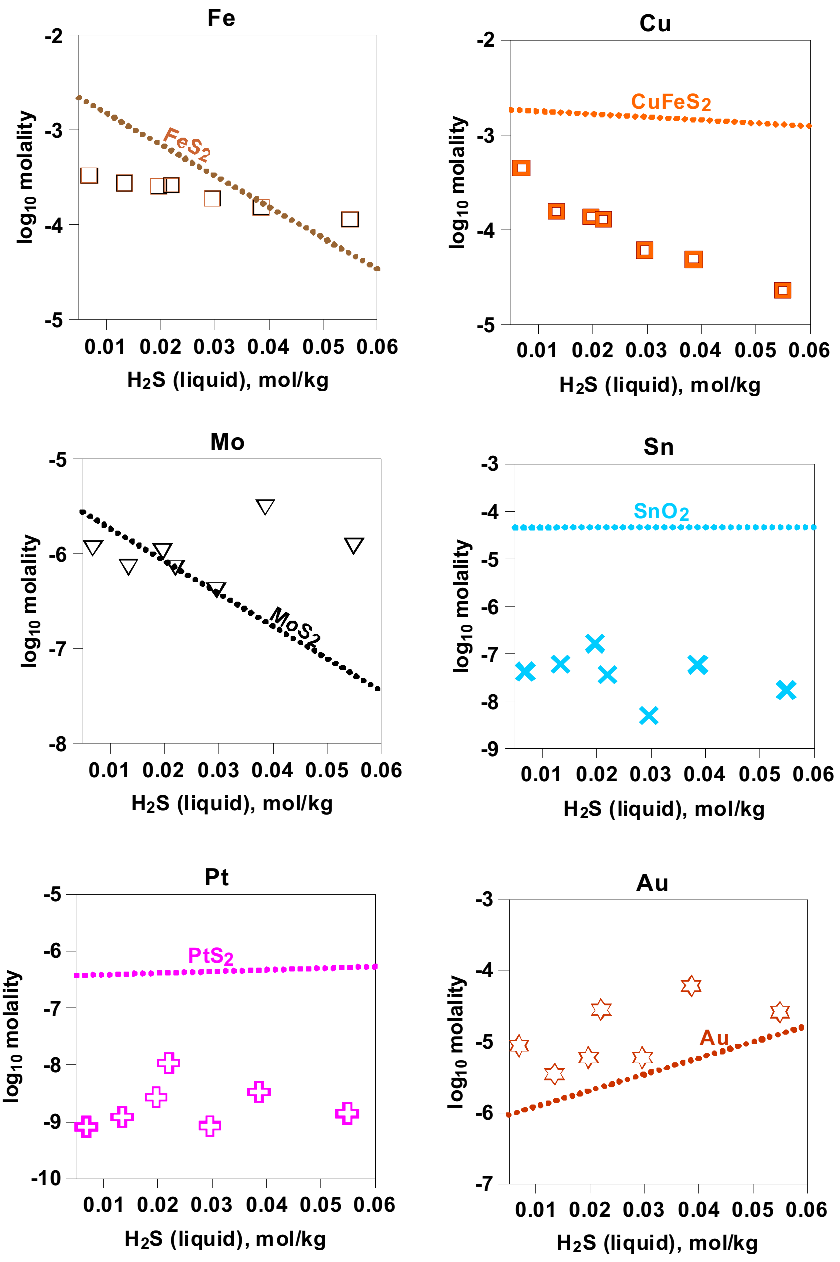

Supplementary Figure EA2. Comparisons between the measured Fe, Cu, Mon Sn, Pt and Au concentrations (symbols) in the liquid phase of the S-bearing experiment (#m28) and calculated solubilities of FeS_2, $CuFeS_2$, MoS_2, SnO_2, PtS_2 and Au metal in solution (dotted curves) using the available thermodynamic data for minerals and aqueous metal species discussed in section 2.5 (main text). The uncertainties on calculated solubilities are typically 1 log unit of metal concentration value for Fe, Cu and Mo, 0.5 log unit for Au, and up to 2 log unit for Sn and Pt.

Chapitre 5. Conclusions et perspectives

5.1. Conclusion générale

Ce travail de thèse avait pour but d'explorer l'effet du CO_2 sur le comportement de divers métaux dans les fluides géologiques de haute température et pression. Cette étude a nécessité un grand effort de mise en œuvre de diverses méthodes expérimentales et analytiques afin d'apprivoiser de tels fluides complexes aux conditions qui ne sont pas facilement accessibles et qui n'ont jamais été étudiées auparavant.

Grâce à la combinaison de ces méthodes expérimentales et analytiques avec une approche de modélisation, nous avons pu obtenir les premières données directes sur la solubilité d'un grand ensemble de métaux d'intérêt économique, comme Fe, Cu, Zn, Sn, Mo, Pt et Au, dans les fluides supercritiques riches en CO_2 (jusqu'à 50 wt%), soufre et sels qui sont typiques des gisements hydrothermaux de ces métaux. Contrairement au paradigme préexistant, la présence du CO_2 n'affaiblit pas toujours le potentiel de transport des métaux par un fluide supercritique. Les solubilités des métaux dans les fluides H_2O-CO_2 peuvent présenter des tendances différentes selon les métaux considérés, la concentration de soufre et de chlore et de la spéciation chimique qui en résulte. Ces nouvelles données ont été interprétées à l'aide d'un modèle électrostatique simple, qui ne nécessite pas de paramètres ajustables et qui est basé sur la variation de la constante diélectrique du fluide mixte et la nature et la stabilité des complexes métalliques dominants dans le fluide aqueux sans CO_2. Quelle que soit l'identité du ligand (HS^-, S_3^-, Cl^-, OH^-), la tendance générale est le renforcement de la stabilité des complexes neutres des métaux avec la teneur croissante en CO_2 dans le fluide. Cela conduit à des comportements contrastés de la solubilité des métaux dont la spéciation est dominée par des espèces neutres ou chargées, en fonction de la nature chimique du soluté (du métal dans notre cas) et de la composition du fluide. Il est à noter qu'une modélisation thermodynamique classique basée sur les propriétés des fluides aqueux, prédit des solubilités constantes de toutes ces espèces quelle que soit la concentration du CO_2, contrairement aux observations expérimentales de cette étude.

Notre modèle, appliqué aux contextes naturels, suggère que la présence de grandes quantités du CO_2 (de 20 à 70 wt%) dans les fluides orogéniques typiques aura pour effet d'enrichir le fluide en Fe par rapport au Cu, tandis que la solubilité d'or est considérablement affaiblie dans les fluides riches en soufre aux pH neutres (où des espèces chargées bi-sulfurées dominent), mais elle n'est pas beaucoup affectée dans les fluides pauvres en soufre aux pH plus acides (où les espèces neutres mono-sulfurées prédominent). Par conséquent, les capacités de tels fluides à transporter l'or restent comparables avec celles des fluides aqueux. Nos prédictions sont en accord avec la grande abondance de Fe (pyrite et pyrrhotine) et les faibles teneurs en Cu dans la plupart des gisements d'or orogénique caractérisés par de fortes teneurs en CO_2 (jusqu'à ~90 wt%). Dans les fluides magmatiques-hydrothermaux typiques des gisements de type porphyre Cu-Au-Mo, avec des teneurs généralement plus faibles de CO_2 (<20 wt%), le fractionnement des métaux induit par le CO_2 est plus faible et peut être masqué par d'autres facteurs multiples liés à l'évolution et à la composition du magma et des fluides qu'il génère.

Les solubilités d'autres métaux étudiés (Pt, Sn, Mo, Zn) montrent des tendances moins contrastées avec l'ajout du CO_2 dans les systèmes expérimentaux (une solubilité soit constante soit modérément croissante). Pour interpréter ces tendances de manière rigoureuse, il faudra tout d'abord une bien meilleure connaissance de la spéciation de ces métaux dans les fluides aqueux de haute température et haute pression. Il semble qu'aucun des métaux étudiés (à l'exception possible de Sn) ne forme pas de complexes (bi)carbonatés dans les fluides hydrothermaux supercritiques aux conditions typiques de la formation des gisements.

Ce travail a également permis de générer les premières données directes sur le fractionnement vapeur-liquide d'un ensemble des métaux de natures chimiques différentes dans le système biphasé H_2O-sels-S-CO_2 le long de la courbe de coexistence des deux phases aux températures (350°C), pressions (de 130 à 300 bar), et compositions de la vapeur (S jusqu'à ~ 3 wt% et CO_2 jusqu'à 50 wt%) typiques des fluides naturels qui subissent des phénomènes d'ébullition et d'immiscibilité vapeur-liquide dans de nombreux gisements hydrothermaux.

Nos données dans le système sans soufre et sans CO_2 montrent des coefficients de partage vapeur-liquide ($K_{v/l}$) largement en faveur du liquide et variant dans la gamme 10^{-5}-10^{-2} dans l'ordre croissant pour Mo < Na, K < Zn, Fe, Cu, Au, Pt < Si (<Sn). En présence de 0.1 à 1 wt% de H_2S en phase vapeur, le partage vapeur-liquide de Mo, Au, Pt augmente de 2 à 4 ordres de grandeur, celui de Cu et Fe d'environ 1 à 2 ordres de grandeur, tandis que celui des métaux alcalins n'est pas affecté. Ces résultats sont en bon accord avec les expériences de laboratoire en l'absence de CO_2 publiées dans la littérature et les données sur des inclusions fluides naturelles pauvres en CO_2. Ils confirment le rôle clé joué par le soufre réduit sur le fractionnement vapeur-liquide de la plupart des métaux chalcophiles (i.e., ceux ayant une forte affinité chimique pour le soufre, comme Au, Pt, Mo, Cu).

L'effet du CO_2 sur le fractionnement vapeur-liquide des métaux dans les systèmes sans soufre est de diminuer légèrement la volatilité de Fe et Cu (moins 1 unité logarithmique à 50 wt% de CO_2 en phase vapeur), tandis que les coefficients de partage des autres métaux (Zn, Mo, Si, K, Na, Sn) restent presque inchangés. En revanche, la présence de faibles teneurs de monoxyde de carbone (CO) semble augmenter les coefficients de partage de Au et Pt en faveur de la phase vapeur de 1 à 2 ordres de grandeur. Dans les systèmes riches en S, aucun effet du CO_2 sur le partitionnement vapeur-liquide n'a pu être détecté dans les limites des incertitudes expérimentales et analytiques pour aucun des métaux, attestant du contrôle dominant de H_2S sur la volatilité des métaux dans nos expériences et de l'absence de solvatation spécifique ou de complexation directe par le CO_2.

Ainsi, l'effet majeur du CO_2 sur le fractionnement vapeur-liquide des métaux, au moins dans les conditions de notre étude, apparaît comme essentiellement indirect, menant à l'extension du domaine d'immiscibilité vapeur-liquide à des températures et pressions plus élevées par rapport à celles dans un système H_2O-S-sels. Ce phénomène favorise le partitionnement des métaux chalcophiles (Au, Pt, Mo, ± Cu) en phase vapeur et la concentration des métaux alcalins et de base (Na, K, Fe ± Cu) dans le liquide riche en sels. Par conséquent, la présence du CO_2 dans le fluide va influencer à la fois la profondeur de dépôt des minerais et la zonation verticale des métaux dans les systèmes hydrothermaux.

5.2. Perspectives

Cette étude a démontré que nous connaissions encore très peu sur les fluides géologiques opérant à haute température et haute pression dans les profondeurs de notre planète. Nos travaux exploratoires sur les fluides riches en CO_2 ont posé plusieurs questions qui ouvrent des perspectives excitantes pour des études futures.

Tout d'abord, en ce qui concerne les fluides aqueux, la spéciation chimique et les propriétés thermodynamiques des espèces aqueuses de Pt, Sn, Mo et bien d'autres métaux de haute valeur technogique (Re, W, autres métaux du groupe du platine) restent peu connues à ce jour dans les fluides de haute température et haute pression aux conditions typiques de formation des gisements de ces métaux. Par exemple, même la stabilité/solubilité des complexes majeures de ces métaux ($Sn(OH)_4^0$, $KHMoO_4^0$, ou $Pt(HS)_2^0$) est sujette à de grandes incertitudes (jusqu'à 2 ou 3 ordres de grandeur en termes de concentration du métal). D'après notre étude, l'étain pourrait également former des complexes (bi)carbonatés dans les fluides riches en CO_2. Cette possibilité devrait également être vérifiée pour d'autres métaux appelés durs qui ont une affinité élevée pour des ligands durs comme le carbonate (e.g., les terres rares, le zirconium, le tantale, le niobium). De telles données pourraient être acquises via une approche combinée de mesures de solubilité, d'études spectroscopiques in-situ (par exemple par spectroscopies d'absorption de rayons X et UV-visible) et de simulations de dynamique moléculaire des structures et stabilités de complexes, couplées à des modèles thermodynamiques (e.g. Pokrovski et al., 2013, 2015).

L'effet du CO_2 (et du CH_4) sur le fractionnement vapeur-liquide des métaux reste également à explorer de manière plus systématique en se basant sur les acquis de notre première étude. Nos expériences exploratoires de partage vapeur-liquide étaient conçues de telle façon que l'augmentation de la concentration du CO_2 dans la phase vapeur était accompagnée d'une chute de la concentration de H_2S due à la nécessité de prélever la phase vapeur. Ce changement des deux paramètres clés en même temps (CO_2 et H_2S) a pu masquer certaines tendances fines de partage des métaux. Par conséquent, de futures expériences doivent être conçues de sorte qu'un des deux paramètres reste fixe, par exemple, en utilisant des assemblages de sulfures de fer en excès, fixant la fugacité de H_2S tout au long de l'essai expérimental, ou bien en faisant varier la teneur en H_2S en maintenant une concentration constante de CO_2 dans le réacteur).

La mobilité des métaux en phase vapeur de CO_2 supercritique aux températures du stockage géologique du CO_2 (<200°C) nécessite également une attention particulière (e.g., Rempel et al., 2010; Jiin-Shuh et al., 2015; Mavhengere et al., 2015). Il est bien connu que les phénomènes de solvatation sélective par le CO_2 supercritique sont plus prononcées à plus basse température et plus fortes densités du CO_2, une propriété du CO_2 servant dans l'industrie pour la purification de composés organiques et l'extraction de métaux (e.g. Glennon et al., 1999; Yang et al., 2010). Il est donc possible que des effets similaires puissent opérer pour certains métaux en trace dans les réservoirs de stockage et ainsi augmenter leur mobilité.

Bien que le CO_2 et le CH_4 soient supposés être les formes majeures du carbone dans la plupart des fluides hydrothermaux aux conditions de formation des gisements dans la croute terrestre (profondeur < 5 km), d'après les données thermodynamiques disponibles et les observations des inclusions fluides portées à la surface de la terre, un regard plus critique sur ces modèles de spéciation est nécessaire. Par exemple, des prédictions thermodynamiques récentes pour les fluides sous de très fortes pressions (> 30 kbar) suggèrent que des formes de carbone de valence intermédiaires, comme les acides carboxyliques, pourraient être des espèces majeures (Sverjensky et al., 2014). Par analogie avec le soufre, qui est présent à basse température et basse pression sous forme de sulfate et de sulfure, mais forme des espèces de valence intermédiaire à haute température et haute pression (comme l'ion trisulfure, S_3^-, Pokrovski and Dubessy, 2015), on pourrait en effet penser que des formes de carbone de valence intermédiaire entre CO_2 et CH_4 existent dans les fluides profonds. La vérification de ces hypothèses nécessitent d'utiliser des méthodes spectroscopiques in-situ (comme, par exemple, la spectroscopie Raman en cellule enclume-diamant; Facq et al., 2014). Une meilleure compréhension de la spéciation du carbone lui-même dans les fluides aux conditions extrêmes est un grand challenge des études futures.

Le rôle des formes de carbone autres que CO_2 sur la spéciation et le transport des métaux doit ainsi être considéré, une fois que la spéciation du carbone sera mieux contrainte. Par exemple, nos premières mesures des coefficients de partage de Au et Pt en présence du CO_2 qui augmentent de 1 à 2 ordres de grandeur impliquent qu'il ne peut pas être exclu que dans les fluides et vapeurs d'autres ligands du carbone tels que CO puissent former des complexes stables avec certains métaux, un effet bien connu par les chimistes pour l'or et les métaux du groupe de platine aux températures ambiantes (e.g. Dell'Amico et al., 2010). De même, le rôle du CH_4, qui est également un volatil abondant dans les environnements métamorphiques en présence du graphite (e.g., Galvez et al., 2013), nécessite des études complémentaires.

En conclusion, ce travail de thèse montre que le vieux carbone, qui est une des plus grandes préoccupations de l'humanité, ne nous a pas encore livré tous ses secrets.

REFERENCES

Dell'Amico D.B., Labella L., Marchetti F. and Samaritani S. (2010) Halo-carbonyl complexes of palladium, platinum and gold. *Coord. Chem. Reviews* **254**, 635-645.

Facq S., Isabelle Daniel I., Gilles Montagnac G., Cardon H., Sverjensky D. A. (2014) In-situ Raman study and thermodynamic model of aqueous carbonate speciation in equilibrium with aragonite under subduction zone conditions. *Geochim. Cosmochim. Acta* **132**, 375–390.

Galvez M.E., Martinez I., Beyssac O., Benzerara K., Agrinier P. and Assayag N. (2013) Metasomatism and graphite formation at a lithological interface in Malaspina (Alpine Corsica, France). *Contrib. Mineral. Petrol.* **166**, 1687-1708.

Glennon J.D., Harris S.J., Walker A., McSweeney C.C. and O'Connell M. (1999) Carrying gold in supercritical CO_2. *Gold Bulletin* **32**, 52-58.

Jiin-Shuh J., Wang C.-L., Hsiang H.-I., Li Z., Yang H.-J., Jiang W.-T., Yang K.-M. and Bundschuh J. (2015) Experimental investigation of trace element dissolution in formation water in the presence of supercritical CO_2 fluid for a potential geological storage site of CO_2 in Taiwan. *J. Natural Gas Science and Engineering* **23**, 304-314.

Mavhengere P., Maphala T., Wagner N. (2015) Physical and structural effects of carbon dioxide storage on vitrinite-rich coal particles under subcritical and supercritical conditions. *Intern. J. Coal Geology* **150-151**, 1-6.

Pokrovski G.S., Roux J., Ferlat G., Jonchiere R., Seitsonen A.P., Vuilleumier R. and Hazemann J.-L. (2013) Silver in geological fluids from in-situ X-ray absorption spectroscopy and first-principles molecular dynamics. *Geochim. Cosmochim. Acta* **106**, 501-523.

Pokrovski G.S. and Dubessy J. (2015) Stability and abundance of the trisulfur radical ion S_3^- image in hydrothermal fluids. *Earth. Planet. Sc. Lett.***411**, 298-309.

Pokrovski G.S., Kokh M.A., Guillaume D., Borisova A.Y., Gisquet P., Hazemann J.-L., Lahera E., Del Net W., Proux O., Testemale D., Haigis V., Jonchière R., Seitsonen, A.P., Ferlat G., Vuilleumier R., Saitta A.M., Boiron M.-C. and Dubessy J. (2015) Sulfur radical species form gold deposits on Earth. *P. NATL. ACAD. SCI USA* , in press; www.P. Natl. Acad. Sci USA .org/cgi/doi/10.1073/P. Natl. Acad. Sci USA .1506378112.

Rempel K.U., Liesbcher A., Heinrich W. and Schettler G. (2011) An experimental investigation of trace element dissolution in carbon dioxide: Applications to the geological storage of CO_2. *Chem. Geol.* **289**, 224–234.

Sverjensky D.A., Stagno V., Huang F. (2014) Important role for organic carbon in subduction-zone fluids in the deep carbon cycle. *Nat. Geosci.* **7**, 909-913.

Yang Z., Yang X., Xu Z. and Yang N. (2010). Molecular simulations of structures and solvation free energies of passivated gold nanoparticles in supercritical CO_2. *J. Chem. Phys.* **133**, 094702.

Annexes I-III

I.1. Corrosion des thermocouples

I.2. Traceurs des fuites au niveau de la cellule flexible

II. Traitement à l'eau régale

III. Calculs des concentrations dans des cas particuliers

Annexe I.1. Corrosion des thermocouples

Pour effectuer les expériences aux conditions choisies en utilisant le réacteur à cellule flexible, il faut pouvoir mesurer la température sous des hautes pressions en phase fluide. Les premiers thermocouples de type K que nous avons utilisés ont été soudés dans l'atelier mécanique du GET. Cette soudure à l'argent, entre la gaine d'acier du thermocouple et le haut du cône d'étanchéité qui est fixé dans l'obturateur du réacteur Coretest, était délicate à faire et elle tenait mal sous pression. Après plusieurs fuites constatées, en collaboration avec l'entreprise TOP Industrie nous avons développé une nouvelle soudure par le bas du cône, côté fluide pour améliorer l'étanchéité. Bien que les fuites au niveau du contact thermocouple-cône aient été éliminées, ce type de soudure a mis en jeu des processus de corrosion en présence du fluide, vraisemblablement dû à des réactions électrochimiques entre le métal de la soudure (Ag) et la gaine en acier du thermocouple (Fe). La corrosion fut aggravée d'avantage en présence de soufre et de CO_2 dans la bombe en raison de fuites des cellules en titane (e.g. on a trouvé 35 ppm de soufre dans une solution prélevée avec la vanne de fuite). Ces corrosions ont provoqué parfois une dégradation complète du thermocouple au niveau de la soudure (Fig. A.1). Par conséquent, nous sommes revenus au soudage par le haut fait par des professionnels de TOP Industrie. De tels thermocouples ont montré une bonne fiabilité pour les températures (≤450°C), les pressions (≤1 kbar) et durée de nos manips (≤2 mois) (Fig. A.2).

Annexe I.2. Traceurs des fuites au niveau de la cellule flexible

Afin de déceler des fuites éventuelles de fluide entre la cellule flexible et la bombe externe du réacteur Coretest, dans les travaux précédents il a été proposé d'utiliser un 'spike', c'est-à-dire un élément chimique soluble qu'on place dans la bombe externe. La présence de cet élément dans le fluide prélevé de la cellule indique un échange entre l'eau externe de la bombe et le fluide interne de la cellule et donc une mauvaise étanchéité de cette dernière. Par exemple, Tagirov et al. (2005)[3] ont utilisé du nitrate de strontium ($Sr(NO_3)_2$) comme traceur de fuite. Cependant, nous avons remarqué que le strontium n'est pas stable dans la solution externe. Le strontium semble réagir avec les composés contenus dans la cellule flexible pendant l'expérience et forme les phases solides $SrCO_3$ ou $SrSO_4$ dans la bombe en acier. Ces phases, très peu solubles à haute température, ont été confirmées par des analyses MEB-EDS (Fig. A.1. E, F). Nous avons donc arrêté d'utiliser le nitrate de strontium comme traceur et l'avons remplacé par le nitrate de césium qui ne forme

---

[3] Tagirov B.R., Salvi S., Schott J. and Baranova N.N. (2005) Experimental study of gold-hydrosulphide complexing in aqueous solutions at 350-500°C, 500 and 1000 bars using mineral buffers. *Geochim. Cosmochim. Acta* **69**, 2119-2132.

pas de phases insolubles. L’utilisation de Cs a été avec succès: il ne réagit pas avec le contenu de l’autoclave pendant l’expérience.

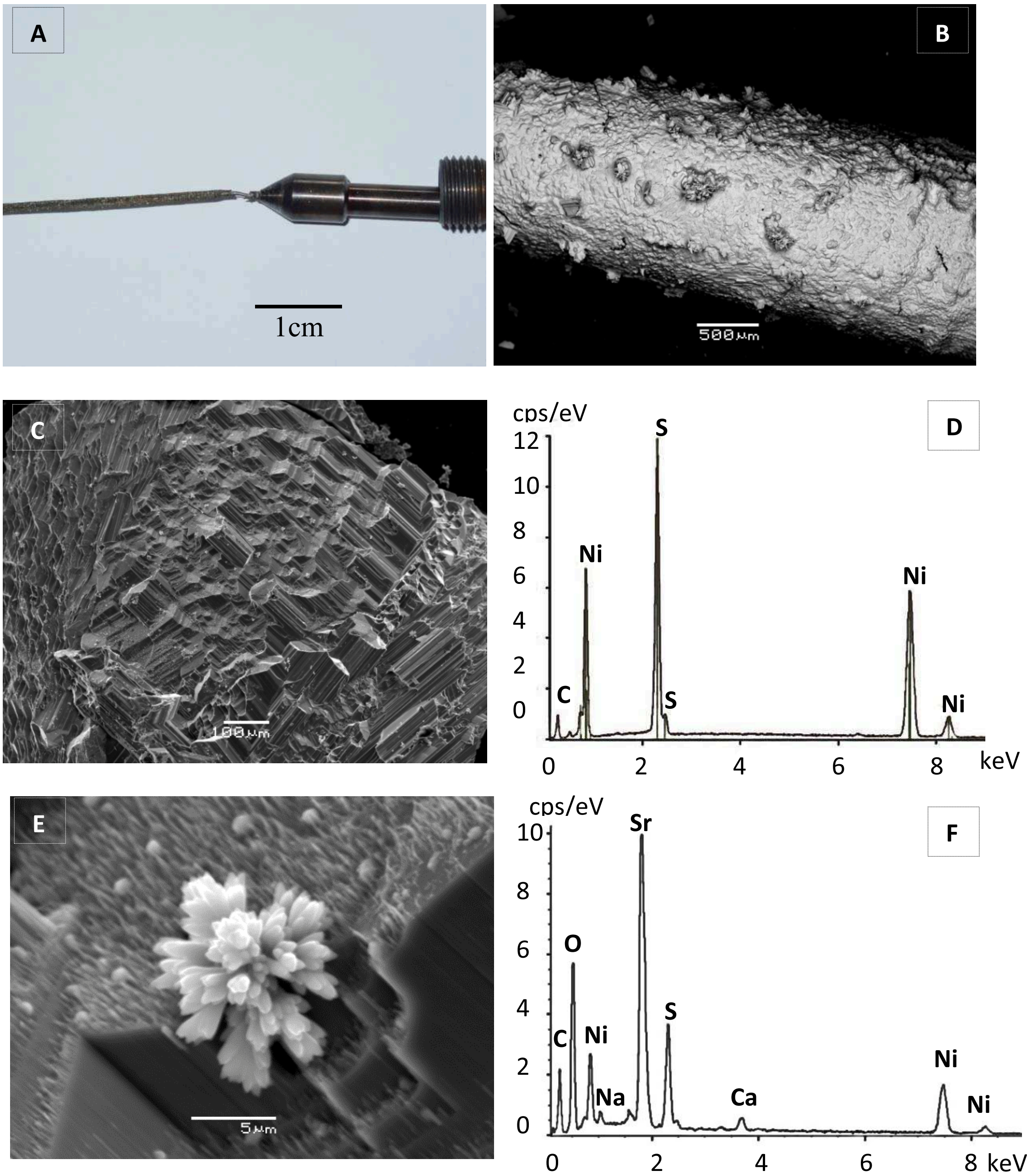

Fig. A.1. La corrosion du thermocouple chromel/alumel (A), images MEB d’un dépôt de composition NiS (B, C) avec des particules de $SrCO_3$ ou $SrSO_4$ (E) et leurs spectres EDS correspondants (D, F).

Fig. A.2. Le cône du thermocouple chromel/alumel fabriqué par l'entreprise TOP Industrie.

Annexe II. Traitement à l'eau régale

Le traitement d'un échantillon prélevé dans de l'ammoniac (Fig. 2.4) pour les analyses des métaux par ICP-MS et ICP-AES implique les procédures suivantes :

1) l'évaporation de l'échantillon sans ébullition (≤90°C) jusqu'à un état de sels humides, se fait dans un Savilex ® sur une plaque chauffante avec extraction;
2) la réaction entre l'eau régale et l'échantillon se fait sous 100-120°C dans le même Savilex cette fois bien fermé jusqu'à la disparition de tout précipité (~2-4 h);
3) l'évaporation de l'eau régale jusqu'à la masse de 0,1-0,3 g et jamais au sec (!), pour éviter la perte de chlorures de certains métaux qui sont volatiles ($SnCl_4$; $MoCl_6$; $AuCl_3$);
4) dilution du résidu dans le Savilex avec une matrice 0.5 wt% HCl et 1.5 wt% HNO_3 pour l'analyse ICP-MS ou ICP-AES.

Annexe III. Calculs des concentrations dans des cas particuliers

Dans certaines analyses par ICP-AES ou ICP-MS, les concentrations calculées par l'appareil selon la courbe d'étalonnage tracée sur toute la gamme de standards pourraient être incorrectes dans les cas suivants: a) la concentration mesurée est en dessous de l'étalon le moins concentré mais au-dessus de la limite de détection, b) le blanc de préparation contient une concentration détectable de l'élément dosé. Ces faibles concentrations ont donc été corrigées manuellement à l'aide de la règle de trois

$$C = \frac{C_{stand} \cdot (I_{sample} - I_{blanc\ de\ préparation})}{(I_{stand} - I_{matrice})}, \qquad \text{(A-1)}$$

où C_{stand} est la concentration de l'élément dans l'étalon le moins concentré, I_{sample} est l'intensité du signal de l'élément dans l'échantillon, I_{stand} est l'intensité du signal de l'élément dans l'étalon, $I_{blanc\ de\ préparation}$ est l'intensité du signal de l'élément dans le blanc de préparation, $I_{matrice}$ est l'intensité du signal de l'élément dans la matrice. Si le blanc de préparation contient un signal de l'élément au-dessus de bruit de fond, on suppose qu'un échantillon avec un signal 2 fois supérieur est quantifiable.

Annexes IV-V

Articles publiés en dehors de mon sujet de thèse sur le CO_2

IV. Article: «"Invisible" gold in covellite (CuS): synthesis and studies by EPMA, LA-ICP-MS, and XPS techniques» B.R. Tagirov, Yu.P. Dikov, M.I. Buleev, E.V. Koval'chuk, D.A. Chareev, M.A. Kokh, S.E. Borisovskii, V.D. Abramova, N.N. Baranova, M.I. Garas'ko, V.A. Kovalenker and N.S. Bortnikov (2014) *Doklady Earth Sci.* **459**, 1381-1386.

V. Article: «Sulfur radical species form gold deposits on Earth» G.S. Pokrovski, M.A. Kokh, D. Guillaume, A.Y. Borisova, P. Gisquet, J.-L. Hazemann, E. Lahera, W. Del Net., O. Proux, D. Testemale, V. Haigis, R. Jonchière, A.P. Seitsonen, G. Ferlat, R. Vuilleumier, A.M. Saitta, M.-C. Boiron and J. Dubessy (2015) *Proc. Natl. Acad. Sci. USA* **112**, 13484-13489.

ISSN 1028-334X, Doklady Earth Sciences, 2014, Vol. 459, Part 1, pp. 1381–1386. © Pleiades Publishing, Ltd., 2014.
Original Russian Text © B.R. Tagirov, Yu.P. Dikov, M.I. Buleev, E.V. Koval'chuk, D.A. Chareev, M.A. Kokh, S.E. Borisovskii, V.D. Abramova, N.N. Baranova, M.I. Garas'ko, V.A. Kovalenker, N.S. Bortnikov, 2014, published in Doklady Akademii Nauk, 2014, Vol. 459, No. 1, pp. 90–95.

"Invisible" Gold in Covellite (CuS): Synthesis and Studies by EPMA, LA–ICP–MS, and XPS Techniques

B. R. Tagirov[a], **Yu. P. Dikov**[a], **M. I. Buleev**[a], **E. V. Koval'chuk**[a], **D. A. Chareev**[c],
M. A. Kokh[a], **S. E. Borisovskii**[a], **V. D. Abramova**[a], **N. N. Baranova**[b], **M. I. Garas'ko**[a],
V. A. Kovalenker[a], and Academician **N. S. Bortnikov**[a]

Received July 2, 2014

Abstract—Samples of covellite CuS(cr) containing up to 0.3 wt % of gold in "invisible" form were obtained by means of hydrothermal synthesis (450–475°C, 1 kbar) and synthesis in eutectic chloride melts (495°C). The studies using EPMA and LA-ICP–MS techniques showed that gold was uniformly dispersed within the volume of covellite grains and Au content increased with increasing of sulfur fugacity. The XPS-analysis of the samples obtained showed no chemical shift of the Au-$4f_{7/2}$ line compared to Au and Au_2S, whereas a positive chemical shift of this line was revealed for mixed Au–Ag sulfides and tellurides. The obtained data allow one to assume that gold does not occur in covellite as an isomorphous admixture (solid solution) but forms nanoparticles of Au or gold sulfide.

DOI: 10.1134/S1028334X14110087

The gold in ores of hydrothermal deposits either occurs in the form of a native mineral—the natural solid solution—or is dispersed in sulfides as an isomorphous admixture, nano-sized inclusions of gold, or its compounds with chalcogenides and semimetals (S, Se, Te, As, Sb, and Bi). The dispersed ("invisible") form of gold is much more difficult to recover in the course of ore treatment, and most of it goes to waste. Therefore, this type of gold is called "refractory". Despite the importance of the problem, a structural and chemical state of "invisible" gold is unknown for most sulfides. For our studies, gold-containing covellite $CuS_{(cr)}$—a mineral occurring under both hypogenous and hypergenous conditions—was selected as the subject. Unlike other minerals of the Cu–Fe–S system, covellite does not form solid solutions with iron, distinguished by this feature from the minerals of the digenite $Cu_{2-x}S$–bornite Cu_5FeS_4–chalcopyrite $CuFeS_2$ group. The stability limit of covellite is 507°C; upwards of this temperature, it is decomposed into digenite and liquid sulfur [1]. Covellite is crystallized in hexagonal syngony and, despite the simple composition, shows the complicate layered structure including two types of Cu atoms in tetrahedral and triangular coordinations and two types of S atoms in the forms of a simple sulfide ion and paired disulfide groups [2]. It is suggested that covellite is a significant concentrator of gold in porphyry copper and epithermal systems [3]. The present study aimed to determine the conditions of gold accumulation and its speciation in covellite using synthetic phases.

The experiments on syntheses were carried out within the field of thermodynamical stability of covellite in two ways: by a hydrothermal procedure and using the eutectic chloride melts. The hydrothermal synthesis was realized at 450 and 475°C under 1 kbar. We used titanium autoclaves; in the upper parts of them, powdered copper or a mixture of powdered synthetic Fe sulfide (troilite, FeS) and copper was placed into a container near which a strip of gold foil was fixed. The autoclaves were filled either with distilled water or with solutions of sulfuric acid, and weighed samples of elemental sulfur were added into them. In the course of the experiment, sulfur interacted with the weighed solid phase and dissolved in the fluid. Then, the dissolved sulfur was disproportionated by the reaction

$$2S + 4H_2O = H_2SO_{4(solution)} + H_2S_{(solution)} + 4H_{2(gas)} \quad (1)$$

---

[a] *Institute of Geology of Ore Deposits, Petrography, Mineralogy, and Geochemistry, Russian Academy of Sciences, Moscow, Russia*
[b] *Vernadskii Institute for Geochemistry and Analytical Chemistry, Russian Academy of Sciences, Moscow, Russia*
[c] *Institute of Experimental Mineralogy, Russian Academy of Sciences, Chernogolovka, Russia*
e-mail: tagir@igem.ru

and the sulfide–sulfate pair controlled the redox potential and fugacity of sulfur (f_{S_2}) in the system. The hermetically closed autoclaves were placed into gradient-less furnaces heated previously to the temperature of the experiments, and exposed for 20 days. As a result, either covellite samples or a mixture of covellite, nukundamite $Cu_{3.4}Fe_{0.6}S_4$, and digenite $Cu_{1.5}Fe_{0.1}S$ (in a single experiment) were obtained.

Grains of covellite up to 2 mm size and their mixture with digenite were obtained by synthesis in the eutectic melt of the chloride mixture at 495°C. The mixture of 68 wt % of CsCl, 17 wt % of KCl, and 15 wt % of NaCl with 478°C melting temperature was used. The initial substances for the synthesis were powdered copper and sulfur sealed into evacuated quartz ampoules (6 mm diameter and ~60 mm length) along with strips of gold foil and a salt flux. The ampoules were exposed in vertical tube furnaces under the required temperatures for a month; then they were quenched by dropping into a mixture of water and ice.

The chemical composition of sulfides was determined in polished sections by means of the EPMA technique with a JXA-8200 electron probe microanalyzer (JEOL Co.). The admixtured Au in the sulfide matrix was measured at integrated conditions with a LIFH crystal analyzer in view of a dip in the background spectrum nearby the AuLα1 analytical line [4] under the accelerating voltage of 20 kV, 100 nA current in the Faraday cup, 200 s exposure, and 2 μm probe diameter. This enabled us to decrease the detection limit (3σ) to 0.01 wt % (100 ppm). The Au content in some of the samples was measured by means of mass spectrometry with inductively coupled plasma and laser sampling (LA–ICP–MS) using a Thermo XSeries 2 quadrupole mass spectrometer and a New Wave 213 laser device. As the external standard, CuS containing 0.22 wt % of gold was used. The standard was made in the form of a tablet obtained by pressing of hydrothermally synthesized covellite of Au content determined by the EPMA. The isotopes ^{33}S (internal standard) and ^{197}Au were measured at the following parameters of the laser: 40 μm diameter, 7–8 J/cm^2 energy, and 10 Hz frequency. The sample was transferred by helium flow (0.6 L/min) with additional 6% of H_2. At the input of the mass spectrometer, helium was mixed with argon (0.8 L/min). The ablation was performed for 30 s after 20 s of the instrumental background. The structural/chemical analysis was carried out by means of the X-ray photoelectron spectroscopy (XPS) using an ESCA-5950 spectrometer (Hewlett Packard Co.) with Al-$K_{\alpha 1,2}$ monochromic radiation for excitation of photoelectrons. The spectrometer was calibrated by C-1*s* line (284.8 eV binding energy).

The analysis of the synthesized phases showed that all the gold occurred in the "invisible" form (i.e., formed no separated phases at the level of the EPMA resolving capacity). Figure 1 presents the LA–ICP–MS spectrum obtained under the line burning over the covellite grain. The oscillation amplitude of a signal for ^{197}Au isotope is somewhat higher than that for ^{33}S (~0.2 and ~0.1 log units, respectively). However, the spectrum of ^{197}Au signal includes no peaks caused by the presence of submicron particles. This is seen from the spectrum of the "adjusted" signal in the inset of Fig. 1. In most of the test points, the content of gold determined by the EPMA varies within the statistical error (Fig. 2). Thus, the homogenous mode of a distribution of "invisible" gold is confirmed both for the laser beam (30 μm diameter and burning depth of a few micrometers) and by the EPMA data (the electron beam of 1 μm diameter).

The data of Fig. 3 show that the content of "invisible" gold in covellite increases by ~0.65 log units with increasing f_{S_2} value by an order of magnitude $\left(\frac{d\log C(\mathrm{Au})}{d\log f_{S_2}} \sim 0.65\right)$. Assuming that the value of the stoichiometric coefficient for sulfur (equal to the slope of the line in Fig. 3) is within 0.5–1, the reactions of the formation of "invisible" Au may be written as

$$Au_{(cr)} + 0.5S_{2(gas)} = AuS_{(sulfide)}, \qquad (2)$$

$$Au_{(cr)} + 0.75S_{2(gas)} = 0.5Au_2S_{3(sulfide)}, \qquad (3)$$

$$Au_{(cr)} + S_{2(gas)} = AuS_{2(sulfide)}. \qquad (4)$$

Note once again that the activity of gold in the system was controlled by the presence of its own phase (crystalline Au), which determined the form of reactions (2)–(4). Most gold compounds are characterized by three oxidation states: 0, +1, and +3; those for sulfur are 0 and –2 (the oxidized S forms are beyond the consideration). As follows from Eq. (2), the "invisible" Au in this case is characterized by the +1 oxidation level, and sulfur of nominally the same oxidation level might form the paired disulfide groups ("dumbbells") like sulfur in the structures of covellite or pyrite (FeS_2). Reaction (3) results in the formation of Au^{3+} and S^{2-}; reaction (4) gives Au^{3+} and Au^{1+} along with the "dumbbells" of sulfur. However, this reasoning is formal and provides no information on the true valent state of elements in the compound.

The data on the true charge state of gold may be obtained from analysis of the XPS spectra. Along with the samples of gold-containing covellites, the X-ray photoelectron spectra were recorded for a series of standards: metallic Au, synthetic sulfides— $Au_2S_{(cr)}$, $AuAgS_{(cr)}$ (petrovskaite), and $Ag_3AuS_{2(cr)}$ (uytenbogaardtite)—and a series of natural tellurides: $(Au_{0.99}Ag_{0.01})Te_{2(cr)}$ (calaverite), $(Au_{1.1}Ag_{0.9})_2Te_{2(cr)}$ (sylvanite), and $Ag_3AuTe_{2(cr)}$ (petzite). The samples represented the gold–telluride associations of pipe-like ore bodies of the Kochbulak deposit in Uzbekistan [6]. In this study, the following lines of core electron levels to determine the charge state were selected: Au-4$f_{7/2}$, Ag-3$d_{5/2}$, S-2*p*, and Te-3$d_{5/2}$. The measurement results for the standards are given in Table 1. The values of binding energy (E_b) of Au-4$f_{7/2}$ for $Au_{(cr)}$ and $AuTe_{2(cr)}$ are close and equal to 84 ± 0.05 eV. The E_b

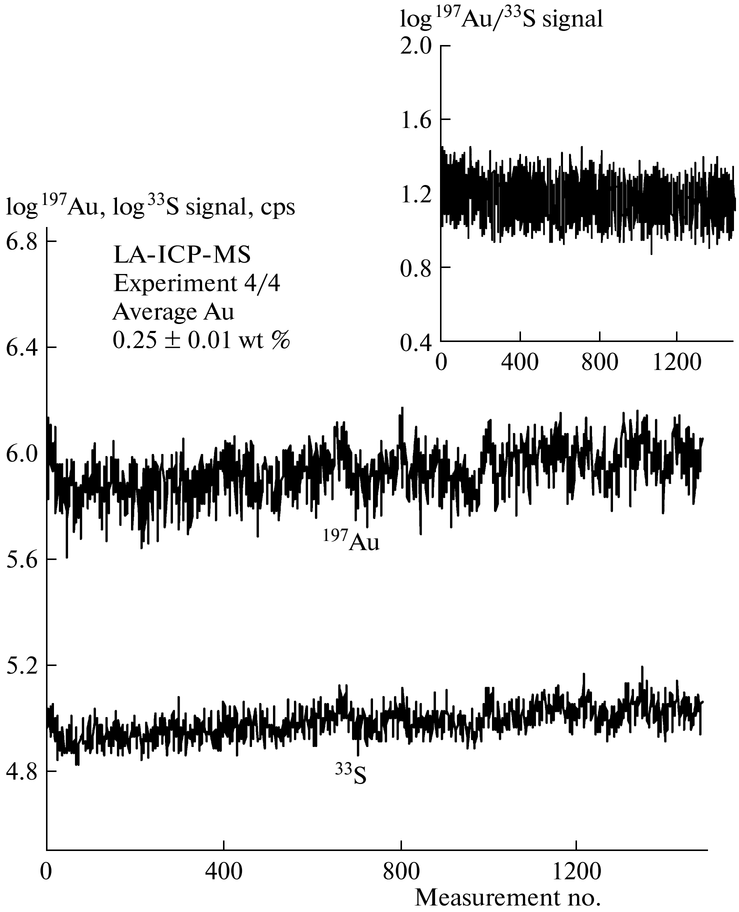

Fig. 1. The LA–ICP–MS spectrum for ^{197}Au and ^{33}S isotopes by the covellite grain (CuS) synthesized in the eutectic melt of chlorides at 495°C. Line length ~300 μm. In the inset, the ^{197}Au signal is specified for that of ^{33}S.

values of Au-4$f_{7/2}$ for two samples of the synthetic sulfide $Au_2S_{(cr)}$ are within 83.65–84.16 eV and increase with sputtering. Most likely, the scattering as such in the values of binding energy is caused by heterogeneity of the phase and the impact of Ar^+ ions under sputtering: Au_2S is a metastable compound synthesized in several stages from cyanide solutions with subsequent cleansing with organic solvents [7], and a pure homogenous surface of the sample is just impossible to obtain. Based on the available data, one may suppose that the average E_b of Au-4$f_{7/2}$ for $Au_2S_{(cr)}$ is also close to 84 eV. Thus, the absence of a Au-4$f_{7/2}$ chemical shift for pure chalcogenides of gold does not enable us to distinguish Au^{1+} in Au_2S and $AuTe_2$ from metallic Au^0. At the same time, a positive chemical shift of the Au-4$f_{7/2}$ line is seen for mixed Au–Ag-sulfides and tellurides: by +0.35 eV for $AgAuS_{(cr)}$ and +0.29 eV for $Ag_3Au_{(cr)}$ in sulfides (on the surface), by +0.25 eV for $(Au_{1.1}Ag_{0.9})_2Te_{4\,(cr)}$ and +0.31 eV for Ag_3AuS_2 in tellurides (Table 1). Thus, the value of E_b of Au-4$f_{7/2}$ for natural tellurides increases regularly with the decrease in the Au content, whereas the opposite effect is seen for Ag and Te: the E_b values of Ag-3$d_{5/2}$ and Te-3$d_{5/2}$ decrease with the decrease in the Au content.

In sulfides, the addition of gold to Ag_2S causes a negative E_b shift of Ag-3$d_{5/2}$ against pure silver and $Ag_2S_{(cr)}$ of E_b (Ag-3$d_{5/2}$) = 368.2 eV [8, 9]. Thus, the “dilution” of pure Au- and Ag-sulfides results in unlike-sign chemical shifts of the core lines: the introduction of silver into Au_2S causes the growth of E_b (Au-4$f_{7/2}$), whereas the value of E_b (Ag-3$d_{5/2}$), conversely, decreased when mixing Ag_2S and Au. As for the S-2p line, the introduction of silver into a gold chalcogenide causes a negative chemical shift.

Summarizing the consideration of XPS data for the standards, one may note that a common feature of sulfides and tellurides is a positive chemical shift of the core Au-4$f_{7/2}$ level in mixed Au–Ag-chalcogenides against pure Au_2S and $AuTe_2$ (the E_b value of the 4f-state increases). A similar effect is registered in binary gold-containing systems: Au–Ag alloys, $AuAl_2$ and $AuGa_2$ compounds [10], Au–Cu-alloys [11], and alloys of other noble metals. In these alloys and compounds, along with the increase of the E_b value of the 4f-level of

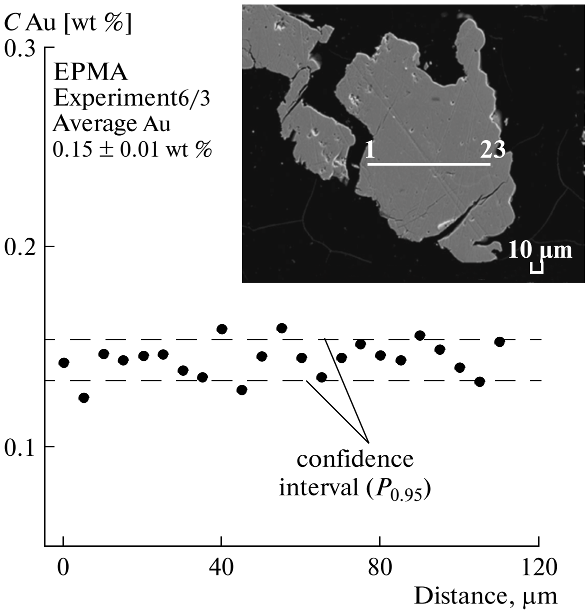

Fig. 2. The profile of the Au concentration obtained by the covellite grain using the EPMA technique. The hydrothermal synthesis at 450°C and 1 kbar.

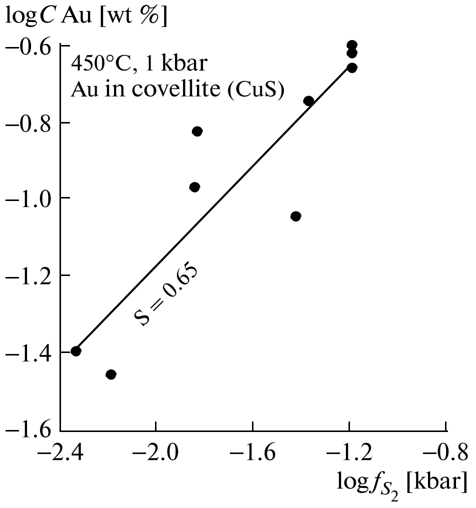

Fig. 3. The dependence of the "invisible" gold concentration on sulfur fugacity for the covellite samples synthesized by the hydrothermal procedure at 450°C and 1 kbar. The f_{S_2} values were controlled by the reaction of sulfur hydrolysis and disproportionation (Eq. 1) and calculated from the system composition using thermodynamic properties of aqueous species, $S_{(l)}$, and $S_{2(gas)}$ from the SLOP 98 database [5].

gold with dilution, the decrease in electron density conforming to the 5*d*-state of gold was found by means of X-ray absorption near edge structure technique (XANES). At the same time, the electron density for the 6*s* and 6*sp* states of the Au atom increases (by Mossbauer spectroscopy [11, 12]). As a result, in general, the overall charge at the Au site increases according to the principle of elecronegativity (gold is the

Table 1. Binding energy (E_b) in sulfides and tellurides of gold and silver determined by means of XPS technique

Phase	Line	Au_2S (1st synthesis)	Au_2S (2nd synthesis)	AgAuS	Ag_3AuS_2	Ag_2S [8]
Surface E_b, eV	Au $4f_{7/2}$	83.65	84.06	84.35	84.29	
	Ag $3d_{5/2}$			367.32	367.51	368.2
	S 2*p*	162.03	161.48	161.56	160.84	161.0
Sputtering 100 Å, E_b, eV	Au $4f_{7/2}$	83.72				
	Ag $3d_{5/2}$					
	S 2*p*	161.45				
Sputtering 200 Å, E_b, eV	Au $4f_{7/2}$	83.81	84.16	84.22	84.14	
	Ag $3d_{5/2}$			366.94	367.47	
	S 2*p*	161.25	161.63	161.60	160.84	
Phase		$AuTe_2$ (1 at % of Ag)		$(Au_{1.1}Ag_{0.9})_2Te_4$	Ag_3AuTe_2	
Surface E_b, eV	Au $4f_{7/2}$	84.00		84.25	84.31	
	Ag $3d_{5/2}$	367.53		367.21	367.18	
	Te $3d_{5/2}$	573.86		573.48	573.32	

most electronegative metal). Conversely, the "dilution" of pure Ag and Cu with gold causes a decrease in the E_b values of the core levels (Ag-$3d_{5/2}$ and Cu-$2p_{3/2}$). The same sign of chemical shift of Ag-$3d_{5/2}$ was ascertained by the authors for Au–Ag-sulfides (Table 1).

For quantitative interpretation of the registered changes in charge states, the charge compensation model was proposed [10]. By this model, just the increase of density of unoccupied Au-5*d* states makes the key contribution to the redistribution of electron density and causes the growth in the Coulomb potential for the core electron levels of gold, resulting in a small increase of E_b of Au-4*f* registered by the XPS technique. It is significant that the registered increase of density of unoccupied Au-5*d* states (and, respectively, the value of the Au-4*f* chemical shift) increases with dilution (or with the increase of a quantity of the closest neighboring atoms being different from gold) [10]. Moreover, a larger difference in the electronegativity of the components of a compound (or an alloy) also causes an increase in the density of unoccupied *d*-states [13] and, hence, may result in a positive Au-4*f* chemical shift. This enables us to understand the absence of chemical shifts in $Au_2S_{(cr)}$ and $AuTe_{2(cr)}$ compared to pure $Au_{(cr)}$: the values of electronegativity of these elements are close (by Pauling, $\chi(Au) = 2.54$, $\chi(S) = 2.58$, and $\chi(Te) = 2.1$) [14].

The XPS data for chalcogenides may be used for interpretation of the structural and chemical state of gold in covellite. The authors examined two samples of $CuS_{(cr)}$ obtained by hydrothermal synthesis; for both of them, values of E_b (Au-$4f_{7/2}$) about 84 eV were obtained (Table 2). Note that gold in covellite samples exists only in the "invisible" state: the EPMA results coincide with the gold content determined after the complete dissolution of a sample, with subsequent analysis by the ICP–MS technique. Therefore, it may be safely assumed that the XPS signal is related to the "invisible" form of gold.

The data obtained testify to the absence of Au^{3+} characterized by an Au-$4f_{7/2}$ chemical shift of over +1 eV. Moreover, the absence of a chemical shift of this line does not confirm the assumption of the formation of the Cu–Au–S solid solution. In this case, like for mixed Au–Ag chalcogenides, the redistribution of electron density between the Au, Cu, and S atoms under Au "dilution" should result in a considerable positive Au-$4f_{7/2}$ chemical shift. Because of this, two forms of gold occurrence in covellite seem to be most likely: (1) nanoparticles of Au sulfide or (2) Au nanoparticles, probably separated from the Cu-containing matrix either with the Au sulfide layer or with any other sulfur-containing cover minimizing Au–Cu interaction. (The interaction as such at the level of nanoparticles constituted by the layers of gold and silver also results in a positive Au-$4f_{7/2}$ chemical shift [15].) The presence of the Au–S-bond in the formed gold-containing sulfide is also testified to by the dependence of the "invisible" gold content on the volatility of sulfur. Thus, despite the high dependence of the "invisible" gold content on the fugacity of sulfur and the homogenous distribution in covellite, no solid solution is formed and gold, most probably, occurs in the CuS matrix in the form of nanoparticles. However, it is unclear whether the gold nanoparticles existed under conditions of the experiment or if they appeared under the decomposition of the solid solution during quench. A more realistic determination of the gold speciation in covellite requires in situ experiments (under the parameters of the synthesis) using the spectral techniques (e.g., XANES/EXAFS) or transmission electron microscopy.

Table 2. Binding energy of Au-$4f_{7/2}$ (E_b, eV) for the samples of gold-containing covellite (0.2–0.3 wt % of Au)

	M-475-27	M-450-1/8
Surface	83.95	83.85
Sputtering, 100 Å	84.01	84.02
Sputtering, 200 Å	83.87	

ACKNOWLEDGMENTS

The authors are very grateful to E.A. Brichkina for the synthesis of standards, to V.A. Sychkova and L.F. Kartashova for providing the analytical works, and to A.V. Zotov for his useful remarks in the course of the studies.

This study was supported by the Russian Scientific Foundation, RSCF, project no. 14-17-00693.

REFERENCES

1. P. B. Barton, Econ. Geol. **68**, 455–465 (1973).
2. H. T. Evans and J. A. Konnert, Am. Mineral. **61**, 996–1000 (1976).
3. S. E. Kesler, S. L. Chryssoulis, and G. Simon, Ore Geol. Rev. **21**, 103–124 (2002).
4. P. G. Self, K. Norrish, A. R. Milnes, J. Graham, and B. Robinson, X-Ray Spectrometry **19**, 59–61 (1990).
5. J. W. Johnson, E. H. Oelkers, and H. C. Helgeson, http://geopig.asu.edu/supcrt92_data/slop98.dat).
6. V. A. Kovalenker, Yu. G. Safonov, V. B. Naumov, and V. L. Rusinov, Geol. Rudn. Mestorozhd. **39** (2), 107 (1997).

7. B. R. Tagirov, N. N. Baranova, A. V. Zotov, J. Schott, and L. N. Bannykh, Geochim. Cosmochim. Acta **70**, 3689–3701 (2006).
8. M. P. Seah, I. S. Gilmore, and G. Beamson, Surf. Int. Anal. **26**, 642–649 (1997).
9. K. V. Kaushik, J. Electron Spectr. Rel. Phen. **56**, 273–277 (1991).
10. R. E. Watson, J. Hudis, and M. L. Perlman, Phys. Rev. **4**, 4139–4144 (1971).
11. M. Kuhn and T. K. Sham, Phys. Rev. **49**, 1647–1661 (1994).
12. C. C. Tyson, A. Bzowski, P. Kristof, M. Kuhn, R. Sammynaiken, and T. K. Sham, Phys. Rev. **45**, 8924–8928 (1992).
13. A. Bzowski, Y.M. Yiu, and Sham T.K, Phys. Rev. B: **51**, 9515–9520 (1995).
14. J. E. Huheey, E. A. Keiter, and R. L. Keiter, Inorhanic Chemistry, 4th ed. (Pearson Education, Singapoure, 2000).
15. S. Nishimura, A. T. N. Dao, D. Mott, K. Ebitani, and S. Maenosono, J. Phys. Chem. **116**, 4511–4516 (2012).

Translated by A. Rylova

Sulfur radical species form gold deposits on Earth

Gleb S. Pokrovski[a,1], Maria A. Kokh[a], Damien Guillaume[a], Anastassia Y. Borisova[a], Pascal Gisquet[a], Jean-Louis Hazemann[b], Eric Lahera[c], William Del Net[c], Olivier Proux[c], Denis Testemale[b], Volker Haigis[d,e], Romain Jonchière[d,e], Ari P. Seitsonen[d], Guillaume Ferlat[e], Rodolphe Vuilleumier[d], Antonino Marco Saitta[e], Marie-Christine Boiron[f], and Jean Dubessy[f]

[a]Groupe Métallogénie Expérimentale, Géosciences Environnement Toulouse (GET), Observatoire Midi-Pyrénées, Université de Toulouse, Centre National de la Recherche Scientifique (CNRS), Institut de Recherche pour le Développement (IRD), F-31400 Toulouse, France; [b]CNRS, Université Grenoble Alpes, Institut NEEL, F-38042 Grenoble, France; [c]Observatoire des Sciences de l'Univers de Grenoble, Université Grenoble Alpes, F-38400 Saint Martin d'Hères, France; [d]École Normale Supérieure, Paris Sciences et Lettres (PSL) Research University, Département de Chimie, Sorbonne Universités, Université Pierre et Marie Curie (UPMC), Université Paris 06, CNRS UMR 8640 Pasteur, F-75005 Paris, France; [e]Sorbonne Universités, UPMC, Université Paris 06 & CNRS,UMR 7590, Institut de Minéralogie, de Physique des Matériaux et de Cosmochimie (IMPMC), F-75005 Paris, France; and [f]Université de Lorraine, CNRS, Centre de Recherches sur la Géologie des Matières Premières Minérales et Energétiques (CREGU), GeoRessources, B.P. 239 F-54506, Vandoeuvre lès Nancy Cedex, France

Edited by Bruce Watson, Rensselaer Polytechnic Institute, Troy, NY, and approved September 4, 2015 (received for review April 20, 2015)

Current models of the formation and distribution of gold deposits on Earth are based on the long-standing paradigm that hydrogen sulfide and chloride are the ligands responsible for gold mobilization and precipitation by fluids across the lithosphere. Here we challenge this view by demonstrating, using in situ X-ray absorption spectroscopy and solubility measurements, coupled with molecular dynamics and thermodynamic simulations, that sulfur radical species, such as the trisulfur ion S_3^-, form very stable and soluble complexes with Au^+ in aqueous solution at elevated temperatures (>250 °C) and pressures (>100 bar). These species enable extraction, transport, and focused precipitation of gold by sulfur-rich fluids 10–100 times more efficiently than sulfide and chloride only. As a result, S_3^- exerts an important control on the source, concentration, and distribution of gold in its major economic deposits from magmatic, hydrothermal, and metamorphic settings. The growth and decay of S_3^- during the fluid generation and evolution is one of the key factors that determine the fate of gold in the lithosphere.

gold | sulfur | ore deposit | hydrothermal fluid | trisulfur ion

The formation of gold deposits on Earth requires aqueous fluids that extract gold from minerals and magmas and transport and precipitate the metal as economic concentrations in ores that are three to six orders of magnitude larger than the Au mean content (~0.001 ppm) of common crustal and mantle rocks (1–9). However, natural data on gold contents in fluids are very scarce due to difficulties of direct access to deep geothermal fluid samples, rarity of representative fluid inclusions trapped in minerals, and analytical limitations for this chemically most inert metal (1, 4, 9, 10). The paucity of direct data makes it difficult to quantify the capacity of the fluids to transport gold and the factors controlling the sources, formation, and distribution of the economic resources of gold and associated metals across the lithosphere. Thus, knowledge of gold speciation and solubility in the fluid phase is required.

Terrestrial hydrothermal fluids systematically contain sulfur and chloride—compounds that have long been known to favor gold dissolution in aqueous solution (e.g., refs. 11 and 12). Following this common knowledge, the interpretation of gold transfers across the lithosphere has been based on the fundamental assumption that only hydrogen sulfide (HS^-) and chloride (Cl^-) can form stable complexes with aurous gold, Au^+, which is the main gold oxidation state in hydrothermal fluids (1–6, 11–15). Among these species, aurous bis(hydrogen sulfide), $Au(HS)_2^-$, and dichloride, $AuCl_2^-$, have long been regarded as the major carriers of gold in hydrothermal fluids, depending on temperature (T), pressure (P), acidity (pH), redox potential (f_{O_2}), and salt and sulfur concentrations (1, 5, 6, 13, 15). In addition, other minor hydroxide, chloride, and sulfide species (AuOH, AuCl, AuHS) have also been tentatively suggested in some studies to account for the low Au solubility (typically part-per-billion level, ppb) measured in dilute S- and Cl-poor experimental solutions (e.g., refs. 6 and 15). Most available data suggest that the sulfide complexes attain significant concentrations (>1 ppm Au) only in H_2S-rich neutral-to-alkaline (pH > 6–7) solutions at low-to-moderate temperatures (<250–300 °C), whereas the chloride complexes contribute to Au solubility only in highly acidic (pH < 3) chloride-rich (typically >10 wt% NaCl equivalent) and strongly oxidizing [above the oxygen fugacity of the hematite–magnetite (HM) buffer] solutions above 300 °C.

In between these two contrasting hydrothermal solution compositions lies a vast domain of geological fluids, which are commonly generated by magma degassing at depth (2, 3, 9) or prograde metamorphism of sedimentary rocks at high temperatures (7, 8, 10). These fluids are characterized by variable salt content, slightly acidic to neutral pH, and the presence of both oxidized (sulfate and sulfur dioxide) and reduced (H_2S) sulfur forms in a wide temperature range (~300–700 °C). Predicted concentrations of the gold sulfide and chloride species in such fluids are generally rather low (<0.1–1.0 ppm) to account for a number of enigmatic features of gold geochemistry such as the existence of large deposits without relation to magmatic plutons in metamorphic and sedimentary rocks (e.g., Carlin-type and orogenic) implying deep, likely mantle-derived, Au-rich sources, the observation of highly anomalous Au grades (up to thousands of parts per million) in hydrothermal veins, and huge variations

Significance

Gold resources on Earth result from an exceptional concentration phenomenon yielding metal contents in ore a thousand to a million times higher than those in common rocks. We show that this process is controlled by sulfur radical ions (S_3^-), which strongly bind Au in aqueous solution at elevated temperatures and pressures and allow very efficient extraction, transport, and deposition of gold by geological fluids. Thus, the most inert metal of the periodic table may be very mobile, which explains key features of known gold deposits and offers new possibilities for resource prospecting. Furthermore, the high capacity of the radical ions to solubilize gold may be used for its selective extraction from ores and hydrothermal synthesis of Au-based nanomaterials.

Author contributions: G.S.P. designed research; G.S.P., M.A.K., J.-L.H., V.H., and R.V. performed research; M.A.K., D.G., A.Y.B., P.G., J.-L.H., E.L., W.D.N., O.P., D.T., V.H., R.J., A.P.S., G.F., R.V., A.M.S., M.-C.B., and J.D. contributed new reagents/analytic tools; G.S.P., M.A.K., A.Y.B., J.-L.H., O.P., D.T., V.H., R.J., A.P.S., G.F., R.V., A.M.S., M.-C.B., and J.D. analyzed data; and G.S.P., M.A.K., A.Y.B., V.H., G.F., and A.M.S. wrote the paper.

The authors declare no conflict of interest.

This article is a PNAS Direct Submission.

[1]To whom correspondence should be addressed. Email: gleb.pokrovski@get.obs-mip.fr.

This article contains supporting information online at www.pnas.org/lookup/suppl/doi:10.1073/pnas.1506378112/-/DCSupplemental.

(more than three orders of magnitude) of the ratio of Au to other metals (e.g., Cu, Ag, Mo) in ores (1–4, 6–10, 16). These fluids, which have created the major part of economic gold resources on Earth (1–4), may carry much higher Au concentrations, of tens to hundreds of parts per million, as reported from rare fluid inclusion analyses (4, 6, 9, 10) and a few laboratory experiments of Au solubility (17–20). How gold is transported by such fluids remains, however, controversial, and a variety of other species with H_2S, Cl, As, and alkali metal ligands (3, 14, 17–20) or Au nanoparticles (4, 6, 12) were suggested. Thus, a consistent picture of Au speciation and transport in deep and hot crustal fluids is lacking, hampering our understanding of geochemical fluxes of gold across the lithosphere and the formation of gold economic resources.

In particular, all existing Au speciation models ignore sulfur radical species such as the trisulfur ion S_3^-, which is ubiquitous in chemical and engineering products (21) and was recently shown to be stable in the aqueous fluid phase over a wide temperature (T from 200 °C to ~700 °C) and pressure (P from saturated vapor pressure to ~30 kbar) range (22–24). The omission of S_3^- in current models of hydrothermal fluids is due to its very rapid breakdown to sulfate and sulfide in aqueous solution upon cooling, which prohibits the detection of S_3^- in experimental and natural fluid (and melt) samples brought to ambient conditions. It is thus only recently that the abundance and thermodynamic stability of this important sulfur species could be systematically characterized at high T–P using in situ Raman spectroscopy (22–24). These studies showed that significant amounts of trisulfur ion (>10–100 ppm) may be reached in fluids typical of magmatic and metamorphic environments, which are characterized by elevated dissolved S concentrations (>1,000 ppm), slightly acidic to neutral pH (between ~3 and 7), and redox conditions enabling coexistence of sulfate (or sulfur dioxide) and hydrogen sulfide.

To quantify the effect of S_3^- on Au behavior in hydrothermal fluids, here we combined in situ X-ray absorption spectroscopy (XAS) and hydrothermal reactor measurements with first-principles molecular dynamics (FPMD) and thermodynamic modeling of Au local atomic structure and solubility in aqueous solutions saturated with gold metal and containing hydrogen sulfide, sulfate and S_3^- (*SI Appendix*). These solutions are representative of fluids that formed major types of gold deposits in the crust: 200–500 °C, 300–1,000 bar, 0.1–3.0 wt% S, $3 < \text{pH} < 8$, and oxygen fugacity f_{O2} between the nickel–nickel oxide (NNO) and HM buffer (1–4).

Results

Stoichiometry and Stability of Gold–Trisulfur Ion Complexes. Our results show that gold solubility measured at conditions at which S_3^- is minor is in agreement with values predicted for equilibrium with Au metal using the available stability constants of $Au(HS)_2^-$, which is by far the most stable species at our experimental conditions among sulfide, chloride, and hydroxide complexes of gold known so far (1, 5, 6, 15). In contrast, in S_3^--rich solutions ($S_3^- > 0.01$ mol/kg), the measured Au concentrations are one to three orders of magnitude higher than predicted, with the difference becoming greater with the increase of S_3^- concentration, S_3^-/HS^- ratio, and temperature (Fig. 1 and *SI Appendix*, Fig. S1). These trends demonstrate that complexes with S_3^- make a major contribution to the gold solubility in these solutions. Stoichiometry and structure of these complexes were constrained from XAS spectra that show quasi-linear S–Au(I)–S moieties (*SI Appendix*, Fig. S2 and Table S1), and the presence of second-shell sulfur atoms arising from (Au–S–S)-like bonds in aqueous complexes (*SI Appendix*, Fig. S3). Furthermore, FPMD simulations demonstrate that $Au(HS)S_3^-$ is the most stable among the possible S_3^--bearing gold species, and its simulated XAS spectrum provides a good match to the experimental spectra in S_3^--rich solutions (*SI Appendix*, Fig. S4 and Table S5).

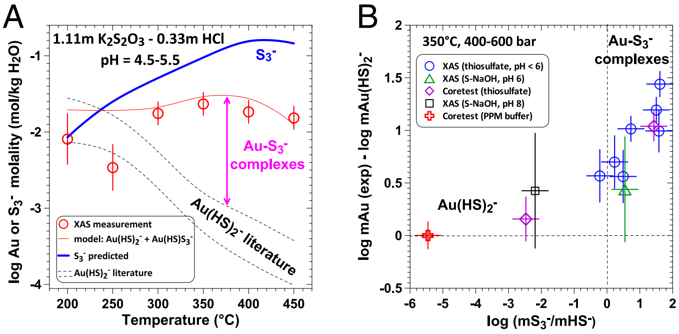

Fig. 1. Direct evidence for gold–trisulfur ion complexes from Au solubility measurements. (*A*) Gold solubility in an aqueous thiosulfate solution of the indicated composition as a function of temperature and S_3^- ion concentration at 600-bar pressure. Symbols represent the measured Au concentrations by in situ XAS; dashed lines delimit the range of calculated $Au(HS)_2^-$ concentrations in equilibrium with metallic gold (6); red curve shows Au solubility calculated including $Au(HS)S_3^-$ in the speciation model (reaction R1); blue curve indicates the predicted concentrations of S_3^- [±0.2 log units (24)]. (*B*) Difference between measured and calculated Au solubility versus the S_3^-/HS^- ratio at 350 °C. Measured Au concentrations are from in situ XAS (*SI Appendix*, Table S1 and ref. 18) and Coretest reactor (*SI Appendix*, Table S2) experiments; $Au(HS)_2^-$ concentrations and the S_3^-/HS^- ratios are calculated using data sources from *SI Appendix*, Table S4. Error bars on data points (2 SD) include uncertainties of Au solubility measurements and thermodynamic calculations.

Thermodynamic analysis of gold solubility data (*SI Appendix*, Tables S1 and S2) using the stoichiometry constraints from XAS and FPMD (*SI Appendix*) is consistent with an equilibrium constant of the exchange reaction $Au(HS)_2^- + S_3^- = Au(HS)S_3^- + HS^-$ (R1) equal to 1 across the investigated T–P range. Such reaction energetics is further supported by the close chemical affinities of the HS^- and S_3^- ions for Au^+ according to the general Au and S chemistry (25) and first-principles calculations on aqueous solutions of this and previous (26) studies. In addition, similar values of the electrostatic Born parameter ($\omega \approx 0.8 \times 10^5$ cal/mol) derived in the framework of the revised Helgeson–Kirkham–Flowers (HKF) equation of state (27, 28) for S_3^- (24) and $Au(HS)_2^-$ (6) imply a close evolution with temperature and pressure of the hydration energies of both ions in aqueous solution. These similarities, together with an isocoulombic nature of reaction (R1), strongly suggest that the reaction energetics is constant over a wide T–P range. Our simple speciation scheme is thus consistent with the ubiquitous presence of S_3^- in S-rich fluids across a large T–P range, to at least 700 °C and 30 kbar (24), and suggests that $Au(HS)S_3^-$ also operates far beyond the T–P conditions of our measurements. Therefore, the findings of gold–trisulfur ion complexes require a revision of Au speciation and transport models in S-rich magmatic–hydrothermal fluids. Furthermore, it cannot be excluded that other Au complexes with S_3^-, in particular uncharged ones or ion pairs with alkali cations, may also form, in addition to $Au(HS)S_3^-$, at high temperatures (>600–700 °C) and moderate pressures (<1–2 kbar) due to the low dielectric constant of the fluid favoring ion association. As such, our predictions are "pessimistic" estimates of the effect of the sulfur radical species on Au solubility and behavior at near-magmatic conditions.

Abundance of Gold–Trisulfur Ion Complexes in Hydrothermal Fluids. Combined with available thermodynamic properties of the other reaction (R1) constituents (6, 24), our data allow, for the first time to our knowledge, the concentration of gold–trisulfur ion complexes and resulting Au solubility to be quantified in natural hydrothermal fluids across a wide T–P range. The abundance of $Au(HS)S_3^-$ is a function of S_3^- itself, and is favored by elevated temperatures, pressures, and sulfur concentrations (>350 °C, >500 bar, >0.5 wt% S), acidic-to-neutral pH, and redox conditions of the

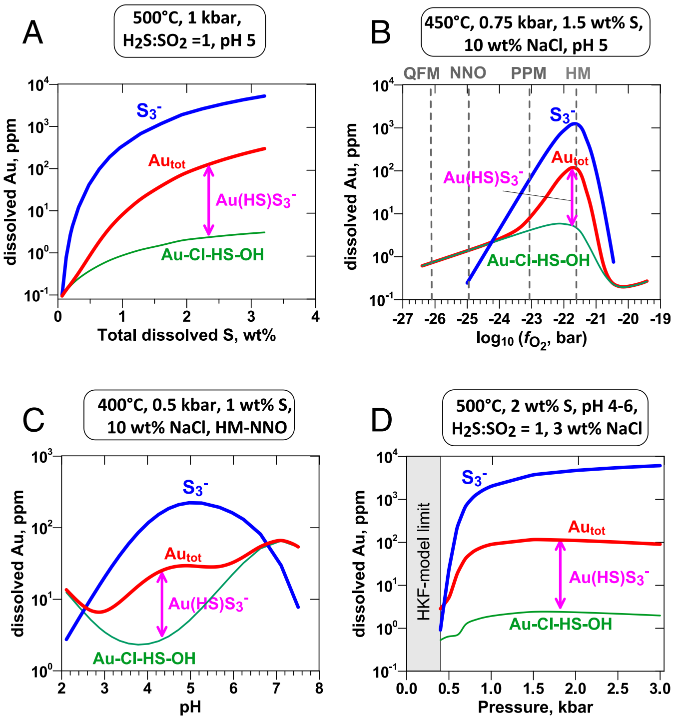

Fig. 2. Gold concentrations and speciation in equilibrium with native Au metal in typical hydrothermal fluids from porphyry Cu–Au–Mo and associated deposits at the indicated *T–P* composition as a function of (*A*) total dissolved S concentration at pH of ∼5 and f_{O2} buffered by H_2S–SO_2 equilibrium, which is very close to the HM buffer; (*B*) redox conditions, with vertical dashed lines indicating the oxygen fugacity corresponding to common redox buffers; (*C*) fluid acidity, pH = $-\log_{10} a(H^+)$ at f_{O2} between HM (acidic pH) and NNO (basic pH); and (*D*) pressure, with the gray shaded area denoting the low-pressure region ($P \leq 400$ bar at 500 °C) in which HKF model predictions are not reliable. In all panels, the curves denote the concentrations of S_3^- (blue, in parts per million of S; same scale as for Au), sum of known Au–HS [AuHS and $Au(HS)_2^-$], Au–Cl ($AuCl_2^-$), and Au–OH (AuOH) species (green), and the total Au solubility including $Au(HS)S_3^-$ (red). The difference between the two latter curves, indicated by the pink arrow, corresponds to the $Au(HS)S_3^-$ species. The thermodynamic properties of Au–Cl–HS–OH species, other fluid constituents, and minerals are from *SI Appendix*, Table S4 (see also *SI Appendix*, Fig. S8 for the distribution of major sulfur species at the same conditions).

H_2S–SO_2 or sulfide–sulfate coexistence, which encompasses a large range of f_{O2}, between NNO (>700 °C) and HM (<500 °C) buffers (Figs. 2 and 3 and *SI Appendix*, Figs. S8 and S10). Such conditions are commonly realized in porphyry and epithermal Cu–Au–Mo deposits within magmatic arcs and in metamorphic belts hosting orogenic and associated Au deposits (2–4, 7, 10, 29–32). In these settings, S_3^- is typically 10–1,000 times more abundant than HS^- in the fluid (e.g., *SI Appendix*, Figs. S7 and S8); consequently, the concentration of $Au(HS)S_3^-$ exceeds that of $Au(HS)_2^-$ by the same factor as imposed by reaction (R1), resulting in gold solubility one to three orders of magnitude higher than previously thought (4, 6, 10, 31). Redox potential is an important parameter affecting both S_3^- concentrations and Au solubility. It can be seen in Fig. 2*B* and *SI Appendix*, Fig. S10 that Au solubility in the form of $Au(HS)S_3^-$ is maximized at f_{O2} of NNO+2 at 700 °C whereas this maximum shifts in between the pyrite–pyrrhotite–magnetite (PPM, ∼NNO+3) and HM (NNO+4) buffers at hydrothermal temperatures (<500 °C), following the major redox trend of porphyry deposits (29–31). The fluid salinity, which may largely vary in porphyry-type fluids during their evolution (from a few to tens of wt% NaCl), exerts a very weak effect on the abundance of S_3^- and its Au complex (*SI Appendix*, Fig. S9). In the presence of large CO_2 concentrations (>10–20 wt%) common in fluids of orogenic-type gold deposits (10, 33–35), the relative abundances of $Au(HS)S_3^-$ versus $Au(HS)_2^-$ are only slightly affected compared with an aqueous solution at the same *T*–*P*–pH–f_{O2} conditions, even though the absolute concentrations of both charged species are expected to be lower in the CO_2–H_2O solvent due to its low dielectric constant, which is unfavorable for the stability of charged species (4, 6). Fluid immiscibility that is common in porphyry, epithermal, and many orogenic deposits (2, 9, 10, 29–35) is another factor influencing both S_3^- and Au behavior. This phenomenon causes breakdown of Au–trisulfur ion species because S_3^- is not stable in the low-density vapor phase (24) (e.g., Fig. 2*D*). This breakdown induces precipitation of a portion of the gold, consistent with numerous observations in different types of deposits where fluid unmixing occurs (29–36), with the balance constrained by the vapor phase as volatile complexes with hydrogen sulfide (4, 17) or chloride (37), depending on the fluid H_2S and HCl content, acidity, temperature, and depth of the vapor–liquid separation. For example, vapor–liquid partitioning coefficients for Au in S-rich (∼1 wt% S) acidic (pH < 5) systems at 400–500 °C are above 1 (17, 36), suggesting an important contribution of the vapor phase to Au transport. Once such H_2S–SO_2 vapor ascends and condenses to liquid below the water critical temperature, S_3^- and its complexes with Au may reform again, along with $Au(HS)_2^-$. With further decrease in temperature and sulfur concentration (<300 °C, <0.1 wt% S), $Au(HS)_2^-$ replaces $Au(HS)S_3^-$ as the main carrier of gold to the sites of ore deposition in shallow orogenic and epithermal settings (1, 4–6, 31–34) (Fig. 3).

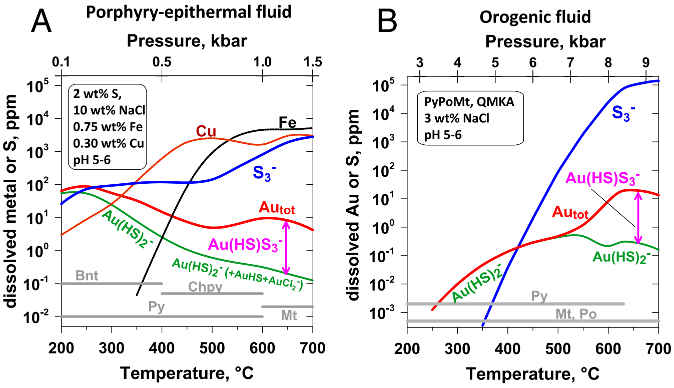

Fig. 3. Gold solubility in aqueous fluids typical of (*A*) magmatic porphyry–epithermal Cu–Au–Mo and (*B*) metamorphic rock-hosted orogenic and sedimentary rock-hosted Carlin Au deposits. (*A*) A magmatic fluid of a typical composition indicated in the figure (H_2S:SO_2 molal ratio = 1), degassed from magma at 700 °C, cools and decompresses in the liquid phase in equilibrium with native Au and alkali aluminosilicate rocks (pH of 5–6 at all temperatures); this is a common scenario of fluid evolution in a porphyry–epithermal setting (4, 9, 29–31). (*B*) A low-salinity metamorphic fluid evolves in equilibrium with native gold and the PPM (PyPoMt) and quartz–muscovite–(K) feldspar–albite (QMKA) mineral assemblages (pH of 5–6) along a typical geothermal gradient of subduction zones (75 °C per 1 kbar) (7, 34). Curves show the concentrations of S_3^- (in parts per million S), Au total solubility (Au_{tot}), the sum of Au hydrogen sulfide (±chloride) complexes [the difference between the two curves corresponds to $Au(HS)S_3^-$ concentration as indicated by the vertical pink arrow], and Fe and Cu solubility (thermodynamic data from *SI Appendix*, Table S4). Uncertainties (2 SD) in Au species concentrations are within a half-log unit below 600 °C and approach 1 log unit at 700 °C. Gray horizontal lines show the temperature range of stability of the indicated minerals (Py, pyrite; Po, pyrrhotite; Mt, magnetite; Bnt, bornite; Chpy, chalcopyrite). Note an increase in $Au(HS)_2^-$ concentration with decreasing *T* in the S-rich fluid in *A*, consistent with the known temperature maximum of 200–250 °C for the stability of this species (1, 5, 6, 18, 31). See also *SI Appendix*, Fig. S7 for distribution of major sulfur and gold species at the same conditions.

Discussion and Geological and Metallogenic Applications

The findings of stable gold–trisulfur ion complexes in hydrothermal fluids have important consequences for the formation, distribution, and exploration of economic gold deposits.

Enhanced Extraction and Transport of Gold. First, the S_3^- ion greatly enhances the fluid capacity to extract Au from magma or rocks and to transport it to ore deposition sites. Thus, the highly soluble $Au(HS)S_3^-$ species can account for Au enrichment in H_2S–SO_2-rich fluids, which are released from magmas in arc settings and form porphyry Cu–Au–Mo and epithermal Cu–Au deposits (2, 3, 9, 31) (Figs. 3 and 4). Our calculations suggest that above 300 °C, the capacity of such fluids to concentrate gold (i.e., until reaching saturation with the metal) attains 10–100 ppm Au as $Au(HS)S_3^-$. Such solubilities are comparable to the highest Au concentrations found in S-rich (>0.5 wt% S) fluid inclusions in porphyry systems (4, 6, 9, 31), but they are 10–100 times higher than predicted from the data on known Au hydrogen sulfide and chloride species (Fig. 3*A*). Our estimates at temperatures close to fluid release from hydrous S-rich magmas in arc settings (e.g., 700 °C) also suggest greatly increased fluid extraction capacities of Au if S_3^- and its Au complexes are considered. For example, 10–100 times more Au may be extracted into the magmatic fluid over a wide range of SO_2/H_2S ratios, from 0.01 to 10 (corresponding to f_{O2} of NNO+1 to NNO+2, *SI Appendix*, Fig. S10), typical of arc magmas (2, 3, 29, 31). In iron-rich metamorphic environments typical of orogenic gold deposits (7, 8, 10, 32–35), the low solubility of pyrite at <500 °C is the major limiting factor for S_3^-; therefore, in such settings, S_3^- is capable of concentrating Au only at hot stages of metamorphism, between 500 °C and 700 °C, where S_3^- concentrations are high enough to yield Au-enriched fluids within amphibolite facies (Fig. 3*B*). This capacity to preconcentrate gold at the amphibolite stage requires a more attentive exploration of high-grade metamorphic terrains for yet undiscovered gold deposits or Au-enriched source rocks. This gold may be subsequently remobilized by later fluids and transported as $Au(HS)_2^-$ to deposition sites hosted in lower-degree metamorphic (mostly greenschist facies) or sedimentary rocks such as Carlin-type deposits. Although the models of formation of this important type of gold deposit are far from being unanimous, suggesting either deep (>10 km) metamorphic (8) or magmatic (38) sources for gold, both types of source are consistent with the enhanced Au mobilization and concentration by sulfur radical species in S-rich high-temperature fluids generated either by prograde metamorphism of Au–pyrite-bearing rocks or magma degassing at depth accompanied by vapor–liquid unmixing, and subsequent transport of Au to the deposition site at lower temperatures (<300 °C) predominantly as $Au(HS)_2^-$.

Focused Precipitation of Gold. Second, the sensitivity of the S_3^- concentration to small changes of T, P, pH, f_{O2}, and S content during the fluid evolution (Figs. 2 and 3) greatly optimizes the efficiency of ore deposition. For example, for a typical porphyry fluid, enriched in H_2S and SO_2 (f_{O2} close to NNO+2), degassing from magma and carrying 10 ppm Au (4, 9), as little as a twofold decrease in S total dissolved concentration, from 1.0 to 0.5 wt%, which is easily achieved by fluid unmixing or Cu and Fe sulfide deposition from the fluid (4, 6, 31), will cause precipitation of 90% of the dissolved gold through $Au(HS)S_3^-$ breakdown, as shown in Fig. 2*A* at 500 °C (similar results are obtained in the wide T range, 600–350 °C, typical of gold precipitation in porphyry deposits). For comparison, if S_3^- and its gold complex are ignored, the maximum transport capacity of the fluid at such conditions is less than 1 ppm Au, only half of which will precipitate following the same twofold drop in S concentration (Fig. 2*A*), resulting in a total deposited Au amount of 20 times less. Similarly, cooling by only 50 °C (from 600 °C to 550 °C) of a S-rich fluid, carrying 10 ppm Au in equilibrium with pyrite-bearing shales at amphibolite facies conditions (7), precipitates 90% of its gold content from the $Au(HS)S_3^-$ species, whereas there is no gold deposition from $Au(HS)_2^-$, which accounts for only ~0.1 ppm Au (Fig. 3*B*). The sharp drop of Au solubility between 600 °C and 500 °C caused by the decay of S_3^- due to decreasing solubility of pyrite (Fig. 3*B*) explains the observation that most gold deposits in metamorphic terrains are hosted by greenschist rock facies that correspond to temperatures ≤500 °C (32–35). When fluids degassing from arc magmas and carrying both reduced and oxidized sulfur, favorable for S_3^- and its Au complex, interact with reduced organic-rich sediments, massive Au precipitation occurs over a small f_{O2} range (e.g., from HM to PPM at 450 °C, Fig. 2*B*), which is consistent with

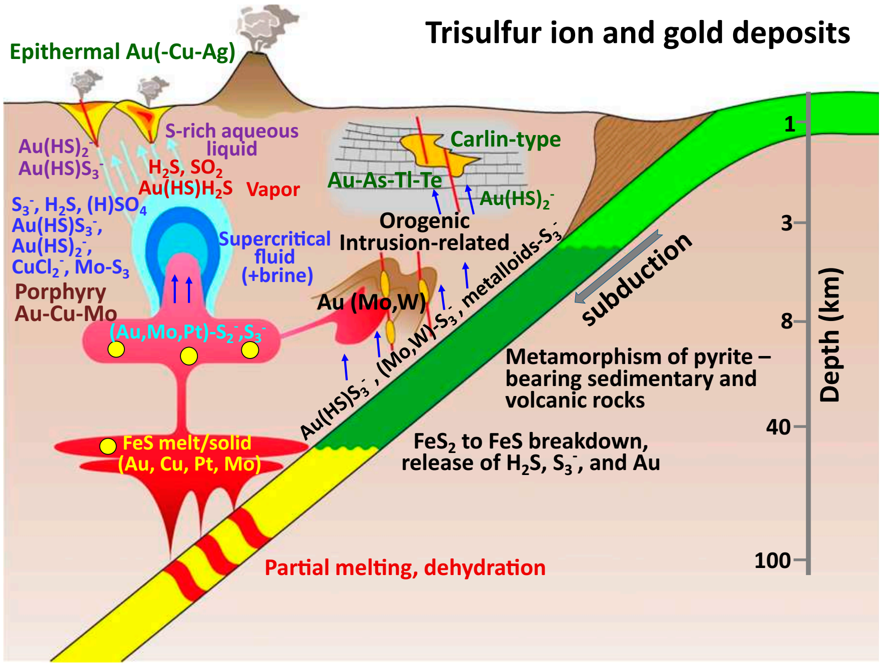

Fig. 4. Geological settings within the lithosphere where the trisulfur radical ion affects the formation of major types of economic gold deposits (not to scale). The main processes of fluid generation and evolution, and the dominant S and Au species in the fluid, are shown. Blue arrows illustrate fluid flow. The S_3^- ion enhances Au (and, potentially, other sulfur-loving trace metals, like Mo, Pt, and metalloids) release into the fluid phase from both sulfide and silicate melts during magma evolution in arc settings, and from pyrite-bearing sedimentary and volcanic rocks upon their prograde metamorphism. Upon fluid cooling, decompression, or reactions with rocks (sulfidation), S_3^- breaks down and precipitates its Au load in porphyry, deep orogenic, and intrusion-related deposits. Part of this gold is subsequently remobilized by later fluids or vapors and transported as hydrogen sulfide (±chloride) complexes to shallow orogenic, Carlin, and epithermal deposits. Thus, S_3^- can either directly bring gold to deposits in high-temperature S-rich environments or create, at deep crustal levels, local Au enrichment in rocks that may further serve as a gold source for shallower deposits.

the close association of gold with carboniferous rocks in some types of deposits (7, 8, 32). For comparison, Au solubility in the form of traditional sulfide or chloride complexes is far less sensitive to variations in oxygen fugacity (Fig. 2*B*). Acidification of porphyry fluid upon cooling below 400 °C, induced by breakdown of SO_2 to H_2S and sulfuric acid (4, 29, 30), also leads to Au precipitation from its S_3^- complex over a narrow pH range (e.g., from pH 4 to 3, Fig. 2*C*), consistent with gold deposition in some Au-rich porphyry deposits in phyllic (chlorite–sericite) alteration zones caused by acidic fluids (29, 30). More generally, any mechanism that triggers ore deposition in different geological settings, such as fluid cooling, decompression and phase separation, interaction with rocks (e.g., sulfidation), and fluid mixing (1, 2, 4, 10, 29–42), will cause S_3^- and $Au(HS)S_3^-$ breakdown in a narrow T–P–pH–f_{O2}–f_{S2} window (Fig. 2) and lead to a sharp decrease in Au solubility and thus massive gold deposition over a limited depth and time range. This chemical control by S_3^- can explain, for example, highly anomalous Au concentrations, in excess of 1,000 ppm Au, in many bonanza epithermal veins (42). Changes in S_3^- concentration, induced by Fe and Cu sulfide precipitation upon porphyry fluid cooling (Fig. 3*A*), can yield oscillatory patterns in Au solubility in the T–P space (depending on the Fe/S ratio in the degassing magmatic fluid and the degree of fluid interaction with alkali aluminosilicate rocks). Such patterns contribute, along with other possible factors evoked so far, such as magma-fluid and vapor–brine separation (3, 16, 30), to the large spatial variations of Au grades and Au/Cu ratios reported between porphyry deposits. Furthermore, the S_3^- may also control incorporation of Au in a chemically bound state into pyrite, which is the major Au host of many epithermal and Carlin-type deposits (8, 38). Because pyrite formation from hydrothermal solution occurs via polysulfide ion precursors (43), S_3^- may play a key role in this mechanism, favoring Au uptake by the sulfide mineral from solutions undersaturated with metallic gold.

Fractionation of Gold from Other Metals. Third, the selective affinity of S_3^- for Au may induce gold fractionation from Cu, Zn, and Pb that do not bind to S_3^- (*SI Appendix*). Thus, along with other multiple factors evoked so far, such as selective vapor-phase transport (10, 36–38), specific metal sources (7, 8), and silicate and sulfide melt evolution at depth (3, 41, 42, 44), S_3^- binding to Au and, possibly, to other sulfur-loving metals and metalloids (e.g., Ag, Sb, Te) may be responsible for the particular ore signatures of Carlin, orogenic and intrusion-related gold deposits enriched in the Au–As–Sb–Tl–Te (±W±Mo) suite, with little Cu, Zn, and Pb (Fig. 4). Another important metal susceptible to bind with S_3^- is molybdenum, which is known to form a variety of oxyhydroxide, chloride, and sulfide complexes in aqueous solution but none of which is able to account for elevated Mo concentrations (hundreds of parts per million) found in fluid inclusions from porphyry systems below 500 °C and economic Mo grades in some epithermal deposits (4, 30). Other metals of high economic value, such as platinum group elements that have similar chemical properties to Au (25), are also expected to form stable complexes with S_3^-, enhancing both the metal mobility in S-rich fluids and focused deposition upon S_3^- decay. Furthermore, another sulfur radical, the disulfur ion (S_2^-), suggested to be stable above 500 °C in sulfate–sulfide aqueous systems (24), may also strongly bind Au and associated metals in magmatic fluids and, potentially, silicate melts. Noteworthy is that Au solubility measured in silicate melts (44, 45) is maximized at the sulfide–sulfate transition, which is also the most favorable redox condition for S_3^- (and S_2^-) in hydrothermal fluids, as shown in this study. If the sulfur radical species are stable in silicate melts, they may further enhance selective extraction of Au from magmatic iron sulfide (Fig. 4), thus preparing an Au-enriched source silicate melt for porphyry deposits. This is in agreement with the association of Au-rich porphyry deposits with oxidized [f_{O2} of quartz–fayalite–magnetite (QFM)+2 at 900 °C] arc magmas (44–46).

Conceptual Models of Gold Deposit Formation. Finally, our results challenge the existing models of ore deposit formation and offer more perspectives for exploration. The large enhancement by S_3^- of the fluid transport capacities for Au, coupled with the efficient Au precipitation triggered by S_3^- breakdown, implies that far smaller but more concentrated amounts of fluid than previously thought (39, 41) are responsible for economic gold deposition at high temperatures. This conclusion offers previously unidentified insights into magmatic and metamorphic ore fluid dynamics that appears to be similar to that for sedimentary rock-hosted base-metal deposits whose formation would occur by periodic injections of anomalously metal-rich batches of fluids during short ore-forming events (40). A smaller amount of S_3^--bearing fluid would imply a smaller volume of the magma source necessary for an economic gold deposit. Furthermore, modern conceptual models of ore deposits require an exceptionally fortuitous combination of Au-rich sources such as Au preconcentration in magmatic sulfides (3, 41, 42) or sedimentary pyrite (7, 8), sustained and focused hydrothermal fluid flow (38, 39), and tectonic and other geochemical triggers of an efficient precipitation mechanism (39–42), all acting in unison to form an economic gold deposit from typically part-per-billion levels of Au concentrations as hydrogen sulfide or chloride complexes in the fluid and silicate melt. The existence of gold–trisulfur ion species with large capacities to extract, transfer, and precipitate gold reduces these requirements and shortens by up to 10–100 times the duration needed to form a given deposit from a much smaller magma or rock source. Consequently, the choice of possible locations where new deposits may be found is significantly extended, both in time and space, thus offering more potential for exploration. The finding of sulfur radicals concentrating gold at depth suggests that huge, so far unknown deposits still await discovery. This conclusion agrees with recent estimations of economic gold resources to a depth of only 3 km of Earth's continental crust (47), which are ∼40 times larger than gold reserves in currently known deposits (48).

Methods Summary

See *SI Appendix* for detailed description of experimental and model systems, methods, and uncertainties.

X-Ray Absorption Spectroscopy and Solubility Measurements. Gold solubility and local atomic structure were measured in aqueous Au-saturated solutions of thiosulfate and elemental sulfur or with an excess of the PPM and quartz–muscovite–(K)feldspar (QMK) mineral assemblages (*SI Appendix*, Tables S1 and S2). These solutions contain variable amounts of hydrogen sulfide, (hydrogen)sulfate, and S_3^- ion (depending on the composition), and provide acidity and redox buffering of the system (18, 23). In situ XAS measurements at Au L_3 edge (11.119 keV) were performed at BM30b-FAME beamline at the European Synchrotron Radiation Facility using a hydrothermal apparatus developed at the Néel Institute that enables simultaneous acquisition of high-quality fluorescence spectra to extract structural information, and of transmission spectra to directly determine the dissolved Au concentration in solution (18). Experiments were conducted at pressures of 600 ± 50 bar and temperatures from 200 °C to 450 °C, similarly to a previous study on Au–S aqueous systems (18). The XAS experiments were complemented by batch reactor measurements of gold solubility at selected T–P (in the range 350–500 °C and 350–750 bar) using a Coretest hydrothermal reactor equipped with a flexible titanium or gold cell and a rapid fluid extraction design (17). Chemical treatments and analyses of the sampled fluid were performed following established protocols for S-rich solutions (17).

Molecular Dynamics Simulations. FPMD modeling was carried out using a cubic simulation box of at least 126 water molecules with several Au^+, HS^-, S_3^-, and H_2S ions or molecules to estimate the stability of different Au–S species, calculate extended X-ray absorption fine structure (EXAFS) spectra for the stable hydrated complexes $Au(HS)S_3^-$, $Au(HS)S_3^{2-}$, $Au(S_3)_2^-$, $Au(HS)_2^-$, and Au(HS), and compute free energy profiles for ligand exchange reaction (R1) via the potential of mean force.

Thermodynamic Analysis of Gold Speciation. Gold solubility in experimental solutions (~50 data points) was modeled using a set of species of various charge and stoichiometry formed between Au^+ and S_3^-, H_2S, and HS^-, and using the constraints from XAS and FPMD results, which suggest the dominant formation of species in which Au^+ is coordinated with two S-bearing ligands. It was found that $Au(HS)_2^-$ and $Au(HS)S_3^-$ provide the best match of the measured solubilities and that additional species are not necessary. The generated Gibbs free energy values of $Au(HS)S_3^-$ at each experimental T and P, combined with the robust thermodynamic properties of $Au(HS)_2^-$, HS^-, and S_3^- (*SI Appendix*, Table S4), allow calculation of the equilibrium constant K_{R1} of the isocoulombic exchange reaction (R1) (*SI Appendix*, Table S3). This constant is close to 1 within errors between 300 °C and 500 °C, consistent with the similar affinity of HS^- and S_3^- for Au^+ as also inferred from our FPMD modeling, further supporting our speciation scheme.

Geochemical Modeling. Calculations of fluid–mineral equilibria involving gold in model systems pertinent to geological settings of magmatic–hydrothermal, porphyry–epithermal Cu–Au–Mo, and metamorphic–sedimentary (orogenic, intrusion related and Carlin) Au deposits were performed for typical mineralogy and fluid compositions inferred from numerous existing studies (1–4, 29–34). The common metals accompanying Au in the fluids, such as Fe, Cu, Zn, and Ag, were also included in the modeling. The data sources for the thermodynamic properties of minerals, aqueous sulfur, and Au–OH–Cl–HS species are reported in *SI Appendix*, Table S4. These sets of data arise from a large number of experimental studies and are described by powerful equations of state (*SI Appendix*), enabling robust extrapolations to temperatures of 700 °C and pressures of 10 kbar. In addition, the effect of S_3^- on the speciation of Cu, Zn, and Ag was estimated using the analogy with reaction (R1).

ACKNOWLEDGMENTS. We are grateful to C. Cavaré-Hester for the help with figure preparation; Y. Shvarov for the help with thermodynamic modeling; and T. Chivers, J. Hedenquist, K. Kouzmanov, and F. Guyot for their constructive comments on earlier versions of the manuscript. The article benefited from the comments of two anonymous referees. We acknowledge European Synchrotron Radiation Facility (ESRF) for providing access to beamtime and infrastructure. This work was funded by the Centre National de la Recherche Scientifique (CNRS), the French National Research Agency (Grant SOUMET, ANR-2011-Blanc SIMI 5-6 009), the University of Toulouse (Grant CO_2MET), the Institut Carnot (Grant ISIFoR), the Institut des Sciences de l'Univers (Grants ORPY-CESSUR and S3MIF-PNP), Lorraine University (Grant ANR Investissements d'Avenir, ANR-10-LABX-21–LABEX RESSOURCES21), and the Cluster of Excellence MATISSE (Matériaux, Interfaces, Surfaces, Environnement) led by Sorbonne Universités (Grant ANR Investissement d'Avenir, ANR-11-IDEX-0004-02). R.J. acknowledges support from the UPMC-Emergence program. V.H., R.J., A.P.S., G.F., R.V., and A.M.S. acknowledge access granted to high-performance computing resources from Grand Equipement National pour le Calcul Intensif (GENCI) and Institut du Développement et des Ressources en Informatique Scientifique (IDRIS) (Allocation x2014082309).

1. Barnes HL, ed (1997) *Geochemistry of Hydrothermal Ore Deposits* (Wiley, New York).
2. Hedenquist JW, Lowenstern JB (1994) The role of magmas in the formation of hydrothermal ore deposits. *Nature* 370:519–527.
3. Simon AC, Ripley EM (2011) The role of magmatic sulfur in the formation of ore deposits. *Rev Mineral Geochem* 73(1):513–578.
4. Kouzmanov K, Pokrovski GS (2012) Hydrothermal controls on metal distribution in porphyry Cu(-Au-Mo) systems. *Soc Econ Geol Spec Publ* 16:573–618.
5. Seward TM (1973) Thio complexes of gold and the transport of gold in hydrothermal ore solutions. *Geochim Cosmochim Acta* 37(3):379–399.
6. Pokrovski GS, Akinfiev NN, Borisova AY, Zotov AV, Kouzmanov K (2014) Gold speciation and transport in geological fluids: Insights from experiments and physical-chemical modeling. *Geol Soc Spec Publ* 402:9–70.
7. Tomkins AG (2010) Windows of metamorphic sulfur liberation in the crust: Implications for gold deposit genesis. *Geochim Cosmochim Acta* 74(11):3246–3259.
8. Large RR, Bull SW, Maslennikov VV (2011) A carbonaceous sedimentary source-rock model for Carlin-type and orogenic gold deposits. *Econ Geol* 106:331–358.
9. Ulrich T, Günther D, Heinrich CA (1999) Gold concentrations of magmatic brines and the metal budget of porphyry copper deposits. *Nature* 399:676–679.
10. Garofalo PS, Fricker MB, Günther D, Barsani D, Lotticí PP (2014) Physical-chemical properties and metal budget of Au-transporting hydrothermal fluids in orogenic deposits. *Geol Soc Spec Publ* 402:71–102.
11. Ogryzlo SP (1935) Hydrothermal experiments with gold. *Econ Geol* 30(4):400–424.
12. Krauskopf KB (1951) The solubility of gold. *Econ Geol* 48(8):858–870.
13. Helgeson HC, Garrels RM (1968) Hydrothermal transport and deposition of gold. *Econ Geol* 63(6):622–635.
14. Boyle RW (1969) Hydrothermal transport and deposition of gold. *Econ Geol* 64(1):112–115.
15. Stefánsson A, Seward TM (2003) Stability of chloridogold(I) complexes in aqueous solutions from 300 to 600°C and from 500 to 1800 bar. *Geochim Cosmochim Acta* 67(23):4559–4576.
16. Murakami H, Seo JH, Heinrich CA (2010) The relation between Cu/Au ratio and formation depth of porphyry-style Cu-Au±Mo deposits. *Miner Deposita* 45(1):11–21.
17. Pokrovski GS, Borisova AY, Harrichoury J-C (2008) The effect of sulfur on vapor-liquid fractionation of metals in hydrothermal systems. *Earth Planet Sci Lett* 266(3-4):345–362.
18. Pokrovski GS, Tagirov BR, Schott J, Hazemann J-L, Proux O (2009) A new view on gold speciation in sulfur-bearing hydrothermal fluids from in-situ X-ray absorption spectroscopy and quantum-chemical modeling. *Geochim Cosmochim Acta* 73(18):5406–5427.
19. Loucks RR, Mavrogenes JA (1999) Gold solubility in supercritical hydrothermal brines measured in synthetic fluid inclusions. *Science* 284(5423):2159–2163.
20. Zajacz Z, Seo JH, Candela PA, Piccoli PM, Heinrich CA (2010) Alkali metals control the release of gold from volatile-rich magmas. *Earth Planet Sci Lett* 297(1-2):50–56.
21. Chivers T, Elder PJW (2013) Ubiquitous trisulfur radical anion: Fundamentals and applications in materials science, electrochemistry, analytical chemistry and geochemistry. *Chem Soc Rev* 42(14):5996–6005.
22. Pokrovski GS, Dubrovinsky LS (2011) The S_3^- ion is stable in geological fluids at elevated temperatures and pressures. *Science* 331(6020):1052–1054.
23. Jacquemet N, Guillaume D, Zwick A, Pokrovski GS (2014) In situ Raman spectroscopy identification of the S_3^- ion in S-rich hydrothermal fluids from synthetic fluid inclusions. *Am Mineral* 99(5-6):1109–1118.
24. Pokrovski GS, Dubessy J (2015) Stability and abundance of the trisulfur radical ion S_3^- in hydrothermal fluids. *Earth Planet Sci Lett* 411:298–309.
25. Cotton FA, Wilkinson G, Murillo CA, Bochmann M (1999) *Advanced Inorganic Chemistry* (Wiley, Chichester, UK), 6th Ed.
26. Mei Y, Sherman DM, Liu W, Brugger J (2013) Complexation of gold in S_3^--rich hydrothermal fluids: Evidence from ab-initio molecular dynamics simulations. *Chem Geol* 347:34–42.
27. Sverjensky DA, Shock EL, Helgeson HC (1997) Prediction of the thermodynamic properties of aqueous metal complexes to 1000 °C and 5 kb. *Geochim Cosmochim Acta* 61(7):1359–1412.
28. Sverjensky DA, Harrison B, Azzolini D (2014) Water in the deep Earth: The dielectric constant and the solubilities of quartz and corundum to 60 kb and 1200 °C. *Geochim Cosmochim Acta* 129:125–145.
29. Seedorff E, et al. (2005) Porphyry deposits: Characteristics and origin of hypogene features. *Economic Geology 100th Anniversary Volume*, eds Hedenquist JW, Thompson JFH, Goldfarb RJ, Richards JP (Soc Econ Geol, Littleton, CO), pp 251–298.
30. Sillitoe RH (2010) Porphyry copper systems. *Econ Geol* 105(1):3–41.
31. Heinrich CA (2005) The physical and chemical evolution of low-salinity magmatic fluids at the porphyry to epithermal transition: A thermodynamic study. *Miner Deposita* 39(8):864–889.
32. Goldfarb RJ, et al. (2005) Distribution, character, and genesis of gold deposits in metamorphic terrains. *Economic Geology 100th Anniversary Volume*, eds Hedenquist JW, Thompson JFH, Goldfarb RJ, Richards JP (Soc Econ Geol, Littleton, CO), pp 407–450.
33. Phillips GN, Evans KA (2004) Role of CO_2 in the formation of gold deposits. *Nature* 429(6994):860–863.
34. Ridley JR, Diamond LW (2000) Fluid chemistry of orogenic lode gold deposits and implications for genetic models. *Rev Econ Geol* 13:141–162.
35. Boiron MC, Cathelineau M, Banks DA, Fourcade S, Vallance J (2003) Mixing of metamorphic and surficial fluids during the uplift of the Hercynian upper crust: Consequences for gold deposition. *Chem Geol* 194(1-3):119–141.
36. Pokrovski GS, Borisova AY, Bychkov AY (2013) Speciation and transport of metals and metalloids in geological vapors. *Rev Mineral Geochem* 76:165–218.
37. Hurtig NC, Williams-Jones AE (2014) An experimental study of the transport of gold through hydration of AuCl in aqueous vapour and vapour-like fluids. *Geochim Cosmochim Acta* 127:305–325.
38. Muntean JL, Cline JS, Simon AC, Longo AA (2011) Magmatic–hydrothermal origin of Nevada's Carlin-type gold deposits. *Nat Geosci* 4(2):122–127.
39. Simmons SF, Brown KL (2006) Gold in magmatic hydrothermal solutions and the rapid formation of a giant ore deposit. *Science* 314(5797):288–291.
40. Wilkinson JJ, Stoffell B, Wilkinson CC, Jeffries TE, Appold MS (2009) Anomalously metal-rich fluids form hydrothermal ore deposits. *Science* 323(5915):764–767.
41. Wilkinson JJ (2013) Triggers for the formation of porphyry ore deposits in magmatic arcs. *Nat Geosci* 6(11):917–925.
42. Richards JP (2013) Giant ore deposits formed by optimal alignments and combinations of geological processes. *Nat Geosci* 6(11):911–916.
43. Schoonen MAA, Barnes HL (1991) Mechanisms of pyrite and marcasite formation from solution: III. Hydrothermal processes. *Geochim Cosmochim Acta* 55(12):3491–3504.
44. Botcharnikov RE *et al.* J (2011) High gold concentrations in sulphide-bearing magma under oxidizing conditions. *Nat Geosci* 4(2):112–115.
45. Zajacz Z, Candela PA, Piccoli PM, Wälle M, Sanchez-Valle C (2012) Gold and copper in volatile saturated mafic to intermediate magmas: Solubilities, partitioning, and implications for ore deposit formation. *Geochim Cosmochim Acta* 91:140–159.
46. Richards JP (2011) Magmatic to hydrothermal metal fluxes in convergent and collided margins. *Ore Geol Rev* 40(1):1–26.
47. Kesler SE, Wilkinson BH (2010) Global hydrothermal gold resources for the next millennium. *Soc Econ Geol Spec Publ* 15:5–18.
48. Frimmel HE (2008) Earth's continental crustal gold endowment. *Earth Planet Sci Lett* 267(1-2):45–55.

TITLE : Role of CO_2 in the transfer of economic metals by geological fluids

ABSTRACT

Carbon dioxide is the second component after water of geological fluids that operate at high temperature (*T*) and pressure (*P*) in the lithosphere, transport the metals and form economic deposits. However, its effect on the mobilization and precipitation of metals remains virtually unknown owing to a lack of direct data and physical-chemical models. In this thesis, we have developped experimental methods and chemical and spectroscopic analyzes of CO_2-rich fluids, coupled with thermodynamic modeling, to systematically quantify, for the first time, the solubility, distribution and speciation of various metals of economic interest (Fe, Cu, Au, Mo, Pt, Sn, Zn) in gas-water-salt systems typical of metalliferous hydrothermal fluids.

Measurements of the solubility of the major minerals of these metals (sulfides, oxides and native metals) and of metal partition coefficients were carried out in supercritical fluids H_2O-CO_2-S-KCl at 450°C and 500-700 bar and in two-phase vapor-liquid systems H_2O-CO_2-NaCl-KCl-S at 350°C, 130-300 bar, using flexible-cell and phase-separation reactors that we have set up. The conditions of acidity, redox potential and sulfur fugacity were controlled by equilibria among iron sulfide and oxide minerals and alkali-aluminosilicate minerals or between sulfate and sulfide in the fluid. The data obtained were analyzed in the framework of a thermodynamic model coupled with a critical review of the literature on the metal speciation in the fluid phase. The electrostatic model that we used does not require any adjustable parameters; it is based on the dielectric constant of the CO_2-H_2O solvent and the Born parameter of the dominant species in the aqueous phase.

Our results show that the mobility of metals in CO_2-rich fluids is controlled by the nature and electrical charge of their main aqueous complexes. The presence of CO_2 favors the stability of the neutral complexes ($FeCl_2^0$, $AuHS^0$, $CuHS^0$, $ZnCl_2^0$, $KMoO_4^0$, $Pt(HS)_2^0$) whereas that of the charged species of these metals ($FeCl_4^{2-}$, $Au(HS)^{2-}$, $CuCl^{2-}$, $ZnCl_4^{2-}$, $HMoO_4^-$, $PtCl_3^-$) is largely weakened. This results is significant fractionations between some metals, depending on the composition of the fluid and the geological context. Our model accounts for the enrichment in Fe and depletion in Cu observed in metamorphic orogenic gold deposits formed by CO_2-rich fluids. The transport of gold by these fluids is favored at low sulfur content ($Au(HS)^0$ is dominant), whereas in S-rich fluids typical of porphyry copper deposits and high *T* orogenic gold deposits where the charged complexes are dominant ($Au(HS)_2^-$, $Au(HS)S_3^-$), the presence of CO_2 leads to lowering the solubility of gold. However, even at high CO_2 content (> 50 wt%), the ability of fluids to carry gold as neutral species (~100s ppb) remains comparable to that of an aqueous fluid, which explains the associations of gold mineralizations with fluids rich in CO_2. The effect of CO_2 on the mobility of Mo, Zn and Si, which form neutral species, is weak in most geological situations, whereas that of Sn could be promoted by carbonate complexes and that of Pt by carbonyl (CO) complexing. The direct role of CO_2 in the vapor-liquid partitioning of most metals is relatively small compared to that of reduced sulfur (H_2S) whose presence strongly favors the enrichment of the vapor by Au, Pt, Mo and Cu. Thus, the main impact of CO_2 in these demixing processes is to expand the fluid *T-P* domain of immiscibility.

This study demonstrates that, contrary to common belief, the presence of CO_2 can promote the mobility of certain metals and cause significant fractionations between different metals during the evolution of fluids in the crust.

AUTEUR : Maria KOKH
TITRE : Rôle du CO_2 dans les transferts des métaux d'intérêt économique par les fluides géologiques
DIRECTEUR DE THESE : Gleb Pokrovski
LIEU ET DATE DE SOUTENANCE : Toulouse, le 22 janvier 2016

RESUME

Le CO_2 est le deuxième après l'eau constituant des fluides de haute température (*T*) et haute pression (*P*) qui opèrent dans la lithosphère, transportent la matière et forment des dépôts économiques des métaux. Cependant, son effet sur la mobilisation et la précipitation des métaux reste quasiment inconnu faute de données directes et de modèles physico-chimiques. Dans ce travail de thèse, nous avons mis en œuvre des méthodes expérimentales et des analyses chimiques et spectroscopiques sur des fluides modèles riches en CO_2, couplées à une modélisation thermodynamique, afin de quantifier, pour la première fois de manière systématique, la solubilité, le partage et la spéciation de divers métaux d'intérêt économique (Fe, Cu, Au, Mo, Pt, Sn, Zn) dans les systèmes eau-gaz-sels typiques des fluides hydrothermaux métallifères.

Des mesures de solubilité des principaux minéraux de ces métaux (sulfures, oxydes et métaux natifs) et de leurs coefficients de partage ont été effectuées dans des fluides supercritiques H_2O-CO_2-S-KCl à 450°C et 500-700 bar et dans des systèmes liquide-vapeur H_2O-CO_2-S-KCl-NaCl à 350°C, 130-300 bar, à l'aide d'autoclaves à cellule flexible et de réacteurs à séparation de phase que nous avons mis au point. Les conditions d'acidité, de redox et de fugacité de soufre ont été contrôlées par des équilibres entre les minéraux sulfures et oxydes de fer et alkali-aluminosilicates ou entre le sulfate et le sulfure en solution. Les données ont été analysées dans le cadre d'un modèle thermodynamique couplé à une révision critique des données sur la spéciation des métaux en phase fluide. Ce modèle électrostatique ne requière pas de paramètres ajustables; il utilise la constante diélectrique du solvant H_2O-CO_2 et le paramètre de Born des espèces dominantes en phase aqueuse.

Nos résultats montrent que la mobilité des métaux dans les fluides riches en CO_2 est contrôlée par la nature et la charge de leurs complexes principaux. La présence du CO_2 favorise la stabilité des complexes neutres ($FeCl_2^0$, $AuHS^0$, $CuHS^0$, $ZnCl_2^0$, $KMoO_4^0$, $Pt(HS)_2^0$) alors que celle des espèces chargées de ces métaux ($FeCl_4^{2-}$, $Au(HS)_2^-$, $CuCl_2^-$, $ZnCl_4^{2-}$, $HMoO_4^-$, $PtCl_3^-$) est considérablement affaiblie. Il en résulte un fractionnement important de certains métaux selon la composition du fluide et le contexte géologique. Notre modèle explique bien l'enrichissement en Fe et l'appauvrissement en Cu des gisements métamorphiques d'or (orogéniques) formés par des fluides riches en CO_2. Le transport de l'or par ces fluides est favorisé à faible teneur en soufre ($Au(HS)^0$ est dominante), alors que dans les fluides riches en soufre, typiques des gisements porphyres cuprifères où les complexes chargés sont dominants ($Au(HS)_2^-$, $Au(HS)S_3^-$), la présence du CO_2 aura pour effet d'abaisser la solubilité de l'or. Cependant, même à fortes teneurs en CO_2 (>50 wt%), la capacité des fluides à transporter l'or sous forme d'espèces neutres (~100s ppb) reste comparable à celle d'un fluide aqueux, ce qui explique les associations de minéralisations aurifères avec des fluides riches en CO_2. L'effet du CO_2 sur la mobilité de Mo, Zn et Si qui forment des espèces neutres, est faible dans la plupart des contextes géologiques, alors que celle de Sn pourrait être favorisée par des complexes carbonatés et celle de Pt par des complexes carbonyles (CO). Le rôle direct du CO_2 sur le partage liquide-vapeur pour la plupart des métaux est relativement faible devant celui du soufre réduit (H_2S) dont la présence favorise fortement l'enrichissement de la phase vapeur en Au, Pt, Mo et Cu. Ainsi le CO_2 intervient dans ces processus de démixtion de manière indirecte, en élargissant le domaine *T-P* d'immiscibilité du fluide.

Cette étude démontre que, contrairement aux modèles métallogéniques actuels, la présence du CO_2 peut favoriser la mobilité de certains métaux et engendrer des fractionnements importants entre différents métaux lors de l'évolution des fluides dans la croûte terrestre.

MOTS-CLES : géochimie expérimentale, CO_2, métaux, fluide hydrothermal, solubilité, gisement métallifère.

DISCIPLINE ADMINISTRATIVE : Géochimie

INTITULE ET ADRESSE DU LABORATOIRE : Géosciences Environnement Toulouse, 14, avenue Edouard Belin, 31400 Toulouse